DISSERTATION

PERSISTENCE TIME SERIES ANALYSES, COMPLEXITY APPLIED TO NATURAL HAZARDS AND THE QUATERNARY LAKE HISTORY OF THE LERMA VALLEY, NW ARGENTINA

BRUCE D. MALAMUD

1998

Digitized by the Internet Archive
in 2022 with funding from
Public.Resource.Org

https://archive.org/details/dissertationpers00bruc

June 9, 1999
To Carl,
with all my love,
Bruce

PERSISTENCE TIME SERIES ANALYSES, COMPLEXITY APPLIED TO NATURAL HAZARDS AND THE QUATERNARY LAKE HISTORY OF THE LERMA VALLEY, NW ARGENTINA

A Dissertation
Presented to the Faculty of the Graduate School
of Cornell University
in Partial Fulfillment of the Requirements for the Degree of
Doctor of Philosophy

by
Bruce D. Malamud
January 1998

CORNELL UNIVERSITY GRADUATE SCHOOL

APPROVAL OF THESIS/DISSERTATION

Name of candidate: Bruce D. Malamud
First Name Middle Name Family Name

Graduate Field: Geological Sciences

Degree: Ph.D.

Title of Thesis/Dissertation:

Persistence Time Series Analyses, Complexity Applied to Natural Hazards, and the Quaternary Lake History of the Lerma Valley, NW Argentina

COMMITTEE SIGNATURES:

Chairperson: Teresa E Jordan Date: 18 Aug 97
Member: Peter C Date: ~~August~~ 8, 1997
Member: Date: Aug 18, 1997
Member: Date: 08/18/97

© 1998 Bruce D. Malamud

PERSISTENCE TIME SERIES ANALYSES, COMPLEXITY APPLIED TO NATURAL HAZARDS AND THE QUATERNARY LAKE HISTORY OF THE LERMA VALLEY, NW ARGENTINA

Bruce D. Malamud, Ph.D.
Cornell University 1998

This dissertation explores the Quaternary history of a NW Argentina valley, persistence in synthetic self-affine time series, and complexity applied to natural hazards. Chapter one is an introduction. Chapter two examines the Lerma Valley in NW Argentina, today an externally drained basin which in the past was partially closed and contained a large fresh-water lake. Using geologic fieldwork, laboratory work, and historical data analysis, we find that the lake was extant 1-50 ky during the period 0.78-0.1 Ma, had a surface area of 800-1300 km^2 and sedimentation rates of 1-10 m/ky. Modern denudation rates could supply enough sediment from the drainage to account for these rates, and the modern hydrologic regime could fill the lake with water in less than 500 years. Chapter three provides a framework to examine persistence techniques in self-affine time series. By using the Fourier spectral method, a white noise is appropriately filtered so that its power spectral density (S) depends upon frequency (f) according to $S \sim f^{-\beta}$. We examine fractional noises and walks with $-3 \leq \beta \leq 5$ and Gaussian and log-normal distributions. The persistence analyses compared include autocorrelation, semivariogram, rescaled-range, Fourier power spectrum, extreme-value, and wavelet

power spectrum. The last two are applied for the first time. In chapter four, self-organized critical (SOC) models are compared with actual events. The models have power-law noncumulative frequency-size distributions with exponent about 1.0, and the actual data have exponents 1.3-1.5 (forest-fires) and 2.3-3.3 (landslides). Actual forest fires are compared here for the first time with the forest-fire model; their robustness in one indicator of SOC behavior. Chapter five examines recurrence intervals of floods using power-law statistics applied to partial-duration series and the federally adopted log-Pearson type 3 (LP3) distribution applied to annual series. The great Mississippi River flood of 1993 has a recurrence interval on the order of 100 years using power-law statistics and 1,000 years using LP3. The power-law technique extended to the Colorado River finds hydrologic data are consistent with inferred paleofloods, whereas LP3 analysis gives recurrence intervals that are orders of magnitude longer. If power-law behavior is applicable, then the likelihood of severe floods is much higher.

BIOGRAPHICAL SKETCH

Bruce D. Malamud was born in Geneva, Switzerland, on July 19, 1963. His father, a high-energy physicist, and his mother, who later returned to graduate school to become a biologist, both had a profound influence on his entry into the sciences. During high school, Bruce spent his free time pursuing classical music, working at light microscopy at the McCrone Research Institute in Chicago, and through the friendship of the Donaldsons, learning photography, a passion that has deepened in the succeeding two decades. During this period, Bruce saw *Lawrence of Arabia*; this great movie strongly impacted Bruce's mental state, beginning his fascination with deserts and camels.

In 1981, Bruce entered the University of California at Santa Cruz, pursuing both music and physics. After his first year of college at UC Santa Cruz, he spent the summer doing archaeology in Southern Illinois. The next year was in Besançon, France, living with a French family and studying French at a language institute, followed by six months in Taipei, Taiwan studying Mandarin Chinese. He then spent two and a half years at Reed College, where he majored in physics while taking various courses in music. His experimental undergraduate thesis at Reed titled *Levitation by Light Pressure* was under the direction of Jean Delord.

Immediately after graduating from college in 1986, Bruce entered the Peace Corps and spent two years in Niger, West Africa, teaching physics and chemistry in French to high school students. He gave ten two-hour lectures every week to students in classes ranging from "Physics for Poets" in general science classes, to calculus-based physics for advanced students studying for the Baccalaureate Certificate. He taught

individual music courses to high school students and colleagues, organized several drawing contests, coordinated a one week in-service training program for new Peace Corps physics teachers from Benin, and served for one summer as the technical training coordinator for new Peace Corps physics and chemistry teachers.

Besides realizing that he loved teaching, the Peace Corps had another strong effect on Bruce's goals. Being in a small African town of six thousand gave him a lot of time to spend outdoors in a relatively unpopulated part of the world. He realized that although wanting to study in an intellectually demanding scientific field, he also wanted to work as an applied scientist concentrating on questions relating to the environment and humans' interaction with the earth around them. His fascination with living in a desert led to a developing interest in climate, global change, and extreme events. He was particularly interested in the climatic extremes that are a way of life in the region and was excited to see how both the land and the people in the area reacted to these extremes. He also realized one of his childhood dreams, owning a camel.

After the Peace Corps, Bruce spent two and a half years at Stanford Linear Accelerator (SLAC). He used this time to readjust to the United States while working in a "challenging" position and deciding what he wanted to study in graduate school. His first year was spent as an accelerator systems operator shaping particle beams, coordinating repairs, and maintaining human safety and accelerator protection systems. He was promoted to a deputy Operations Engineer where he monitored hardware status, ensured systems were operable when needed, coordinated each shift's research program, supervised and trained operators, and acted as person-in-charge for SLAC emergency response.

His last half year at SLAC he was promoted further to Alarms and Warnings Systems Analyst, where his position consisted of determining which alarms happened when and why, interpreting that information, and coordinating physicists, engineers, and technicians to solve the many problems found. When the money started getting good at SLAC, and the job responsibilities interesting, Bruce realized that if he did not leave soon, he might never leave this world of magnets and monitors.

In 1991, Bruce began a doctoral program in the geological sciences at Cornell University. The first three years were devoted to taking a wide variety of classes in the geological sciences, a hydrology minor, and one year of Spanish. His first year was spent as a teaching assistant and the next two years were supported by Teresa Jordan on an NSF grant. Under the direction of Teresa Jordan, Bruce did geologic fieldwork and used laboratory techniques as applied to a million-year old lake in NW Argentina. During graduate school, Bruce was fortunate to participate in various overseas field geology projects, bringing him to Argentina, Bolivia, Chile, and Norway. For the last three years of his thesis, Bruce worked under a NASA grant "Complexity and Natural Hazards" awarded to Donald Turcotte. The work with Donald Turcotte involved persistence time series analyses and the applications of complexity to natural hazards, including floods, forest-fires, earthquakes, and landslides. His Ph.D. thesis now completed, Bruce is at his next turning point in life. He aims to combine his language and cultural skills with his academic knowledge in ways that are beneficial to society and the relationship it has to the environment. Presently, Bruce is a visiting lecturer doing post-doctoral research at Cornell University and in mid-1998, he will begin research on natural hazards in Argentina as part of a Fulbright.

To my family

Although we are geographically spread far around the world,
the love I hold for you will always keep us close.

My mother and father:
Jean Goldstein Malamud and Ernest Ilya Malamud

My brother and sister:
Carl Andrew Malamud and Yvette Malamud Ozer

and

My grandfather:
Nathan Malamud

ACKNOWLEDGMENTS

It is a pleasure at this point in my dissertation to acknowledge many people for their contributions, assistance, support, and friendship during my six-year graduate career.

First and foremost, I thank my dissertation committee, Teresa Jordan, Donald Turcotte, Gerhard Jirka, and Peter Thomas. Terry and Don exercised incredible patience and skill in guiding me through the graduate experience, both had an immense impact on my current view of science. Although by nature I am detail-oriented, both Don and Terry have worked independently of each other to help me see for myself the larger issues involved in science. Both have encouraged my growth, not as a myopic scientist, but rather encouraging me to take on many different and varied projects. Terry has through excellent course teaching skills, and many conversations, helped me to gain a profound sense of the amount of time captured (and more importantly, not captured) in the stratigraphic record. Don has shared his amazing intuition of how the earth works. Over the years, both Don and Terry have been extremely generous in sharing with me their time, thoughts, and ideas; treating me at all times as a valued coworker. I also thank both for their encouragement and funds to present our research at many different conferences.

I thank the other two members of my committee, Gerhard Jirka in civil engineering and Peter Thomas in space sciences. Gerhard worked with me in an independent study on flume sediment transport, and Peter worked with me on an independent study in aeolian sediment transport. A special thanks to Wilfred Brutsaert in civil engineering, who in addition to

being my professor in an extremely interesting hydrology course, stepped in at the last minute as proxy for Gerhard Jirka at my defense.

My Lerma Valley research in Argentina (chapter two) was aided by many people. The main contact for helping me with this research was Ricardo Alonso of the University of Salta. He was the original person who contacted Teresa Jordan with the idea of studying lacustrine sediments in the Lerma Valley. He showed me many outcrops, shared his ideas, and included me in many dinners with his friends, colleagues, wife Mónica Vasile, and relatives. Finally, he helped me keep the fieldwork vehicle, a cute red Ford pickup truck, in working condition. Two graduate students at the University of Salta helped me quite a bit. Eduardo Gallardo took the time to show me Quaternary outcrops he had studied in the Lerma Valley. Raúl "Chirola" González provided an immense amount of logistical help, studied outcrops with me a number of times, and was a joy to talk to with in regards to stratigraphy.

A special thanks to William Wayne (University of Nebraska) for a large amount of intellectual and moral support in the field while he was in Salta with his wife, Naomi, on a Fulbright. They were both "other Americans" for me to turn to while in Argentina, particularly on days like Thanksgiving. Apolo Ortiz, in Buenos Aires, shared many of his extremely well-thought out ideas and theories with regards to the Quaternary history of the Lerma Valley. Undergraduate geology students at the University of Salta who helped me included Benjamín Heit, Esteban, César Abraham, Pablo Dib Ashur, and Wálter. A particular thanks to Pablo's family, who put me up for a week at their house in Salta, and Benjamin's family who put me up in their house for many weeks. Julio Betancourt (USGS, Tucson), who I met in Argentina, has

over the years provided very useful advice on which labs are good for certain analyses.

Many lab analyses and other support were required for my research in the Lerma Valley. I thank Linda Godfrey for ICP-MS analyses and interpretations, along with many other discussions related to Quaternary geochemistry; Matt Gorring, Sue Kay, and Bob Kay, for assistance with INAA analyses and interpretations; J. G. Viramonte (University of Salta) for access to the immensely useful Thematic Mapper image of the Lerma Valley; Jorge Marcuzzi (Dirección de Minería, Salta) for access to 1:50,000 Lerma Valley air photos; Julia Morgan (Cornell University) for considerable help in making a clay thin section (with only a few microcracks!); Jeff Walker (Vassar College) for XRD analyses and the time he spent with me showing how the analyses are run; D. Champion (USGS, Menlo Park) and Ken Verosub (UC Davis) for guidance and use of their paleomagnetic facilities; and Sheri Kelley (New Mexico Institute of Mining and Technology), who did all of the zircon fission track dating.

My research in time series persistence (chapter three), both theoretical and applied, benefited greatly from my association with Jon Pelletier, another student of Don Turcotte who is now at Caltech. Jon is a unique and very impressive individual, and I gratefully acknowledge him for numerous long and thought-provoking discussions in both the practical and theoretical issues involved with many aspects of fractals, persistence times series, and SOC. I particularly thank Jon for his friendship these last couple of years. In addition, I appreciated going to so many scientific conferences together. My research in persistence also benefited from the previous research of Larry Smith, who originally used the idea of examining variance in a wavelet transform.

A number of people contributed to my research on natural hazards and self-organized criticality (chapter four). April Ruebel originally found the Australian forest fire data on the internet. John Chiment made many useful comments on the manuscript which chapter four was based. Andrei Gabrielov, Chris Barton, Bill Newman, John Rundle, and Volodia Kossobokov, have all made contributions to the earthquake section of this research. Gleb Morein has done numerous detailed forest-fire model computations, a number of them used as part of my work. Gleb and I have spent many hours together discussing theoretical aspects and implications of the forest-fire model (in addition to sharing a bottle of wine and a number of stock market discussions).

Suggestions to improve the flood chapter (chapter five) when it was in manuscript form came from Jeffrey Masek, Larry Smith, and Jon Pelletier of Cornell University, Ron Charpentier and Skip Vecchia of the USGS at Denver, and one anonymous reviewer. Greg Hunt, at Cornell University, made substantial suggestions to the flood manuscript, improving dramatically its readability. Brenda Nations (USGS, Iowa City) provided recent data for the Koekuk, Iowa hydrologic station. Steve Faust (USGS, Denver) worked on putting together some of the original data. The flood research was begun during the summer of 1994, which I spent at the Denver USGS, hosted by Chris Barton. Chris provided me with office space, computers, and actively included me in his research and as a friend. Now at the USGS in Florida, Chris and his wife Sarah Tebbens, have over the years continued to provide me with friendship.

I have been on a number of very enjoyable field geology excursions over the past six years, each one aiding me to becoming a more proficient geologist. The first time I was in the field was with Rick Allmendinger

(Cornell University). Rick, an outstanding field geologist, took me in the field to Utah and Nevada the month before I started at Cornell University. Although I knew nothing about geology (this is an understatement), Rick was amazingly patient with me during these two weeks. He provided me with a particularly enjoyable and spectacular introduction to field geology which I will never forget (snow, rain, and a beautiful field area).

During the summer of 1993, I spent one month with Chris Schmidt (Western Michigan University) doing geological fieldwork in San Luis, Argentina. Carlos Costa, Carlos Gardini, and David Rivarola helped significantly in this fieldwork. Directly following Argentina, I spent one month in the Hornelen Basin in western Norway as a field assistant with Donna Anderson (Colorado School of Mines), a stratigraphy graduate student. The time with her gave me practical experience in identifying many different kinds of sedimentary structures and in stratigraphic interpretation. Others during that one-month period included Tim Cross, her advisor, and Ron Steel (UNIS, Norway).

In September 1993, I spent two weeks with Johan Erikson (Cornell University) doing field geology in Bartolo, Bolivia. Our assistants were Walter Méndez and Nelson. All field equipment for this trip was provided by Chevron in Santa Cruz, Bolivia. Johan proved to me how much fieldwork can be done in Bolivia, even with tires bursting, rivers in the way, and other “minor” setbacks. During all situations, he maintained perfect calm (except for that rather large spider one night in our room…).

In addition to the above, many other people in Argentina helped me. Jose Ares, Hector Cuappesoni, and Silvia Bordón, all at the Servicio Meteorológico Nacional in Buenos Aires, helped me in my quest for historical climatologic data. María Barón and Magarita Loyarte at

IADIZA in Mendoza spent a wonderful day with me discussing arid land issues and dunes around the Mendoza area. Víctor and Teresa Fernández were around each time for numerous things the few times I went to San Juan. Víctor Ramos at the University of Buenos Aires provided the opportunity for me to give a number of talks at the university, introduced me to many of his friends, and was an amazing person to discuss science with. Rosa Compagnucci, head of the department of meteorology at the University of Buenos Aires, has been the source of numerous interesting conversations about fractals over the years. Wolfgang Volkheimer, director of the Argentine Institute of Snow, Glaciers, and Environmental Sciences, has been especially helpful over the years. He obtained money from the United Nations so that I could come to Argentina and give a short course in fractals and chaos theory. He also has been the source of many conversations and contacts in Argentina.

Many people at Snee Hall (the Department of Geological Sciences) have helped make my research easier and added to my “quality of life.” Steve Gallow, computer person extraordinaire, in addition to insightful conversations, has always been around to help for many and varied computer problems. Joe Weaver helped with UPS, vehicles, office furniture, and many other miscellaneous items. Thanks to the many administrative staff, Tom Trenansky, Sue Peterson, Marilyn Grant, Cathy Paolangeli, Sally Carland, Lauri Wellin, and Matthew Kleinmann. All were there when I needed help.

Many scientists in the department have spent numerous hours with me on a multitude of subjects, ranging from computers, science, education, and advice. These include Muawia Barazangi, Bill Bassett, Art Bloom, Larry Brown, Larry Cathles, John Cisne, Jack Oliver, and Maura

Weathers. Rick Allmendinger, Kerry Cook, Bryan Isacks, Teresa Jordan, Bob Kay, Sue Kay, and Bill Travers, in addition to being around for numerous discussions, have all opened their houses to me and others during parties and dinners. I particularly thank Rick and Terry for the memorable and wonderful dissertation defense party they threw for me.

Jim Jenkins, in Theoretical and Applied Mechanics, spent many hours with me in a very enjoyable independent study of the physics of sediment transport. Zulma Iguina, professor of Spanish, played a major roll in me being able to communicate in Spanish the first time down to Argentina. Bill Brice, a visiting summer professor at Cornell each year, took with easy temperament the fact that his T. A. for his introduction to geology course had just come from a physics laboratory in California and had never taken a course in geology. Bill has a wonderful, non-jaded view of science, keeping science and society in easy perspective. He and his wife, Heather, have many times opened their lives to me. Thank you. Jean-Pierre Habicht of the Department of Nutritional Sciences has provided a large amount of thoughtful advice on science, third-world development issues, and life in general; he has become another real friend over the years. Three scientists from my years before Cornell continue to inspire me, Walter and Lucy McCrone at the McCrone Research Institute in Chicago, and Jean Delord at Reed College.

Many others at Snee have become friends and/or helped me with research related items. These include Alex Calvert, Chris Achong, Linda Godfrey, Matt Gorring, Dirk Vandervoort, Julia Morgan, André Revil, Kris Blouke, Joan Ramage, Jennifer Yu, Enid Williams, Elías Gomez, Kirk Haselton, Ben Brooks, Eric Fielding, Jeff Masek, Andrew Klein, Rick Forster, Aníbal Fernández, Doug Alsdorf, Troy Blodgett, Bill

Sangrey, Nathan Niemi, Francisco Gomez, Dogan Seber, Eric Sandvol, Christine Orgren, Marisa Valve, Naomi Ussami, and Peter Flemings.

Thanks to Lesley Greene (and Robbert), Chris Duncan (and Andrea), David Baird and Karen Harpp, who all included me in many activities over the years. A very special thanks to Karen Harpp, an amazing pianist, for her friendship and the hours and hours spent playing the recorder with her. *Almost Baroque* will hopefully play again someday. Jeff Abbruzzi proved to have the same love of languages and the world that I do, and we spent hours and dinners discussing topics ranging from geology to the world. Tomás Zapata and I started graduate school at about the same time, and through many hours together, he and his wife Carmen added greatly to my pleasure in being in Ithaca. Mary Parke, officemate for many years, has become a good friend and we have seen many things together during our joint stay at Cornell. Claire McCorkle, first as an undergraduate and now as a graduate student, has been a joy to be with as a student and now as a friend. Matt Burns, an officemate for a year, became a friend in that short time. Both Claire and Matt have helped considerably my appreciation of many kinds of wine.

Outside the people I have met in Snee Hall, I have gotten to know many others. We have spent many enjoyable hours together, watching movies, playing games (board games, for those who wonder), going on hikes, doing dinners, having discussions, and numerous other social activities. These have included Andy Hanushevsky, Jim Jennings, Todd Landreneau, Sandeep D'Souza, John Chiang, John Morse, Lisa Sansoucy, Mahesh Patki, James Nieh, TanTrung LeTran, Sylvain Gilat, Bijan Etemad-Moghadam, Sze Kit Hui, and Julian Kilker.

During the summer I spent lodged at the Colorado School of Mines, I spent many hours hiking and doing other activities with two physics students from Mexico, Alexander Osorio and Luis Enrique Fong de los Santos. Thank you both. A special thanks to Seth Kibel, a music major at Cornell, who spent many hours with me playing recorder duets. His inclusion of me for two pieces in his senior recital meant a lot and our duet performance at the Johnson Museum was a lot of fun. George Torres, one of the best classical guitar and lute players I have heard, also included me in a concert.

My two best friends in Ithaca have helped make the years I have spent here very special. Cleve Thomas, there are not enough words to express the admiration I have for you and your philosophy of life. Greg Hunt, partner for almost two years and now best friend. You have helped me grow in so many ways through so many experiences. Thank you.

As the people who have helped shape and support me over the years, I extend loving thanks to my family, to which this thesis is dedicated.

I gratefully acknowledge the generous support of two major research grants, both of which provided me with educational, research, travel, and living expenses for my graduate years: NSF grant EAR-9022811 awarded to Teresa Jordan and NASA innovative research grant "Complexity applied to Natural Hazards" NAGW-4702 awarded to Donald Turcotte.

TABLE OF CONTENTS

Biographical Sketch iii
Dedication vi
Acknowledgements vii
Table of Contents xvi
List of Tables xix
List of Figures xx

1 Introduction 1

2 The Quaternary Lake History of the Lerma Valley, Salta Province, NW Argentina 5
ABSTRACT 5
INTRODUCTION AND STUDY AREA 6
METHODS EMPLOYED 9
STRATIGRAPHY 9
TOPOGRAPHY AND LAKE SIZE 23
GEOCHRONOLOGY 25
PROVENANCE AND FINGERPRINTING 31
SEDIMENT AND WATER BUDGET 38
CONCLUSIONS 44
APPENDIX 2.1. BLACK AND WHITE OF FIGURE 2.6 45
REFERENCES 46

3 Persistence Analyses of Self-Affine Time Series 48
ABSTRACT 48
3.1 INTRODUCTION 50
3.1.1 *Brief Overview of Paper* 50
3.1.2 *What is a Time Series?* 52
3.1.3 *How is a Time Series Quantified?* 56
3.1.4 *Autocorrelations and Semivariograms* 59
3.1.5 *Self-Affine Fractals* 65
3.1.6 *Gaussian White Noises and Brownian Motions* 71
3.2 SPECTRAL ANALYSIS 80
3.2.1 *The Fourier Transform* 80
3.2.2 *The Power-Spectral Density* 85
3.2.3 *The Relation of β, Ha, and D* 95
3.2.4 *Weak vs. Strong Persistence* 100
3.2.5 *Spectral Variance and Leakage* 102
3.3 SYNTHETIC FRACTIONAL NOISES AND MOTIONS 106
3.3.1 *What are they?* 106
3.3.2 *Spectral Analysis* 107

3.3.3 *Method of Successive Random Additions* 122
3.3.4 *Semivariograms* 127
3.4 LOG-NORMAL NOISES AND MOTIONS 130
3.4.1 *Log-normal Distributions* 130
3.4.2 *Fractional Log-normal Noises and Motions* 133
3.4.3 *Spectral Analysis* 136
3.4.4 *Semivariograms* 137
3.5 RESCALED-RANGE (R/S) ANALYSIS 141
3.5.1 *The Method* 141
3.5.2 *Applications to Fractional Gaussian Noises and Motions* 146
3.5.3 *Applications to Fractional Log-normal Noises and Motions* 149
3.6 AVERAGE EXTREME-VALUE ANALYSIS 152
3.6.1 *The Method* 152
3.6.2 *Applications to Fractional Gaussian Noises and Motions* 153
3.6.3 *Applications to Fractional Log-normal Noises and Motions* 156
3.7 WAVELET ANALYSIS 159
3.7.1 *The Method* 159
3.7.2 *Applications to Fractional Gaussian Noises and Motions* 163
3.7.3 *Applications to Fractional Log-normal Noises and Motions* 170
3.8 SUMMARY 176
APPENDIX 3.1. ABBREVIATIONS AND SYMBOLS 181
REFERENCES 184

4 Self-Organized Criticality Applied to Natural Hazards 190
ABSTRACT 190
INTRODUCTION 191
SELF-ORGANIZED CRITICALITY 193
Sandpile Model 193
Slider-Block Model 194
Forest-Fire Model 195
FOREST FIRES 196
Forest-Fire Model 196
Forest-Fire Model Results 199
Site-Percolation Model 204
Cumulative vs. Noncumulative Data 208
Actual Forest Fires 212
LANDSLIDES 220
Sandpile Model 220
Sandpile Model Results 222
Sandpiles in the Laboratory 223
Turbidites 224
Actual Landslides 227
EARTHQUAKES 237
Slider-Block Model 237
Slider-Block Model Results 240

Actual Earthquakes ... 243
The Seismic Intensity ... 253
CONCLUSIONS ... 261
APPENDIX 4.1. ABBREVIATIONS AND SYMBOLS ... 264
APPENDIX 4.2. BLACK AND WHITE OF FIGURES 4.19 AND 4.20 ... 266
REFERENCES ... 270

5 The 1993 Mississippi River Flood: A One Hundred or a One Thousand Year Event? ... 278
ABSTRACT ... 278
INTRODUCTION ... 279
DISTRIBUTIONS ... 281
Power-Law ... 281
Log-Pearson Type 3 ... 284
DATA ANALYSIS ... 284
Annual and Partial-Duration Flood Series ... 284
Data ... 286
RESULTS ... 287
Mississippi River at Keokuk, Iowa ... 287
Colorado River Paleofloods ... 293
DISCUSSION ... 296
CONCLUSIONS ... 298
REFERENCES ... 300

LIST OF TABLES

2.1 Global lake distribution today 24
2.2 LOI and XRF trace and major elements for Lerma Valley tuffs and clays 35
2.3 Characteristics of three hydrologic stations, Salado drainage basin 41
2.4 Filling rate for the Lerma Valley given modern-day climatic conditions 43

3.1 Legend for symbols used in Gaussian noise and motion analyses 113
3.2 Legend for symbols used in log-normal noise and motion analyses 136

4.1 Levels of regional seismicity 256

LIST OF FIGURES

2.1 Map view of the central Andes; topographic profile at 24° 47’ S........................7
2.2 Lerma Valley topography overlaid on an area TM satellite image....................10
2.3 Lerma Valley topography without underlying TM image. Minimum and maximum Lerma lake extents indicated....................................12
2.4 Stratigraphic cross sections for Arroyos San Vicente and Tajamar...................15
2.5 Stratigraphic sections and chronologic data for Q units in the Lerma Valley....16
2.6 Photographs of Tajamar Formation lacustrine clays, Rumical outcrop 21
2.7 Lerma Valley tuffs: Zircon fission-track ages and histograms 26
2.8 Geomagnetic inclination *vs.* stratigraphic level in the Rumical outcrop............29
2.9 Paleomagnetism, Zijderveld diagram for Rumical lacustrine clay, meter 5 30
2.10 Quaternary geomagnetic polarity chart with Lake Lerma age constraints.........32
2.11 X-ray fluorescence (XRF) and loss on ignition analyses of Rumical clays.......34
2.12 Comparison of trace elements, Rumical clays and Lerma Valley tuffs 37
2.13 Drainage network for NW Argentina...38
2.14 Filling Pleistocene Lake Lerma with sediment given denudation rates today...40
2.15 Filling Pleistocene Lake Lerma with water given climatic conditions today 42

3.1 Three examples of time series...54
3.2 Illustration of a deterministic self-affine fractal...68
3.3 Box-counting technique applied to a self-affine fractal 70
3.4 Four Gaussian white noises summed to give Brownian motions.......................72
3.5 Box counting for the standard deviations of a self-affine fractal 76
3.6 Two power-spectral analysis examples, white noise and Brownian motion......88
3.7 Rescaling a self-affine time series...96
3.8 Stationarity and nonstationarity of self-affine time series...............................102
3.9 An example of power-spectral filtering..108
3.10 Five fractional Gaussian noises (fGN’s) and five fractional Brownian motions (fBM’s) created by spectral filtering and summing 110
3.11 Example of windowing, the power-spectral density for a fBM with $\beta = 2.5$...114
3.12 Same as Figure 3.11, but for a fBM with $\beta = 1.5$..117
3.13 The dependence of the power-spectral exponent, β_{PS}, on β, for a series of synthetic fGN’s and fBM’s 121
3.14 Illustration of fBM generation using successive random additions 123
3.15 A sequence of fBM’s generated by successive random additions 126
3.16 Semivariograms for fGN’s and fBM’s...128

3.17 Dependence of the Hausdorff measure, *Ha*, on β, for fGN's and fBM's 129
3.18 Probability distribution function for the log-normal distribution.....................132
3.19 Examples of synthetic fractional log-normal noises and motions....................135
3.20 Dependence of the power-spectral exponent, β_{PS}, on β, fractional log-normal noises and motions 138
3.21 Semivariograms for fractional log-normal noises and motions, $c_v = 0.5$.........139
3.22 Dependence of the Hausdorff measure, *Ha*, on β, fractional log-normal noises and motions 140
3.23 Illustration of rescaled-range (*R*/*S*) analysis...142
3.24 Rescaled-range (*R*/*S*) analyses for fGN's and fBM's......................................147
3.25 Dependence of the Hurst exponent, *Hu*, on β, fGN's and fBM's 148
3.26 Rescaled-range (*R*/*S*) analyses for fractional log-normal noises, $c_v = 0.5$ 150
3.27 Dependence of the Hurst exponent, *Hu*, on β, fractional log-normal noises and motions 151
3.28 Average extreme-value analyses for fGN's and fBM's 154
3.29 Dependence of the extreme-value exponent, *He*, on β, fGN's and fBM's 155
3.30 Average extreme-value analyses for fractional log-normal noises and motions 157
3.31 Dependence of the extreme-value exponent, *He*, on β, fractional log-normal noises and motions 158
3.32 Mother Mexican hat wavelet...161
3.33 Wavelet transform *W*(*t*, *a*) for fGN's and fBM's 164
3.34 Wavelet variance analyses for fGN's and fBM's...168
3.35 Dependence of the wavelet variance exponent, *Hw*, on β, fGN's and fBM's .169
3.36 Wavelet transform *W*(*t*, *a*) for fractional log-normal noises and motions........171
3.37 Wavelet variance analyses for fractional log-normal noises and motions 174
3.38 Dependence of the wavelet variance exponent, *Hw*, on β, fractional log-normal noises and motions 175

4.1 Illustration of the forest-fire model 198
4.2 Four examples of typical model forest fires 200
4.3 Noncumulative frequency-size distributions for model forest fires, constant grid size and changing firing frequency 202
4.4 Noncumulative frequency-size distributions for model forest fires, changing grid size and constant firing frequency 203
4.5 Illustration of cumulative *vs.* noncumulative frequency-size distributions......209
4.6 Cumulative frequency-area distributions, USA and Australia forest fires.......213
4.7 Noncumulative frequency-area distributions, USA and Australia forest fires.217

4.8 Illustration of the sandpile model 221
4.9 Noncumulative frequency-size distributions, sandpile model 223
4.10 Cumulative frequency-thickness distributions, turbidites 226
4.11 Cumulative frequency-area distributions, actual landslides 228
4.12 Noncumulative frequency-area distributions, actual landslides 231
4.13 Illustration of the two-dimensional slider-block model 238
4.14 Noncumulative frequency-size distributions, slider-block model 242
4.15 Worldwide cumulative and noncumulative number of earthquakes per year ..244
4.16 Number of earthquakes per year occurring in southern CA 247
4.17 Cumulative number of earthquakes for each year, 1980-1994, southern CA ..249
4.18 Cumulative number of earthquakes per year, Memphis-St. Louis 252
4.19 Global map of the seismic intensity factor 254
4.20 USA and Europe maps of the seismic intensity factor 257
4.21 Similarity basis for extending the seismic intensity factor to higher earthquake magnitudes 260

5.1 USA map showing upper MI River basin and extent of 1993 flooding 282
5.2 Data and best fits (LP3 and power-law) for Keokuk, Iowa, 1879-1992 288
5.3 Data and best fits (LP3 and power-law) for Keokuk, Iowa, 1879-1995 289
5.4 Best-fit curves for Keokuk, Iowa, extrapolated to the maximum flow during the 1993 Mississippi flood 292
5.5 Data and best fits for Lees Ferry, Arizona (1921-1962), along with two paleoflood discharge estimates 294

Chapter One: Introduction

This dissertation explores the Quaternary history of the Lerma valley in NW Argentina, persistence in synthetic self-affine time series, and complexity applied to natural hazards. Ranging from geological fieldwork to statistical geophysics, my research illustrates several different approaches that can be applied in studying the environment

In chapter two, I examine the Lerma Valley in NW Argentina, today an externally drained basin which in the past was partially closed and contained a large fresh-water lake. The primary motivations for doing this research were to examine outcrop lake deposits presently found in various locations in the valley, provide spatial and temporal constraints on this past lake, and determine whether the lake could only have existed in a climate much different than that of today. Research included geologic fieldwork, historical data analysis, and laboratory work--major and trace element identification, paleomagnetism and fission track dating.

My main conclusions in this research were that the lake was extant 1 to 50 ky (thousand years) during a period from 0.78-0.1 Ma (million years ago), had a surface area of 800-1,300 km^2 and sedimentation rates of 1-10 m/ky. Modern denudation rates can supply enough sediment from the drainage to account for these rates. The lake origin and demise were probably related to valley damming, possibly by landslides, and dam rupturing at the present outlet of the valley. Contrary to what scientists who knew of the Lerma Valley lacustrine outcrops previously thought, the climate did not have to be (although it could have been) much different than today's climate for the lake to form.

Geochronology has been another contribution of my Lerma Valley research. Four tuffs and ashes were dated and correlated in time with others using trace and major elements; all provide useful time boundaries for future research in the valley. More importantly, my tuff dating of a Piquete Formation horizon shows that the last major phase of deformation in the Lerma Valley occurred more recently than 1.1±0.2 Ma. Previous to my research, this last major phase of deformation had always been thought to precede the Pliocene/Pleistocene boundary (1.76 Ma).

Chapter three provides a framework to examine persistence techniques in self-affine time series. Persistence refers to the memory or internal correlation within a time series. Many statistical techniques assume that the values in a time series are completely independent, *i.e.* similar to a white noise where there is no correlation. If persistence exists, care needs to be taken in the statistical techniques used. Ranging from biology to hydrology to economics, scientists in the last couple of decades have been concerned with the range and strength of persistence in time series. They have used the persistence qualities of a time series to improve the statistical techniques used in understanding other attributes of the time series, designed physical models which incorporate persistence (*e.g.* forecasting), and designed theoretical models based on the idea that certain systems in nature always have a given degree of persistence.

In chapter three, I have constructed synthetic time series (fractional noises and motions) with known persistence properties. These included both Gaussian and log-normal distributions. Then, after discussing the theoretical aspects, I examine how different persistence techniques compare to each other in the analysis of the synthetic time series. The fractional noises are constructed by using the Fourier spectral method,

where a white noise is appropriately filtered so that its power spectral density (S) depends upon frequency (f) according to $S \sim f^{-\beta}$. I examine fractional noises and motions with $-3 \leq \beta \leq 5$.

The persistence analyses that are compared include autocorrelation, semivariogram, rescaled-range, Fourier power spectrum, extreme-value, and wavelet power spectrum. My research provides a framework for the general issue of persistence in time series. Also, I apply extreme-value and wavelet power spectrum analyses to fractional Gaussian noises and motions for the first time. Additionally, none of these techniques have been compared before with respect to log-normal noises. Among my conclusions, I find that the Hurst technique, used commonly by hydrologists, does a poor job of estimating the correct persistence of a time series as the statistical distribution gets farther away from Gaussian, and also has significant problems with estimation as the size of the data set decreases. Another conclusion is that wavelets are a superior way, compared to previously used techniques, of extracting the persistence properties of time series, both with Gaussian and log-normal distributions.

Chapters four and five are both concerned with complexity as applied to natural hazards. My interest in these chapters is in taking theoretical ideas from fractals and self-organized criticality (SOC), and applying these to real-world problems. One of these problems is how to forecast how often a given natural hazard will occur, and what is the underlying frequency-size distribution of these events. This has relevance to insurance companies, engineers, and in general, to hazard mitigation.

In chapter four, self-organized critical models are compared with actual forest fires, landslides, and earthquakes. Forest fires from a variety of geographic regions are found to have nearly equal fractal dimensions.

Their robustness is one indicator of SOC behavior, indicating that forest fires are possibly a good example for SOC behavior. Before my research, the only well-know example of a natural hazard exhibiting SOC behavior was earthquakes. The research in this chapter includes the first time actual forest fires have been compared with the forest-fire model. Besides the theoretical questions of SOC behavior, there is the more practical one of the underlying frequency-area distribution for forest fires. My research shows that this distribution has very robust power-law statistics. Therefore, given historical forest-fire data for a region, one can forecast how big a fire one would expect over a given time period. This chapter also examines landslides from a variety of regions. I find similar fractal dimensions for different regions, and a dimension that is clearly different from that of forest fires and earthquakes. The sandpile model is not found to be a good analog for actual landslides. My main contribution in this chapter is taking various natural hazards, and showing how they fit into a framework of self-organized criticality.

Chapter five examines recurrence intervals of floods using power-law statistics applied to partial-duration series and the federally adopted log-Pearson type 3 (LP3) distribution applied to annual series. Data from Keokuk, Iowa, shows the great Mississippi River flood of 1993 has a recurrence interval on the order of 100 years using power-law statistics and 1,000 years using LP3. The power-law technique extended to the Colorado River finds hydrologic data are generally consistent with inferred paleofloods, whereas LP3 analysis gives recurrence intervals that are orders of magnitude longer. Power-law statistics predict much shorter recurrence intervals (a much higher likelihood of severe floods) than federally adopted LP3 statistics.

Chapter Two: The Quaternary Lake History of the Lerma Valley, Salta Province, NW Argentina[*]

ABSTRACT

Lying along the eastern flank of the Andes is a narrow climatic and topographic transition zone from the Puna plateau to the Chaco plains. Valleys in this zone contain sediments that are potentially sensitive registers of Quaternary paleoclimates. One such example is the Lerma Valley in the Salta Province of NW Argentina. Today, the Lerma Valley and the eastern Andean Cordillera is an externally drained basin but in the past was partially closed with a spillway and contained a large fresh-water lake. Existing topography and spatial distribution of lake facies indicate that Lake Lerma was 70-90 km long (N-S), 14-18 km wide (W-E), and had a surface area of 800-1,300 km^2. Dates on intercalated volcanic tuffs indicate that, after tectonic deformation (<1.3±0.2 Ma), fluvial (Calvilmonte Formation) and then lacustrine systems (Lake Lerma) were both active 1.05-0.1 Ma. Based on normal magnetic polarity, these fluvial and lacustrine deposits probably accumulated in the time span 0.78-0.1 Ma. La Viña Formation aggradation has occurred since 0.1 Ma. Lake clays are rhythmic, expressed in millimeter to cm-thick white layers alternating with mm-thick darker colored layers. A systematic shift of 45° in magnetic inclination through 6 m of lake rhythmites may indicate that 0.5-5 ky are spanned by that outcrop. If so, the average 1 cm thick rhythmites are 1-10 yr events with sedimentation rates 1-10 m/ky. Modern denudation rates could supply enough sediment from

---

[*] Published as: Malamud, B. D., Jordan, T. E., Alonso, R. A., Gallardo, E. F., González, R. E., and Kelley, S. A. (1996) Pleistocene Lake Lerma, Salta Province, NW Argentina: *Proceedings of XIII Argentine Geology Congress, Buenos Aires, Argentina, Oct 13-18, 1996*, **4**:103-114.

the drainage network to account for these accumulation rates and to deposit all the Lake Lerma deposits in 1-50 ky. The source of lake clay might be secondary transport of wind-blown ashes which have similar trace element patterns. An alternative source is basement rocks that cover much of the drainage network feeding into the Lerma Valley. The origin and demise of Lake Lerma were probably related to valley damming and dam rupturing at the present outlet of the Cabra Corral reservoir, which feeds into the Río Juramento, rather than to major climate change.

INTRODUCTION AND STUDY AREA

Along the eastern flank of the Andes in Bolivia and Argentina, there is a 50-200 km wide climatic and topographic transition zone from the high arid Puna plateau to the low, much more humid, Chaco plains (Figure 2.1). Valleys in this narrow zone, such as the Lerma Valley in the Salta Province of NW Argentina (Figure 2.1) contain little-studied sediments that are potentially sensitive registers of Quaternary paleoclimates. Today, the intermontane Lerma Valley is an externally drained basin, but in the past it was partially closed with a spillway and contained a large fresh-water lake.

In this paper we: 1) constrain the size of the lake using topographic data, 2) constrain the age of Lake Lerma using paleomagnetism and ages of tuffs from above and below the lake, 3) advance a hypothesis for the temporal content of individual rhythmites using paleomagnetic secular variations, 4) present elemental and mineralogical information obtained from lake clays and ashes, and 5) discuss the origin and demise of Lake Lerma and the possible provenance of the large quantity of well-sorted lacustrine clays deposited within the lake.

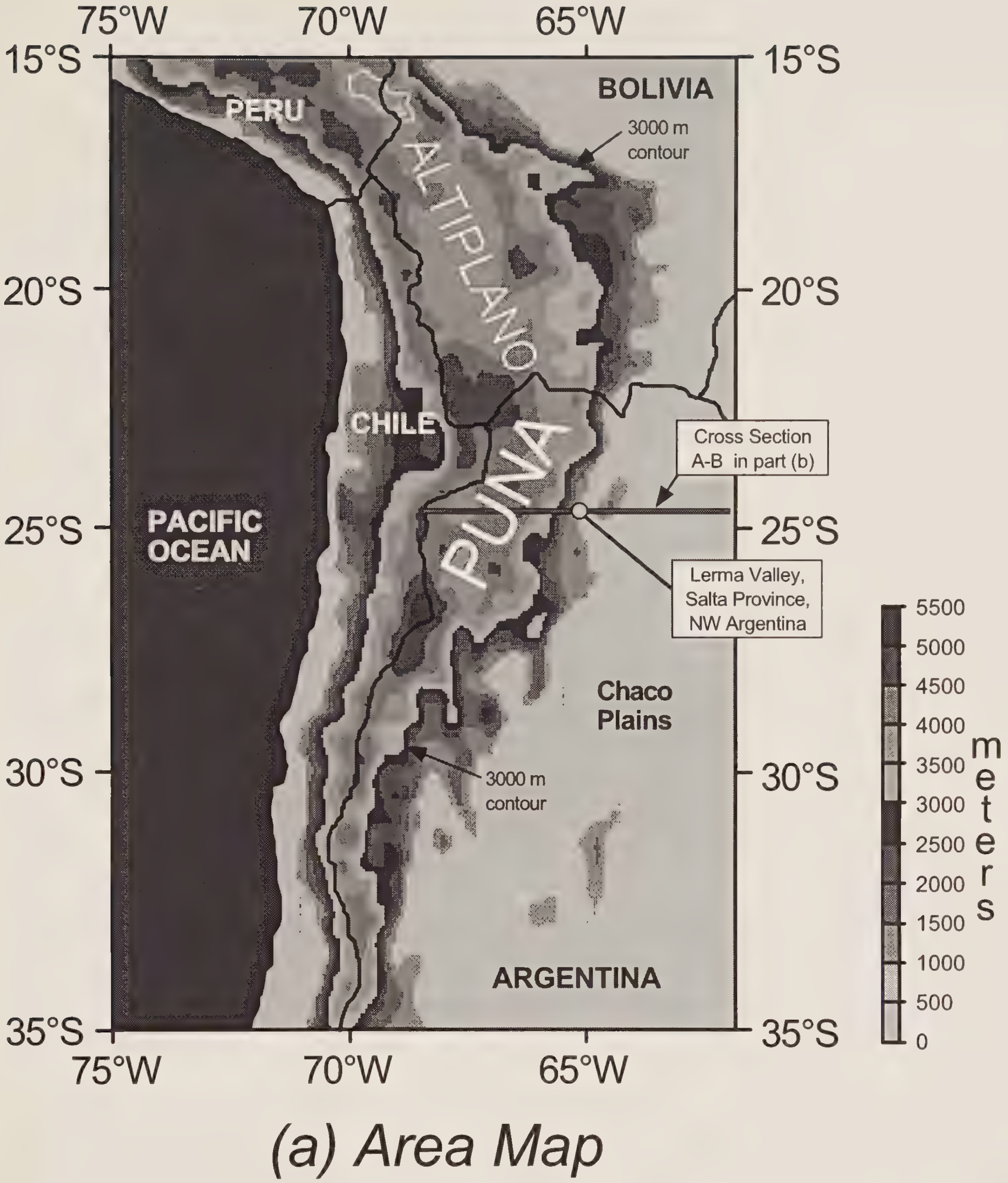

Figure 2.1. (a) Map view of central Andes topography in meters above sea level. The study area, Lerma Valley, is marked. Elevation data from ETOPO-5 (NOAA). (b) Topographic profile at 24°47' S passing through Salta from the Puna to the Chaco plains. Figure after the *Atlas Total de la República Argentina, Físico* (p. 90, 1981)

Figure 2.1 (Continued)

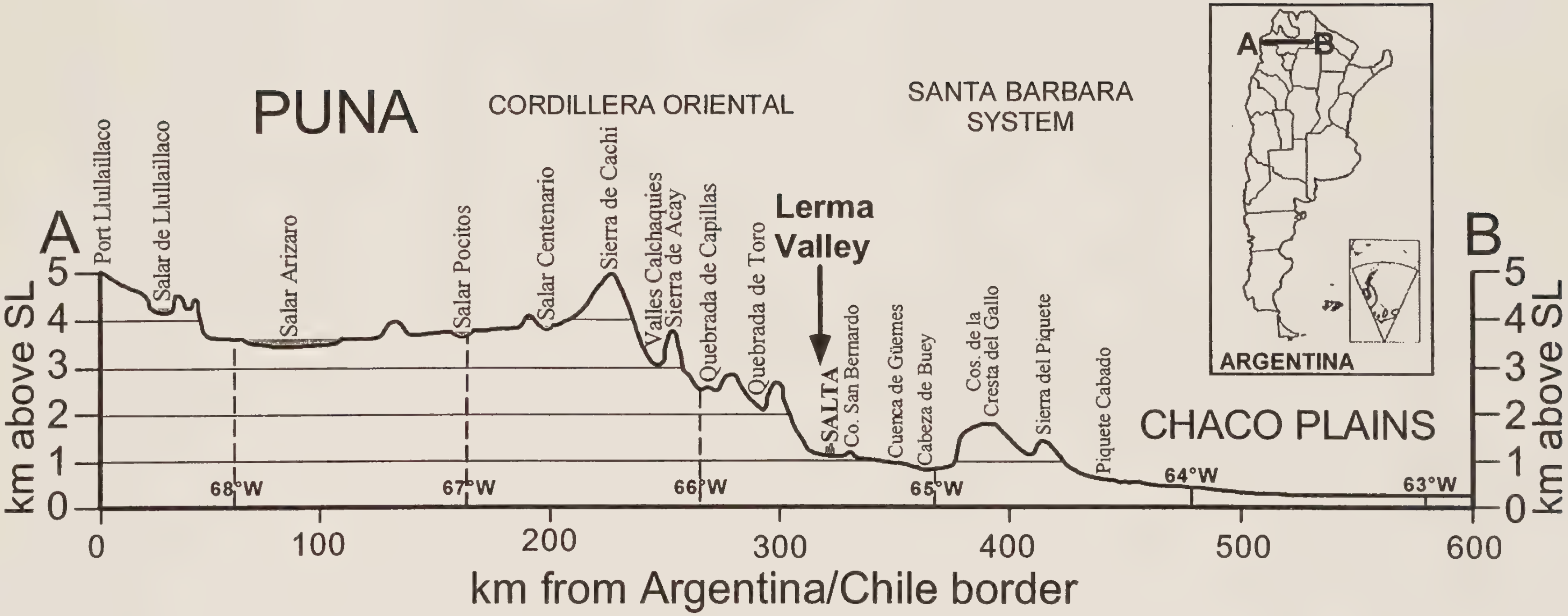

(b) Cross-Section

METHODS EMPLOYED

This investigation of Lake Lerma uses topographic data, fieldwork, historical climate data, and laboratory techniques. Topographic data at 100 m contour intervals (Figures 2.2, 2.3) combined with elevation measurements of lacustrine facies allow us to constrain the size of Lake Lerma. Fieldwork included stratigraphic interpretations and sample collection at road cuts and arroyo walls; four representative outcrops are discussed (Figures 2.4, 2.5). Laboratory work consisted of (i) relative and absolute geochronology using C-14 (Figures 2.4b, 2.5d), zircon fission-tracks (Figure 2.7), paleomagnetism (Figures 2.8 and 2.9), and (ii) element and mineralogical analysis of clays and tuffs using neutron activation (Figure 2.12), mass spectrometry (Figure 2.12), X-ray Fluorescence (Figure 2.11, Table 2.2), and X-ray Diffraction. Historical climate data allow us to compare modern denudation rates with clay accumulation rates in Lake Lerma, and to calculate whether modern conditions are sufficient to form a lake of Lake Lerma's magnitude. Those data include watershed area, evaporation, river suspended sediment loads and discharge (Figure 2.13).

STRATIGRAPHY

The stratigraphy of Lerma Valley Tertiary sediments is summarized by *González* (1995). The Quaternary nomenclature used here, Calvilmonte, Tajamar, and La Viña Formations, follows the extensive studies of *Gallardo* (1985). Locations of outcrops we used in this study are shown in Figures 2.2 and 2.3.

Figure 2.2. Lerma Valley topographic contours at 1100, 1200, and 1300 m are overlaid on a Thematic Mapper (TM) satellite image of area. Shown are locations of several representative Quaternary outcrops in the Lerma Valley: Campo Alegre, Río Arenales (A), Rumical (R), Arroyos San Vicente and Tajamar. Stratigraphic sections for these outcrops are given in Figures 2.4 and 2.5. Sumalao (S) and Calvilmonte (C) are outcrops very similar to Rumical. Color photocopy of TM images 231-77 (11/14/86) and 231-78 (9/11/86), bands 741, processed by K. Erpenstein, FU Berlin Geoinformatik. Topography from 1:50,000 *Mapa Base Topográfico del Valle de Lerma* (1987). Due to different projections, the TM image and topographic contours do not align perfectly.

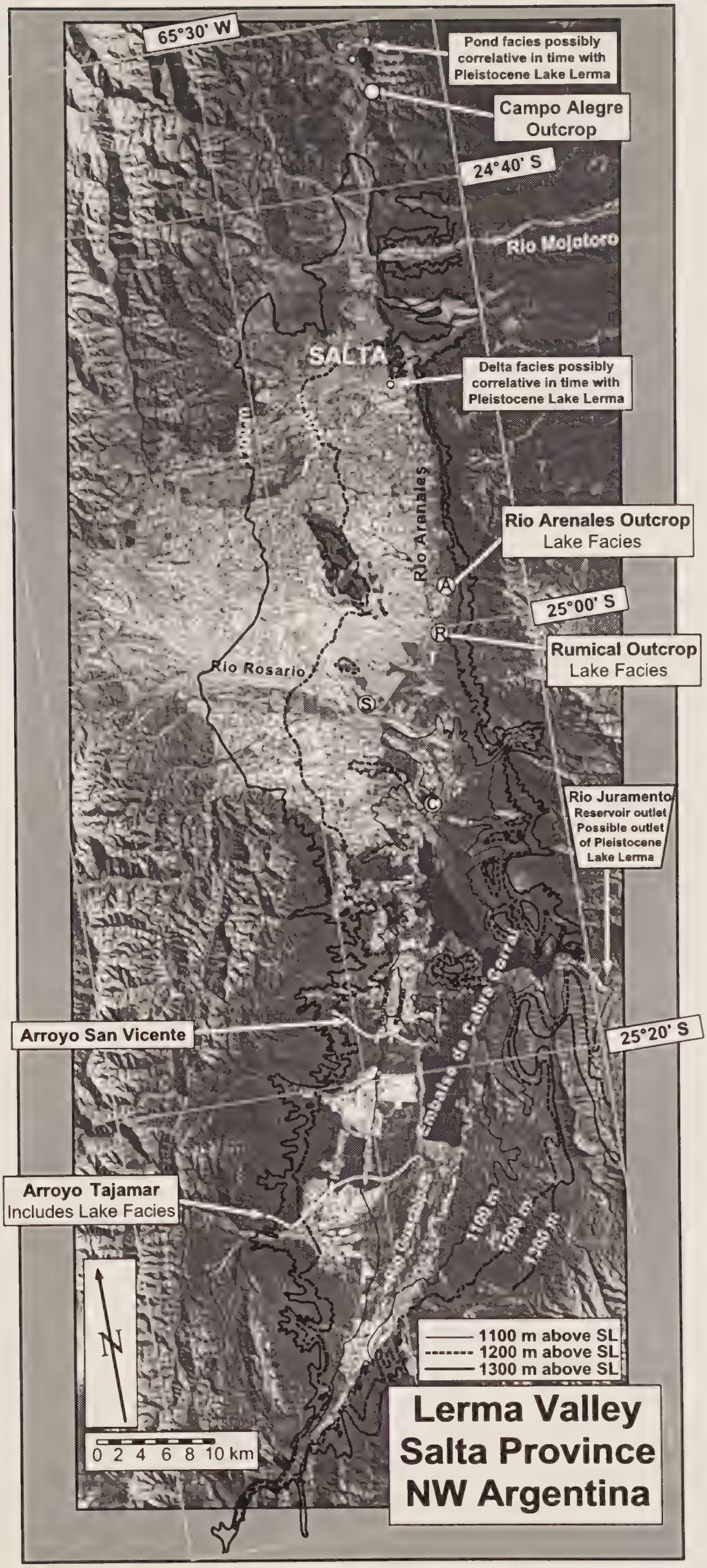
65°30' W
Pond facies possibly correlative in time with Pleistocene Lake Lerma
Campo Alegre Outcrop
24°40' S
Rio Mojotoro
SALTA
Delta facies possibly correlative in time with Pleistocene Lake Lerma
1200m
Rio Arenales
Rio Arenales Outcrop Lake Facies
A
25°00' S
R
Rumical Outcrop Lake Facies
Rio Rosario
S
C
Rio Juramento Reservoir outlet Possible outlet of Pleistocene Lake Lerma
Embalse de Cabra Corral
Arroyo San Vicente
25°20' S
Arroyo Tajamar Includes Lake Facies
1100 m
1200 m
1300 m
N
0 2 4 6 8 10 km
1100 m above SL
1200 m above SL
1300 m above SL
Lerma Valley
Salta Province
NW Argentina

Figure 2.3. Lerma Valley topography without underlying TM Image. The elevation of lake facies and existing topography aid in constraining the surface area of Lake Lerma. The minimum lake extents are at about 1,140 m elevation and are shown in gray. The maximum lake extents are at about the 1,200 m contour line.

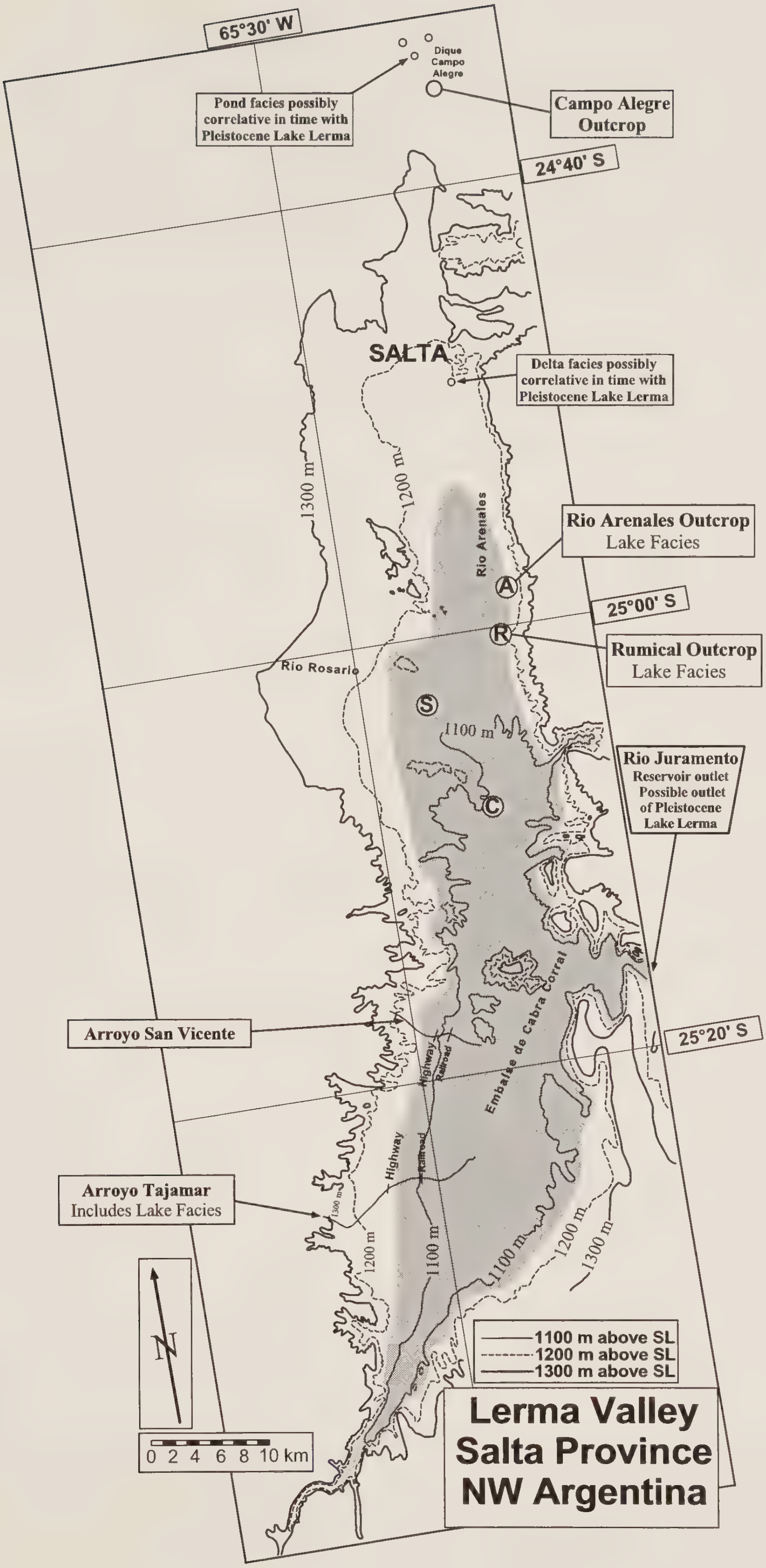
65°30' W
Dique Campo Alegre
Pond facies possibly correlative in time with Pleistocene Lake Lerma
Campo Alegre Outcrop
24°40' S
SALTA
Delta facies possibly correlative in time with Pleistocene Lake Lerma
1300 m
1200 m
Rio Arenales
Rio Arenales Outcrop
Lake Facies
A
25°00' S
R
Rumical Outcrop
Lake Facies
Rio Rosario
S
1100 m
Rio Juramento
Reservoir outlet
Possible outlet of Pleistocene Lake Lerma
C
Embalse de Cabra Corral
Arroyo San Vicente
25°20' S
Highway
Railroad
Highway
Railroad
Arroyo Tajamar
Includes Lake Facies
1300 m
1200 m
1100 m
1100 m
1200 m
1300 m
N
0 2 4 6 8 10 km
1100 m above SL
1200 m above SL
1300 m above SL
Lerma Valley
Salta Province
NW Argentina

The Piquete Formation (Figures 2.4a, 2.5d) is part of the strongly deformed Oran Group and is the youngest formation in this region that exhibits major tilting. This aggrading alluvial system with beds of conglomerate intercalated with sandstone is widespread over hundreds of kilometers, exceeding thicknesses of 1,000 m in the southern Lerma Valley. Dated Tuff A (1.3 ± 0.2 Ma, Figure 2.7) demonstrates that Piquete deposition in this area continued into the Pleistocene.

The Calvilmonte Formation (Figures 2.4b, 2.5d) is found only in the southern part of the Lerma Valley and is composed of fluvial deposits consisting of fine- to medium-grained sandstone. Calvilmonte has a minimum thickness of 10 m and its base is exposed nowhere in the valley.

The Tajamar Formation (Figure 2.4b, 2.5bcd) consists of lacustrine system deposits and is dominated by horizontally laminated clay rhythmites of millimeter to cm-thick white or pink layers alternating with mm-thick darker colored layers. These darker layers vary from black, yellow, red, to orange. Tajamar overlies Calvilmonte across a sharp planar unconformity and is remarkable for its large quantity (>10 m) of very fine-grained material (70% clay size particles). Photographs of Tajamar formation lacustrine clays from the Rumical outcrop are given in Figure 2.6.

La Viña Formation (Figures 2.4, 2.5cd) is found throughout the Lerma Valley and consists of aggrading fluvial system deposits including overbank and channel deposits, paleosols, and ashes. With thicknesses up to 20 m, La Viña overlies Tajamar and older formations across an erosional unconformity containing channels with greater than 10 m relief.

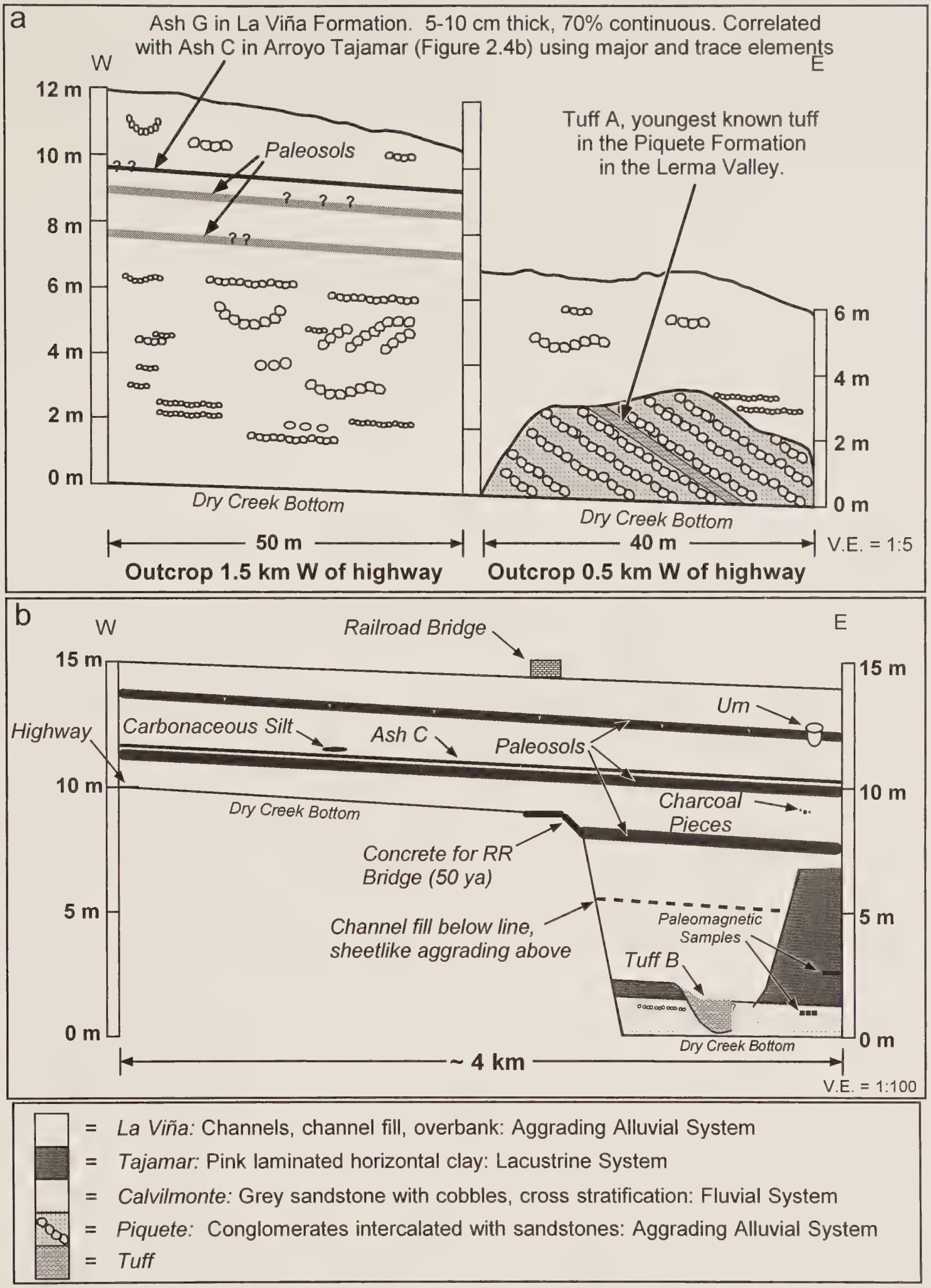
a
Ash G in La Viña Formation. 5-10 cm thick, 70% continuous. Correlated with Ash C in Arroyo Tajamar (Figure 2.4b) using major and trace elements
W
E
12 m
10 m
8 m
6 m
4 m
2 m
0 m
Paleosols
? ?
? ? ?
Tuff A, youngest known tuff in the Piquete Formation in the Lerma Valley.
6 m
4 m
2 m
0 m
Dry Creek Bottom
Dry Creek Bottom
50 m
40 m
V.E. = 1:5
Outcrop 1.5 km W of highway
Outcrop 0.5 km W of highway
b
W
E
Railroad Bridge
15 m
15 m
Highway
Carbonaceous Silt
Ash C
Paleosols
Um
10 m
10 m
Dry Creek Bottom
Charcoal Pieces
Concrete for RR Bridge (50 ya)
5 m
5 m
Channel fill below line, sheetlike aggrading above
Paleomagnetic Samples
Tuff B
0 m
0 m
Dry Creek Bottom
~ 4 km
V.E. = 1:100
= La Viña: Channels, channel fill, overbank: Aggrading Alluvial System
= Tajamar: Pink laminated horizontal clay: Lacustrine System
= Calvilmonte: Grey sandstone with cobbles, cross stratification: Fluvial System
= Piquete: Conglomerates intercalated with sandstones: Aggrading Alluvial System
= Tuff

Figure 2.4. Stratigraphic cross sections of two Lerma Valley arroyos (locations in Figures 2.2, 2.3). (a) Arroyo San Vicente includes La Viña and Piquete formations. (b) Arroyo Tajamar includes Calvilmonte, Tajamar, and La Viña formations.

Figure 2.5. Stratigraphic sections and distribution of chronologic data for Quaternary units in the Lerma Valley (locations in Figures 2.2 and 2.3). (a) In the Campo Alegre Section, Tuff D is found in the context of a generally aggrading alluvial system with thin intercalations of paleosols and/or possible pond deposits. Strata exposed at (b) the Rumical Section and (c) the Río Arenales Section exemplify the Tajamar Formation lacustrine facies of the northern region of Lake Lerma. The Rumical section is also representative of sites S and C in Figures 2.2 and 2.3. (d) In this composite stratigraphic section for the southwestern Lerma Valley, Arroyo Tajamar (Figure 2.4b) is used to construct 0-20 m and Arroyo San Vicente (Figure 2.4a) is used to place the Piquete Formation.

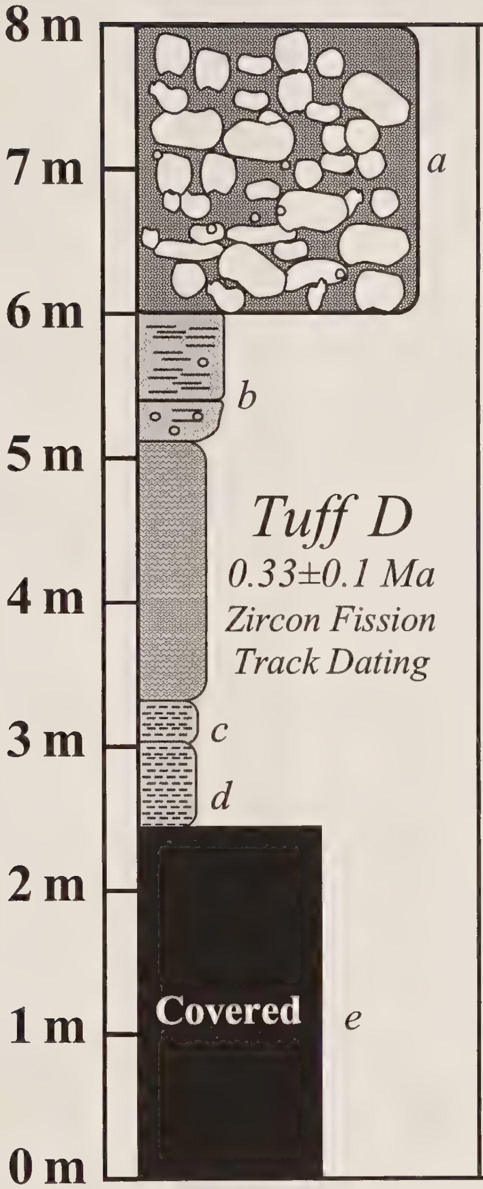

a) This **aggrading alluvial system** consists of subrounded to rounded gravel, 1-10 cm clasts, matrix supported with a sharp contact which has 1 m of relief on the bottom. As we get higher in the section (outcrop to N), the section has finer grained sediments, but is still part of an aggrading alluvial system.

b) This section consists mostly of **silty-clay**, is 75 cm thick with 5-10% 10-15 cm pebbles in the first 15 cm, then very few pebbles. Manganese filaments and clay skins are present. Sharp contacts, top and bottom.

Tuff D is 0.5-2 m thick, thins to the N and S over 20 m (trough). It is not seen in nearby outcrops and has sharp contacts, top and bottom. It is located on RP 9, km 1626.0, at 24° 34.85' S, 65° 21.77' W.

c) This **overbank** section is 20 cm thick, sandy silt, with burrowing and manganes threads. The overbank material is probably part of an alluvial system. The top is very sharp.

d) Buried soil or shallow pond that is 50 cm thick, silty clay, with very dark brown large blocky masses, manganese filaments, oxidation, and clay skins. The top is gradational.

e) The bottom of this section is **covered**. This section may be stratigraphically above outcrops to the south which consist of 1-5 cm sized clasts that are in a suported conglomerate matrix with hardened oxidized layers.

(a) Campo Alegre Section

Figure 2.5 (Continued)

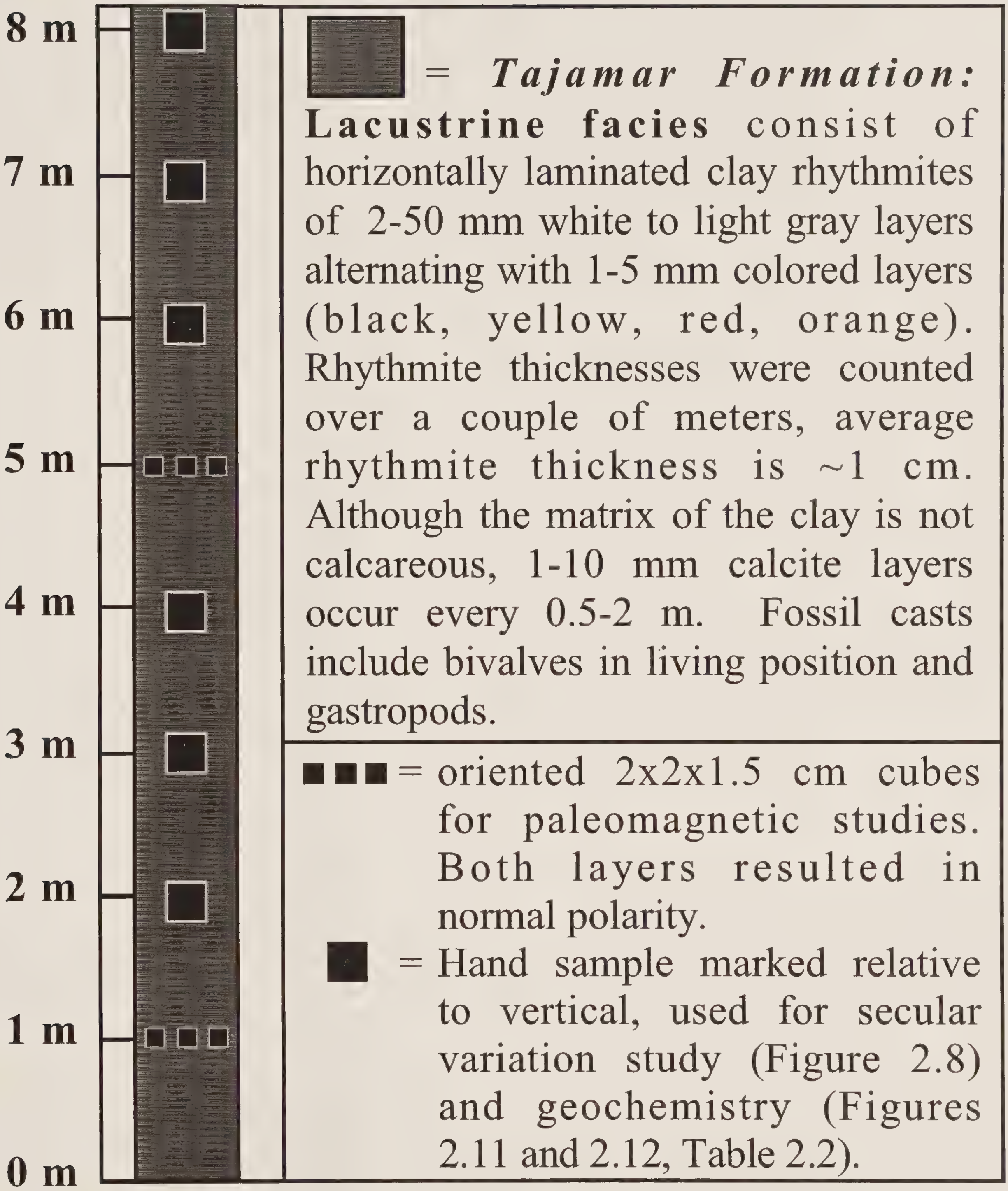

▨ = ***Tajamar Formation:*** **Lacustrine facies** consist of horizontally laminated clay rhythmites of 2-50 mm white to light gray layers alternating with 1-5 mm colored layers (black, yellow, red, orange). Rhythmite thicknesses were counted over a couple of meters, average rhythmite thickness is ~1 cm. Although the matrix of the clay is not calcareous, 1-10 mm calcite layers occur every 0.5-2 m. Fossil casts include bivalves in living position and gastropods.

■■■ = oriented 2x2x1.5 cm cubes for paleomagnetic studies. Both layers resulted in normal polarity.

■ = Hand sample marked relative to vertical, used for secular variation study (Figure 2.8) and geochemistry (Figures 2.11 and 2.12, Table 2.2).

(b) Rumical Section

Figure 2.5 (Continued)

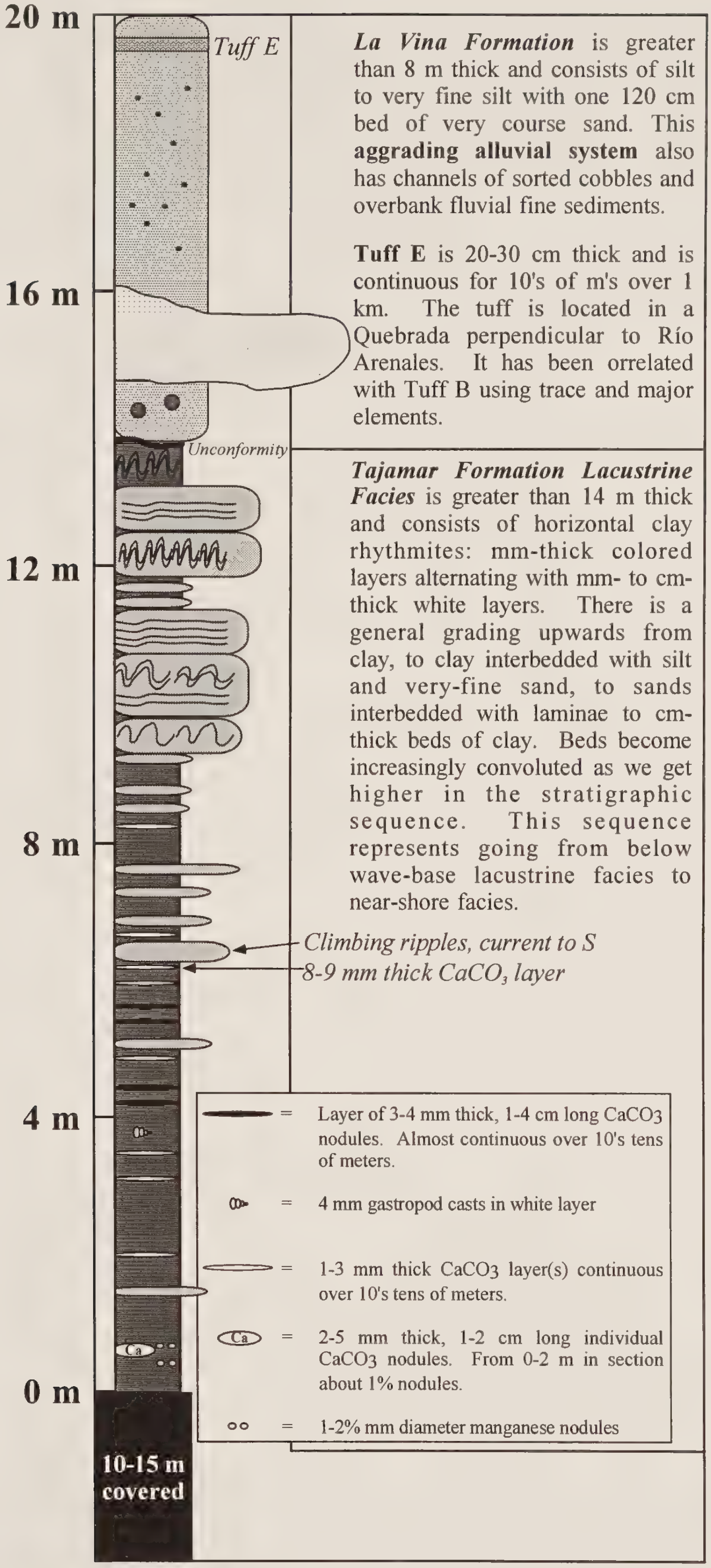

La Vina Formation is greater than 8 m thick and consists of silt to very fine silt with one 120 cm bed of very course sand. This **aggrading alluvial system** also has channels of sorted cobbles and overbank fluvial fine sediments.

Tuff E is 20-30 cm thick and is continuous for 10's of m's over 1 km. The tuff is located in a Quebrada perpendicular to Río Arenales. It has been orrelated with Tuff B using trace and major elements.

Tajamar Formation Lacustrine Facies is greater than 14 m thick and consists of horizontal clay rhythmites: mm-thick colored layers alternating with mm- to cm-thick white layers. There is a general grading upwards from clay, to clay interbedded with silt and very-fine sand, to sands interbedded with laminae to cm-thick beds of clay. Beds become increasingly convoluted as we get higher in the stratigraphic sequence. This sequence represents going from below wave-base lacustrine facies to near-shore facies.

Climbing ripples, current to S

8-9 mm thick $CaCO_3$ layer

▬ = Layer of 3-4 mm thick, 1-4 cm long $CaCO_3$ nodules. Almost continuous over 10's tens of meters.

= 4 mm gastropod casts in white layer

= 1-3 mm thick $CaCO_3$ layer(s) continuous over 10's tens of meters.

Ca = 2-5 mm thick, 1-2 cm long individual $CaCO_3$ nodules. From 0-2 m in section about 1% nodules.

○○ = 1-2% mm diameter manganese nodules

(c) Río Arenales Section

Figure 2.5 (Continued)

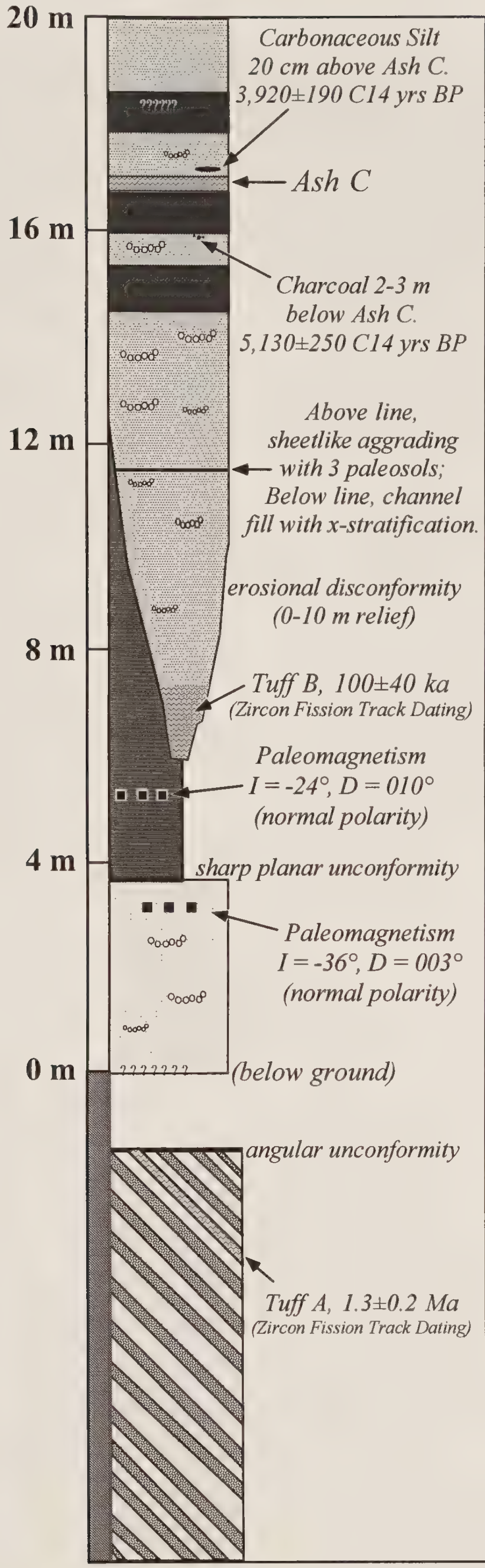
20 m
16 m
12 m
8 m
4 m
0 m
??????
Carbonaceous Silt 20 cm above Ash C. 3,920±190 C14 yrs BP
Ash C
Charcoal 2-3 m below Ash C. 5,130±250 C14 yrs BP
Above line, sheetlike aggrading with 3 paleosols; Below line, channel fill with x-stratification.
erosional disconformity (0-10 m relief)
Tuff B, 100±40 ka (Zircon Fission Track Dating)
Paleomagnetism I = -24°, D = 010° (normal polarity)
sharp planar unconformity
Paleomagnetism I = -36°, D = 003° (normal polarity)
???????
(below ground)
angular unconformity
Tuff A, 1.3±0.2 Ma (Zircon Fission Track Dating)

La Viña Formation is greater than 15 m thick and consists of silt to fine sand with channels comprised of sorted cobbles. It is an **aggrading alluvial system** and includes several paleosols.

Ash C is 5-10 cm thick, white, 70% continous over km's and is probably airfall. It is located just E of RP 68, within and 3-5 m below the top of La Viña Formation.

Tuff B is greater than 2m thick. It is **channel fill** which is white and found directly above a disconformity in incised channels. Cross stratification and intraclasts of clay are present. The tuff is located 100 m E of RR bridge, 25° 24.8' S, 65° 31.1' W.

The ***Tajamar Formation*** here is a **lacustrine facies**, greater than 10 m thick and consists of pinkish, horizontally parallel, laminated clay/silt. Rhythmites are on average 1-2 mm thick.

The ***Calvilmonte Formation*** is a fluvial system which is greater than 4 m thick and consists of grey fine-medium sand with 5% cobbles and <1% intraclasts.

The ***Piquete Formation*** is widespread over hundreds of km's with thicknesses of over 1 km in the S of the Lerma Valley. It represents an **aggrading alluvial system**, and in Arroyo San Vicente consists mostly of 5-10 m beds of conglomerates intercalated with sandstones.

Tuff A is 25 cm thick, white, and is located 0.5 km west of RP 68 at 25° 18.30' S, 65° 30.30' W.

(d) San Vicente + Tajamar Section

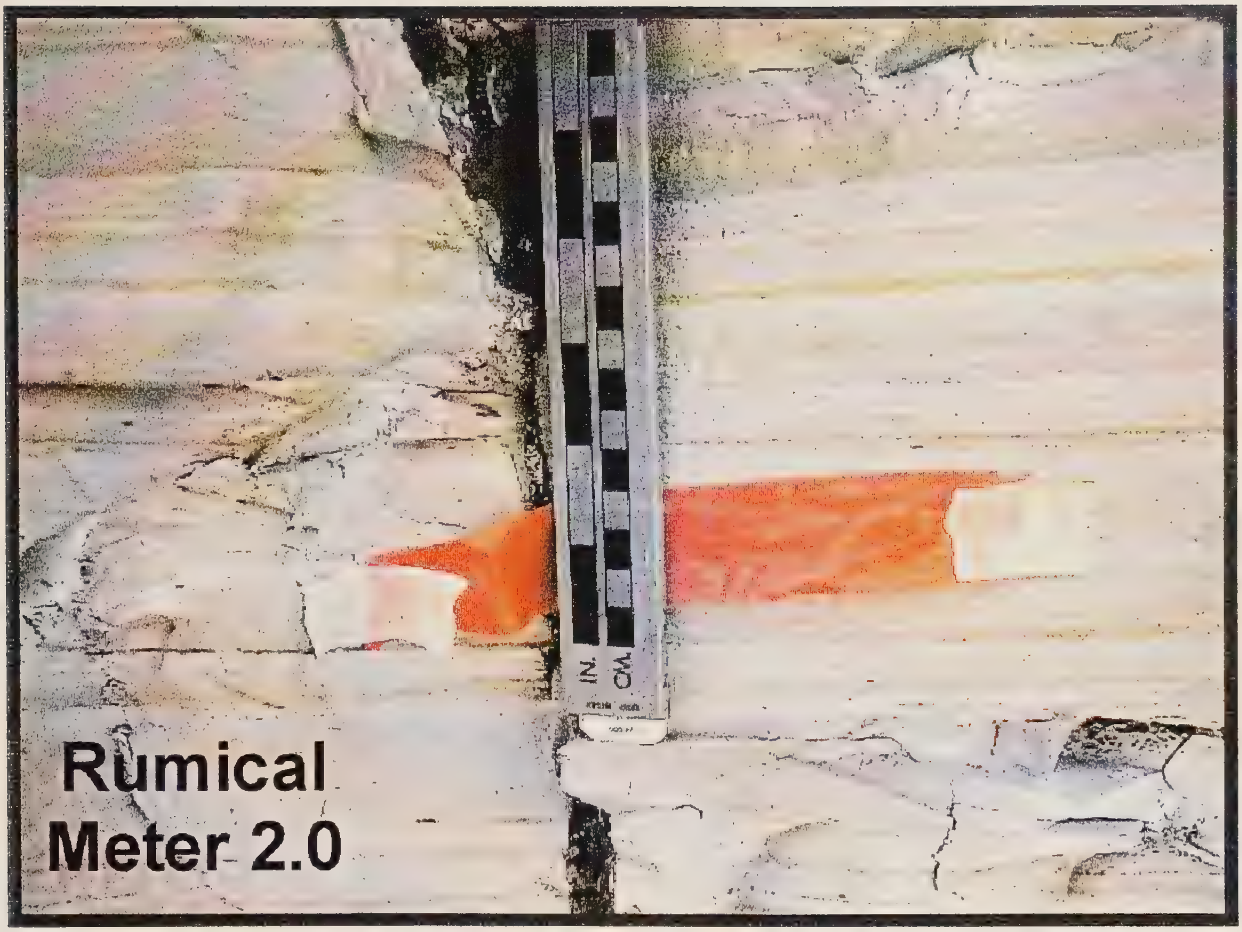

Figure 2.6. Two photographs of Tajamar Formation lacustrine clays from the Rumical outcrop. The location of the Rumical outcrop is indicated by an R in Figure 2.2 and 2.3 with a stratigraphic section given in Figure 2.5b. The first photograph is Rumical meter 2 and is a close-up view of the outcrop in the field. Parallel layers are horizontally laminated clay rhythmites (see text and Figure 2.5b for more detail). The second photograph is a hand sample from Rumical meter 8, oriented the same as the outcrop. Rumical meter 8 was used for XRF element and LOI analyses (Table 2.2, Figure 2.11) and ICP-MS element analyses (Figure 2.12). This hand sample shows similar clay rhythmites as those of Rumical meter 2. Both photographs are representative of the clay facies in the Tajamar Formation.

Figure 2.6 (Continued)

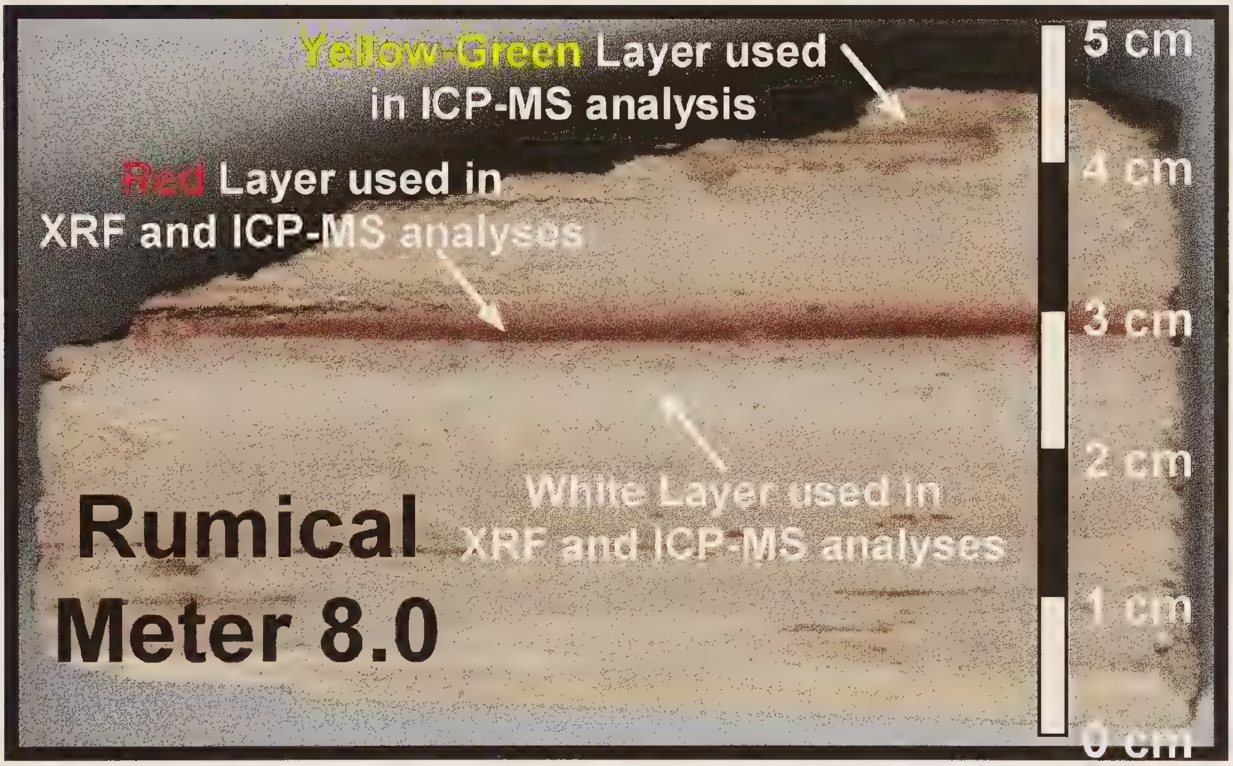
Yellow-Green Layer used in ICP-MS analysis
Red Layer used in XRF and ICP-MS analyses
White Layer used in XRF and ICP-MS analyses
Rumical Meter 8.0
5 cm
4 cm
3 cm
2 cm
1 cm
0 cm

TOPOGRAPHY AND LAKE SIZE

Figures 2.2 and 2.3 show locations of several lacustrine clay outcrops deposited by Lake Lerma (Arroyo Tajamar, Río Arenales (A), Rumical (R), Sumalao (S), and Calvilmonte (C)). The texture, lack of ripples, and erosional features indicate that the lacustrine clay deposits at A, R, S, and C were deposited below wave base. Elevation of the lake facies in each outcrop was determined with an altimeter calibrated with published elevations of meteorological stations. To improve accuracy of elevation readings, multiple altimeter readings over a period of a couple of months were taken at each location. Lake clays at outcrop locations A, R, S, and C are at 1,120±10 m and for Arroyo Tajamar at 1080±10 m. Figure 2.2 compares the physiography of the Lerma Valley to its topography by overlaying a Thematic Mapper image of the area with 100 m contour topography. If Lake Lerma filled the valley to a level of 1,120 m, the surface area of the lake is tightly constrained in the S, W, and E due to the steep walls of the valley.

The lacustrine clays at 1,120 m are below the action of waves; therefore, the lake surface was higher than 1,120 m. *Sly* (Figure 5.4, 1994) provides general relationships between lake size and maximum water depth of wind-wave erosion. Using his relationships with modern-day wind estimates in the Lerma valley (*Servicio Meteorologico Nacional*, 1992), and the area of the lake if water filled the valley to an elevation of 1,120 m, we postulate that wave base was at least 20 m below the lake surface. This brings the minimum elevation of the lake surface to 1,140 m. The lake level was probably much higher than this, possibly to 1,200 m, as there is an outcrop just south of Salta with possible delta facies.

If Lake Lerma filled the valley to a level between 1,140 to 1,200 m, the resulting lake is shown in Figure 2.3. Lake Lerma had a surface area of 800-1,300 km^2, length 70-90 km (N-S), and width 14-18 km (W-E). The distribution of areas of global lakes today is given in Table 2.1. There are over five million lakes in the world with a surface area greater than 0.01 km^2; if Lake Lerma were extant today its surface area would rank among the world's top 144 lakes (*Lerman et al.*, 1995).

Table 2.1. Global lake distribution today (*Lerman et al.*, 1995)

Lake area (km^2)	***Total Lake Number***
0.01 to 0.1	4,260,000
0.1 to 1	738,000
1 to 10	83,000
10 to 100	9,440
100 to 1,000	1,118
1,000 to 10,000	124
10,000 to 100,000	18
>100,000	1

None of the Lerma Valley stratigraphic sections have any indication of shoreline movement or saline facies. Therefore, the hydrologic basin was probably not completely closed, but instead a spillway existed for the lake. We speculate that lake origin and demise were related to valley damming and dam rupturing near the present outlet of the Cabra Corral reservoir, which feeds into the Río Juramento (A. Ortiz, personal communication, 1993). This outlet, some hundreds of meters high and on the order of a hundred meters wide, could have been blocked by a landslide in the past.

GEOCHRONOLOGY

Zircon fission-track dating of Tuffs A, B, and D (Figure 2.7) aids in constraining the age of Lake Lerma. Analyses were done by Sheri Kelley (Department of Geosciences, New Mexico Institute of Mining and Technology). Zircon populations of these tuffs are dominated by juvenile grains. Nevertheless, in Tuffs A and B, 20% of the zircons were identified as detrital on the basis of a set of older fission track ages (Figure 2.7b) and grain populations of distinctive color and morphology. Older populations may be due to sedimentary reworking of the tuff or entrainment of older material during volcanic eruption. Detrital grains were not used in these age calculations. Age calculations are based on the techniques of *Galbraith* (1981, 1984) and *Galbraith and Laslett* (1985). Figure 2.7a shows χ^2 probability and errors in age (one standard deviation).

Tuff A (1.3±0.2 Ma) places a maximum age on the lake facies; the tuff lies beneath an angular unconformity below the lake deposits. Tuff B (0.1±0.04 Ma) places a minimum age on the lake facies; it is part of La Viña formation and overlies the lake deposits above an erosional unconformity. Correlation of Tuff D (0.33±0.1 Ma), located in the northern Lerma Valley, to the environmental history of the central part of the valley, is not well understood.

Carbon-14 was used to date carbonaceous silt 20 cm above ash C and charcoal 2-3 m below ash C (Figures 2.4b, 2.5d). These dated horizons constrain the ash age to 3,700-5,400 C-14 yrs before present (*Geochron Labs*, Cambridge, MA, USA).

Figure 2.7. (a) Zircon fission-track ages for Lerma Valley tuffs with the standard error given as one standard deviation. Ages given are calculated using those grains that are not detrital. See specific tuffs in Figure 2.5 for descriptions of sample localities. (b) Age histograms and probability density functions for the same tuffs. The histograms show the frequency of all zircons (including those interpreted to be detrital) in each sample *vs.* their age, bracketed in 1 My intervals. The curve shows the probability density function (age spectrum) for all zircons (including detrital) in each sample. This age spectrum indicates the probability that a certain number of zircon grains in a sample will have ages within a given age interval. The standard error is given as one standard deviation (σ). The spectral peak age is given in (a). Fission track analyses were done by Sheri Kelley (*Department of Geosciences, New Mexico Institute of Mining and Technology*, USA).

	Tuff A Arroyo San Vicente Piquete Formation	**Tuff B** Arroyo Tajamar La Viña Formation	**Tuff D** Campo Allegre
Grains Counted	20	20	13
Detrital Grains (removed)	4	4	0
Fossil Tracks/cm^2 (*10^5) [# of Tracks]	2.5 [77]	1.34 [6]	0.52 [11]
Induced Tracks/cm^2 (*10^6) [# of Tracks]	2.11 [3247]	1.49 [3328]	17.86 [1875]
Neutron Flux (*10^{15} N/cm^2)	1.88	1.88	1.88
Central Age (Ma)	**1.3**	**0.10**	**0.33**
Standard Error (1σ, My)	**0.2**	**0.04**	**0.10**
Spectral Peak Age (Ma)	1.2	0.1	0.4
Uranium Content (PPM)	359	253	304
χ^2 Probability (%)	99	96	90

(a) Zircon Fission Track Ages

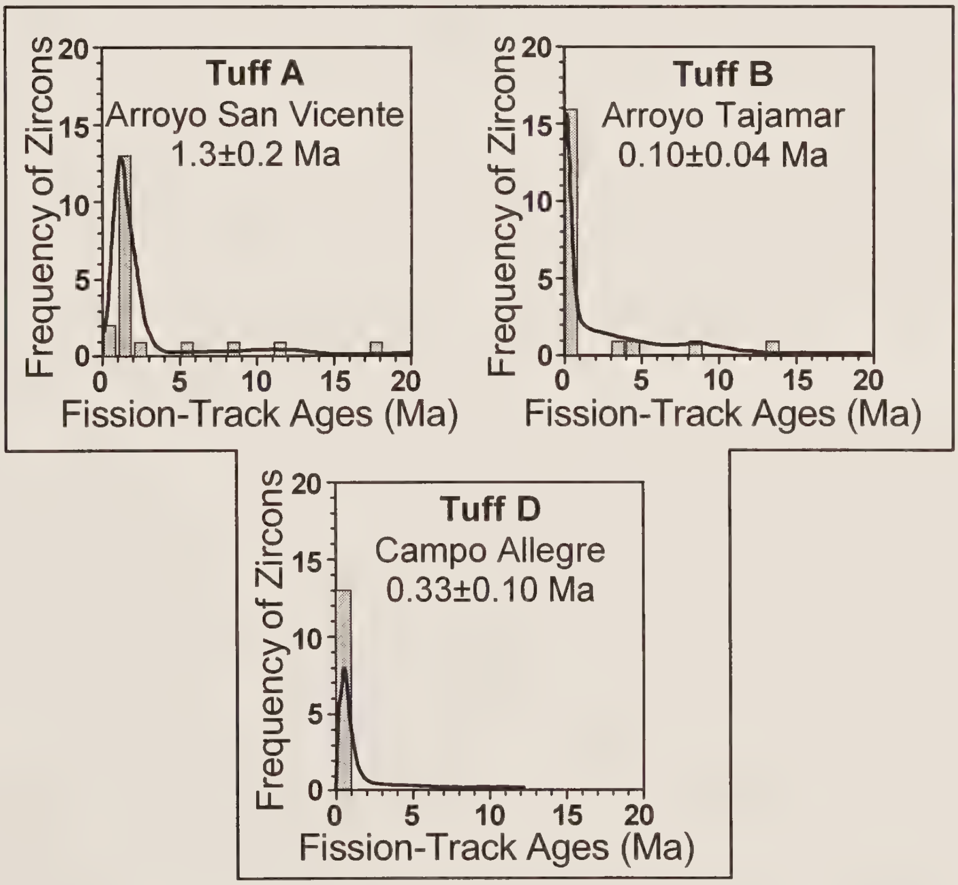

(b) Age Histograms and Probability Density Functions

Magnetic polarities for the Calvilmonte and Tajamar Formations are normal at Arroyo Tajamar (Figures 2.4b, 2.5d). Polarity for the Calvilmonte formation at Calvilmonte (marked C in Figures 2.2 and 2.3) is also normal. At Rumical (R in Figures 2.2 and 2.3) we took multiple layers for paleomagnetic determination. We sampled the Tajamar Formation horizontally laminated lacustrine clay (Figure 2.5b) at Rumical from meters 1 through 8. We oriented the samples at meters 1 and 5 relative to both magnetic north and vertical, whereas we oriented the hand samples at the other six levels relative only to vertical. Thermal demagnetization and principal component analysis result in inclination values for all horizons, and declination values for meters 1 and 5 (Figure 2.8). All samples are of normal polarity and displayed very clear paleomagnetic components with inclinations and declinations that remained constant during the course of thermal demagnetization. The behavior of Rumical meter 5 sample B during demagnetization (upper left plot, Figure 2.9) is typical of all of the Rumical samples and suggests that the principal magnetic carrier is hematite.

The vertical trend in inclination through the eight sampled Rumical horizons (Figure 2.8) indicates an inclination change of about 45° in 6 m. Given that the average secular variation period ranges from 1-10 ky (*Butler*, 1992) and that the curve suggests up to half a secular variation period, the time for deposition of 6 m plausibly ranges from 500-5,000 yrs. Rhythmite thicknesses measured over several meters averaged approximately 1 cm, implying an average rate of deposition of 1-10 yrs for each cm-thick rhythmite.

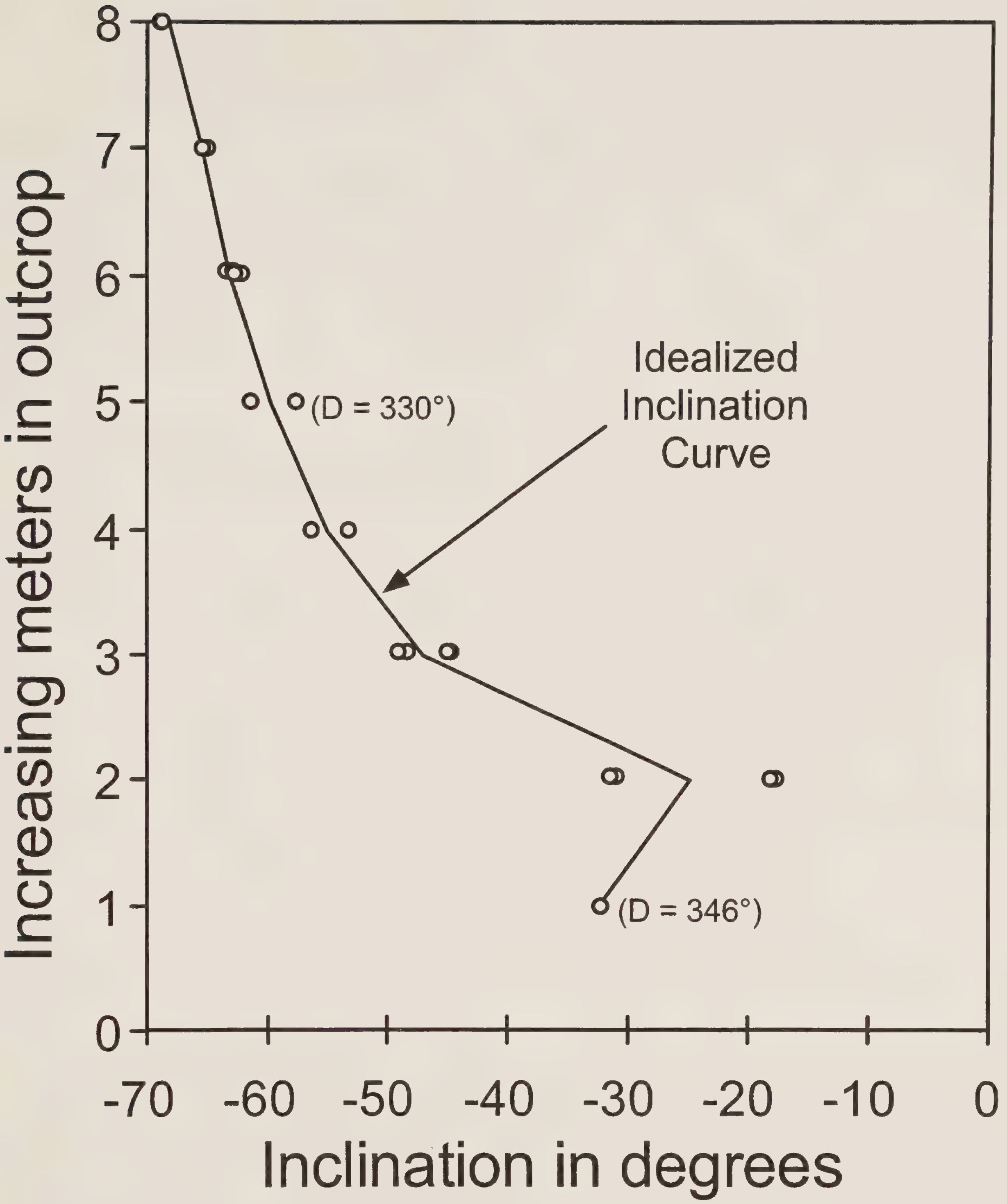

Figure 2.8. Geomagnetic inclination *vs.* stratigraphic level at Rumical. Inclinations were obtained from paleomagnetic analyses on samples from eight horizons of the Rumical outcrop. An example of one of the analyses is given in Figure 2.9. An idealized inclination curve is drawn through the values, and is seen to vary by at least 45° over 6 meters.

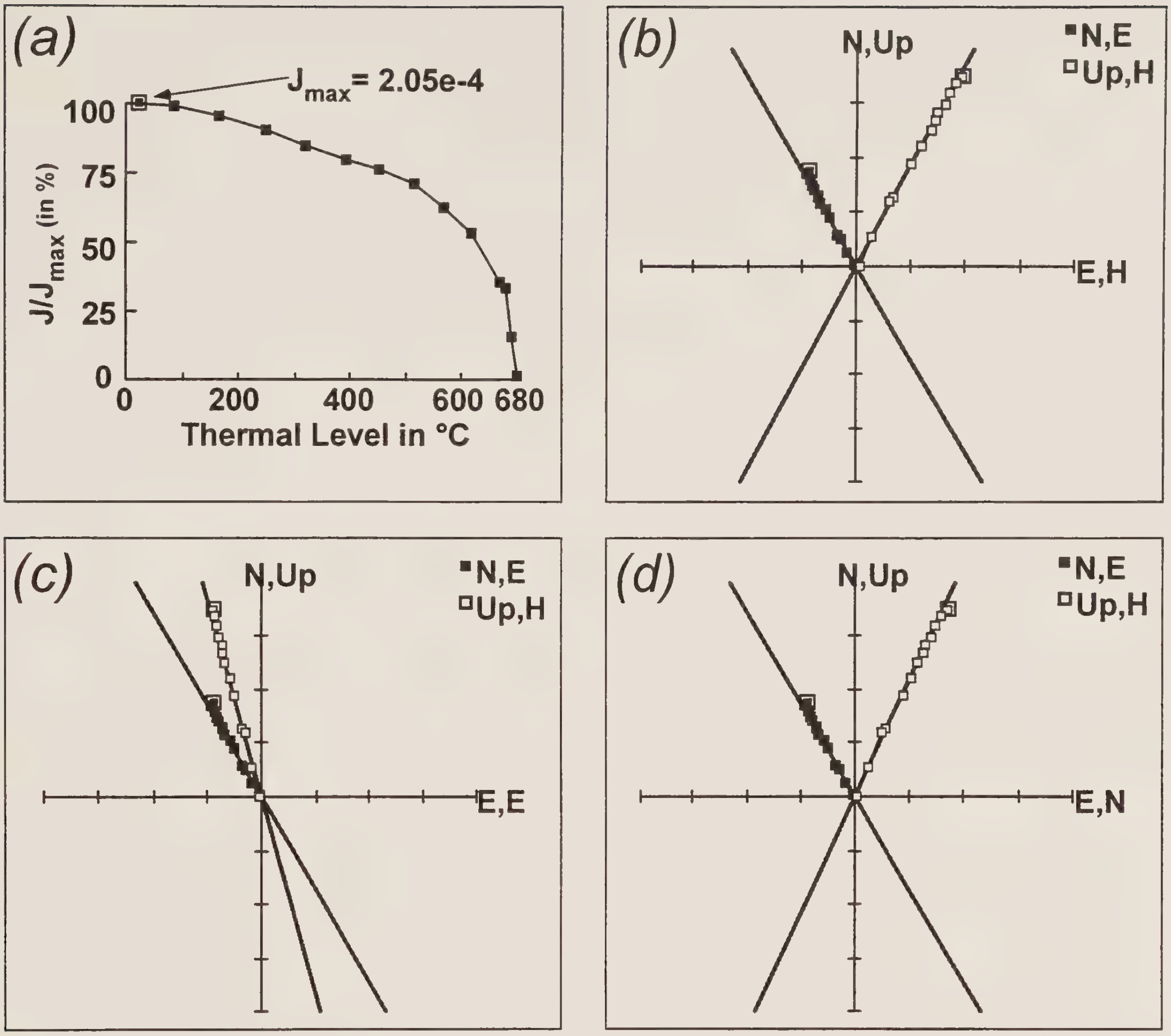

Figure 2.9. Example of paleomagnetism Zijderveld diagram and intensity decay plot. This sample is from the Tajamar Formation lacustrine clay from Rumical meter 5. In (a) is shown the results of thermal demagnetization. In (b) through (d) are shown the resulting Zijderveld diagrams for this sample. The results of principle component analysis for this sample are declination, D = 329.7 and inclination, I = -61.8, with MAD(1) = 24.7 and MAD(3) = 1.3.

The combination of dated tuff horizons and normal polarity further constrains the age of Lake Lerma (Figure 2.10) to 1.05-0.1 Ma. Given its normal polarity, the lake was probably active during the period 0.78-0.1 Ma. Furthermore, the paleomagnetic data constrain its duration. Ten-meter thick lacustrine facies with a deposition rate of 1-10 yrs per cm-thick rhythmite imply 1-10 ky for deposition of the clays. The Rumical clays are exposed at an elevation about 50 m higher than those at Arroyo Tajamar. If we hypothesize that the Rumical clays are underlain by 50 m of buried clay, then for similar accumulation rates Lake Lerma was active on the order of 5-50 ky.

PROVENANCE AND FINGERPRINTING

X-ray diffraction (XRD) analysis performed on a red and a white layer from Rumical meter 8 (Figure 2.6) was done using two forms, a block smoothed to a red or white layer and a <2 μm clay-size fraction from a centrifuge mounted on a thin section. Analyses were performed by Jeff Walker at Vassar College. Each mount was analyzed both in air (dry) and after being placed in an ethylene glycol vapor for 24 hrs at 60° C. The clay-size fraction is 65-70% by weight of the total. The red and white layers in both the clay blocks and clay-size fractions have smectite, chlorite, and illite. Quartz and feldspar are found in the clay blocks but not the clay-size fraction. Kaolinite may be present in the white-layer block and hematite in the red-layer block. The smectite is a good indication that the clays, in part, have a volcanic ash source. Given that the clays also bear chlorite, an alternative source is low-grade metamorphic rocks that cover much of the drainage network feeding into the Lerma Valley.

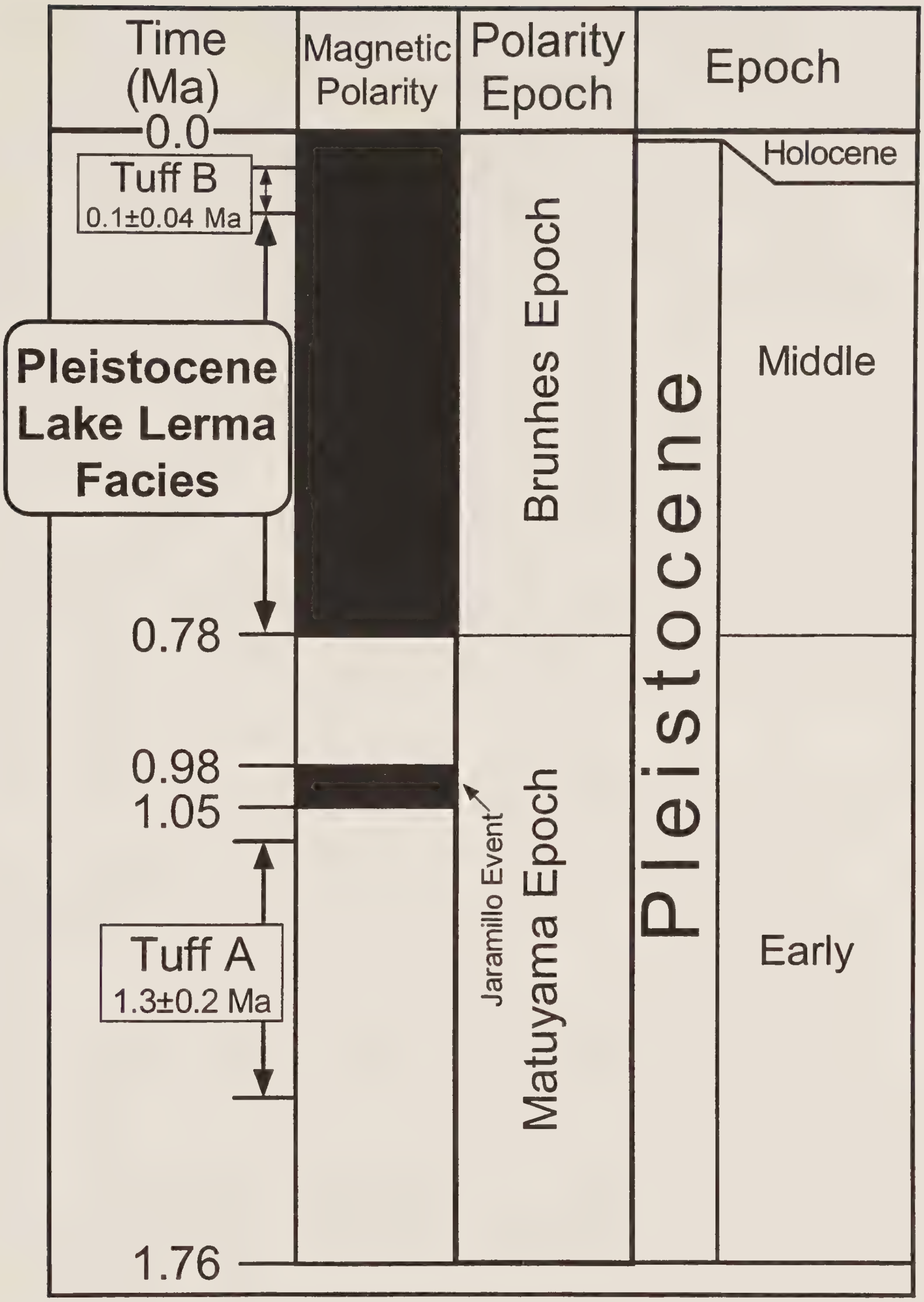

Figure 2.10. Quaternary geomagnetic polarity timescale (*Cande and Kent*, 1992). Tuffs A and B have ages as shown. Pleistocene Lake Lerma facies have normal polarity and are located in time between these two tuffs. We postulate that Pleistocene Lake Lerma facies were most likely active during a subinterval of the time between 0.78 and 0.1 Ma.

X-ray fluorescence (XRF) major and trace element analysis and loss on ignition (LOI) were performed on clay and tuff samples. Analyses were performed by Geochemical Labs, McGill University, Canada. Results are presented in Table 2.2. XRF major elements analysis and LOI reveal that a red and a white clay layer from Rumical meter 8 (Figure 2.6) differ principally in Si, Ca, and LOI (Table 2.2, Figure 2.11). Assuming that the other colored layers are like the two analyzed layers, these differences imply either that the *source* of the sediments changed on a regular basis or that there was a climatic and/or environmental cycle that affected the amount of Ca and Si *deposited.* Color variation in the rhythmites might reflect either summer plus winter deposition or ENSO-type events.

XRF analyses (Table 2.2) of major and trace elements are used to postulate correlations of dated and undated tuffs and ashes. Tuff E, located stratigraphically above lake facies in the Río Arenales section (Figure 2.5c), is sufficiently similar in composition to the 0.1 Ma Tuff B from the Tajamar section (Figures 2.4b, 2.5d), that we interpret them to be the same ash event. Tuff F, in the Arroyo San Alejo Piquete Formation 4-5 km W of Campo Alegre, is compositionally similar to the 1.3 Ma Piquete Formation Tuff A from the San Vicente section (Figures 2.4a, 2.5d), and therefore probably correlative. Ash G, the upper ash in Arroyo San Vicente (Figure 2.4a), is remarkable similar to the 5 ka Ash C in Arroyo Tajamar (Figures 2.4b, 2.5d); we interpret them to be the same ash unit.

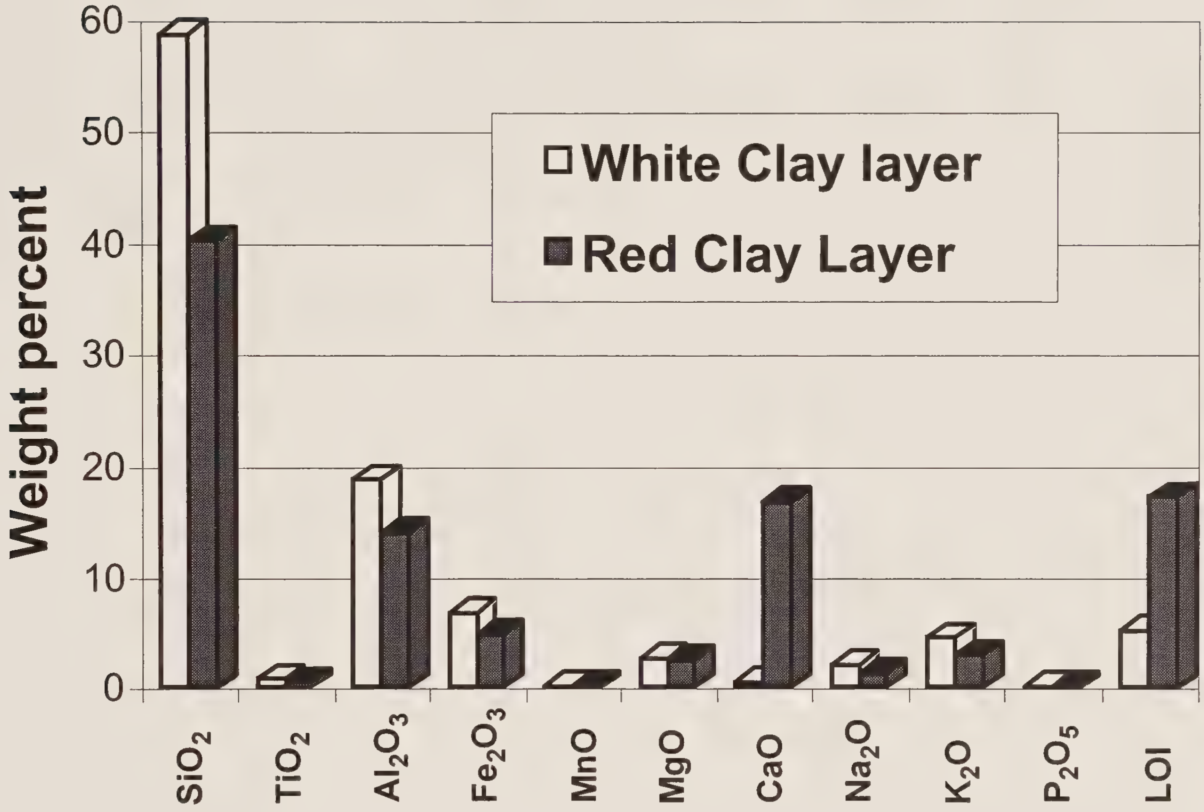

Figure 2.11. Clay major element geochemistry. XRF major element and loss on ignition (LOI) analyses were performed on two clay layers from Rumical meter 8.0 (Geochemical Labs, McGill University, Canada). See Figure 2.6 for a photograph of the layers used in the analyses and Table 2.2 for XRF procedure and numerical data.

Table 2.2. Loss on ignition (LOI) and XRF trace and major elements for Lerma Valley tuffs and clays.[1]

			(%)									
	Outcrop location[2], Formation	Age[3]	SiO_2	TiO_2	Al_2O_3	Fe_2O_3	MnO	MgO	CaO	Na_2O	K_2O	P_2O_5
Tuff A	Arroyo San Vicente, Piquete	1.3±0.2 Ma	68.9	0.47	13.1	3.04	0.061	1.24	2.24	2.83	3.63	0.141
Tuff B	Arroyo Tajamar, La Viña	0.1±0.04 Ma	70.6	0.28	13.5	2.26	0.062	0.48	1.37	3.55	4.67	0.084
Ash C	Arroyo Tajamar, La Viña	3700-5400 C-14 yr BP	73.7	0.17	12.3	1.22	0.081	0.34	1.51	3.24	4.22	0.046
Tuff D	Campo Alegre, ?	0.33±0.1 Ma	70.7	0.43	13.0	2.06	0.018	0.27	1.25	1.95	5.14	0.094
Tuff E	Río Arenales, La Viña		69.5	0.42	14.4	2.48	0.070	0.86	1.75	3.42	4.35	0.142
Tuff F	Arroyo San Alejo, Piquete		67.6	0.40	14.5	2.68	0.052	1.01	2.28	2.63	4.36	0.112
Ash G	Arroyo San Vicente, La Viña		73.5	0.12	13.0	0.97	0.085	0.21	0.64	3.67	4.72	0.025
White clay layer	Rumical Meter 8.0		58.7	0.80	18.7	6.78	0.092	2.72	0.52	2.07	4.50	0.153
Red clay layer	Rumical Meter 8.0		40.1	0.50	13.9	4.83	0.119	2.44	16.63	1.30	3.00	0.126
Detection Limits[4]			0.0060	0.0035	0.0120	0.0030	0.0030	0.0095	0.0015	0.0075	0.0025	0.0035

	(ppm)																		(%)	(%)
	BaO	Ce	Co	Cr_2O_3	Cu	Ni	Sc	V	Zn	Ga	Nb	Pb	Rb	Sr	Th	U	Y	Zr	LOI	Total
Tuff A	563	68	24	21	13	<d/l	16	52	81	15	16	25	217	182	22	8	25	157	4.2	100.0
Tuff B	726	85	19	16	20	<d/l	<d/l	<d/l	81	16	33	21	177	214	16	3	23	195	3.6	100.6
Ash C	186	47	34	<d/l	27	<d/l	<d/l	19	65	17	46	27	299	60	14	16	31	100	3.5	100.4
Tuff D	747	96	<d/l	<d/l	30	<d/l	<d/l	33	68	15	17	19	294	133	51	15	31	170	4.8	100.0
Tuff E	902	92	30	24	22	4	<d/l	30	80	16	28	19	161	296	12	1	23	249	3.0	100.5
Tuff F	496	57	41	17	53	<d/l	<d/l	41	92	17	14	28	256	226	22	13	19	135	4.9	100.6
Ash G	64	42	<d/l	<d/l	14	<d/l	<d/l	<d/l	66	19	55	32	364	29	18	21	34	78	3.3	100.2
White clay layer	670	91	21	122	43	38	12	107	141	24	18	21	191	87	9	<d/l	38	156	5.2	100.5
Red clay layer	541	61	<d/l	75	60	22	23	70	106	17	12	18	129	154	5	2	37	92	17.2	100.3
Detection Limits[4]	17	15	10	15	2	3	10	10	2	1	1	1	1	1	1	1	1	1		

[1] Loss on ignition (LOI) determined at 950° C for 2 hrs. Major element analyses done on fused beads prepared from ignited samples. Trace element analyses done on pressed pellets. <d/l = less than detection limits. All samples ground in a Tungsten carbide disc mill. Laboratory analyses performed by Geochemical Laboratories, McGill University, Canada.

[2] Outcrop locations in Figures 2.2 and 2.3; Arroyo San Alejo located 4-5 km W of Campo Alegre.

[3] Tuff A, Tuff B, Tuff D all dated with zircon fission tracks (Figure 2.7); Ash C dated with C-14 constraints (Figure 2.5d).

[4] Detection limits are reported at the three sigma level.

Inductively coupled plasma mass spectrometry (ICP-MS) was used to determine trace elements in three clay layers from Rumical 8.0 m (photograph in Figure 2.6). ICP-MS analyses were performed by Linda Godfrey, Cornell University. The results (Figure 2.12) were compared to the trace elements of Tuffs A, B, and C as determined by instrumental neutron activation analyses (INAA). These analyses were performed by Matt Gorring, Cornell University. The clays are chemically similar to the ashes, with the exception of Th and U, which are considerably more enriched in the ashes than in the clays. The red and white clay layers are almost indistinguishable based on the chondrite normalized trace elements presented in Figure 2.12. In contrast, the yellow-green layer has an order of magnitude higher Ba concentration and a higher Eu concentration than the red and white layers, such that there is no Eu anomaly. The trace element patterns for the lacustrine clays are generally similar to those of the Lerma Valley tuffs. It is possible, then, that the source of the clays might be secondary transport of wind-blown ashes (what are now tuffs in the Lerma Valley).

Similar to XRF, INAA indicates that the dated ashes are readily distinguishable by their elemental ratios. INAA results suggest that the high-K Tuzgle volcanic center (*Coira and Kay*, 1993), the center closest to Salta, was not the source of Tuffs A, B, or D. These three tuffs probably came from a belt of Quaternary calc-alkaline stratovolcanoes located at least 300 km to the W, SW and NW of the Lerma Valley. The INAA results indicate that Ash C (youngest) is a high-silica rhyolite, Tuff A (oldest) a dacite, and Tuffs B and D are rhyodacites.

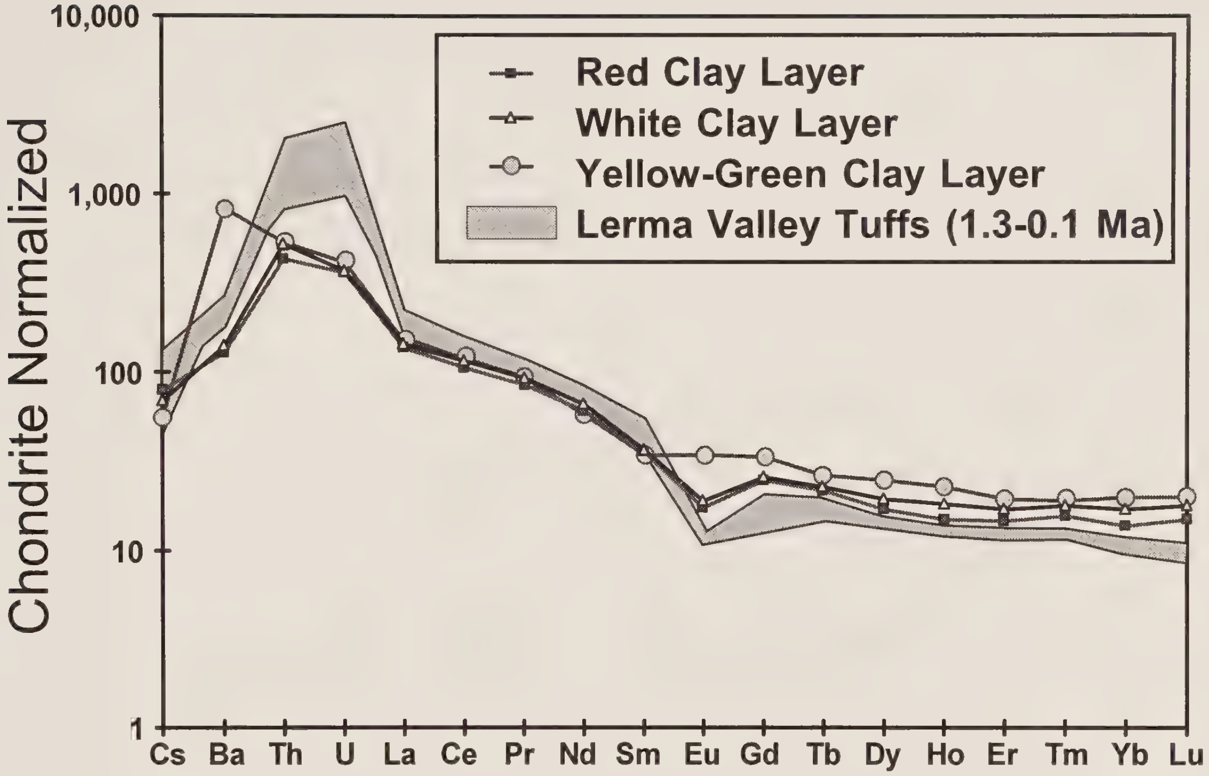

Figure 2.12. Clay and tuff chondrite normalized trace element data. ICP-MS analyses were used to determine trace elements in three layers from Rumical meter 8.0 (ICP-MS by Linda Godfrey, Cornell, USA). For a photograph of the clays layers used in the analyses, see Figure 2.6. The results were compared to trace element results from INAA on Tuffs A, B, and C (INAA by Matt Gorring, Cornell, USA). The results have been normalized to the C1 chondrite (*Sun and McDonough*, 1989). For comparison to trace elements obtained using ICP-MS and INAA, numerical XRF results for these three tuffs and two of the clay layers is reported in Table 2.2.

SEDIMENT AND WATER BUDGET

Figure 2.13 shows the drainage network for NW Argentina and highlights the drainage network upstream of Cabra Corral (32,000 km^2). Lerma Valley is in the Salado River drainage basin, containing both Salta, and the Cabra Coral reservoir.

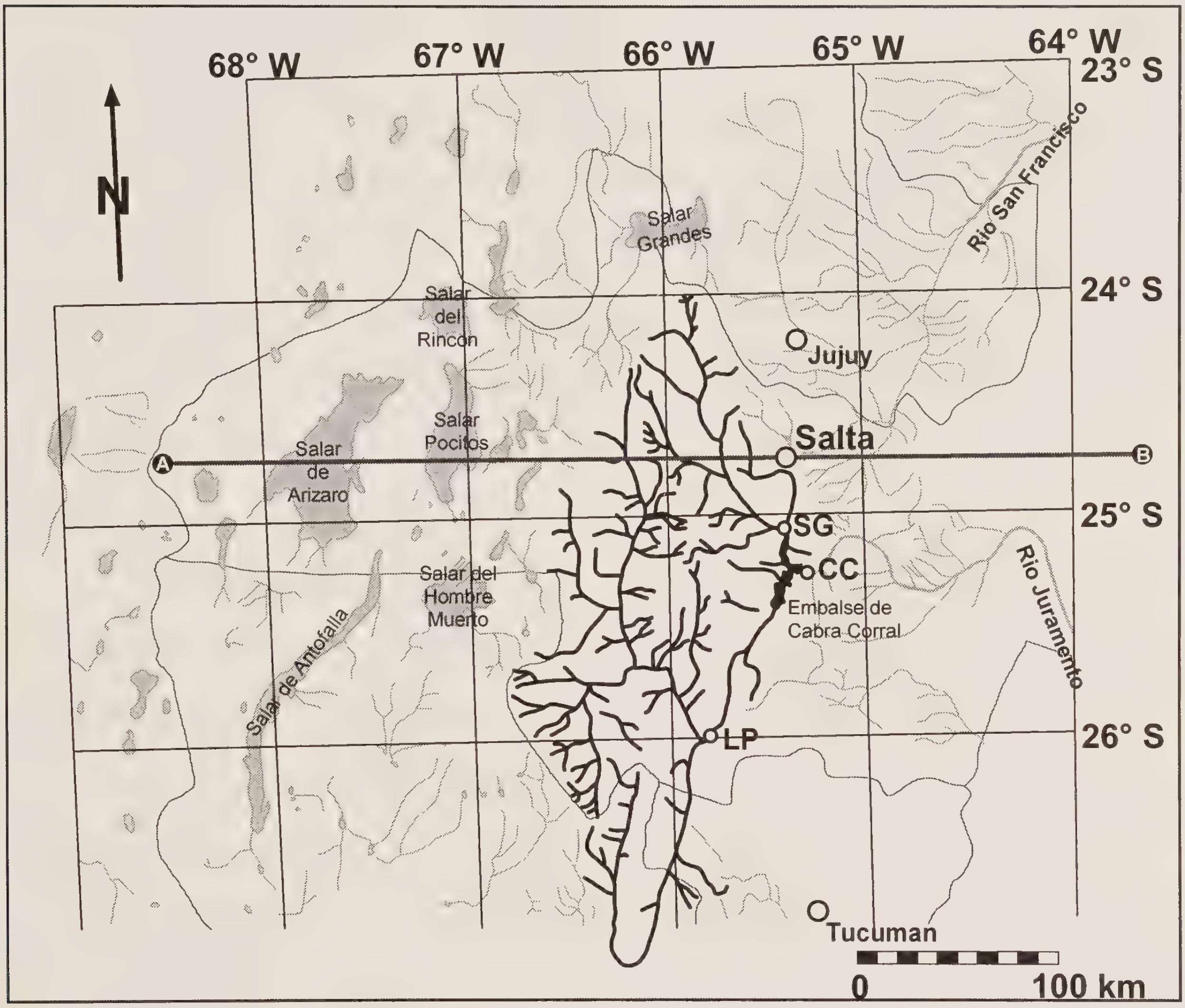

Figure 2.13. Drainage network for NW Argentina. The drainage basin of the Salado River upstream of Cabra Corral has an area of 32,000 km^2 and is shown in bold lines. The A-B cross section on the map is the same one given in Figure 2.1. Three hydrologic stations are shown: SG = San Gabriel, Río Arias, LP = La Punilla, Río Calchaqui, and CC = Cabra Corral, Río Juramento. Discharge and other characteristics of these stations are given in Table 2.3.

In Figure 2.13, headwaters of the Salado River drainage basin begin at altitudes of 3-4 km along the eastern edge of the Puna. The headwaters drain eastward through multiple valleys at decreasing altitudes until feeding into the Lerma Valley (once Pleistocene Lake Lerma), the Cabra Corral reservoir, the Juramento River, and finally the Salado River (not shown in Figure 2.13).

Using historical sediment load data for the last 30 yrs in the Lerma Valley (*Agua y Energía*, 1991) and a sediment grain density of 2.75 g/cm, we calculate that average denudation rate over the part of this drainage basin upstream of Salta has a lower bound of 10-20 cm/ky. This is considered a lower bound for two reasons. First, the sediment load data used only considers suspended sediment, and not the dissolved or bedload quantities. Second, wind-borne sediment exists in an important quantity in this area.

Using this denudation, we then calculate what the rate of sedimentation would be if an area the size of the Salado River drainage basin upstream of Cabra Corral were to drain all of its sediment into a closed basin with a surface area the size of Pleistocene Lake Lerma (Figure 2.14). Lake Lerma occupied a surface area of about 1,000 km^2, or 1/32 of the present drainage area. If the sediment presently removed by fluvial activity (10-20 cm/ky) were deposited over an area the size of Lake Lerma, then modern accumulation rates would average 300-600 cm/ky. Hence, modern denudation rates could supply enough sediment from the drainage network to account for Lake Lerma sediment accumulation rates as derived from the paleomagnetic record of secular variation (Figure 2.8, 100-1,000 cm/ky).

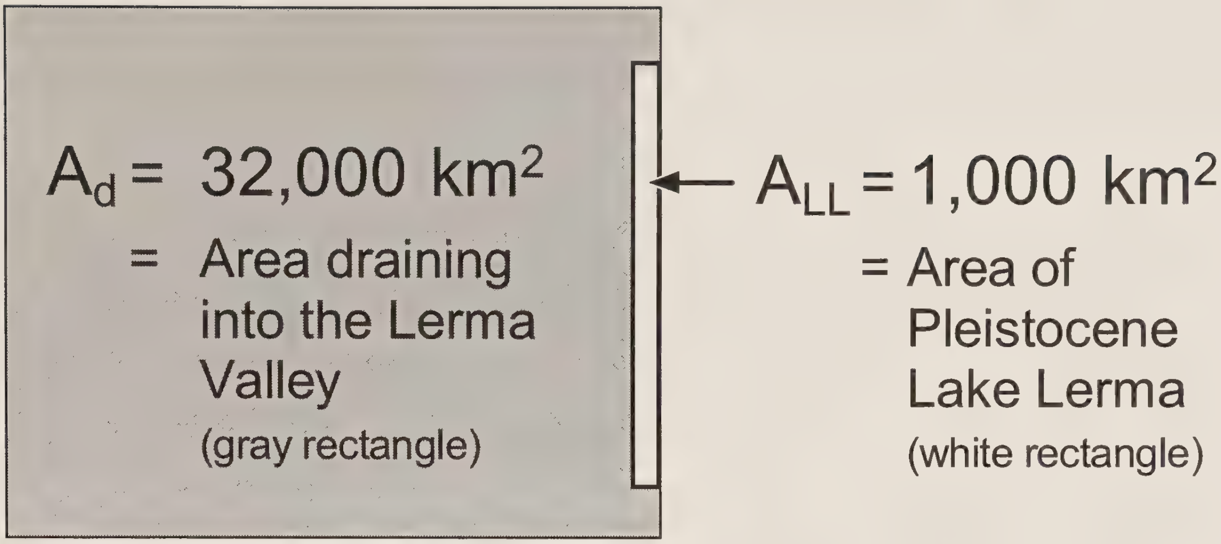
$A_d = 32{,}000$ km^2
= Area draining into the Lerma Valley
(gray rectangle)
$A_{LL} = 1{,}000$ km^2
= Area of Pleistocene Lake Lerma
(white rectangle)

Figure 2.14. Filling Pleistocene Lake Lerma with sediment. The area of the Salado River drainage basin feeding into the Lerma Valley today is $A_d \approx 32{,}000$ km^2 (Figure 2.13). Pleistocene Lake Lerma had a surface area of $A_{LL} \approx 1{,}000$ km^2. The ratio of $A_d/A_{LL} \approx 1/32$ and the rate of *erosion* (based on suspended sediment loads) at various stations in the Salado River drainage basin is on the order of e = 10-20 cm/kyr. If all of the sediments in A_d were to be deposited into the area A_{LL} (*i.e.*, into a closed basin) then the *sedimentation* in A_{LL} would be $s = 32e$ = 300-600 cm/kyr.

Now we calculate the rate of filling a lake the size of Pleistocene Lake Lerma with water given modern hydrologic and climatologic conditions. If the Lerma Valley were filled with a lake today, we compute that the evaporation off the lake would be about E = 1.0 m/yr. This calculation is based on a hydrologic model developed at Cornell University (*Blodgett et al.*, 1997) and average meteorological data for Salta from the *Servicio Meteorologico Nacional* (1992), including air pressure, relative humidity, air temperature, wind speed, and cloud fraction. Average discharge and other characteristics of three hydrologic

stations in the Salado River drainage basin have been obtained from *EVARSA* (1994) and are given in Table 2.3.

Table 2.3. Characteristics of three hydrologic stations in the Salado River drainage basin (Figure 2.13). Data from *EVARSA* (1994).

	Location	***River***	***Elevation (m)***	***Drainage Area (km^2)***	***Years of Record***	***Average Discharge Q (m^3/s)***
LP	La Punilla	Calchaqui	1790	19,800	1949-67	6.5
SG	San Gabriel	Arias	1150	7,100	1943-67	24.4
CC	Cabra Corral	Juramento	945	31,900	1949-68	31.0

The first two stations, La Punilla (LP, Figure 2.13) and San Gabriel (SG, Figure 2.13) have drainage areas that are 7,100 km^2 and 19,800 km^2 respectively, constituting 90% of the area that drains into Cabra Corral (CC, Figure 2.13). The combined discharge of La Punilla and San Gabriel is about Q = 31 m^3/s which is approximately the same as the discharge at Cabra Corral, $Q = 31$ m^3/s. We will take as a rough estimate, that the historical average discharge entering the Lerma Valley is about $Q = 30$ m^3/s.

Given today's water budget, should the Río Juramento mouth be blocked by a landslide, the valley would fill up quickly with water. A volume with a surface area $A = 500$ km^2 and depth $h = 50$ m approximates the dimensions of Lake Lerma below 1,080-1,100 m elevation. A cartoon of this blocky "lake" is given in Figure 2.15.

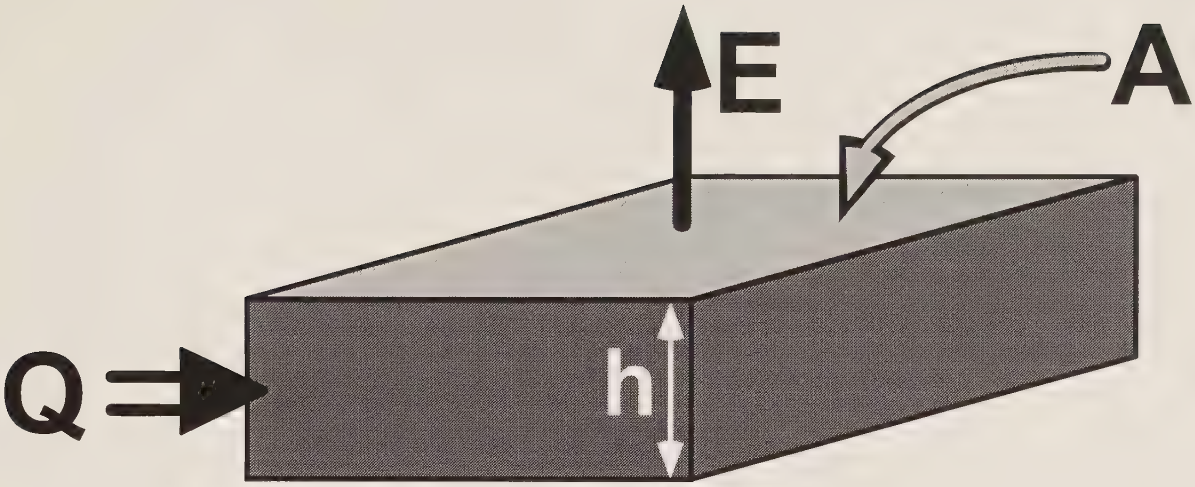

Figure 2.15. Filling a volume the size of Pleistocene Lake Lerma with water. We model the valley as a solid rectangle with depth, *h*, and surface area, *A*. Average discharge, *Q*, enters the block (the Lerma Valley) and the surface area, *A*, has an average yearly rate of evaporation, *E*. In Table 2.4, for several sets of these variables, we calculate how long it would take to fill a "closed" Lerma Valley. Given today's climatic conditions, we could easily fill a volume the size of Pleistocene Lake Lerma with water in a geologically short amount of time.

If the water input to the Lerma Valley is $Q = 30\ \text{m}^3/\text{s}$ ($3.9\ \text{km}^3/\text{yr}$) and evaporation $E = 1.0$ m/yr over $A = 500\ \text{km}^2$, then the valley would fill up in 56 yrs; with $E = 1.3$ m/yr, this would change to 85 yrs. A volume with $A = 900\ \text{km}^2$ (90% the surface area of Lake Lerma), 20 m deep (the "top" part of the lake), and $E = 1.0$ m/yr, would fill in about 400 yrs. This is summarized in Table 2.4. The existence of Lake Lerma in the past was not necessarily due to a change in climate from today's conditions and could be due entirely to the valley being dammed by a landslide.

Table 2.4. Filling rate for the blocky “lake” given in Figure 2.15.

Discharge ***Q*** ***(m^3/s)***	***Evaporation*** ***E*** ***(m/yr)***	***Surface Area*** ***A*** ***(km^2)***	***Depth*** ***h*** ***(m)***	***Time to fill the lake*** ***(yrs)***
30	1.0	500	50	56
30	1.3	500	50	85
30	1.0	900	20	400

CONCLUSIONS

Existing topography and the spatial distribution of lake facies indicate that Lake Lerma was 70-90 km long (N-S), 14-18 km wide (W-*E*), and had a surface area of 800-1,300 km^2. If the present outlet of the Cabra Corral reservoir were dammed by a landslide, the lake could have filled entirely in less than 500 yrs with no change in climate from today's conditions.

Lake clays contain smectite and have trace element patterns similar to several area ashes. The source of the lake clay might be secondary transport of wind-blown ashes. Given that the clays also bear chlorite, an alternative source is low-grade metamorphic rocks that cover much of the drainage network feeding into the Lerma Valley.

Tuff and ash dating indicate that, after tectonic deformation (<1.3±0.2 Ma), fluvial (Calvilmonte Formation) and then lacustrine depositional systems (Lake Lerma) were both active 1.05-0.1 Ma. Based on normal polarity from magnetostratigraphy, they were probably active 0.78-0.1 Ma. La Viña aggradation has occurred since 100 ka.

A systematic shift of 45° in magnetic inclination through 6 m of lake rhythmites may indicate that 0.5-5 ky are spanned by that outcrop. If so, the average 1 cm thick rhythmites are 1-10 yr events with sedimentation rates of 1-10 m/ky. Modern denudation rates could supply enough sediment from the drainage network to account for accumulation rates and for accumulation of all the Lake Lerma deposits in 1-50 ky.

APPENDIX 2.1.
BLACK AND WHITE OF FIGURE 2.6

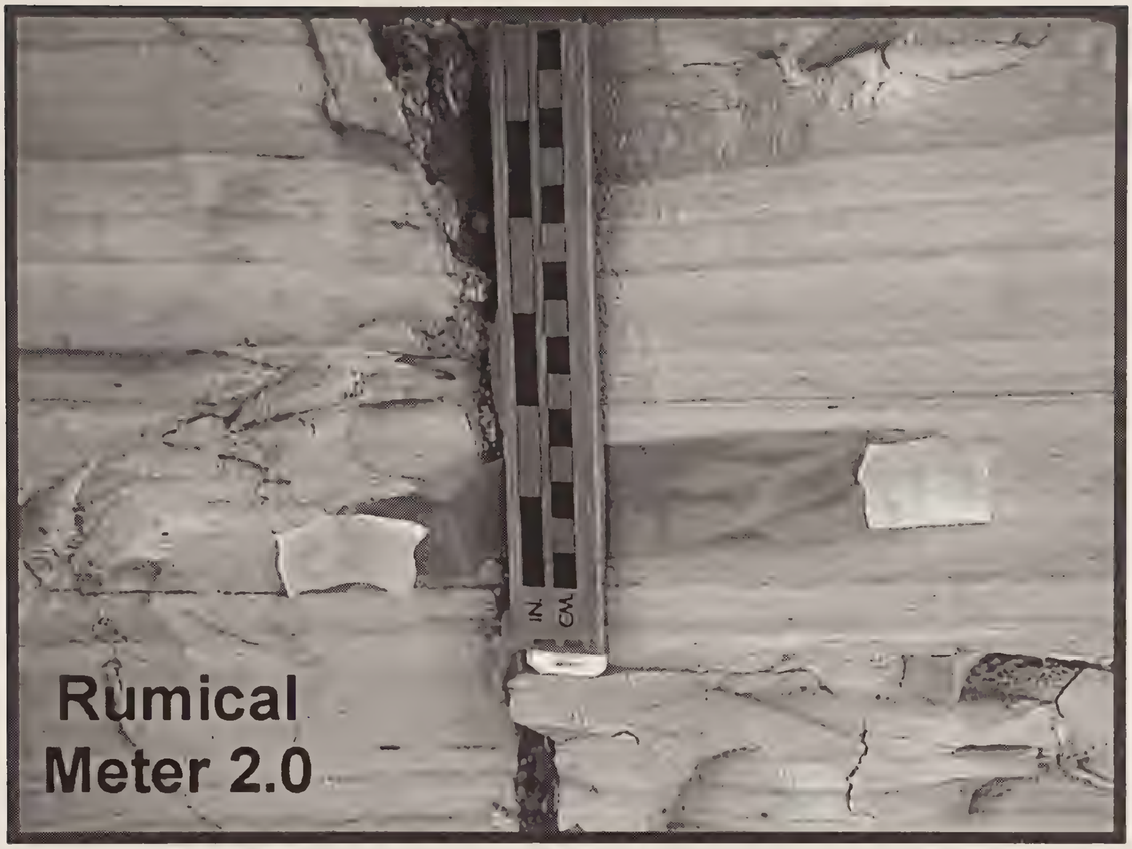

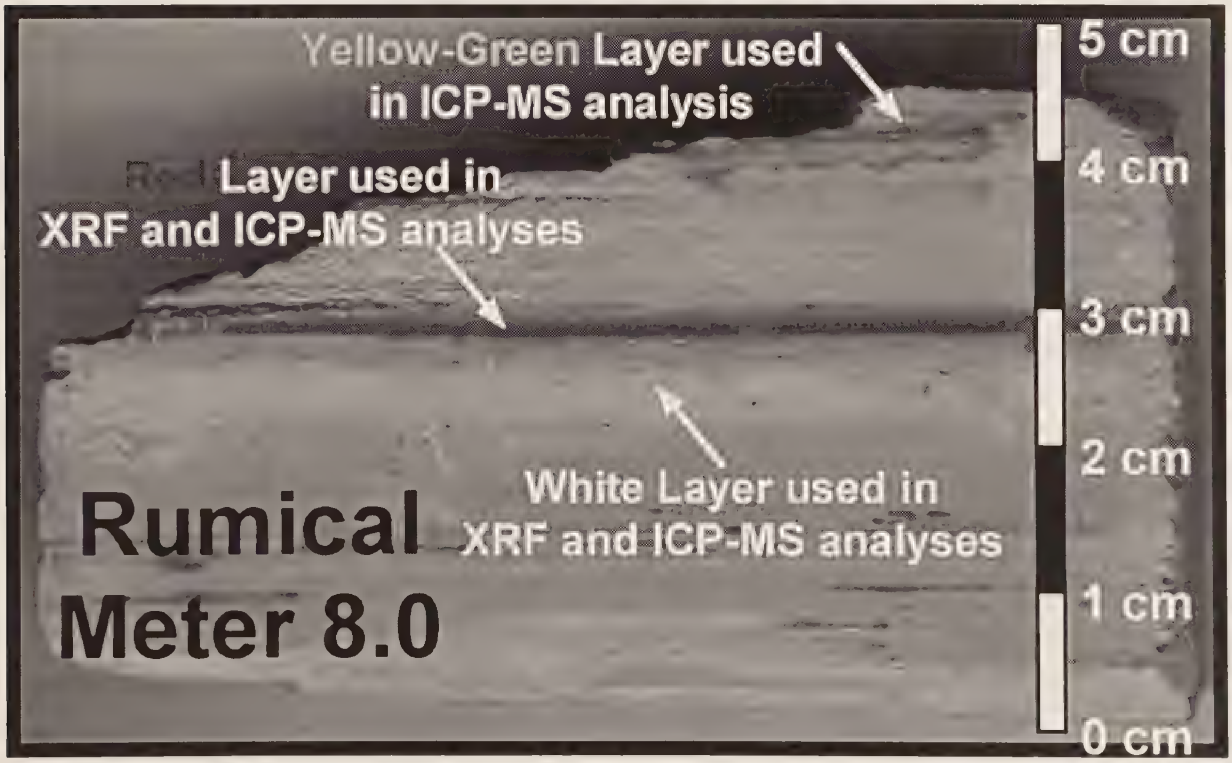
Yellow-Green Layer used in ICP-MS analysis
Red Layer used in XRF and ICP-MS analyses
White Layer used in XRF and ICP-MS analyses
Rumical
Meter 8.0
5 cm
4 cm
3 cm
2 cm
1 cm
0 cm

REFERENCES

AGUA Y ENERGIA (1991). *Estadística hidrológica hasta 1990, Sedimentología.* Gerencia de Ingeniería (Buenos Aires), 300 p.

ATLAS TOTAL DE LA REPÚBLICA ARGENTINA (1981). Físico. Centro Editor de América Latina (Buenos Aires), 160 p.

BLODGETT, T.A., LENTERS, J.D., AND ISACKS, B.L. (1997). Constraints on the Origin of Paleolake Expansions in the Central Andes. *Earth Interactions*, **1** [Available online at http://EarthInteractions.org.].

BUTLER, R.F. (1992). *Paleomagnetism.* Blackwell (London), 319 p.

CANDE, S.C., AND KENT, D.V. (1992). A new geomagnetic polarity time scale for the Late Cretaceous and Cenozoic. *JGR*, **97**:13,917-51.

COIRA, B., AND KAY, S.M. (1993). Implications of Quaternary volcanism at Cerro Tuzgle for crustal and mantle evolution of the Puna Plateau, Central Andes, Argentina. *Contribution to Mineralogy and Petrology*, **113**:40-58.

EVARSA (1994). *Estadística hidrológica, Tomo I and II.* Secretaría de Energía (Buenos Aires), 651 p.

GALBRAITH, R.F. (1981). On statistical models for fission tracks counts. *Journal of Mathematical Geology*, **13**:471-8.

GALBRAITH, R.F. (1984). On statistical estimation in fission track dating. *Journal of Mathematical Geology*, **16**:653-69.

GALBRAITH, R.F., AND LASLETT (1985). Some remarks on statistical estimation in fission-track dating. *Nuclear Tracks*, **10**:361-3.

GALLARDO, E.F. (1985). *Estratigrafía y tectónica del cuaternario en la Cordillera Oriental de Salta y Jujuy.* Informe Final CONICET (Salta), 88 p.

González, R.E. (1995). *Estratigrafía, sedimentología y tectónica del subgrupo Jujuy (Terciario) en la cadena Subandina Argentina, provincias de Salta y Jujuy.* Informe Final CONICET (Salta), 130 p.

Lerman, A., Gat, J., and Imboden, D., eds. (1995). *Physics and chemistry of lakes.* Springer-Verlag (London), 334 p.

Mapa Base Topografico del Valle de Lerma (1987). Hoja 1 and 2: 1:50,000. Camara del Tabaco de Salta.

Servicio Meteorologico Nacional (1992). *Climate statistics, 1981-1990 (Estadísticas climatológicas).* **B(37)**, Buenos Aires.

Sly, P.G. (1994). Sedimentary processes in lakes. In K. Pye (ed.), *Sediment transport and depositional processes*, Blackwell Scientific Publications (Oxford), 157-91.

Sun, S.-S., and McDonough, W.F. (1989). Chemical and isotopic systematics of oceanic basalts: implications for mantle composition and processes. In A.D. Saunders and M.J. Norry (eds.), *Magmatism in the Ocean Basins*, GSS, **42**:313-45.

Chapter Three:
Persistence Analyses of Self-Affine Time Series*

ABSTRACT

In this paper, we examine self-affine time series and their persistence. Self-affine time series, where the power-spectral density scales as a power of the frequency, appear in a wide variety of geophysical contexts; examples include climate variations, sea level, and elevation. Stochastic time series are characterized by a statistical distribution of values and by their persistence or antipersistence. Persistence is the degree to which values in a time series are internally correlated and can be classified in terms of range, short-range or long-range, and in terms of strength, weak or strong. Self-affine time series are scale invariant, thus always exhibit long-range persistence. Synthetic self-affine time series are generated using the spectral method, where a Gaussian white noise is appropriately filtered such that its power-spectral density (S_{m}) depends upon frequency (f_{m}) according to $S_{\mathrm{m}} \sim f_{\mathrm{m}}^{-\beta}$. As β increases, values in the series become more correlated and profiles are increasingly smoothed. We generate fractional Gaussian noises (fGn's), $-1 \leq \beta \leq 1$. These are summed to give fractional Brownian motions (fBm's), $1 \leq \beta \leq 3$. Self-affine time series with $\beta > 1$ have systematically different behavior than those with $0 < \beta < 1$. With $\beta > 1$, the time series are nonstationary and moments of the time series depend upon its length. Over the range $1 \leq \beta \leq 3$, fBm's, the time series are self-affine fractals with fractal dimension $1 \leq D \leq 2$. With $\beta = 2$,

---

*This chapter has been submitted to *Advances in Geophysics* as Malamud, B. D., and Turcotte, D. L., Self-Affine Time Series: Generation and Analyses.

the series is a Brownian motion. Time series in the range $-1 \leq \beta \leq 1$ are fGn's and are stationary; $\beta = 0$ is a white noise. We define self-affine time series with $\beta > 1$ ($\beta < 1$) to have strong (weak) persistence. We use a variety of techniques to quantify the strength of persistence of synthetic self-affine time series with $-3 \leq \beta \leq 5$ and both Gaussian and log-normal distributions: (1) *Semivariograms* for fractional noises correlate well with the self-affine fractal relation, $\gamma \sim \tau^{2Ha}$ (γ, semivariogram; τ, lag; Ha, Hausdorff measure). Semivariograms quantify the strength of persistence in the range $1 \leq \beta \leq 3$. (2) *Rescaled-range (R/S) analyses* applied to fGn's correlate well with Hurst's fractal relation, $(R/S) = (\tau/2)^{Hu}$ (Hu, Hurst exponent) and quantifies the strength of persistence in the range $-1 \leq \beta \leq 1$. (3) *Average extreme-value analyses* quantify the strength of persistence in the range $1 \leq \beta \leq 3$. Taking a synthetic time series of length T, the maximum value y_e is assigned a period $\tau = T$. After the period is broken into two parts each of length $T/2$, the maximum value for each part is found. The average of the two values, $(y_e)_{av}$, is assigned the period $\tau = T/2$ and the process is repeated for $\tau = T/4, T/8, \ldots$. The results correlate well with $(y_e)_{av} \sim \tau^{He}$ (He, extreme value exponent). (4) *Fourier spectral* techniques quantify the strength of persistence for all β. For self-affine time series with prescribed β, spectral techniques provide direct confirmation of β using the power dependence of S_m on f_m. (5) *Wavelet variance analyses* quantify the strength of persistence for all β. Wavelet analyses locate both periodic and non-periodic events in time permitting transient or time-dependent features to be detected, it is particularly appropriate for nonstationary time series and lacks many of the inherent problems that are found in Fourier power-spectral analysis.

3.1. INTRODUCTION

3.1.1. Brief Overview of Paper

Mandelbrot (1967) introduced the concept of fractals in terms of statistical self-similarity, the idea that the shape of an object does not define its size. The original example was the length of a rocky coastline; a map of a rocky coastline gives no indication of its scale. Subsequently, many natural phenomena have been shown to exhibit statistical self-similarity. Examples include earthquakes, rock fragments, volcanic eruptions, river networks, and mineral deposits (*Turcotte*, 1997). For real applications, scale invariance is valid only over a limited range; for example, in terms of fragments, there will always be a largest fragment and a smallest fragment.

Mandelbrot and Van Ness (1968) extended the concept of statistical self-similarity to time series. This was done within the context of the self-affine time series. The classic example of a self-affine time series is a Brownian motion. In this paper, we consider, in detail, methods of generating synthetic self-affine time series and methods for their analysis. Our basic definition of a self-affine time series is that the power-spectral density of the time series has a power-law dependence on frequency. The concepts of persistence and stationarity are examined in detail.

Examples of time series in geophysics include global temperature, the strength of the Earth's magnetic field, and the flow in a river. After obvious periodicities and trends in a time series have been removed, the remaining values are the stochastic component. The two main aspects of

the stochastic component of a time series are its statistical distribution of values and its persistence. Typical statistical distributions are Gaussian (normal) and log-normal. The persistence measures the correlations between adjacent values within the time series. The persistence of values with respect to each other can be strong, weak, or nonexistent (a white noise). A strong correlation implies a "memory" of previous values in the time series. Values of a time series can affect other values in the time series that are not only nearby in time (short-range) but also far away in time (long-range). Since self-affine time series have a power-law dependence of the power-spectral density function on frequency, they exhibit long-range persistence.

There are many statistical approaches currently in use for the purpose of quantifying geophysical data sets. The purpose of this paper is to systematically compare many of these statistical approaches, and illustrate their robustness and utility through applications to synthetic data sets whose properties are known. To achieve this purpose, we generate self-affine synthetic fractional noises and motions with a wide range of persistence strengths and two different statistical distributions, Gaussian and log-normal. These synthetic noises and motions have similar properties to many time series found in geophysics and other fields. The persistence analyses we use to quantify these time series are semivariogram analysis, rescaled-range analysis, average-extreme value analysis, Fourier power-spectral analysis, and wavelet variance analysis. The last two techniques measure the strength of persistence over a broad range of self-affine time series, whereas the others measure the strength

only over specific subsets. We discuss the theory behind each technique and its use in measuring the strength of persistence for self-affine time series.

3.1.2. What is a Time Series?

A time series is the set of numerical values of any variable that changes with time. A time series is generally either continuous or discrete. A continuous time series $y(t)$ is a set of values that are continuous in time over the interval T. Examples include the continuous record of the atmospheric temperature at a specified point in space and the discharge down a river measured at a gauging station. A discrete time series consists of a set of values that are not continuous. The values of a discrete time series y_n are often specified at equal increments of time δ so that we have values of y_n given at $t_n = n\delta$, $n = 1, 2, 3, \ldots, N$ with $T = N\delta$. Examples of a discrete time series include the sequence of daily rainfall totals at a measuring station, the yearly accumulation of sediment in a lake, and the maximum flood discharge at a gauging station each year. For the latter case, y_1 would be the maximum discharge during the first year, $t = 0$ to 1, y_2 would be the maximum discharge during the second year, $t = 1$ to 2, and so forth.

Time series are generally a set of values given as a function of time, t; for instance, current as a function of time can be represented as $I(t)$. However, time series are also good representations of other kinds of data sets. For example, topographic elevations along linear transects, $h(x)$ are essentially equivalent to continuous time series. Here, the

topographic elevation, h, is a function of the horizontal coordinate, x. Another example is the concentration of a mineral as a function of depth in a drill core. The actual concentrations are continuous, with possibly a few exceptions, but from practical considerations, measurements of concentrations are carried out at discrete intervals, giving a discrete time series. Well logs are an example of a time series in a geological context; digitized measurements of density, porosity, and/or permeability at prescribed depth intervals represent discrete time series. Three examples of geophysical time series are given in Figure 3.1.

Although time series are defined to be sets of values as a function of a single variable, *i.e.* $y(t)$, time series can be extended to functions of more variables. An example is topography, $h(x, y)$, where the elevation h is a function of two horizontal coordinates, x and y. In this paper, we will only examine time series that are functions with one variable and can be plotted in two dimensions (two coordinates).

A time series may be characterized by any combination of the following: a trend component, one or more periodic components, and a stochastic component. The trend component is a long term increase or decrease in the series; for example, trends in stream-flow series often result from gradual human-induced changes to the land. Many time series have periodic components; for example, an atmospheric temperature time series will have strong daily and yearly periodicities. The stochastic component is the fluctuations not included in either the trend or periodic components.

Figure 3.1. Three examples of time series. (a) The number of worldwide earthquakes with seismic moments $M_0 > 10^{25}$ N·m in successive 30-day intervals, 1977-1995 (*Harvard Centroid-Moment Tensor Database*, 1997). (b) Average daily river discharges (*Slack and Landwehr*, 1992) for the hydrologic gauging station at Salt River near Roosevelt, AZ, 10/1/13 - 9/30/88, drainage area 11,200 km^2. (c) Elevation h as a function of position x. Earth's topography from 70W, 55S (southern tip of S America) to 70W, 10S (intersection of Bolivia, Peru, and Brazil). Both (a) and (b) are examples of discrete time series, and (c) is an example of a continuous time series. In (a), the values are independent of one another; this is an example of an uncorrelated time series. In both (b) and (c), the values in each time series are positively correlated with one another; these are examples of persistent time series.

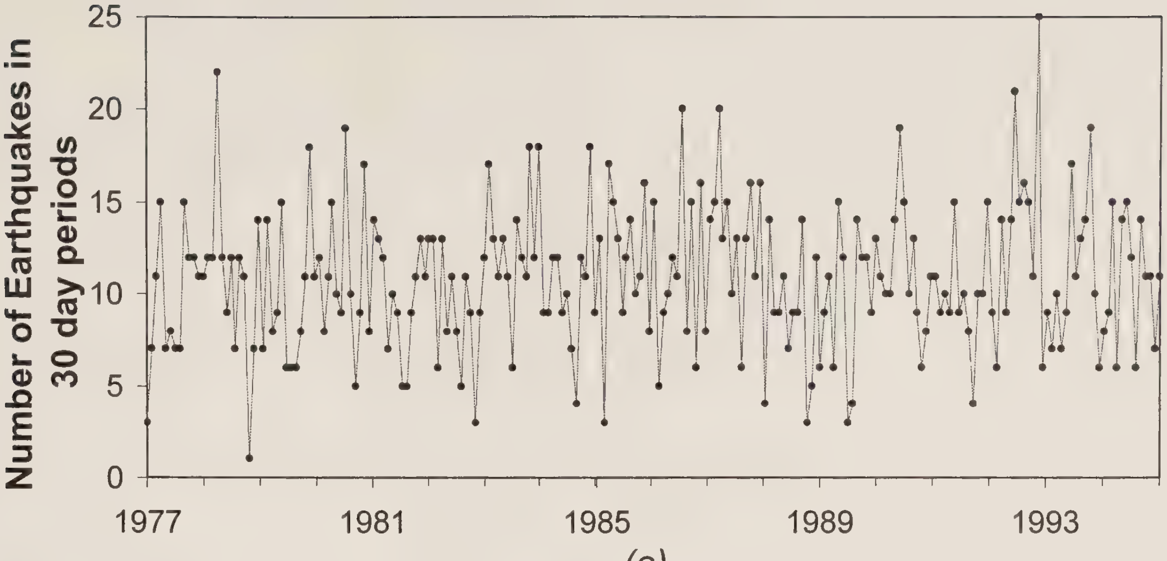
Number of Earthquakes in 30 day periods
0
5
10
15
20
25
1977
1981
1985
1989
1993

(a)

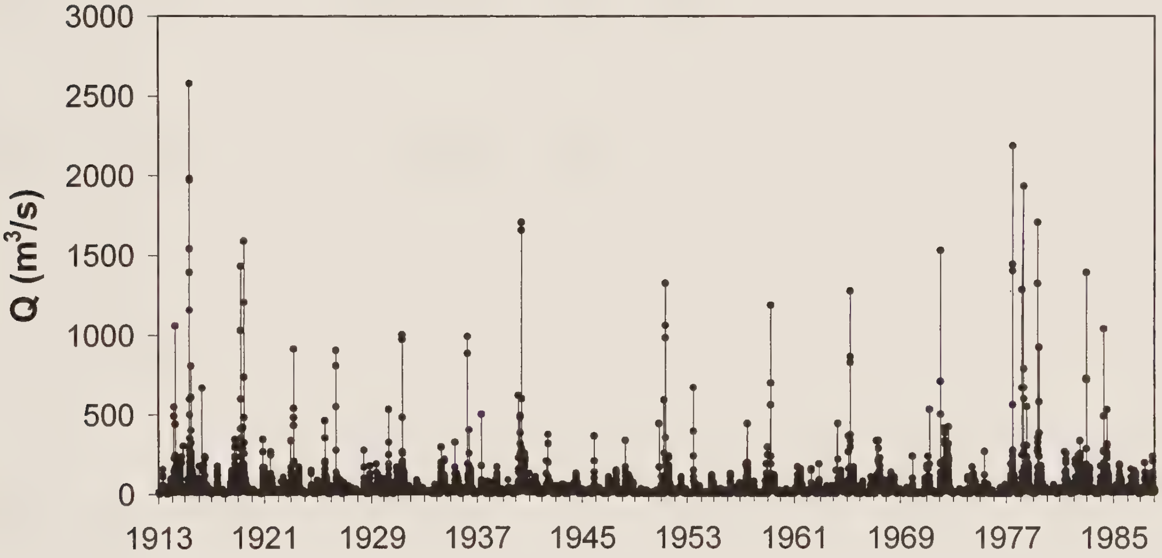
Q (m³/s)
0
500
1000
1500
2000
2500
3000
1913
1921
1929
1937
1945
1953
1961
1969
1977
1985

(b)

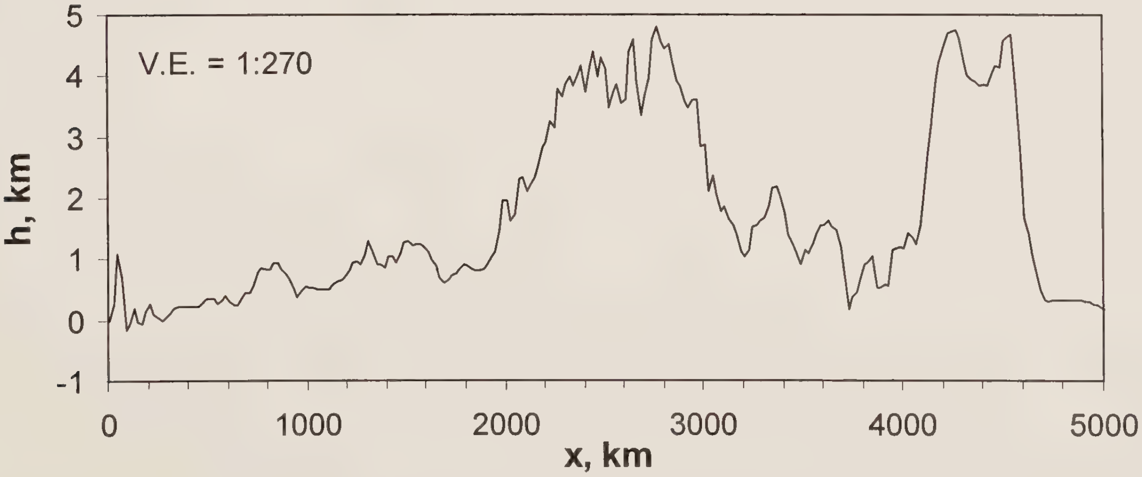
V.E. = 1:270
h, km
-1
0
1
2
3
4
5
0
1000
2000
3000
4000
5000
x, km

(c)

3.1.3. How is a Time Series Quantified?

In order to quantify the stochastic component of a time series it is necessary to specify:

(1) The statistical distribution of values.
(2) The persistence (or antipersistence).

The values of the variable in a natural time series may take on any statistical distribution of values. The most commonly used distributions may be divided into four families: the normal family (normal, log-normal, log-normal type 3), the general extreme-value (GEV) family (GEV, Gumbel, log-Gumbel, Weibull), the Pearson type 3 family (Pearson type 3, log-Pearson type 3), and the generalized Pareto distribution. *Stedinger et al.* (1993) provide an excellent discussion and review of these different distributions.

In many cases, the distribution of values is well approximated by a Gaussian (normal) distribution. For example, the discrete time series of the number of worldwide earthquakes occurring during successive 30-day periods (Figure 3.1a) is closely approximated by a Gaussian distribution. In other cases, the distribution may be strongly skewed with only positive values possible and it is appropriate to consider log-normal distributions. An example is the discrete time series of daily river discharges illustrated in Figure 3.1b. Hydrologic time-series studies have been considered in detail by *Bras and Rodriguez-Iturbe* (1993) and *Salas* (1993). The values in a discrete time series are defined by y_n, $n = 1, 2, 3, \ldots, N$. Usually, the time between each successive n is a constant interval δ. However, the

values of y_n may occur arbitrarily during δ, (*e.g.*, floods), occur at exactly every δ interval (*e.g.*, hourly temperature readings), or they can be the integral of the continuous time series taken over each interval of time δ (*e.g.*, a yearly time series of lake sediment accumulation). Note that in this paper, we connect individual points in a discrete time series by straight lines; this can give the false impression of continuous observation, but aids the eye in following the time series.

In addition to the statistical distribution of values, it is also necessary to specify whether a time series is persistent, uncorrelated, or antipersistent. The stochastic component of a time series is persistent if adjacent values are positively correlated; *i.e.* adjacent values are on average closer to each other than for an uncorrelated time series. It is antipersistent if adjacent values are anticorrelated; *i.e.* adjacent values are on average further apart than for an uncorrelated time series. *Beran* (1992, 1994) and *Bassingthwaighte et al.* (1994) give good overviews of statistical methods for treating data with persistence, and consider a variety of applications. Persistence is also known as the "memory" or internal-correlation of a process.

An example of a persistent time series is the discrete time series of average daily river discharges given in Figure 3.1b. Adjacent values of the average daily river discharges are positively correlated with one another. If a value for an average daily discharge is greater than the mean of the average daily discharges, then the next successive average daily discharge will have a high probability of also being greater; big values have a tendency to follow other big values, and small ones tend to follow

small. A continuous time series is, by definition, persistent. An example is the topography profile given in Figure 3.1c. Topography clearly has horizontal persistence; adjacent values of topography are correlated. If adjacent values in the time series are independent of one another then the stochastic component is uncorrelated. For example, the number of worldwide earthquakes occurring during successive 30-day periods (Figure 3.1a) is a sequence of independent measurements and the values in the time series are uncorrelated.

Persistence can be either weak or strong, short-range or long-range. The terms weak and strong are taken here to mean how strongly time series values that are separated by a given number of points (the lag) are correlated with one another. Short-range *vs.* long-range persistence specifies whether there is persistence for only short lags, or also for much longer lags. For instance, if values have a strong correlation with one another, but only for short lags, this is strong persistence over a short-range. Topography is an example of a process that exhibits strong persistence over a long-range.

There is a large literature on models containing short-range persistence, examples include autoregressive (AR) processes, moving average (MA) processes, and combinations of the two (ARMA) (*e.g. Salas*, 1993; *Box et al.*, 1994). A number of fields, for example hydrology, use models based on short-range persistence. In this paper, we examine time series models that exhibit long-range persistence. We create synthetic self-affine time series with long-range persistence and systematic variations in the strengths of persistence, similar to many time

series found in geophysics and other fields. We examine a variety of techniques that quantify the strengths of persistence in self-affine time series, and discuss the relative merits of each technique.

3.1.4. Autocorrelations and Semivariograms

In many cases the persistence (or antipersistence) of a time series can be quantified by using the autocorrelation function *r*. Many books and papers discuss this function. A very readable and comprehensive review of the use of the autocorrelation function for times-series analysis is given by *Box et al.* (1994).

The autocorrelation function measures the correlation of a time series with itself, $y(t+s)$ compared with $y(t)$, at increasing values of s the lag. For a continuous time series, the autocorrelation function, $r(s)$, at lag s, that is, the correlation between $y(t+s)$ and $y(t)$, is given by

$$r(s)=\frac{c(s)}{c(0)} \tag{3.1}$$

with the autocovariance function, $c(s)$, given by

$$c(s)=\frac{1}{(T-s)}\int_0^{T-s}\left[y(t+s)-\bar{y}\right]\left[y(t)-\bar{y}\right]dt \tag{3.2}$$

and the autocovariance function at 0 lag, $c(0)$, given by

$$c(0)=\frac{1}{T}\int_0^T\left[y(t)-\bar{y}\right]^2 dt=V \qquad (3.3)$$

The time series, $y(t)$, is prescribed over the interval $0 \leq t \leq T$. The average and variance of $y(t)$ over the interval T are $\bar{y}$ and V. The autocorrelation function, $r(s)$, is dimensionless and does not depend on the units of $y(t)$ or t. With $s = 0$ we have $c(s) = c(0) = V$, the variance of the time series over the period T, and $r(s) = 1$. The times series when compared with itself (0 lag) has a correlation of 1, the most positive that $r(s)$ can be. With increasing lag, s, the values of $r(s)$ become smaller as the statistical correlations of $y(t + s)$ with $y(t)$ decrease. The plot of $r(s)$ versus s is known as a correlogram. Although the autocorrelation (3.1) at a particular lag, s, can give insight into the data, one is generally more interested in the overall structure of the autocorrelation function taken over a range of lags. Large values of $r(s)$ indicate a strong correlation between those points in the time series that are separated by lag s, small values of $r(s)$ indicate weak correlation, and values of $r(s) = 0$ indicate no correlation (a white noise). Persistence here can be defined as a sequence of $r(s)$ that have positive values. If the values of $r(s)$ are large, but then quickly drop to $r(s) = 0$, we have an example of strong persistence over a short range of values. If the values of $r(s)$ are small (non-zero) and continue to stay small for very large lags, then the persistence is weak and long-range.

For a discontinuous time series, the autocorrelation function, r_k, is given by

$$r_k = \frac{c_k}{c_0} \tag{3.4}$$

with the autocovariance, c_k, given by

$$c_k = \frac{1}{(N-k)} \sum_{n=1}^{N-k} (y_{n+k} - \bar{y})(y_n - \bar{y}) \tag{3.5}$$

and the autocovariance at 0 lag (the variance) given by

$$c_0 = \frac{1}{N} \sum_{n=1}^{N} (y_n - \bar{y})^2 = V \tag{3.6}$$

Increasing values of k correspond to increasing lag. The variance, V, is taken over the N values of y_n. For an uncorrelated stochastic time series (a white noise), the values of r_k will be near zero. Positive values of r_k indicate persistence while negative values indicate antipersistence. The power spectrum of a time series is the Fourier transform of the autocorrelation function. The power spectrum, a measure of long-range persistence and antipersistence, is used frequently in the analysis of geophysical time series and will be discussed in detail in sections 3.2.2 and 3.2.3.

Note that in (3.2) and (3.5) some authors use T and N instead of $(T - s)$ and $(N - k)$; there is little difference for values of k less than about $N/4$. For a discussion of the two different quantities, see *Jenkins and Watts* (1968) and section 6.2 in *Percival and Walden* (1993). We use

$(T - s)$ and $(N - k)$ to maintain the same nomenclature that is used with the definition of semivariograms introduced later in this section.

One of the most important aspects of time series is the question of stationarity. Broadly speaking, a time series is said to be stationary if there are no systematic changes in the mean (*i.e.* no trend), no systematic changes in variance, and if periodic components have been removed (*Chatfield*, 1996). A time series is said to be strictly stationary if all moments are independent of the length of the time series considered. For instance, if either the mean, $\bar{y}$, or the variance, V, changes as a function of the length of the record, T, the time series is nonstationary. The mean is the first moment of the time series and the variance is the second moment. For this paper, we use a restricted definition of stationarity rather than strict stationarity, namely second-order or weak stationarity (*Chatfield*, 1996). In second-order stationarity, the mean of a time series does not change, the autocorrelation function (3.1 and 1.4) of the time series depends only on the lag, and the variance of the time series does not change. In other words, in addition to a time series that has a constant mean and variance, the correlation between $y(t)$ and $y(t + s)$ is the same as that between $y(t)$ and $y(t - s)$, where s is the lag. In the rest of this paper, the term "stationarity" should be taken to mean second-order stationarity.

It is inappropriate to use correlograms for nonstationary time series, because the autocorrelation function, r, has the mean, $\bar{y}$, in its definition. An alternative way to measure long-range correlations, which is valid for both stationary and nonstationary time series, is the

semivariogram γ. Like the autocorrelation function, the semivariogram measures the dependence of values in a time series that are separated by a lag, s. The variogram was developed by a French professor of mining and engineering, *Matheron* (1962, 1963a, 1963b), for the analysis of ore reserves and their distribution. The variogram is a quantification of the mean-square successive differences within a time series taken at increasing lag, s; *i.e.*, how much the values on average vary from one another, hence the term "variogram." Note that the variogram is not a measure of the variance (second moment), V, of a time series, but rather the variance of increments within the time series. Geostatisticians (*e.g. Journel and Huijbregts*, 1978) generally use half of the variogram, called the semivariogram. There are many examples of the use of the semivariogram in geology and geophysics; for example, *Oliver and Webster* (1986) have applied semivariograms to landforms and soil properties, and *Hewett* (1986), along with a review of many other fractal techniques, uses semivariograms for the analysis of fluid transport.

For a continuous time series, the semivariogram, $\gamma(s)$, is given by

$$\gamma(s) = \frac{1}{2(T-s)} \int_0^{T-s} \left[y(t+s) - y(t) \right]^2 dt \tag{3.7}$$

Note that neither the mean, $\bar{y}$, nor the variance, V, is used in this definition. For a discontinuous time series we have

$$\gamma_k = \frac{1}{2(N-k)} \sum_{n=1}^{N-k} \left(y_{n+k} - y_n \right)^2 \tag{3.8}$$

Increasing values of s or k correspond to increasing lag. The plot of γ_s *vs.* s or γ_k *vs.* k is known as a semivariogram. For a stationary time series the semivariogram, γ_k, and the autocorrelation function, r_k, are related. The mean of the time series, $\bar{y}$, can be added and subtracted within the summation in (3.8) to give

$$\gamma_k = \frac{1}{2(N-k)} \sum_{n=1}^{N-k} \left[(y_{n+k} - \bar{y}) - (y_n - \bar{y}) \right]^2 \tag{3.9}$$

When expanded this gives

$$\gamma_k = \frac{1}{2(N-k)} \left[\sum_{n=1}^{N-k} (y_{n+k} - \bar{y})^2 + \sum_{n=1}^{N-k} (y_n - \bar{y})^2 - \sum_{n=1}^{N-k} 2(y_{n+k} - \bar{y})(y_n - \bar{y}) \right] \tag{3.10}$$

Provided the time series is stationary, two of the terms in (3.10) are equivalent to the variance (3.6), giving

$$\gamma_k = V - \frac{1}{(N-k)} \sum_{n=1}^{N-k} (y_{n+k} - \bar{y})(y_n - \bar{y}) \tag{3.11}$$

Substituting the definition for c_k (3.5) into (3.11), and using the definitions of c_0 (3.6) and r_k (3.4) we find

$$\gamma_k = (V - c_k) = \left(V - V \frac{c_k}{c_0} \right) = V(1 - r_k) \tag{3.12}$$

For an uncorrelated time series we have $r_k = 0$ and $\gamma_k = V$. In section 3.3.4, we use semivariograms to quantify some nonstationary time series that exhibit long-range persistence; the quantification will give us a measure of the strength of the persistence.

Both the autocorrelation function and semivariograms have been applied by a number of authors to synthetic time series that exhibit long-range persistence, similar to the synthetic time series used in this paper. *Schepers et al.* (1992) applied the autocorrelation function to synthetic stationary time series. *Gallant et al.* (1994) applied the semivariogram to both stationary and nonstationary synthetic time series. *Beran* (1992, 1994) has an extensive discussion of the relationship between the autocorrelation function and long-range persistence; in addition, he gives extensive references to applications.

3.1.5. Self-Affine Fractals

Before continuing our discussion of time series, we introduce the concept of the self-affine fractal and the Hausdorff measure. Extensive work has been done in this area over the last two decades (*Mandelbrot*, 1982, 1985, 1986; *Feder*, 1988; *Meakin*, 1988; *Turcotte*, 1997; *Korvin*, 1992; *Hastings and Sugihara*, 1993; *Schmittbuhl et al.*, 1995).

The concept of fractals finds its origins in the concept of scale invariance. In the geological sciences, there are many examples of scale invariance. For example, a photograph of a geological outcrop requires a scale, such as a person or a rock hammer, in order for the viewer to have an idea of how big or how small the folds, layers of rocks, and other

structures are in the outcrop. *Mandelbrot* (1967) introduced the concept of fractals by examining the length of the coastline of Britain with different size measuring rods, and found a power-law dependence (scale invariance) of the total length of the coastline on the length of the measuring rod. In addition, a distribution of objects is fractal if the frequency-size distribution satisfies a power-law. Examples include the frequency-size distributions of faults, earthquakes, volcanic eruptions, mineral deposits, and oil fields. We first examine the concept of self-similar fractals, and then the more general case of self-affine fractals.

A statistically self-similar fractal is by definition isotropic. In two dimensions defined by x- and y-coordinates, the results do not depend on the geometrical orientation of the x- and y-axes. A formal definition of a self-similar fractal in two-dimensional xy-space is that $f(rx, ry)$ is statistically similar to $f(x, y)$ where r is a scaling factor. This result is quantified by the fractal relation (*Turcotte*, 1997)

$$N_{\mathrm{i}} \sim r_{\mathrm{i}}^{-\mathrm{D}} \tag{3.13}$$

where the number of objects, N_{i}, with a characteristic linear dimension, r_{i}, are related by a power law, and the constant exponent, D, is the fractal dimension. There are also formal limits on the acceptable values of D. Fractals on a line have $0 \leq D \leq 1$, fractals on a surface have $0 \leq D \leq 2$, and fractals in a volume have $0 \leq D \leq 3$.

One method for determining the fractal dimension of a rocky coastline is to determine the number of boxes required to cover a map of the coastline. If the number of boxes with dimension r_1 required to cover

the rocky coastline is N_1 and if the number of boxes with dimensions r_2 required to cover the rocky coastline is N_2, then the rocky coastline is a self-similar fractal if N_1 and N_2 satisfy (3.13), *i.e.* $(N_1/N_2) \sim (r_1/r_2)^{-D}$.

A statistically self-affine fractal is generally not isotropic; the x- and y-coordinates can scale differently. The boxes used to quantify self-affine fractal are rectangular instead of square. A definition of a self-affine fractal (*Mandelbrot*, 1982; *Voss*, 1985c) in a two-dimensional *xy* space is

$$f(rx, r^{Ha}y) \text{ is statistically similar to } f(x, y) \tag{3.14}$$

where x and y are variables, r is a scaling factor, and Ha, the Hausdorff measure, is a constant.

For the special case where $Ha = 1$, the self-affine fractal is also self-similar. Topography along a linear track is usually an example of a naturally occurring, self-affine fractal. Consider the mean of many Δh, where Δh is the difference in elevation between pairs of points separated by a horizontal distance L. Self-affinity of topography implies that

$$\Delta \mathrm{h} \sim \mathrm{L}^{\mathrm{Ha}} \tag{3.15}$$

where Ha is again the Hausdorff measure. Ahnert (1984) found that actual topography is in good agreement with (3.15) taking $Ha = 0.6 \pm 0.1$.

A deterministic construction of a self-affine fractal is illustrated in Figure 3.2 (*Mandelbrot*, 1985; section 3.3 *Barabási and Stanley*, 1995).

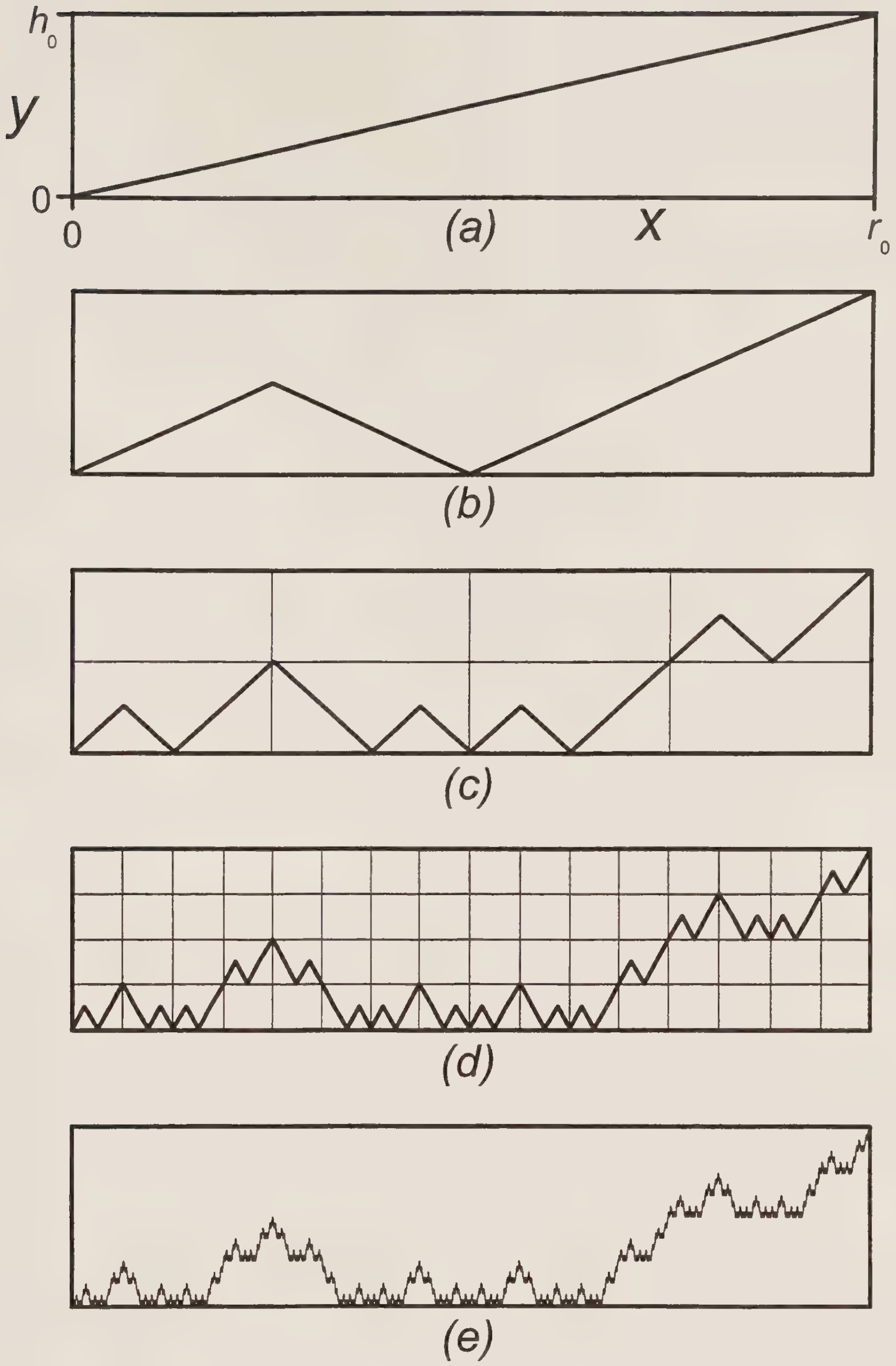

Figure 3.2. Illustration of a deterministic self-affine fractal. (a) At zero order, a rectangle of width r_0 and height h_0 is considered. A straight-line segment extends from (0, 0) to (r_0, h_0). (b) The first-order self-affine fractal is given. This construction also serves as the generator for higher-order fractals. (c) Each first-order straight-line segment in Figure 3.2b is replaced by the rescaled generator from Figure 3.2b to give the second-order fractal construction. (d) Each second-order straight-line segment in Figure 3.2c is replaced by the rescaled generator from Figure 3.2b to give the third-order fractal. (e) The construction is carried out to sixth-order.

In this deterministic construction, a rectangular region with width r_0 and height h_0 is considered. Note that the aspect ratio of this rectangle is irrelevant since the units of r_0 and h_0 are arbitrary. At all orders this fractal construction will begin at (0, 0) and end at (r_0, h_0). At zero order, Figure 3.2a, a straight line is drawn between (0, 0) and (r_0, h_0). At first-order, Figure 3.2b, the self-affine fractal is defined by dividing the horizontal coordinate into four equal parts so that $r_1 = r_0/4$ and dividing the vertical coordinate into two equal parts so that $h_1 = h_0/2$. Connecting the points (0, 0), $(r_0/4, h_0/2)$, $(r_0/2, 0)$, and (r_0, h_0) gives the generator that will be used for second and higher orders in this fractal construction, where the generator will replace each straight-line segment of preceding orders.

In the second-order fractal illustrated in Figure 3.2c, the generator has replaced each straight-line segment in the first-order fractal. At second-order, the horizontal coordinate has been divided into sixteen equal parts so that $r_2 = (r_0/16)$, and the vertical coordinate has been divided into four equal parts so that $h_2 = h_0/4$. In terms of the formal definition of a self-affine fractal given in (3.14), $f(x/4, y/2)$ is statistically similar to $f(x, y)$; at each step the horizontal coordinate has been divided into four equal parts and the vertical coordinate into two equal parts. Thus the Hausdorff measure can be obtained from $r = 1/4$ and $r^{\mathrm{Ha}} = 1/2$. This gives $(1/4)^{\mathrm{Ha}} = 1/2$ with the result $Ha = 1/2$. This construction of a self-affine fractal is extended to third order in Figure 3.2d, where the generator has replaced each straight-line segment in the second-order fractal. In Figure 3.2e, we extend this construction to sixth order. Note

that this sixth-order construction looks very similar to a profile of topography. As we see later, this deterministic self-affine fractal construction has the same long-range persistence characteristics as both topography and Brownian motions.

To determine the fractal-dimension of this self-affine fractal we use the box-counting method (*Voss*, 1988). For self-similar fractals we use square boxes, but for self-affine fractals it is necessary to use rectangular boxes. At zero-order consider the single rectangular box with width r_0 and height h_0; thus $N_0 = 1$. At first-order we have $r_1 = r_0/4$, so we will use rescaled rectangular boxes with width $r_0/4$ and height $h_0/4$. The rescaled boxes have the same aspect ratio as the original rectangular box. We wish to determine how many of these boxes are required to cover the first-order fractal illustrated in Figure 3.2b. This is illustrated in Figure 3.3 where we find $N_1 = 8$.

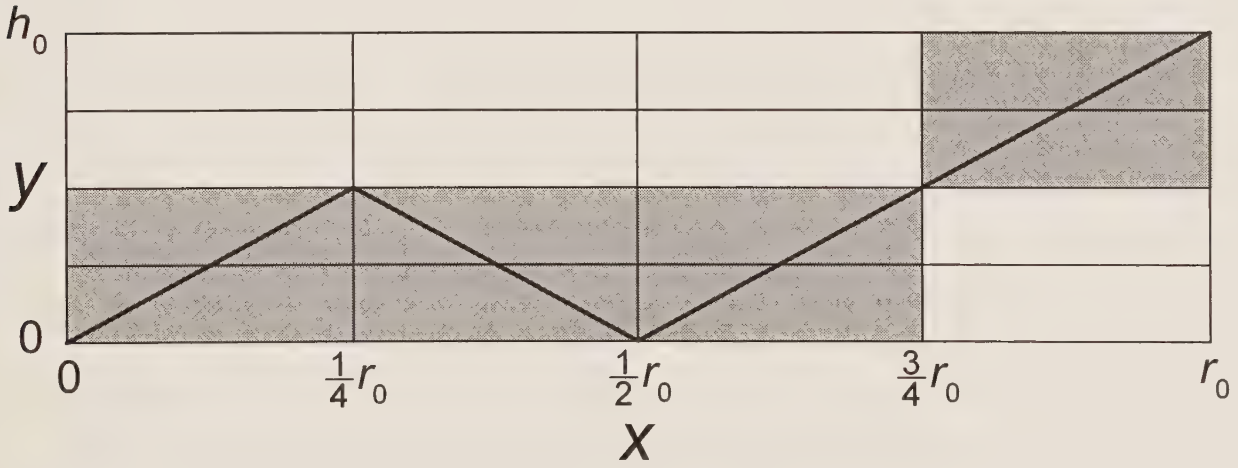

Figure 3.3. Box-counting technique applied to the first-order self-affine fractal given in Figure 3.2b. To determine its fractal dimension, rectangular boxes with width $r_1 = r_0/4$ and height $h_1 = h_0/4$ are used. This results in $N_1 = 8$ shaded boxes (out of 16) covering the fractal construction. Noting that $N_0 = 1$ box for the single box of width r_0 and height h_0, we find the fractal dimension $D = 1.5$.

Using (3.13), we find

$$D = \frac{\ln(N_1/N_0)}{\ln(r_0/r_1)} = \frac{\ln(8)}{\ln(4)} = \frac{3\ln(2)}{2\ln(2)} = \frac{3}{2} = 1.5 \tag{3.16}$$

The fractal dimension, *D*, can be an integer, in which case it is equivalent to a Euclidean dimension. Euclidean dimensions of a point, line, square, and cube, are respectively, 0, 1, 2, and 3. In general, *D* is not integer, but some fraction between integers, this is the origin of the word fractal. The fractal dimension $D = 1.5$ from (3.16) is intermediate between $D = 1$ for a straight line and $D = 2$ for a square.

3.1.6. Gaussian White Noises and Brownian Motions

The classic example of a stationary, discontinuous time series is a Gaussian white noise. Consider a variable ε_n, $n = 1, 2, 3, ..., N$, with a Gaussian distribution of values that are uncorrelated and random; the distribution has zero mean and a variance, $V_\varepsilon = \sigma_\varepsilon^2$, where σ_ε is the standard deviation of ε_n. The time series is stationary so the variance does not vary for different subintervals. If a time series is constructed with a set of $y_n(wn) = \varepsilon_n$, then adjacent values are uncorrelated and random, and this is a white noise. Four examples of synthetic Gaussian white noises are given in Figure 3.4a. In each case, $V_\varepsilon = 1$ and a different set of random numbers has been used.

The classic example of a nonstationary time series is a Brownian motion, obtained by summing a Gaussian white-noise sequence.

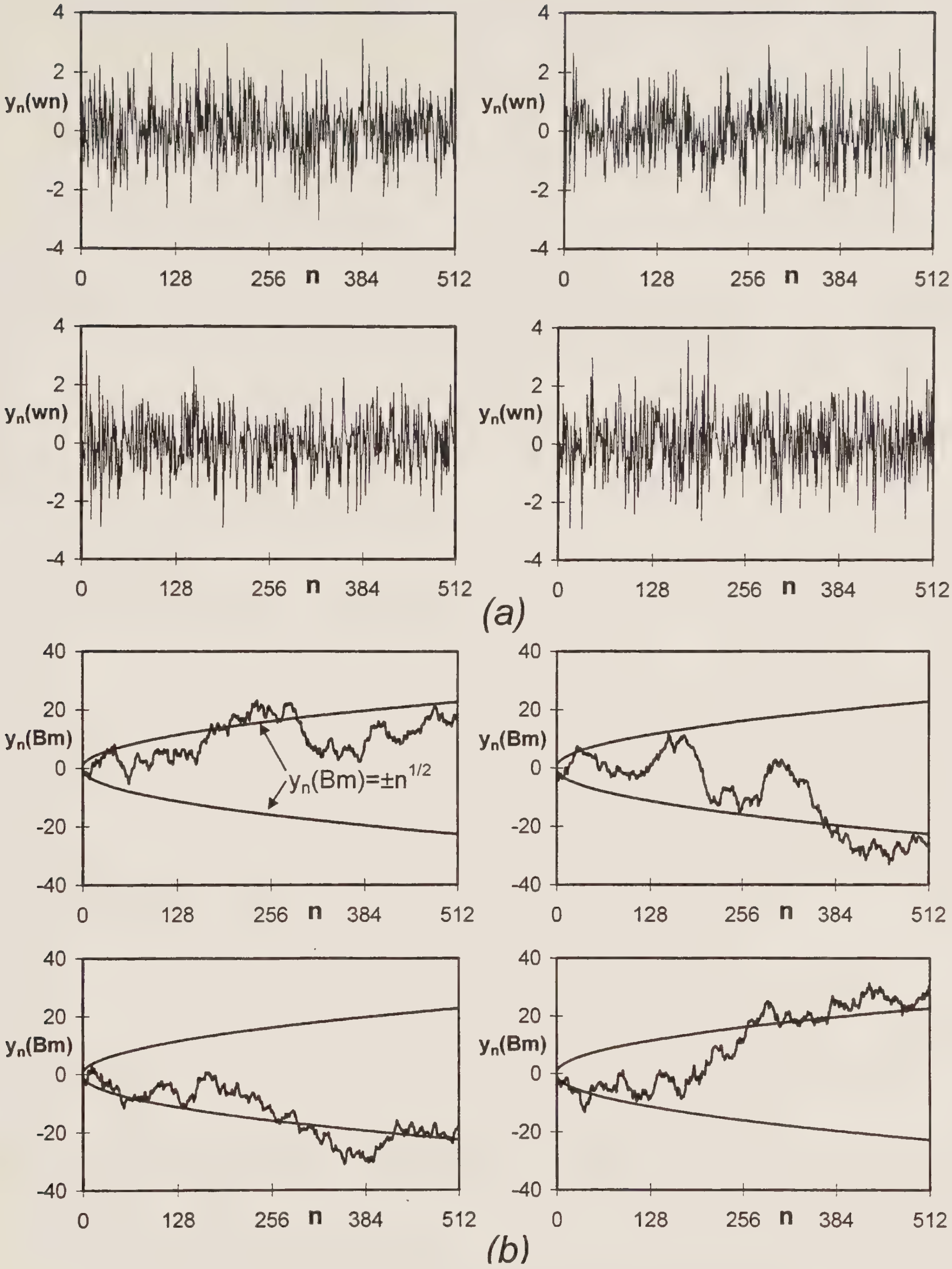

Figure 3.4. (a) Four examples of Gaussian white noises. Successive values are chosen randomly from a Gaussian distribution with zero mean ($\bar{y} = 0$) and unit variance ($V = 1$). Adjacent values are not correlated. (b) The four white noises in (a) are summed using (3.17) to give four Brownian motions. In each case, the standard deviation after n steps, given by (3.19), is included.

The values in a Brownian-motion time series $y_n(Bm)$ are given by

$$y_n(Bm) = \sum_{i=1}^{n} \varepsilon_i \tag{3.17}$$

The white-noise sequences shown in Figure 3.4a have been summed to give the four Brownian motions illustrated in Figure 3.4b. For an excellent review of the theory and history of the Brownian motion, see *Wang and Uhlenbeck* (1945).

The variance of a Brownian motion, after *n* values of the white noise have been summed, is given by

$$V_n(Bm) = \sigma_\varepsilon^2 n \tag{3.18}$$

where $\sigma_\varepsilon^2 = V_\varepsilon$ is the variance of the white-noise sequence. The corresponding standard deviation of the motion is given by

$$\sigma_n(Bm) = \pm\sigma_\varepsilon n^{1/2} \tag{3.19}$$

This result is compared with each of the four Brownian motions illustrated in Figure 3.4b.

In (3.14), the Hausdorff measure, *Ha*, was introduced in the context of the self-affine scaling relation, where $f(rx, r^{\mathrm{Ha}}y)$ is statistically similar to $f(x, y)$, and the vertical and horizontal coordinates can scale differently. The standard deviation of a self-affine time series taken over *n* values is given by σ_n. We can associate σ_n with the *y*-coordinate of the self-affine

relation, and the variable n with the x-coordinate. Then the dependence of the standard deviation, σ_n, on n can be expressed in terms of the Hausdorff measure, *Ha*, (*Mandelbrot and Van Ness*, 1968) according to

$$\sigma_n \sim n^{Ha} \tag{3.20}$$

with the corresponding variance given by

$$V_n \sim n^{Ha} \tag{3.21}$$

For a white noise, σ_n is independent of n, thus $Ha = 0$. For any stationary time series, σ_n must be independent of n, by definition, thus again $Ha = 0$. From (3.19) and (3.20) we find $Ha = 0.5$ for a Brownian motion. We also obtained $Ha = 0.5$ for the deterministic self-affine fractal illustrated in Figure 3.2.

In section 1.5, we gave an example of a deterministic fractal construction with a Hausdorff measure of $Ha = 0.5$, and calculated this construction to have a self-affine fractal dimension of $D = 1.5$. We now obtain a general relation (*Voss*, 1988), one that can be applied to self-affine time series, between the Hausdorff measure, *Ha*, and the self-affine fractal dimension, *D*. A derivation of the fractal dimension of a self-affine time series can be obtained by using the box-counting method. We first introduce a rectangular reference "box" with a width T; the height of the reference "box" is $\sigma_T \equiv \sigma(T)$, where $\sigma(T)$ is the standard deviation of

the signal y over the interval T. Since $\sigma(T)$ is in general a function of T, we are studying, by definition, nonstationary processes; the standard deviation changes with the interval considered. The units of the signal y, and therefore the units of the signal's standard deviation σ_T, can differ from the units of the interval T. Therefore, the aspect ratio (width to height = T/σ_T) of the box can have arbitrary units. As an example, we consider the sixth-order deterministic self-affine fractal construction illustrated in Figure 3.2e. This is analogous to a time series, with y varying from 0 to h_0 over the interval 0 to r_0. The standard deviation of this series of data (Figure 3.5a) over the interval $T = r_0$ is calculated to be $\sigma_T = h_0/4$. The reference "box" for this example (Figure 3.5b) has a width of $T = r_0$ and a height of $\sigma_T = h_0/4$.

We next divide the interval T into N equal-sized smaller intervals with length $\tau = T/N$. The standard deviation of the signal y over each of these smaller intervals will be approximately the same, and is given by $\sigma_\tau \equiv \sigma(\tau)$. In our example (Figure 3.5a), we let $\tau = T/4 = r_0/4$; the standard deviation of the signal y over each of the smaller intervals τ is calculated to be $\sigma_\tau = h_0/8$. We then introduce smaller rescaled boxes of width $\tau = T/N$ and height $\sigma_N = \sigma_T/N$. These boxes have the same aspect ratio as the reference box. However, the standard deviation of the signal y over the interval τ, $\sigma_\tau = \sigma(\tau)$, is not necessarily equal to $\sigma_N = \sigma_T/N$. In our example (Figure 3.5b) we divide our reference box into scaled smaller boxes with width $\tau = T/4 = r_0/4$ and height $\sigma_N = \sigma_T/4 = h_0/16$.

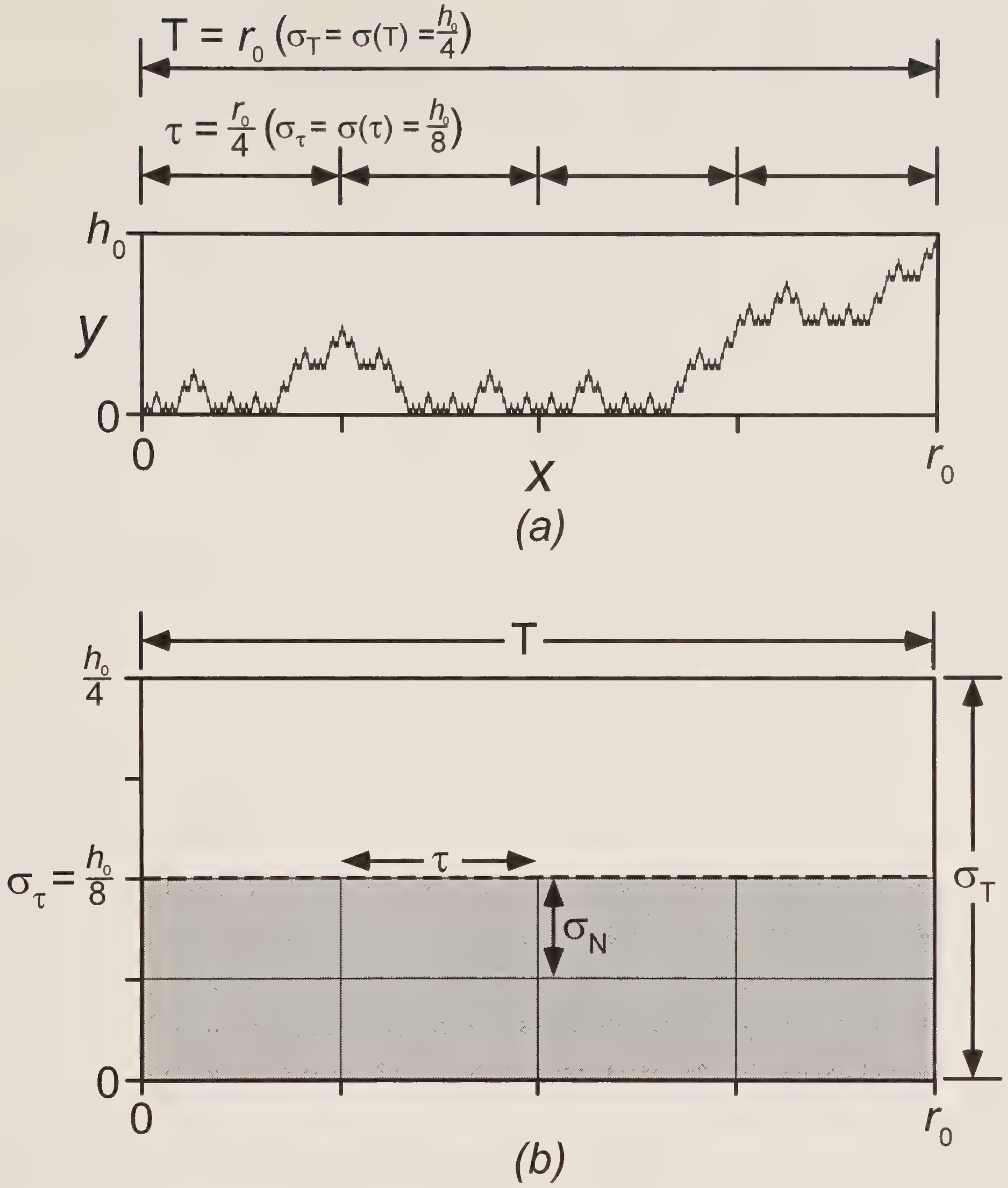

Figure 3.5. (a) The sixth-order deterministic self-affine fractal construction from Figure 3.2e is shown with the calculated standard deviations for the entire series ($T = r_0$) and for four equal smaller subdivisions of the series ($\tau = r_0/4$). (b) Box counting for the standard deviations. The reference "box" has width T, the length of the original series, and height σ_T, the standard deviation for the entire series. The reference box is scaled by four in width and height, giving smaller boxes with width $\tau = T/4$ and height $\sigma_N = \sigma_T/4$. The number of smaller scaled boxes (τ by σ_N) required to cover an area T by σ_τ, where σ_τ is the standard deviation of the series over each smaller subinterval τ, is $N_b = 8$.

We determine the number of scaled smaller boxes N_b of size τ by σ_N that are required to cover the area of width T and height σ_τ. In our example (Figure 3.5b) we find $N_b = 8$ boxes. This construction is generalized by writing

$$N_b = \frac{T\sigma_\tau}{\tau\sigma_N} = N\frac{\sigma_\tau}{\sigma_N} = N^2\frac{\sigma_\tau}{\sigma_T} \tag{3.22}$$

However, from (3.20) we have

$$\sigma(T) \sim T^{\mathrm{Ha}} \tag{3.23}$$

so that we can write

$$\frac{\sigma_\tau}{\sigma_T} = \frac{\sigma(\tau)}{\sigma(T)} = \frac{\sigma(\frac{T}{N})}{\sigma(T)} = \left(\frac{\frac{T}{N}}{T}\right)^{Ha} = \frac{1}{N^{Ha}} \tag{3.24}$$

and combining (3.22) and (3.24) gives

$$N_b = N^2\left(\frac{1}{N^{Ha}}\right) = N^{2-Ha} = \left(\frac{T}{\tau}\right)^{2-Ha} \tag{3.25}$$

In our example (Figure 3.5), $N_b = 8$, and $T/\tau = 4$, *i.e.* $(8) = (4)^{2-\mathrm{Ha}}$ giving $(2 - Ha) = 1.5$, thus $Ha = 0.5$. Equation (3.25) is a fractal relation: the number of boxes, N_b, is inversely proportional to the size of the

subinterval considered, raised to a constant power (2 – *Ha*). The interval over which the signal y is considered, T, is a constant. We can extend this analysis to smaller intervals of τ, and at each different subinterval considered, τ_i, there will be a corresponding N_{bi} boxes. Equation (3.25) becomes

$$N_{bi} = \left(\frac{T}{\tau_i} \right)^{2-Ha} \tag{3.26}$$

If we compare this to the power-law relation (3.13) and associate τ_i with r_i and N_{bi} with N_i, then

$$Ha = 2 - D \tag{3.27}$$

For a Brownian motion, $Ha = 0.5$ and we have $D = 1.5$. We obtained the same result for our deterministic self-affine fractal example illustrated in Figure 3.2: $Ha = 0.5$ and $D = 1.5$. Since for the self-affine fractals illustrated here, the value for D is always between 1 (a line) and 2 (a square), *Ha* for a self-affine fractal is between 0 and 1. We have derived here a general equation for *Ha* as a function of D. Self-affine fractal time series, $1 \leq D \leq 2$, are a subset of self-affine time series. A smooth time series (low frequencies dominate over high frequencies) approaches a straight line so that it has a fractal dimension near one. A very rough time series (with a large high-frequency component) becomes area filling and has a fractal dimension near two.

An alternative measure of a self-affine time series is that the semivariogram, $\gamma(s)$ and γ_k from (3.7) and (3.8), scales with s and k, the lag, such that (*Mandelbrot and Van Ness*, 1968)

$$\gamma(s) \sim s^{2Ha} \tag{3.28}$$

and

$$\gamma_k \sim k^{2Ha} \tag{3.29}$$

where, again, *Ha* is the Hausdorff measure. The dependence of the semivariogram on the lag is directly analogous to the dependence of the variance of a time series, V_n on the length of the time series, n, as given in (3.21). We verify this relation when we determine the semivariograms of synthetic fractional motions in section 3.3.4.

The Hausdorff measure, *Ha*, and the fractal dimension, *D*, are both measures of the strength of persistence for a subclass of self-affine time series, for which $0 < Ha < 1$ ($1 \leq D \leq 2$). There are a number of other measures for the strength of persistence, discussed in this paper, which can be used to calculate the strength of persistence for self-affine time series that do not fall in the range where *Ha* and *D* are useful. A general discussion of methods used to estimate *Ha*, *D*, and other measures of the persistence of time series has been given by *Korvin* (1992), *Schepers et al.* (1992), and *Schmittbuhl et al.* (1995).

3.2. SPECTRAL ANALYSIS

3.2.1. The Fourier Transform

Spectral analysis is a technique that estimates the spectral density function, or spectrum, of a time series. In the past, most spectral analyses were concerned with finding periodicities in data; today, they are widely used to obtain a complete spectrum over a wide range of frequencies. One standard approach is to carry out a Fourier transform on a time series. Fourier analysis is essentially concerned with approximating a function by a sum of sine and cosine terms. A large body of literature has been written on Fourier analysis and spectral analysis in general; comprehensive summaries have been given by *Priestley* (1981) and *Percival and Walden* (1993). *Press et al.* (1994) provides an easy to understand basic theory and computational implementation of most techniques found in spectral analysis.

A time series can be prescribed either in the time domain as $y(t)$ or in the frequency domain in terms of the Fourier transform, $Y(f)$, where f is the frequency. The quantity $Y(f)$ is generally a complex number indicating both the amplitude and phase of the signal. We first begin with the general case where $g(t)$ is a continuous function that satisfies $g(t) = g(t + kT)$, $k = 0, \pm1, \pm2, \pm3, \ldots$, and the function $g(t)$ is defined for all t, $-\infty < t < +\infty$. If T is the smallest number that satisfies $g(t) = g(t + kT)$, then the function $g(t)$ is periodic with a period T. If there is no value of k (other than $k = 0$) for which $g(t) = g(t + kT)$ holds, then $g(t)$ is non-periodic. The Fourier transform, $G(f)$, of the periodic continuous function, $g(t)$, is defined as

$$G(f) = \int_{-\infty}^{\infty} g(t) e^{2\pi i f t} dt \tag{3.30}$$

The complementary inverse Fourier transform is then given by

$$g(t) = \int_{-\infty}^{\infty} G(f) e^{-2\pi i f t} df \tag{3.31}$$

The exponents in (3.30) and (3.31) represents an infinite number of sine and cosine functions, with $e^{-2\pi i f t} = \cos(2\pi f t) + i \sin(2\pi f t)$. The i in the exponents is the square root of -1. One goes between $g(t)$ and $G(f)$ by the use of the Fourier transform equations given in (3.30) and (3.31). The Fourier transform, $G(f)$, of the time series represents the contribution of each sine and cosine function at each frequency, and is commonly called the Fourier spectrum of $g(t)$.

A time series with three periodic components at periods T, $T/2$, and $T/5$, will have spikes in its Fourier spectrum at the frequencies $f = 1/T$, $2/T$, and $5/T$. If T has the units of seconds, then f will have the units of cycles per second. A white noise has no embedded frequencies and its Fourier spectrum is approximately flat. We use frequency, f, instead of the alternative angular frequency, $\omega = 2\pi f$, because f is more informative for the time series we consider in this paper.

For this paper, we are interested in stochastic time series that are non-periodic and defined over a finite interval, $0 \leq t \leq T$. For t outside of this interval ($t < 0$ and $t > T$), we require $y(t) = 0$. A periodic time series

is normally composed of a finite number of subperiods, corresponding to a finite number of spikes at discrete frequencies in the resulting Fourier spectrum. A non-periodic function has no fixed period or subperiods, and instead can be viewed as being composed of an infinite number of subperiods in the time domain, or a continuous and infinite range of frequencies in the Fourier frequency domain. We use the notation $Y(f, T)$ when taking the Fourier transform of $y(t)$ over the interval $0 \leq t \leq T$. For a stochastic non-periodic time series, the Fourier transform pair given by (3.30) and (3.31) becomes (*Priestley*, 1981)

$$Y(f,T) = \int_0^T y(t)e^{2\pi ift}\,dt \tag{3.32}$$

and

$$y(t) = \int_{-\infty}^{\infty} Y(f,T)e^{-2\pi ift}\,df \tag{3.33}$$

In the time domain (3.32), the integral is from $0 \leq t \leq T$, since $y(t) = 0$ outside of this range; however, in the frequency domain (3.33), there is a continuous range of frequencies possible, $-\infty < f < +\infty$, since we are dealing with a non-periodic function. In (3.32) we could have defined $y(t)$ to range from $-T/2 \leq t \leq T/2$ (commonly done in many texts) instead of $0 \leq t \leq T$; however, the result in (3.32) would be the same except that the integral would be $-T/2$ to $T/2$ instead of 0 to T. The units of the Fourier transform depend on the units of the time series $y(t)$. For

example, if the units for $y(t)$ are in amperes and the units for t in seconds, then the Fourier transform, $Y(f, T)$, has the units of ampere-second, and the frequency, f, has the units of second^{-1}.

The concepts described above are easily modified for discrete time series. Consider the discrete time series, y_n, $n = 1, 2, 3, \ldots, N$, where the total time interval, T, has been divided into N equal intervals of length δ, *i.e.* $\delta = T/N$. The units of δ are those of T; N is dimensionless. Many authors do not include δ in their studies of discrete time series, they assume $\delta = 1$ time unit. We include δ in the equations that follow so that the units will be analogous to the equations given for continuous time series. If we approximate the integrals given in (3.32) and (3.33), then the discrete Fourier transform (DFT) applied to the discrete time series, y_n, is (*Priestley*, 1981)

$$Y_m = \delta \sum_{n=1}^{N} y_n e^{2\pi i n m/N}, \qquad m = 1, 2, 3, \ldots, N \tag{3.34}$$

and the inverse DFT is

$$y_n = \frac{1}{N\delta} \sum_{m=1}^{N} Y_m e^{-2\pi i n m/N}, \qquad m = 1, 2, 3, \ldots, N \tag{3.35}$$

There are now discrete values in both the time and frequency domains. Many variations on the DFT pairs exist (see *e.g.*, *Percival and Walden*, 1993, for a complete discussion). Some authors let the running

variable in (3.34) and (3.35) vary from 0 to ($N - 1$). For consistency with the rest of this paper, we allow the index to run from 1 to N; the Fourier pairs are equivalent for the two different running indices (*Priestley*, 1981). The Fourier coefficients, Y_m, $m = 1, 2, 3, \ldots, N$, are associated with frequencies $f_m = m/(N\delta)$. As before, the Fourier coefficients, Y_m, are complex numbers with real and imaginary parts, $Y_m = a_m + ib_m$. The complex modulus of Y_m is

$$|Y_m| = \sqrt{(a_m^2 + b_m^2)} \tag{3.36}$$

The Fourier coefficients are symmetric such that

$$|Y_m| = |Y_{N-m}| \tag{3.37}$$

For example, if $N = 4{,}096$, then $|Y_1| = |Y_{4095}|$, $|Y_2| = |Y_{4094}|$, etc. The highest frequency resolvable using Fourier analysis of a discrete time series, y_n, $n = 1, 2, 3, \ldots, N$, is the frequency with a period of two time units, 2δ. Any spectral components of a higher frequency cannot be distinguished from lower frequency components, this is aliasing. Consequently, the highest frequency that we can resolve in Fourier space, will be $f_m = 0.5$, where $f_m = m/(N\delta)$; the unique Fourier coefficients will be given by Y_m, $m = 1, 2, 3, \ldots, N/2$.

3.2.2. The Power-Spectral Density

The modulus of the complex number $Y(f) = (a + bi)$ is given by $|Y(f)| = (a^2 + b^2)^{1/2}$. In the frequency domain, a measure of the energy distribution of a signal as a function of frequency is $|Y(f, T)|^2$. As T approaches infinity, the total energy diverges and also approaches infinity. Thus it is standard practice to convert the energy to power, that is we divide $|Y(f, T)|^2$ by T. The power-spectral density function of $y(t)$ is defined (*Priestley*, 1981) as

$$S(f) = \lim_{T\to\infty}\left\{\frac{|Y(f,T)|^2}{T}\right\} \tag{3.38}$$

A plot of $S(f)$ against f is known as a periodogram, where the function we are plotting is the power-spectral density function. In terms of units, if $y(t)$ is in amperes, t (and T) in seconds, and $Y(f, T)$ in ampere-seconds, then $|Y(f, T)|^2$ has the units of ampere^2-second^2, and the power-spectral distribution function, $S(f)$, has the units of ampere^2-second.

The quantity $S(f)\mathrm{d}f$ in a periodogram represents the contribution to the total power from those components in the time series, $y(t)$, whose frequencies lie in the interval between f and $f + \mathrm{d}f$. For a time series that is self-affine, the power-spectral density is defined (*e.g.*, *Voss*, 1985a) to have a power-law dependence on frequency

$$S(f) \sim f^{-\beta} \tag{3.39}$$

This relation also defines a self-affine fractal in the same way that $N_i \sim r_i^{-D}$ (3.13) defines a self-similar fractal. The implications of (3.39) will be a major focus of this paper. Because of the power-law dependence of $S(f)$ on f, self-affine time series with $\beta > 0$ exhibit long-range persistence, and self-affine time series with $\beta < 0$ exhibit long-range antipersistence. The value of β, the slope of the best-fit straight line to $\log(S(f))$ *vs.* $\log(f)$, is a measure of the strength of persistence or antipersistence in a time series.

The power-spectral density function, S_m, for a discrete time series y_n, can be written as

$$S_m = \lim_{N\to\infty}\left\{\frac{2\left|Y_m\right|^2}{N\delta}\right\}, \qquad m = 1, 2, 3, \ldots, \frac{N}{2} \tag{3.40}$$

The factor of 2 in (3.40) is a result of summing Y_m from $m = 1$ to $N/2$ instead of N. For a discrete self-affine time series, the power-spectral density, S_m, again has a power-law dependence on frequency

$$S_m \sim \left(\frac{m}{N\delta}\right)^{-\beta}, \qquad m = 1, 2, 3, \ldots, \frac{N}{2} \tag{3.41}$$

This is equivalent to

$$S_m \sim f_m^{-\beta}, \qquad m = 1, 2, 3, \ldots, \frac{N}{2} \tag{3.42}$$

As an example, we obtain the discrete power-spectral density for two discrete time series. We use the fast Fourier transform (*e.g.*, *Press et al.*,

1994), an algorithm that is commonly used to speed up the computation of the discrete Fourier transform. The first time series is a white noise (Figure 3.6a), where the values are randomly chosen from a Gaussian (normal) distribution with mean $\bar{y} = 0$ and variance $V = 1$. The second time series is the corresponding Brownian motion (Figure 3.6c) obtained by summing the white noise given in Figure 3.6a using (3.17). The Brownian motion has a mean $\bar{y} = -23$ and variance $V = 950$. Both time series have $N = 4{,}096$ points.

The two resulting periodograms, S_{m} plotted as a function of f_{m} with log-log scaling, are shown in Figures 3.6b,d. Plotted on log-log axes, there are many more values of S_{m} at the high frequencies (f_{m} large) than at low frequencies. Therefore, to obtain the best-fit straight line to $\log(S_{\mathrm{m}})$ *vs.* $\log(f_{\mathrm{m}})$, we bin the data. We first divide the f_{m} axis into equal log-increments, then for each $\log(f_{\mathrm{m}})$ bin calculate the average of all the $\log(S_{\mathrm{m}})$ that are in that bin. The best-fit least-squares straight line is then calculated for the resulting average($\log(S_{\mathrm{m}})$) as a function of the center of each $\log(f_{\mathrm{m}})$ bin; these values are plotted as circles in Figures 3.6b,d, with the best-fit straight line to these circles shown.

We use β_{PS} to indicate the negative of the slope of the best-fit straight line when applying power-spectral analysis (3.42). Because the white noise is a stationary uncorrelated time series, we expect the power spectrum to be essentially flat; *i.e.*, all frequencies are present in equal amounts. For the example given in Figure 3.6b we find $\beta_{\mathrm{PS}} = -0.03$, close to the theoretical value of $\beta = 0$.

Figure 3.6. Two examples of power-spectral analysis. Two time series are given in (a) and (c) with their respective periodograms given in (b) and (d). The first time series (a) is a white noise with $N = 4{,}096$ points, and was obtained by randomly choosing values from a Gaussian distribution of values with a mean, $\bar{y} = 0$, and a variance, $V = 1$. The second time series (c) is a Brownian motion obtained by summing the white noise in (a); it has a mean, $\bar{y} = -23$, and a variance, $V = 950$. The Fourier power spectrum (periodograms) for the white noise and Brownian motion are shown, respectively, in (b) and (d). In both periodograms, the power spectral-density function, S_{m}, from (3.40) is given as a function of frequency $f_{\mathrm{m}} = m/N$, where $m = 1, 2, 3, \ldots, N/2$. The circles are obtained by averaging the $\log(S_{\mathrm{m}})$ into equal $\log(f_{\mathrm{m}})$ bins. In the log-log plots, the value of β_{PS} is the negative of the slope of the best-fit least-squares straight line to the circles. The white noise has $\beta_{\mathrm{PS}} \approx 0$, and the Brownian motion has $\beta_{\mathrm{PS}} \approx 2$.

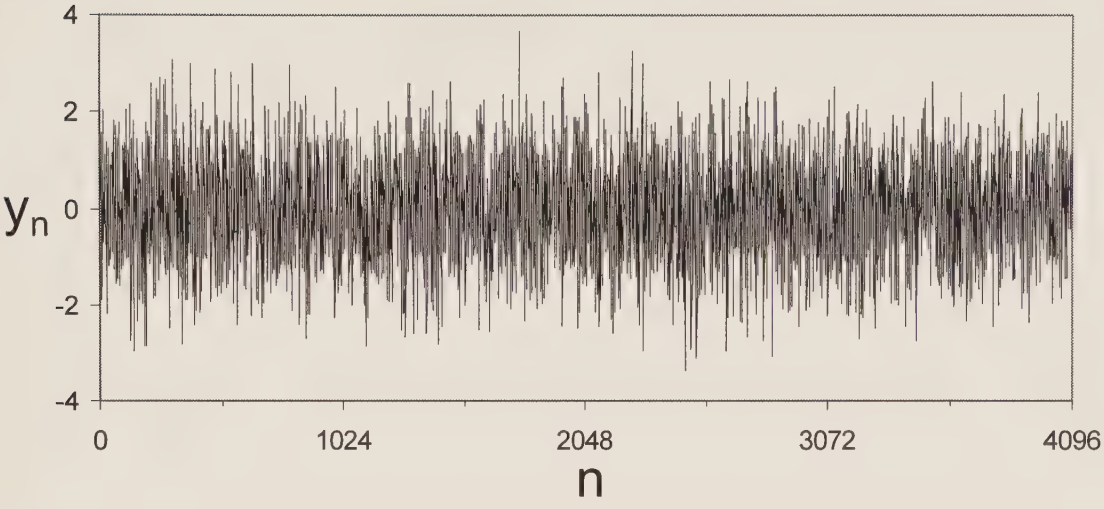
4
2
0
-2
-4
y_n
0
1024
2048
3072
4096
n

(a)

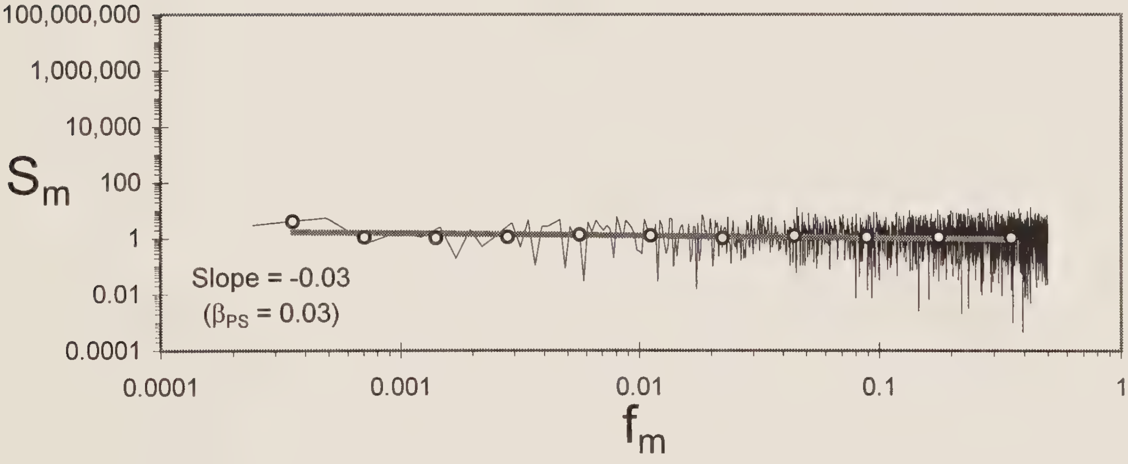
100,000,000
1,000,000
10,000
100
1
0.01
0.0001
S_m
Slope = -0.03
(β_{PS} = 0.03)
0.0001
0.001
0.01
0.1
1
f_m

(b)

Figure 3.6 (Continued)

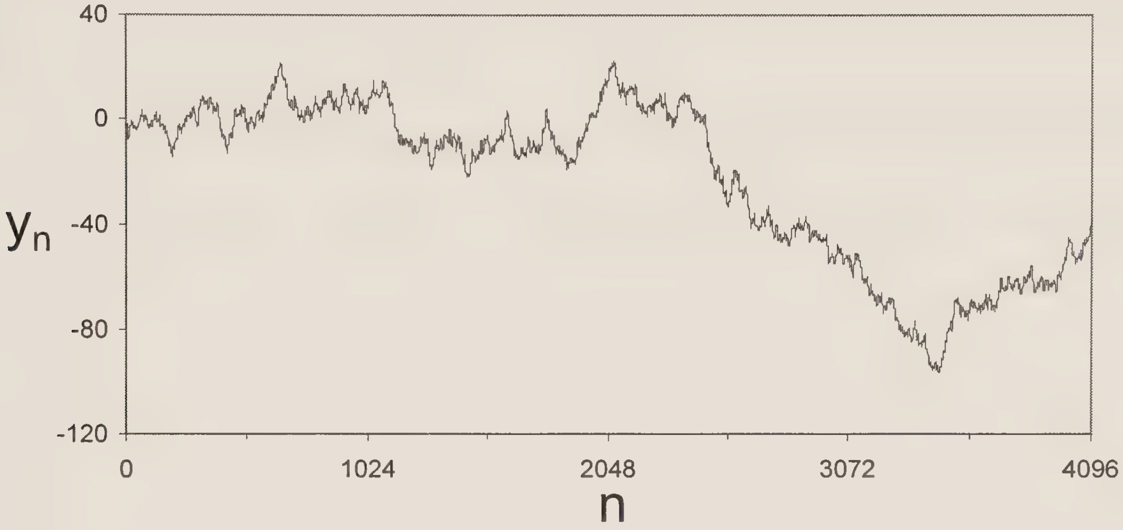

(c)

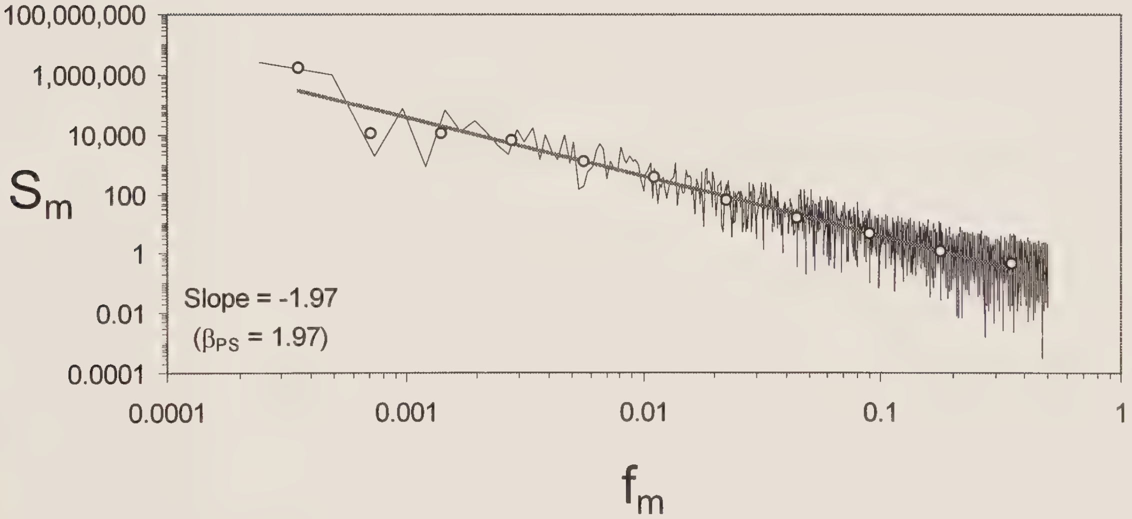

(d)

The Brownian motion (Figure 3.6c) is a nonstationary signal that is much "smoother" than the white noise (Figure 3.6a). Thus, we expect that the low frequencies (f_m small) will be dominant over the high frequencies (f_m large), and that the slope of the best-fit straight line will be negative and β positive. This is found to be true; the Brownian motion has a slope –1.97, *i.e.* $\beta_{PS} = 1.97$.

We found that a Brownian motion (a summed white noise) has $\beta_{PS} \approx 2$ and a white noise has $\beta_{PS} \approx 0$; the summed time series has a β_{PS} that is approximately +2 larger than the nonsummed time series. This can be generalized to all self-affine time series: summing a self-affine time series shifts the theoretical power-spectral density exponent, β, by +2. We can also reverse the process; the differences in adjacent values (the first differences) of a Brownian motion result in a white noise. This can also be generalized to all self-affine time series: taking the first differences shifts the theoretical power-spectral density exponent, β, by -2. We will now show that this is true by considering the derivative (first difference) of a self-affine time series.

The self-affine time series, $y(t)$, has a corresponding Fourier transform, $Y(f, T)$, defined by (3.32) and a power-spectral density function, $S(f)$, defined by (3.38). The derivative of $y(t)$, $y'(t)$, with its corresponding inverse Fourier transform (3.33), is given by

$$y'(t) = \frac{dy(t)}{dt} = \int_{-\infty}^{\infty} Y'(f,T) e^{-2\pi i f t} df \qquad (3.43)$$

The corresponding Fourier transform (3.32) of $y'(t)$ is

$$Y'(f,T) = \int_0^T y'(t) e^{2\pi i f t} dt \tag{3.44}$$

Taking the derivative of both sides of (3.33) gives

$$y'(t) = \frac{dy(t)}{dt} = \frac{d}{dt}\left[\int_{-\infty}^{\infty} Y(f,T) e^{-2\pi i f t} df\right] = \int_{-\infty}^{\infty} (-2\pi i f) Y(f,T) e^{-2\pi i f t} df \tag{3.45}$$

Comparing the right sides of (3.43) and (3.45), the integrands must be equal, therefore

$$Y'(f,T) = (-2\pi i f) Y(f,T) \tag{3.46}$$

Using (3.38), the power-spectral density function, $S'(f)$, corresponding to $y'(t)$ is

$$S'(f) = \lim_{T\to\infty}\left\{\frac{|(-2\pi i f) Y(f,T)|^2}{T}\right\} = \left(4\pi^2 f^2\right) S(f) \tag{3.47}$$

where $S(f)$ is the power-spectral density function (3.38) of $y(t)$. Finally, from (3.39), where the power-spectral density function has a power-law dependence on frequency, we can write

$$f^{-\beta'} \sim \left(4\pi^2 f^2\right) f^{-\beta} \tag{3.48}$$

which simplifies to

$$f^{-\beta'} \sim f^{-\beta+2} \tag{3.49}$$

and

$$\beta' = \beta - 2 \tag{3.50}$$

If the self-affine time series, $y(t)$, is characterized by a power-spectral exponent, β, then the first difference (derivative) of that time series is characterized by a power-spectral exponent of β - 2. We can use the same logic as that shown in equations (3.43) through (3.50) to show that if $y(t)$ has a characteristic β, then the running sum (integral) of $y(t)$ is characterized by a power-spectral exponent of β + 2. Since $\beta = 0$ for a white noise, we expect $\beta = 2$ for a Brownian motion, close to the value found. In subsequent sections, we will use this summing and differencing property as part of the construction of a variety of synthetic self-affine time series.

The power-spectral density function can also be related to other statistical measures of time series. We introduced the autocorrelation function $r_k = c_k/c_0$ in (3.4), with c_k given by (3.5) and c_0 (the variance) by (3.6). The autocorrelation function is directly related to the power-spectral density (*Box et al.*, 1994) by

$$S_m = 2\left\{c_0 + 2\sum_{k=1}^{N-1}\left[\left(1-\frac{k}{N}\right)c_k \cos\left(\frac{2\pi mk}{N}\right)\right]\right\}, \qquad m = 1, 2, 3, \ldots, \frac{N}{2} \tag{3.51}$$

The power-spectral density is the Fourier transform of c_k. There are no sine components in (3.51) because the autocorrelation function is even (symmetric around the y axis). There is a $(1-k/N)$ in (3.51) because of the way we defined the autocorrelation function in (3.5), note that in many texts this factor would not be included in (3.51). The autocorrelation function and the power-spectral density are equivalent ways of describing a stochastic process; both contain the same information but express it in different ways. In this paper, we use the power-spectral density in order to quantify the persistence in time series.

We next relate the power-spectral density function, S_m, to the variance, V_N, of a discrete time series, y_n, $n = 1, 2, 3, \ldots, N$. The successive values of the time series y_n are prescribed at equal increments of time, δ. Using Parseval's theorem (*e.g.*, *Percival* and *Walden*, 1993) we write

$$V_N = \frac{1}{N}\sum_{n=1}^{N}\left(y_n - \bar{y}\right)^2 = \frac{2}{N^2\delta^2}\sum_{m=1}^{N/2}\left|Y_m\right|^2 = \frac{2}{N\delta}\sum_{m=1}^{N/2} S_m \qquad (3.52)$$

The variance, V_N, is proportional to the summation of S_m, the power-spectral density function. Parseval's theorem states that the total power in a signal is the same whether it is computed in the time domain or the frequency domain. Note that many authors take $\bar{y} = 0$ in writing Parseval's theorem. Equation (3.52) gives the result that the variance of a discrete time series of length N is proportional to the sum of the power-spectral density coefficients, S_m. We can verify (3.52) by summing the S_m

from the periodograms in Figure 3.6 and multiplying by $2/(N\delta)$, where $N = 4{,}096$. The white noise (Figure 3.6a) has variance $V_N = 1.0$, and in agreement with (3.52), the S_m (Figure 3.6b) give $(\Sigma S_m)/2{,}048 = 1.0$. The same agreement is found for the Brownian motion (Figure 3.6c), which has variance $V_N = 950$ and corresponding S_m (Figure 3.6d) such that $(\Sigma S_m)/2{,}048 = 950$.

3.2.3. *The Relation of β, Ha, and D*

Using a derivation from *Voss* (1985c), we now obtain a relationship between the power β, the Hausdorff measure *Ha*, and the fractal dimension *D*. Consider a time series $y_1(t)$ specified over the interval $0 \le t \le rT$. Next consider two time series that are based on $y_1(t)$: $y_1(rt)$ with $0 \le t \le T$, and $y_2(t)$ also with $0 \le t \le T$. These are related by

$$y_2(t) = \frac{1}{r^{Ha}} y_1(rt), \qquad 0 \le t \le T \tag{3.53}$$

where *Ha* is the Hausdorff measure. This process is illustrated in Figure 3.7 for $r = 0.2$, $Ha = 0.5$ and $T = 1.0$. In Figure 3.7a, we show a time series $y_1(t)$, $0 \le t \le T$, with the area under the curve of $y_1(t)$ shaded from $0 \le t \le rT$. Figure 3.7b shows $y_1(rt)$ from $0 \le t \le T$; *i.e.*, the time axis of $y_1(t)$ in Figure 3.7a has been "stretched out" in Figure 3.7b by a factor of $(1/r) = 5$. Finally, in Figure 3.7c, we have stretched the amplitude of $y_1(rt)$ by a factor of $(1/r)^{-Ha} = 5^{0.5} \approx 2.24$.

Figure 3.7. Rescaling a self-affine time series. (a) A Brownian motion ($Ha = 0.5$) is given by the time series $y_1(t)$, with $0 \leq t \leq T$. The Brownian motion has a Hausdorff measure, $Ha = 0.5$, and was obtained by summing a Gaussian white noise. For this example, we let $r = 0.2$ and $T = 1.0$. The area under the curve of $y_1(t)$ is shaded from $0 \leq t \leq rT$. (b) The time axis of $y_1(t)$, the time series shown in Figure 3.7a, is "stretched" by a factor of $(1/r) = 5$. The new time series, $y_1(rt)$, is shown for $0 \leq t \leq T$. The shaded area represents the part of $y_1(t)$ from Figure 3.7a that was expanded. The "*A*" in all three figures is to aid the eye in following the part of the time series that is rescaled from step to step. (c) The amplitude of the "stretched" time series from Figure 3.7b, $y_1(rt)$, is now expanded by a factor of $(1/r)^{-\mathrm{Ha}} = 5^{0.5} = 2.24$, giving a new time series $y_2(t)$, $0 \leq t \leq T$. Since the original time series, $y_1(t)$, was self-affine, the new time series, $y_2(t)$, has the same statistical properties as the original time series.

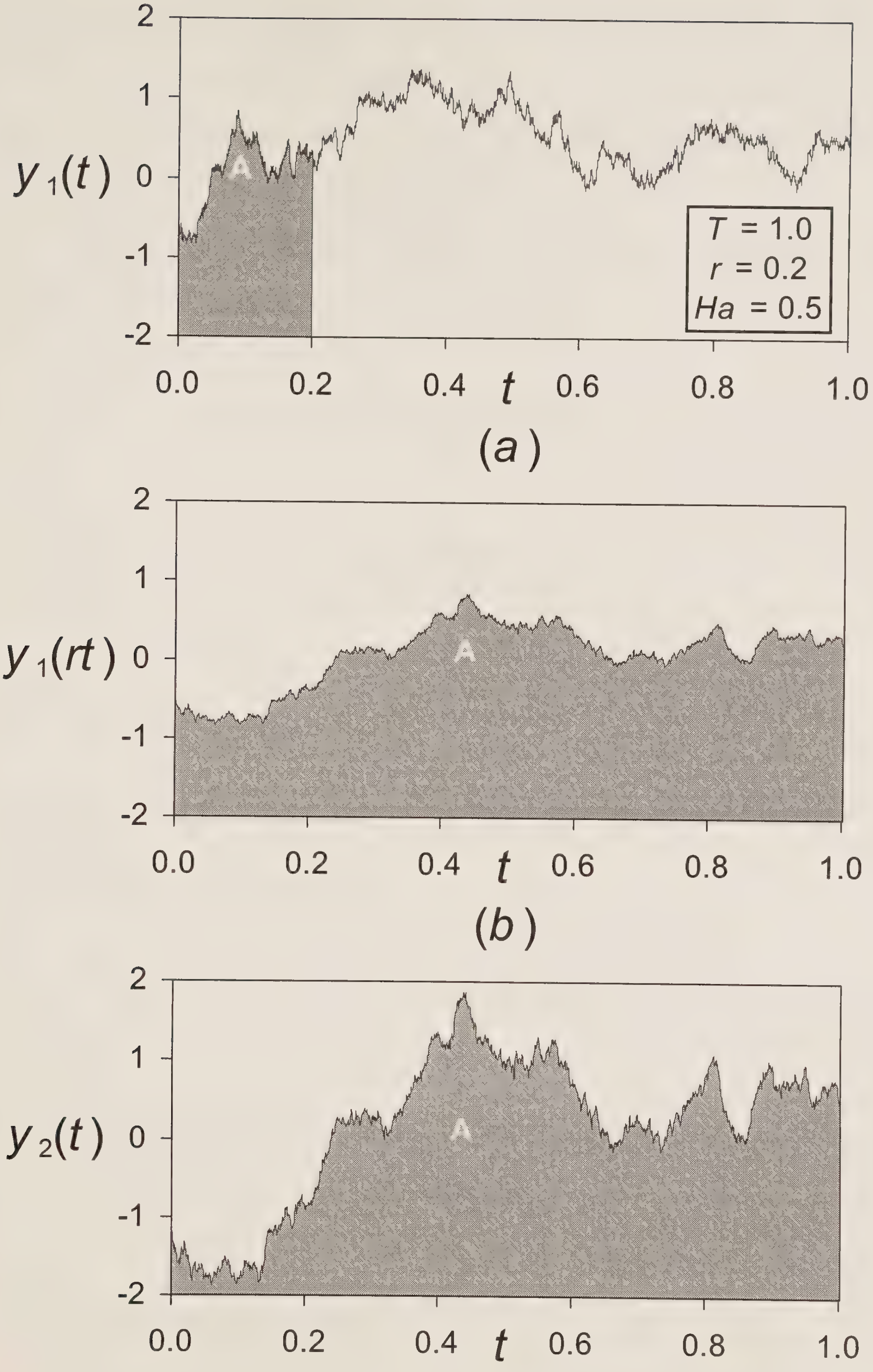

(a)

(b)

(c)

The fundamental property of a self-affine time series is that $y_1(t)$ over the time period rT (shaded part in Figure 3.7a) has the same statistical properties as $y_2(t)$ over the time period T (shaded part in Figure 3.7c), with $y_1(rt)$ and $y_2(t)$ related by (3.53).

The Fourier transform (3.32) of $y_2(t)$ over T has a continuous range of frequencies, f, and is given by

$$Y_2(f,T)=\int_0^T y_2(t)e^{2\pi ift}\,dt \tag{3.54}$$

Substituting (3.53) and making the change of variable $t' = rt$, we obtain

$$Y_2(f,T)=\int_0^{rT}\frac{y_1(t')}{r^{Ha}}e^{2\pi ift'/r}\,\frac{dt'}{r} \tag{3.55}$$

Simplifying (3.55), substituting $f' = f/r$ and $T' = T/r$ into (3.55), and using (3.32) we have

$$Y_2(f,T)=\frac{1}{r^{Ha+1}}\int_0^{T'} y_1(t')e^{2\pi if't'}\,dt' = \frac{1}{r^{Ha+1}}Y_1(f',T') \tag{3.56}$$

From the definition of the power-spectral density (3.38) and using it in the right hand side of (3.56) we obtain

$$S_2(f)=\lim_{T\to\infty}\left\{\frac{1}{T}\left|Y_2(f,T)\right|^2\right\}=\lim_{T\to\infty}\left\{\frac{1}{T}\left|\frac{1}{r^{Ha+1}}Y_1(f',T')\right|^2\right\} \tag{3.57}$$

Simplifying (3.57), substituting $T' = T/r$, and again comparing with the definition of the power-spectral density (3.38) we arrive at

$$S_2(f) = \frac{1}{r^{2Ha+1}} \lim_{T' \to \infty} \left\{ \frac{1}{T'} \left| Y_1(f', T') \right|^2 \right\} = \frac{1}{r^{2Ha+1}} S_1(f') \tag{3.58}$$

We next use the fact that the power-spectral density has a power-law dependence on frequency (3.39) and let $S_2(f) = Af^{-\beta}$ and $S_1(f') = A(f')^{-\beta}$, where A is a constant of proportionality. Then (3.58) becomes

$$Af^{-\beta} = \frac{A(f')^{-\beta}}{r^{2Ha+1}} \tag{3.59}$$

The frequency $f' = f/r$ so

$$f^{-\beta} = \frac{1}{r^{2Ha+1}} \left(\frac{f}{r} \right)^{-\beta} \tag{3.60}$$

which simplifies to

$$1 = \frac{r^{\beta}}{r^{2Ha+1}} \tag{3.61}$$

For the right hand side of (3.61) to be 1, and from the fact that $Ha = 2 - D$ (3.27), it follows that

$$\beta = 2Ha + 1 = 5 - 2D \tag{3.62}$$

For a self-affine fractal ($0 \leq Ha \leq 1$, $1 \leq D \leq 2$) we have $1 \leq \beta \leq 3$. For a Brownian motion with $Ha = 0.5$ ($D = 1.5$) we have $\beta = 2$. Although Ha, the Hausdorff measure, is only applicable for self-affine time series from $0 \leq Ha \leq 1$, the spectral-power exponent, β, is a measure of the strength of persistence which is valid for all β, not just $1 \leq \beta \leq 3$. For self-affine time series, a white noise has $\beta = 0$, an antipersistent time series has $\beta < 0$, and a persistent time series has $\beta > 0$.

3.2.4. *Weak vs. Strong Persistence*

We now look at the strength of persistence of a self-affine time series and relate it to the stationarity of the time series. Substitution of the power-law dependence of the power-spectral density coefficients, S_m, on frequency f_m (3.42) into (3.52) gives

$$V_N = \frac{1}{N\delta} \sum_{m=1}^{N/2} S_m = \frac{A}{N\delta} \sum_{m=1}^{N/2} (f_m)^{-\beta} \tag{3.63}$$

where the frequency associated with each S_m is $f_m = m/N$, A is a positive constant of proportionality, and V_N is the variance of the discrete time series, y_n, $n = 1, 2, 3, \ldots, N$. The minimum value for the frequency f_m is $f_m = 1/N$; this will approach 0 as N approaches infinity. The maximum value for f_m will always be a constant, $f_m = (N/2)/N = 0.5$. We convert the sum in (3.63) to an integral by dividing the limits of the sum into $(N - 1)$ intervals of $\Delta f = (1/N\delta)$, with the result

$$V_N = A\sum_{m=1}^{N/2}\frac{\Delta f}{f_m^{\beta}} = A\int_{1/N}^{1/2}\frac{df}{f^{\beta}} = V(N) \tag{3.64}$$

We consider the definite integral in (3.64) for two cases, $\beta < 1$ and $\beta > 1$

$$V(N) = \begin{cases} \left(\dfrac{A}{1-\beta}\right)\left[\left(\dfrac{1}{2}\right)^{1-\beta} - \left(\dfrac{1}{N}\right)^{1-\beta}\right] & \textit{if } \beta < 1 \\ \left(\dfrac{A}{1-\beta}\right)\left(2^{\beta-1} - N^{\beta-1}\right) & \textit{if } \beta > 1 \end{cases} \tag{3.65}$$

The factor $[A/(1-\beta)]$ is positive for $\beta < 1$ and negative for $\beta > 1$. As N becomes large, the variance converges for values of $\beta < 1$ and diverges for $\beta > 1$. This is illustrated in Figure 3.8, where the variance, $V(N)$, from (3.65) is given as a function of N for several values of β in the range $-1 \leq \beta \leq 3$. The variance converges to a finite value for large N when $\beta < 1$, but diverges to infinity as $N \to \infty$ when $\beta > 1$. The value $\beta = 1$ is a natural cross over between weak and strong persistence in a self-affine time series. Below this value, the time series is stationary, above this value the time series is nonstationary. This classification is

$$\begin{array}{ccc} \beta > 1 & \textit{Strong persistence} & \textit{Nonstationary} \\ 1 > \beta > 0 & \textit{Weak persistence} & \textit{Stationary} \\ \beta = 0 & \textit{Uncorrelated} & \textit{Stationary} \\ \beta < 0 & \textit{Antipersistence} & \textit{Stationary} \end{array} \tag{3.66}$$

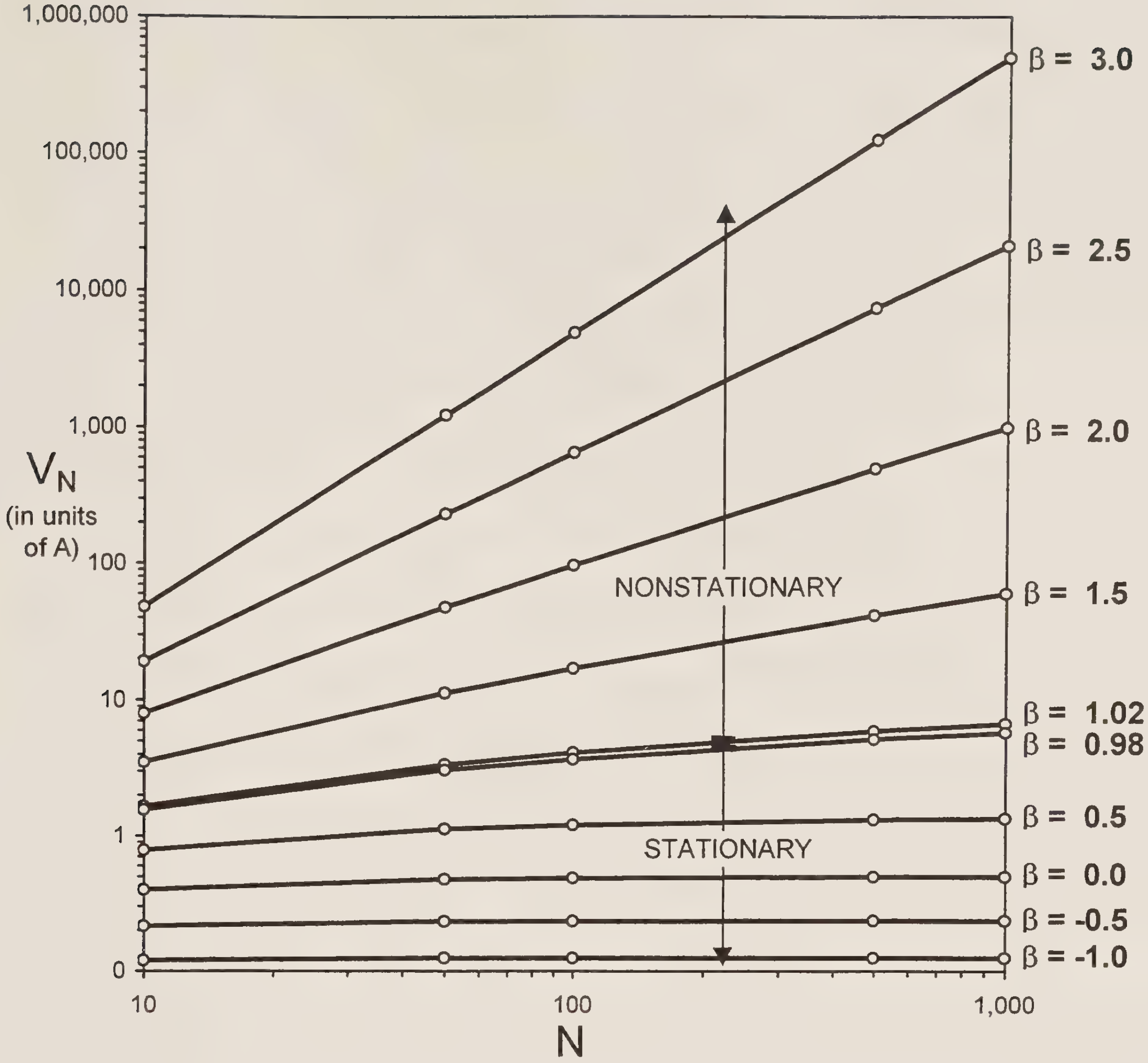

Figure 3.8. The variance, V_N, (3.65) of a time series, y_n, is plotted as a function of the length of record, N, for values of β in the range $-1 \leq \beta < 1$ and $1 < \beta \leq 3$. As N gets larger the variance quickly converges for values of $\beta < 1$ and diverges for $\beta > 1$. Self-affine time series are stationary for $\beta < 1$ and nonstationary for $\beta > 1$

3.2.5. Spectral Variance and Leakage

The discrete Fourier transform (3.34) does not always provide an accurate representation of the actual statistics of a time series. Two of the main problems in using a discrete Fourier transform are spectral variance and leakage. These have been discussed comprehensively by many authors, for example *Priestley* (1981) and *Percival and Walden* (1993).

The first problem, spectral variance, concerns the large amount of scatter of the S_m with respect to the best-fit straight line. A clear illustration of spectral variation is seen in Figure 3.6. The standard deviation of S_m is 100% of the mean value of S_m (*i.e.*, after many realizations) at f_m (*Press et al.*, 1994). Thus when plotted on logarithmic scales, the periodogram exhibits approximately the same scatter at all frequencies; *i.e.*, the "width" of the scatter on a log-log plot is constant. One solution to spectral variance is to average over many realizations of the time series of interest. For each realization calculate S_m, $m = 1, 2, 3, \ldots, N/2$, and then average at each corresponding f_m all of the values for S_m. This method will reduce the standard deviation of the scatter by the square root of the number of realizations (*Press et al.*, 1994). In this paper, we choose not to reduce the amount of scatter, as the general trend of the periodograms is very clear, even with scatter.

Leakage is also a serious problem. For a discrete Fourier transform, a discrete set of frequencies $f_m = m/(N\delta)$, $m = 1, 2, 3, \ldots, N/2$, is considered. The width of a frequency bin is $\Delta f = 1/(N\delta)$. For a stochastic time series, there is generally a continuous range of associated frequencies possible, both integer and non-integer m. Ideally, in one frequency bin, Δf, we would like the S_m that represent the whole bin to be some sort of an average of all of the S_m associated with the continuous f_m in the bin. This is not the case. The power associated with integer-m frequencies is correctly represented in the frequency domain. However, the power that is associated with each fractional-m frequency is distributed to not only its own bin, but also "leaks" into other bins. The

result is a bias that can seriously affect the resulting power-spectral distribution. “Windowing” of the time series is one method of reducing leakage.

Windowing (also called tapering, weighting, shading, fading) involves multiplying the N values of a time series, y_n, $n = 1, 2, 3, \ldots, N$, by the N values of the “window”, w_n, $n = 1, 2, 3, \ldots, N$, before carrying out the Fourier transform. If $w_n = 1$ for all n, then w_n is a rectangular window (the original series is left unmodified). The window (or taper) is normally constructed to change gradually from zero to a maximum to zero as n goes from 1 to N. For a complete discussion of the statistics involved with tapering, the reader is referred to *Percival and Walden* (1993). Many books discuss the mechanics of how and which windows to use, including *Press et al.* (1994) and *Smith and Smith* (1995). Two commonly used windows are

$$w_n = 1 - \left(\frac{n - \frac{1}{2}N}{\frac{1}{2}N} \right)^2 \qquad n = 1,2,3,\ldots,N \quad \textit{Welch Window} \qquad (3.67)$$

$$w_n = \frac{1}{2}\left[1 - \cos\left(\frac{2\pi n}{N} \right) \right] \qquad n = 1,2,3,\ldots,N \quad \textit{Hann Window} \qquad (3.68)$$

The Fourier coefficients (3.34) are then given by

$$Y_m = \delta \sum_{n=1}^{N} w_n y_n e^{2\pi i n m / N}, \qquad m = 1, 2, 3, \ldots, N \qquad (3.69)$$

Windowing significantly reduces the leakage when Fourier transforms are carried out on self-affine time series, particularly for those with high positive β's (above $\beta = 2$) and negative β's.

The variance of y_n will be different from the variance of $(w_n y_n)$; this will affect the total power (variance) in the periodogram, and the amplitude of the power-spectral density function will be shifted. One remedy is to normalize the time series y_n so it has a mean of 0, calculate the Fourier coefficients Y_m based on (3.69), and then calculate the final S_m using

$$S_m = \frac{1}{W_{ss}} \left[\frac{2|Y_m|^2}{N\delta} \right], \qquad m = 1, 2, 3, \ldots, \frac{N}{2} \tag{3.70}$$

where

$$W_{ss} = \frac{1}{N} \sum_{n=1}^{N} (w_n)^2 \tag{3.71}$$

This will normalize the variance of $(w_n y_n)$ such that it now has the variance of the original unwindowed y_n.

We close this section with a brief discussion of detrending. Many statistical packages and books recommend removing the trend and the mean of a time series before performing a Fourier analysis. The mean of a time series can be set equal to 0; this will not affect the resulting Fourier coefficients. If a window is to be used, then the mean of the original time series should be set equal to 0, or the resulting power-spectra will be improperly biased by the window. The variance of a time

series can be normalized to 1, and the slope (-β) of the resulting power-spectral density function will not be effected. However, detrending a time series is controversial, and care should be taken. One way of detrending is to take the best-fit straight line to the time series and subtract it from all of the values. Another way of detrending is to connect a line from the first point and the last point, and subtract this line from the time series; this forces $y_1 = y_N$. If a time series shows a clear linear trend, where the series appears to be closely scattered around a straight line, the trend can be safely removed without affecting any but the lowest frequencies in the power spectrum. However, if there is no clear linear trend, detrending can cause the statistics of the periodogram (in particular the slope) to change significantly.

3.3. SYNTHETIC FRACTIONAL NOISES AND MOTIONS

3.3.1. What are they?

As discussed above, a Brownian motion has a power-law spectrum so that (3.39) is applicable with β = 2. We now generate synthetic time series that have power-law spectra with arbitrary values of β. These are referred to as fractional noises and motions, which were first introduced by *Kolmogorov* (1940). Extensive studies of fractional noises and motions have been carried out by *Mandelbrot and Wallis* (1968, 1969a, b, c) and by *Mandelbrot and Van Ness* (1968). A range of applications has been discussed by *Voss* (1985a, b, c, 1986, 1988, 1989).

3.3.2. *Spectral Analysis*

Fractional Gaussian noises may be generated synthetically from Gaussian white noises using the following steps:

(1) A Gaussian white noise sequence is generated. Four examples have been given in Figure 3.4a.

(2) A discrete Fourier transform (3.34) is taken of the uncorrelated stochastic time series. Because the transform is taken of a Gaussian white noise sequence, the resulting Fourier spectrum will be flat; that is, $\beta_{PS} = 0$ in (3.42). Except for the statistical scatter, the amplitudes of the $|Y_m|$ will be equal. Figure 3.9b is an example of the power spectrum of a white noise.

(3) The resulting Fourier coefficients Y_m are filtered using the relation

$$Y_m' = \left(\frac{m}{N}\right)^{-\beta/2} Y_m \qquad (3.72)$$

The power $\beta/2$ is used because the power-spectral density is proportional to the amplitude squared of the Fourier coefficients. The amplitudes of the small-*m* coefficients correspond to short wavelengths and high frequencies. The large-*m* coefficients correspond to long wavelengths and low frequencies. Examples for $\beta = -1$ and $\beta = 1$ are given in Figure 3.9a,c.

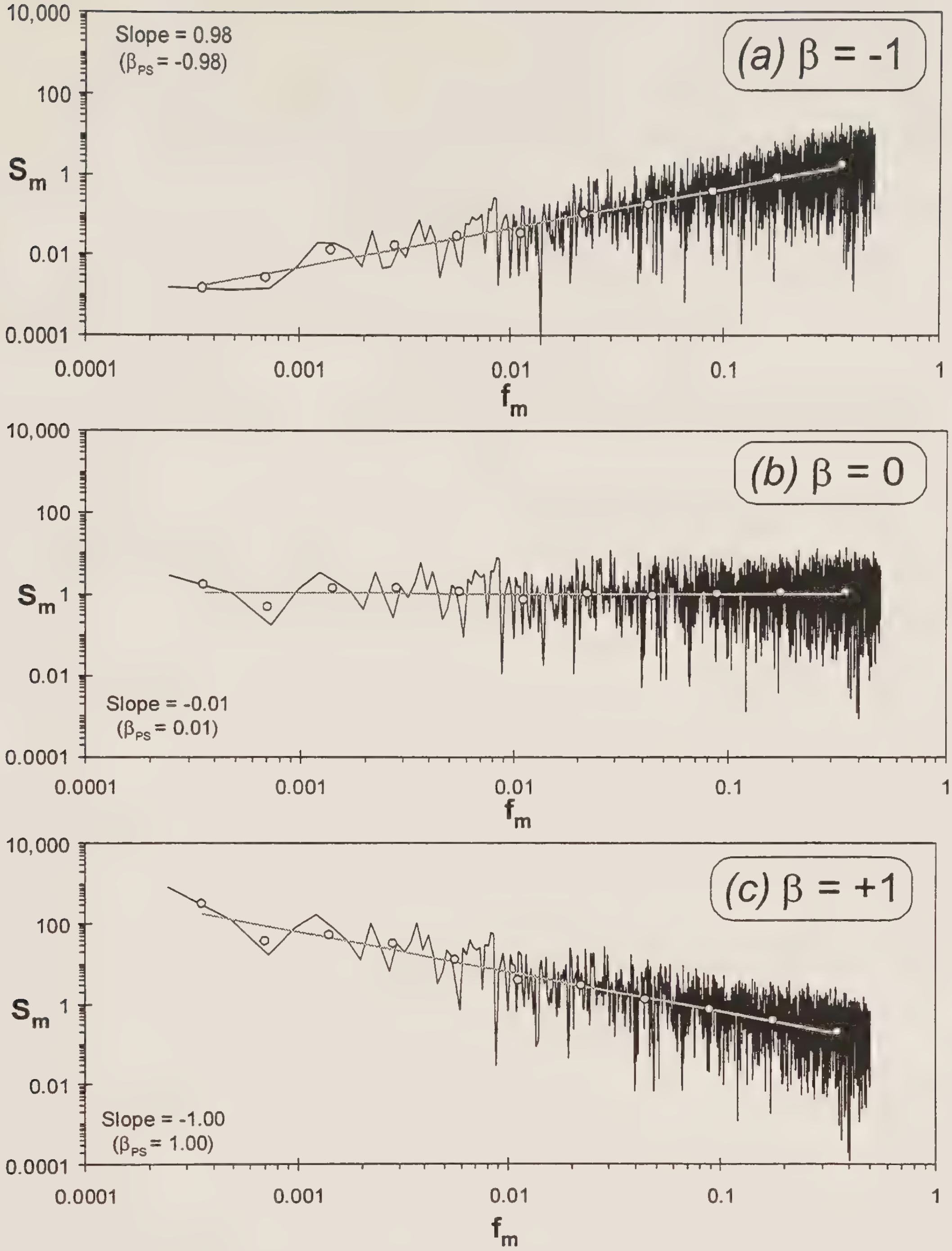

Figure 3.9. An example of power-spectral filtering. The Fourier power spectrum of a Gaussian white noise with $N = 4096$ points is given in (b). The Fourier coefficients of the spectrum have been filtered using (3.72) to give spectra with $\beta = -1$ (a) and $\beta = +1$ (c). The power spectral-density function, S_m, equal to $2/N$ multiplied by the square of the amplitudes of the complex Fourier coefficients, is given as a function of frequency $f_m = m/N$, where $m = 1, 2, 3, \ldots, N/2$. The value for β_{PS} is the negative of the slope of the best-fit straight line to the circles using a least-squares fit and log-log scales.

(4) An inverse discrete Fourier transform (3.35) is taken of the filtered Fourier coefficients. These points constitute the fractional Gaussian noise. To remove edge effects (periodicities), only the central portion is retained.

Several examples of fractional Gaussian noises are given in Figure 3.10. In each case the Gaussian white noise sequence $\beta = 0$ has been filtered using the steps given above. Fractional Gaussian noises are given for $\beta = -1.0, -0.5, 0.5$ and 1.0. Note that the range of β's corresponding to fractional Gaussian noises is $-1 \leq \beta \leq 1$.

Just as a Gaussian white noise ($\beta = 0$) can be summed to give a Brownian motion ($\beta= 2$), fractional Gaussian noises can be summed to give fractional Brownian motions (see section 3.2.2). In each case (3.50) $\beta_{\mathrm{fBm}} = 2 + \beta_{\mathrm{fGn}}$. Fractional Brownian motions are self-affine fractals and are restricted to the range $1 \leq \beta \leq 3$ as discussed above. The white and fractional Gaussian noises in Figure 3.10a ($\beta = -1.0, -0.5, 0, 0.5, 1.0$) have been summed using (3.17) to give the fractional Brownian motions illustrated in Figure 3.10b ($\beta = 1.0, 1.5, 2.0, 2.5, 3.0$). Each fractional noise and motion given in Figure 3.10 has $N = 512$ points, and has been rescaled (normalized) to have zero mean ($\bar{y} = 0$) and unit variance ($V = 1$). The fractional Gaussian noise in Figure 3.10a with $\beta = 1.0$ is statistically identical to the fractional Brownian motion in Figure 3.10b with $\beta = 1.0$.

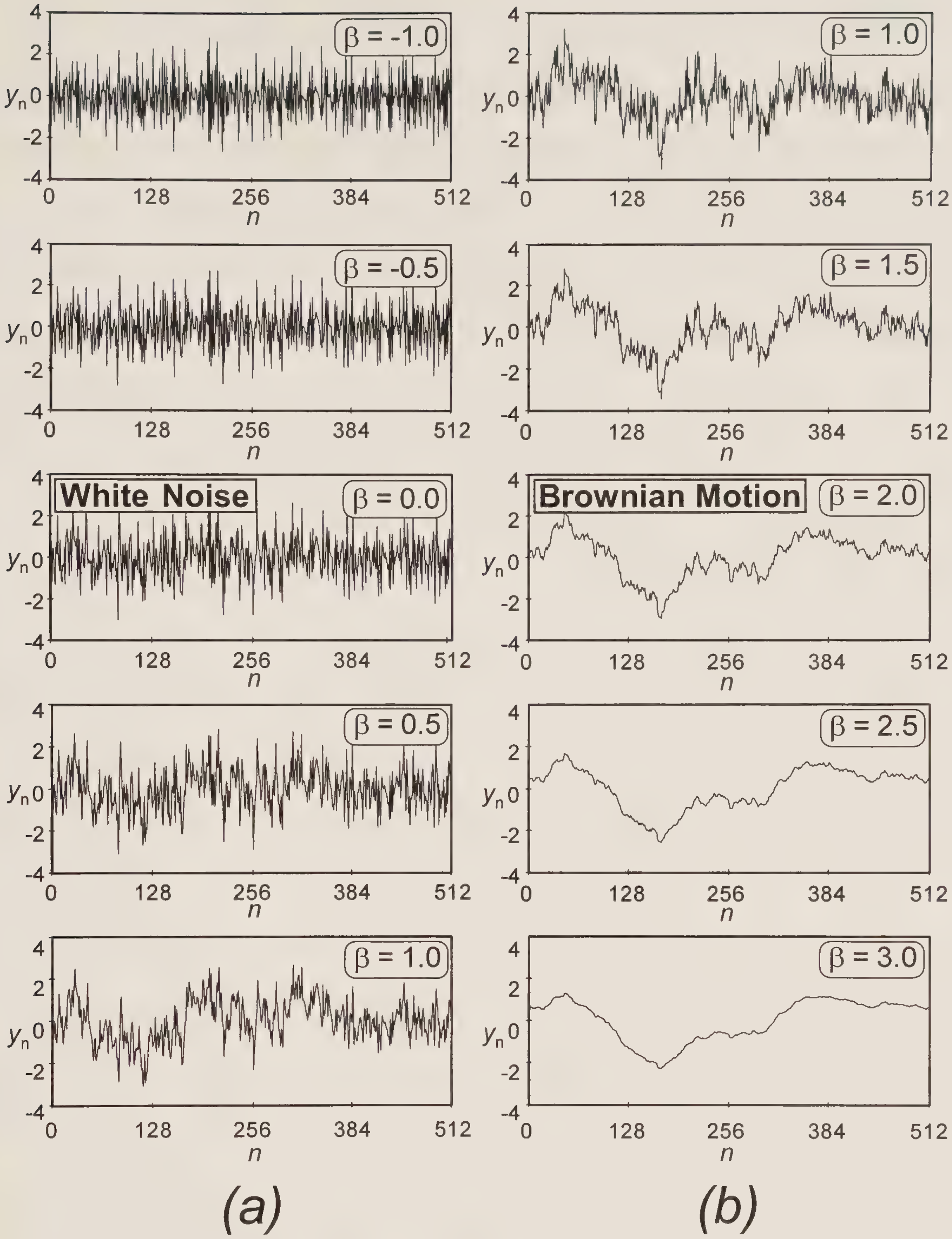

Figure 3.10. (a) The Fourier coefficients of the white Gaussian noise ($\beta = 0$) have been filtered to give fractional Gaussian noises with $\beta = -1.0, -0.5, 0.5$, and 1.0. (b) Each of these fractional Gaussian noises with β_{fGn} has been summed using (3.17) to give fractional Brownian motions with $\beta_{fBm} = 2 + \beta_{fGn}$, $\beta = 1.0, 1.5, 2.0, 2.5, 3.0$. Each fractional Gaussian noise and fractional Brownian motion has $N = 512$ points, and has been rescaled to have zero mean ($\bar{y} = 0$) and unit variance ($V = 1$).

In Figure 3.4a, four white noises were created by randomly choosing values from a Gaussian distribution with zero mean ($\bar{y} = 0$) and unit variance ($V = 1$). Although the distribution from which these white noises were derived had a zero mean ($\bar{y} = 0$), the white noises have a mean that is slightly non-zero when taken over the N values. The white noises were summed to give the Brownian motions illustrated in Figure 3.4b. Because the mean of each white noise is not identically zero, the values at the beginning and end of the Brownian motion are not the same, $y_1 \neq y_N$. However, in the fractional noises illustrated in Figure 3.10a, each noise has been forced to have a mean of exactly 0 over the N values in the time series. Thus, the Brownian motion is forced to begin and end at the same value, $y_1 = y_N$. In the analyses that follow, there is little difference between allowing beginning and ending points of a time series to be the same, or different. Statistically, the underlying persistence is the same.

In Figure 3.10, as β is increases from -1 to +3, the contribution of the high-frequency (short-period) terms is reduced. With $\beta = -1.0$ and -0.5, the high-frequency contributions dominate over the low-frequency contributions. These time series are antipersistent; adjacent values are anti-correlated relative to a white noise ($\beta = 0$). For an antipersistent time series, a value larger than the mean tends to be followed by a value smaller than the mean. With $\beta = 0$ the high-frequency contributions are equal to the low-frequency contributions. The result is an uncorrelated time series; adjacent values have no correlation with one another.

With β = 0.5, 1.0, 1.5, 2.0, 2.5, and 3.0, the low-frequency contributions become increasingly dominate over the high-frequency

contributions. The result is that adjacent values in the time series become more strongly correlated and profiles are smoothed. The persistence in the time series is increased. For a persistent time series, a value larger than the mean tends to be followed by another value larger than the mean. As the persistence becomes greater, the tendency for large to be followed by large becomes greater, and will affect other values farther and farther away in the time series.

As previously discussed, we use the division between fractional noises, $\beta < 1$, and fractional motions, $\beta > 1$, to define weak persistence as $0 < \beta < 1$ and strong persistence as $\beta > 1$. In all cases, however, a self-affine time series with a non-zero β has long-range (as well as short-range) persistence and anti-persistence. For small β, the correlations with large lag are small but are non-zero. This can be contrasted with time series that are not self-affine; these may have only short-range persistence (either strong or weak).

The fractional Gaussian noises with $-1 \leq \beta \leq 1$, generated using the Fourier filtering technique, can be summed to give fractional Brownian motions with $1 \leq \beta \leq 3$. Similarly, the fractional Brownian motions with $1 \leq \beta \leq 3$ can be differenced to give fractional Gaussian noises with $-1 \leq \beta \leq 1$. We can repeat the differencing and obtain extended fractional Gaussian noises with $-3 \leq \beta \leq -1$. Similarly, extended fractional Brownian motions with $3 \leq \beta \leq 5$ can be obtained by summing fractional Brownian motions with $1 \leq \beta \leq 3$. In this paper we use the Fourier filtering technique to generate synthetic fractional noise self-affine time series, each with $N = 4{,}096$ points over the range $-1 \leq \beta \leq 1$. These are

extended over the range $-3 \leq \beta \leq 5$ by appropriately differencing and summing (Table 3.1). We will verify the β ascribed to these self-affine time series by using power-spectral analysis.

Table 3.1. Legend for symbols used in fractional Gaussian noise and Brownian motion analyses

Symbol	***Symbol represents results of analyses on...***	***Which have a range of Beta that is...***	***And were created by...***
□	*extended fractional motions*	$3 \leq \beta \leq 5$	***summing*** *the fractional Brownian motions*
○	*fractional Brownian motions*	$1 \leq \beta \leq 3$	***summing*** *the Fourier filtered fractional Gaussian Noises*
△	*fractional Gaussian noises*	$-1 \leq \beta \leq 1$	***filtering*** *the Fourier coefficients of a white noise*
◇	*extended fractional Gaussian noises*	$-3 \leq \beta \leq -1$	***differencing*** *the Fourier filtered fractional Gaussian Noises*

The effects of windowing on power-spectral analysis are illustrated first. A windowing example using the Welch window (3.67) is given for two time series; the first, with $\beta = 2.5$, is illustrated in Figure 3.11a, and the second, with $\beta = 1.5$, is illustrated in Figure 3.12a. Each of these two time series has been rescaled to zero-mean and unit-variance. For illustration purposes, the beginning and ending values of each time series are not the same, $y_1 \neq y_N$.

Figure 3.11. Example of power-spectral density with and without a window. (a) A fractional Brownian motion (y_n) constructed to have $\beta = 2.5$ is convoluted with the Welch window (w_n) given in (3.67), resulting in (b) the new windowed time series ($w_n y_n$). The original discrete time series, y_n, $n = 1, 2, 3, \ldots, N$, was constructed with $N = 4{,}096$ points, a mean, $\bar{y} = 0$, a variance, $V = 1$, and $\beta = 2.5$. This same time series is presented later in Figure 3.15d. (c) Periodogram of y_n, where using log-log scales, the power-spectral density, S_m (3.42), is plotted as a function of f_m, $f_m = 1, 2, 3, \ldots, N/2$. The value for β_{PS} is the negative of the slope of the best-fit straight line to the circles using a least-squares fit and log-log scales. (d) Periodogram of the windowed time series, ($w_n y_n$) where S_m (3.71) is now based on a normalization by W_{ss}, the window squared and summed. The power-spectral analyses for the (a) nonwindowed time series, y_n, results in (c) $\beta_{PS} \approx 1.9$ and for the (b) windowed time series, $w_n y_n$, results in (d) $\beta_{PS} \approx 2.5$.

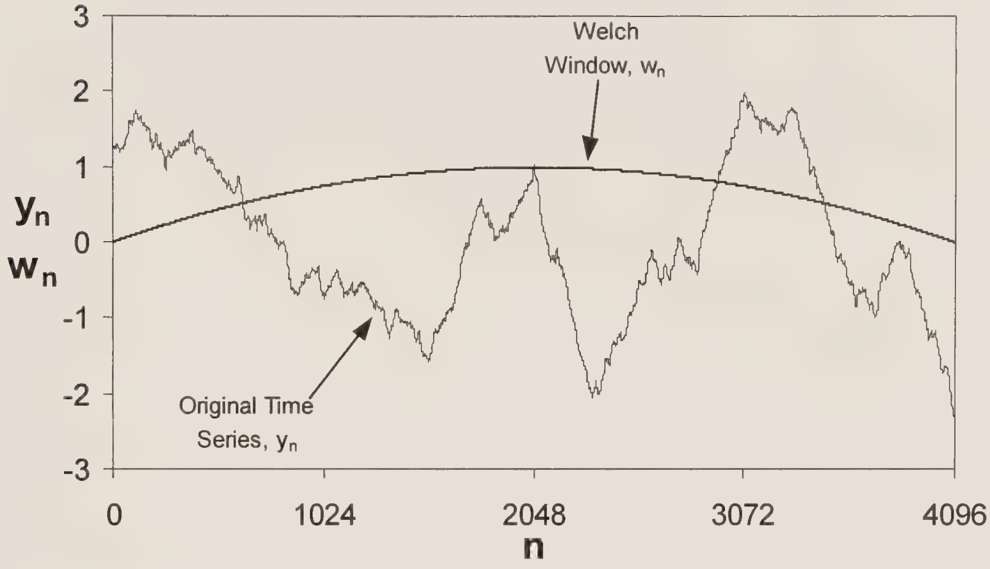
3
2
1
0
-1
-2
-3
y_n
w_n
Welch Window, w_n
Original Time Series, y_n
0
1024
2048
3072
4096
n

(*a*)

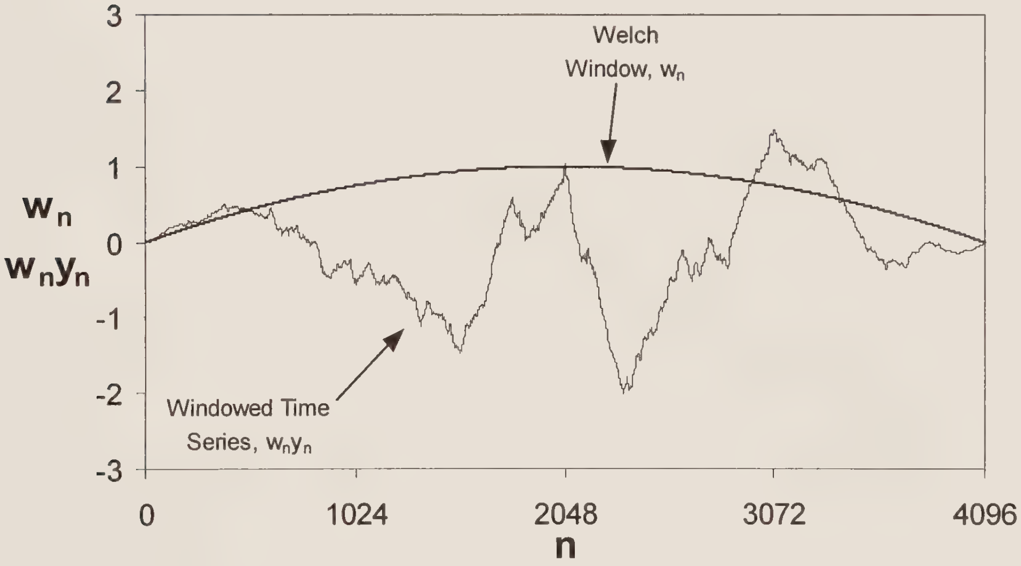
3
2
1
0
-1
-2
-3
w_n
$w_n y_n$
Welch Window, w_n
Windowed Time Series, $w_n y_n$
0
1024
2048
3072
4096
n

(*b*)

Figure 3.11 (Continued)

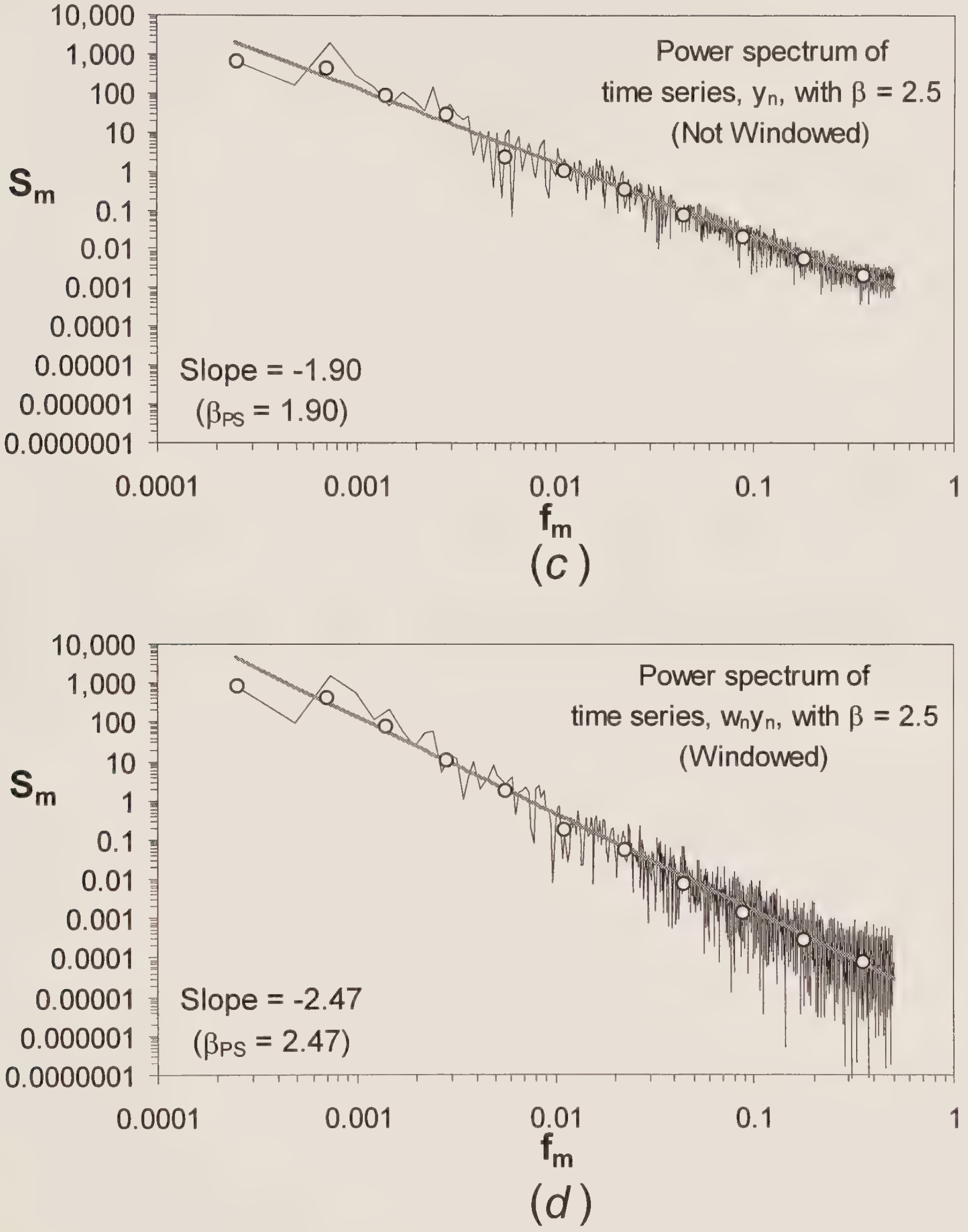

Figure 3.12. Same as Figure 3.11, but for a fractional Brownian motion constructed to have $\beta = 1.5$. This same time series is presented later in Figure 3.15b. For both the (a) nonwindowed time series, y_n, and (b) windowed time series, $w_n y_n$, power-spectral analysis (c) and (d) results in equivalent $\beta_{PS} \approx 1.5$.

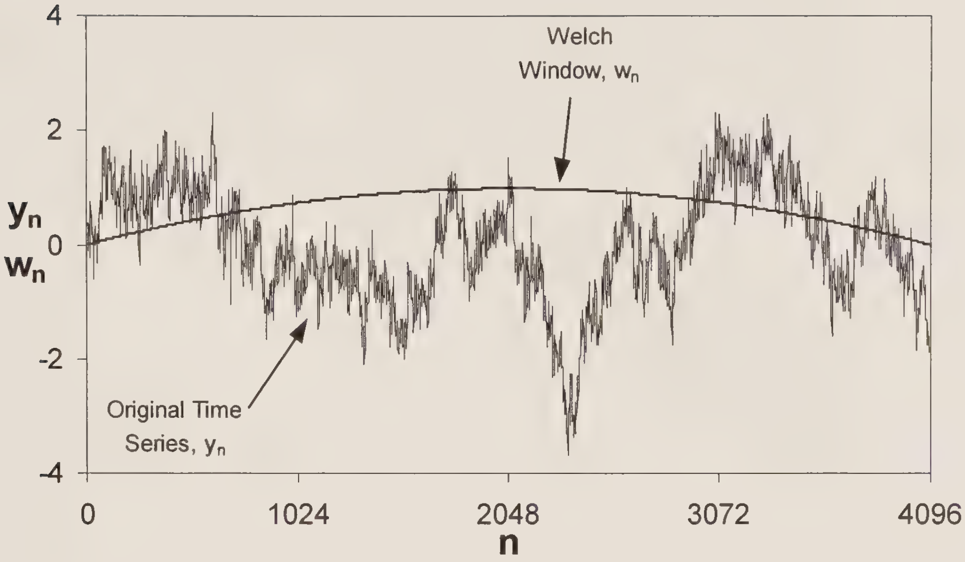
4
2
0
-2
-4
y_n
w_n
Welch Window, w_n
Original Time Series, y_n
0
1024
2048
3072
4096
n

(*a*)

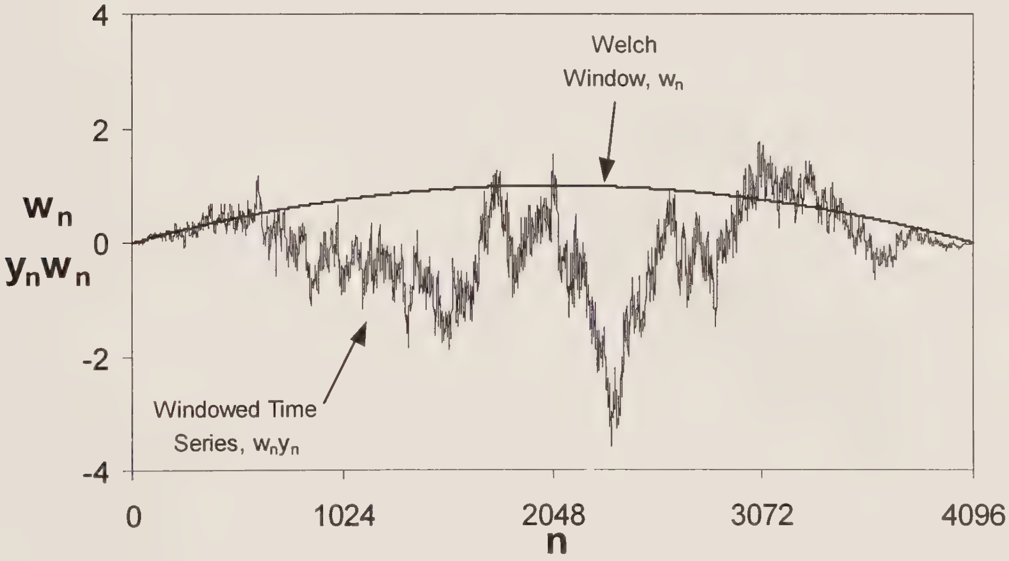
4
2
0
-2
-4
w_n
y_nw_n
Welch Window, w_n
Windowed Time Series, w_ny_n
0
1024
2048
3072
4096
n

(*b*)

Figure 3.12 (Continued)

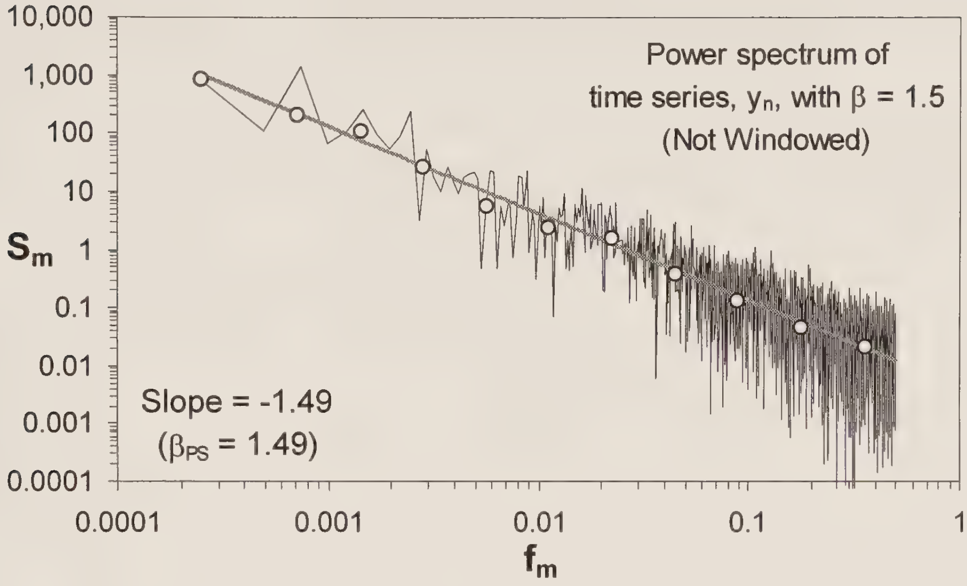

(*c*)

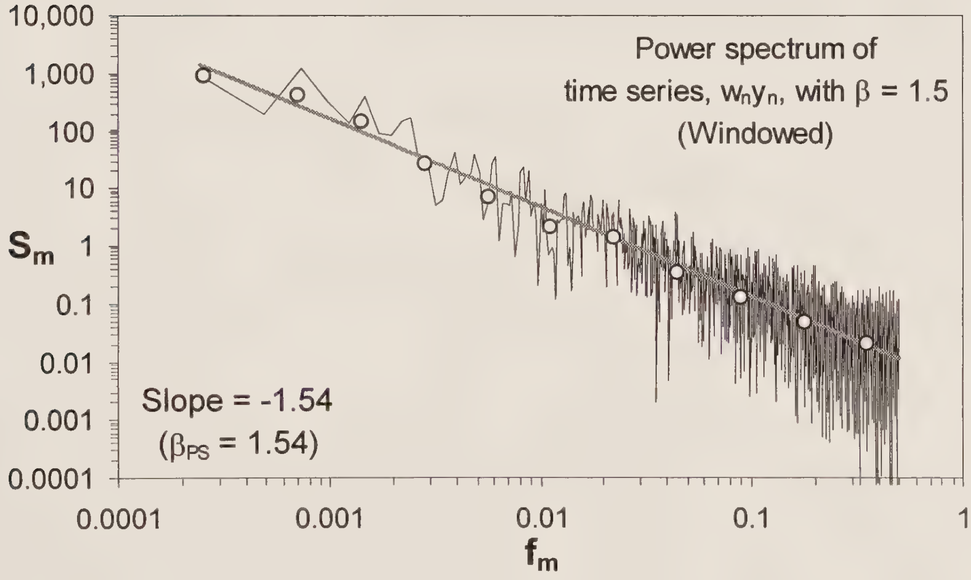

(*d*)

The time series before and after windowing, along with the Welch window, are shown in Figure 3.11a,b for the noise with $\beta = 2.5$ and Figure 3.12a,b for $\beta = 1.5$. The power-spectral density function with and without the Welch window are shown in Figure 3.11c,d ($\beta = 2.5$) and Figure 3.12c,d ($\beta = 1.5$). For the time series with $\beta = 2.5$, the best-fit lines have slopes resulting in $\beta_{PS} = 1.9$ without windowing (Figure 3.11c) and $\beta_{PS} = 2.5$ with windowing (Figure 3.11d). For the time series with $\beta = 1.5$, the best-fit lines have slopes resulting in $\beta_{PS} = 1.5$ without windowing (Figure 3.12c) and $\beta_{PS} = 1.5$ with windowing (Figure 3.12d). Windowing clearly makes a difference for the time series constructed with $\beta = 2.5$.

The spectral exponent obtained by power-spectral analysis is denoted by β_{PS}. Results of these power-spectral analyses, β_{PS} *vs.* β, are given in Figure 3.13 using the Welch window (3.67). There is excellent correlation between β_{PS} *vs.* β, for $\beta < 4$. Natural self-affine time series with $\beta > 4$ are rare, therefore the Welch window is probably fine to use.

In addition to being self-affine time series, the fractional Brownian motions given in Figure 3.10b with $1 \leq \beta \leq 3$ have from (3.62) $1 \leq D \leq 2$, thus they are self-affine fractals. A Brownian motion ($\beta = 2$) is a special case which is not only a self-affine fractal, but is also statistically self-similar because the amplitude of the signal and wavelength both scale similarly. Although the mathematical definition of self-affine fractals restricts the applicable range of β to $1 \leq \beta \leq 3$, naturally occurring self-affine time series with a power-law dependence of the power-spectral density on frequency have values of β outside this range.

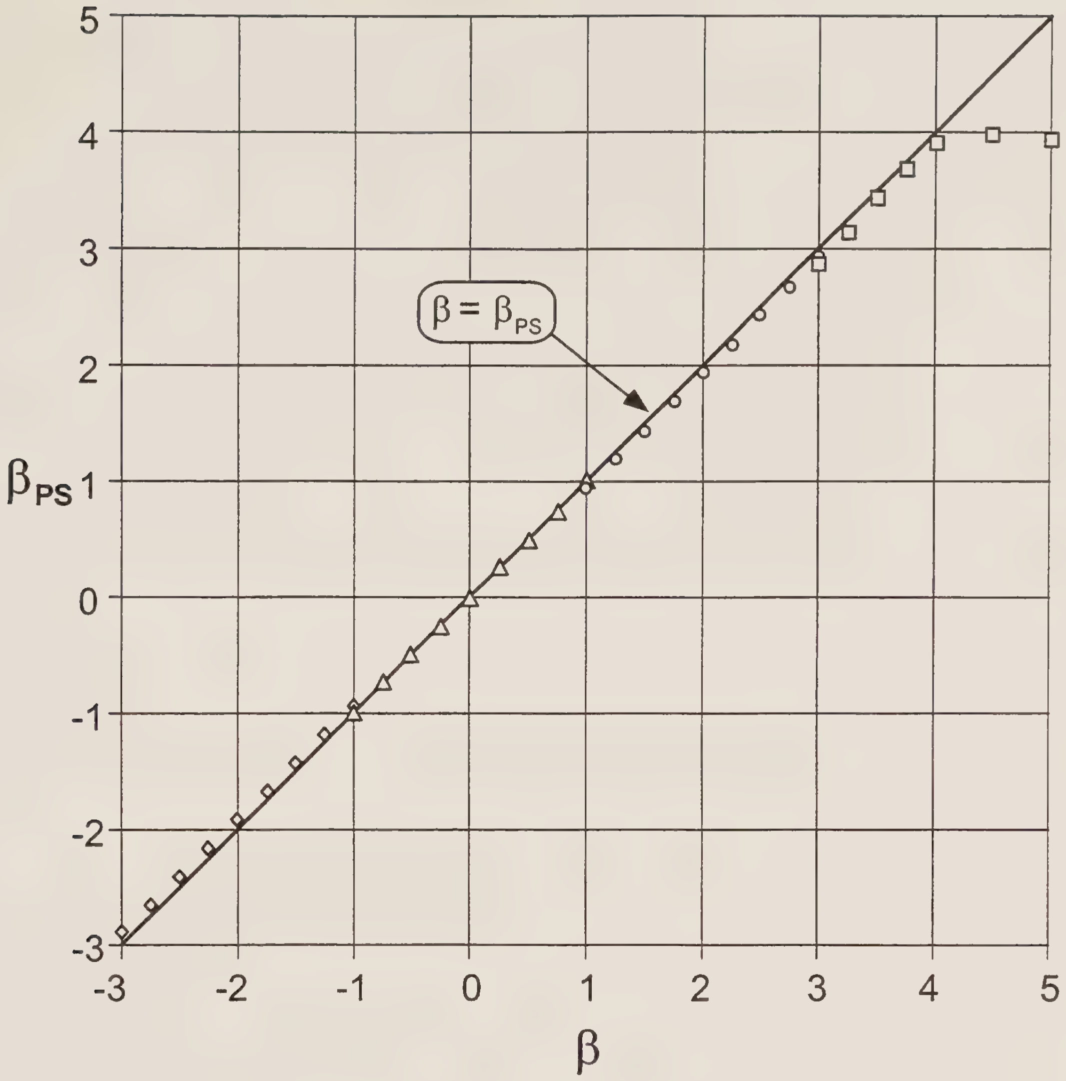

Figure 3.13. The dependence of the power-spectral exponent, β_{PS}, on β for a series of synthetic fractional Gaussian noises and fractional Brownian motions with N = 4,096 points. The fractional noises and motions are constructed to have a theoretical power-spectral exponent, β, using the Fourier filtering technique (section 3.3.2). The synthetic noises and motions are then windowed using the Welch window (3.67). Finally, we verify the power-spectral exponent of each synthetic fractional noise and motion by finding the best fit of $S \sim f^{-\beta}$ (3.39) and denoting it by β_{PS}. Results are given for $-3 \le \beta \le 5$; each symbol represents the best-fit β_{PS} at a given β. The straight-line correlation is $\beta = \beta_{PS}$. The diamonds ($-3 \le \beta \le -1$), triangles ($-1 \le \beta \le 1$), circles ($1 \le \beta \le 3$), and squares ($3 \le \beta \le 5$) are explained in Table 3.1.

In *Pelletier and Turcotte* (1998), power-spectral analyses have been carried out on a variety of naturally occurring time series in geophysics, including temperature, river discharges, tree rings, solar luminosity, sedimentary bed thicknesses, and the earth's magnetic field. They find that many of these time series exhibit self-affine behavior. In some of the time series, a single value of β is applicable over all frequencies; in other cases, subsets of the frequency domain are characterized by different values of β. Their paper also includes extensive references to time series analyses of geological and geophysical data sets.

3.3.3. Method of Successive Random Additions

An alternative method for the direct generation of fractional Brownian motions is the method of successive random additions (*Voss* 1985a, b, 1988). Consider the time interval $0 \leq t_n \leq 1$ as illustrated in Figure 3.14. The values of t_n are discrete, with $t_n = n/N$, $n = 1, 2, \ldots, N$. Random values for $y_1(t_n)$ are generated based on a Gaussian probability distribution with zero mean, $\bar{y} = 0$, and unit variance, $V(1) = 1$. Three of these values ($N = 3$, $n = 1, 2, 3$) are placed at $t_n = 0$, 1/2, 1 as shown in Figure 3.14a. Note that the mean of these three values is not forced to zero, but rather the Gaussian distribution from which the three values are randomly chosen has zero mean ($\bar{y} = 0$). Two straight lines are drawn between these three points. The midpoints of these two line segments are taken as initial values for $y_2(t_n)$ at $t_n = 1/4$ and 3/4 as illustrated in Figure 3.14b.

Figure 3.14. Illustration of the generation of a fractional Brownian motion using the method of successive random additions. (a) Three random numbers are generated using a Gaussian distribution with zero mean and unit variance, these are placed at $t = 0, 1/2, 1$. (b) Values at $t = 1/4$ and $3/4$ are obtained by linear interpolation. (c) Assuming $Ha = 1/2$, five random numbers are generated using a Gaussian distribution with zero mean and $V = (1/2)^{2\mathrm{Ha}} = 1/2$. (d) The random numbers in (c) are added to the values in (b). (e) Values at $t = 1/8, 3/8, 5/8, 7/8$ are obtained by linear interpolation. (f) Nine random numbers are generated using a Gaussian distribution with zero mean and $V = (1/4)^{2\mathrm{Ha}} = 1/4$. (g) The random numbers in (f) are added to the values in (d). (h) The construction has been continued to 4097 points; the result is a Brownian motion.

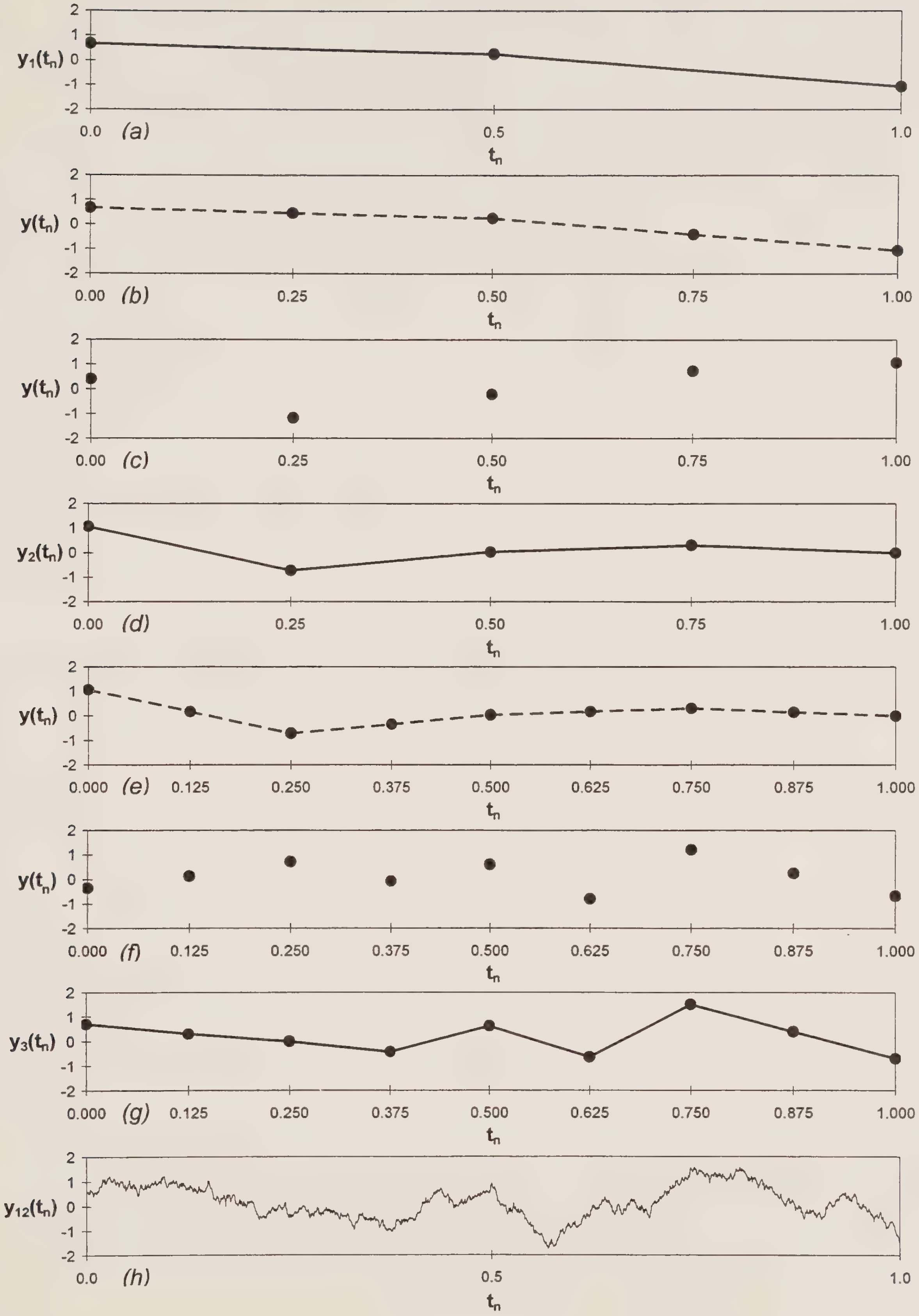
$y_1(t_n)$
(a)
0.0
0.5
1.0
t_n
$y(t_n)$
(b)
0.00
0.25
0.50
0.75
1.00
t_n
$y(t_n)$
(c)
t_n
$y_2(t_n)$
(d)
t_n
$y(t_n)$
(e)
0.000
0.125
0.250
0.375
0.500
0.625
0.750
0.875
1.000
t_n
$y(t_n)$
(f)
t_n
$y_3(t_n)$
(g)
t_n
$y_{12}(t_n)$
(h)
t_n
2
1
0
-1
-2

The five points are now given random additions. These random additions are also based on a Gaussian probability distribution with zero mean, $\bar{y} = 0$, but with a reduced variance given by $V(T) = (T)^{2Ha}$ (3.23). Since the interval has been reduced by a factor of two, the variance is given by $V(1/2) = (1/2)^{2Ha}$. For our example, $Ha = 1/2$ so that $V(1/2) = 1/2$. The five resulting random additions are given in Figure 3.14c. After addition to the five values of $y(t_n)$ in Figure 3.14b, the resulting five values for $y_2(t_n)$ are given in Figure 3.14d. Again the five points are connected by four straight-line segments and the four midpoints are taken as initial values for $y_3(t_n)$ at $t = 1/8$, 3/8, 5/8, and 7/8 as illustrated in Figure 3.14e.

All nine points are now given random additions using a Gaussian probability distribution with zero mean but a further reduced variance from (3.23) $V(1/4) = (1/4)^{2Ha}$. Again, taking $Ha = 1/2$ gives $V(1/4) = 1/4$. The nine random additions are given in Figure 3.14f. After addition to the nine values of $y(t_n)$ given in Figure 3.14e, the resulting nine values for $y_3(t_n)$ are given in Figure 3.14g. The process is repeated until the desired number of points is obtained. A 12th order construction, $y_{12}(t_n)$ with 4,097 points, is given in Figure 3.14h. With $Ha = 1/2$ and $\beta = 2$ this is a Brownian motion and strongly resembles the Brownian motions given in Figures 3.4 and 3.10.

A sequence of fractional Brownian motions generated by the method of successive random additions is given in Figure 3.15.

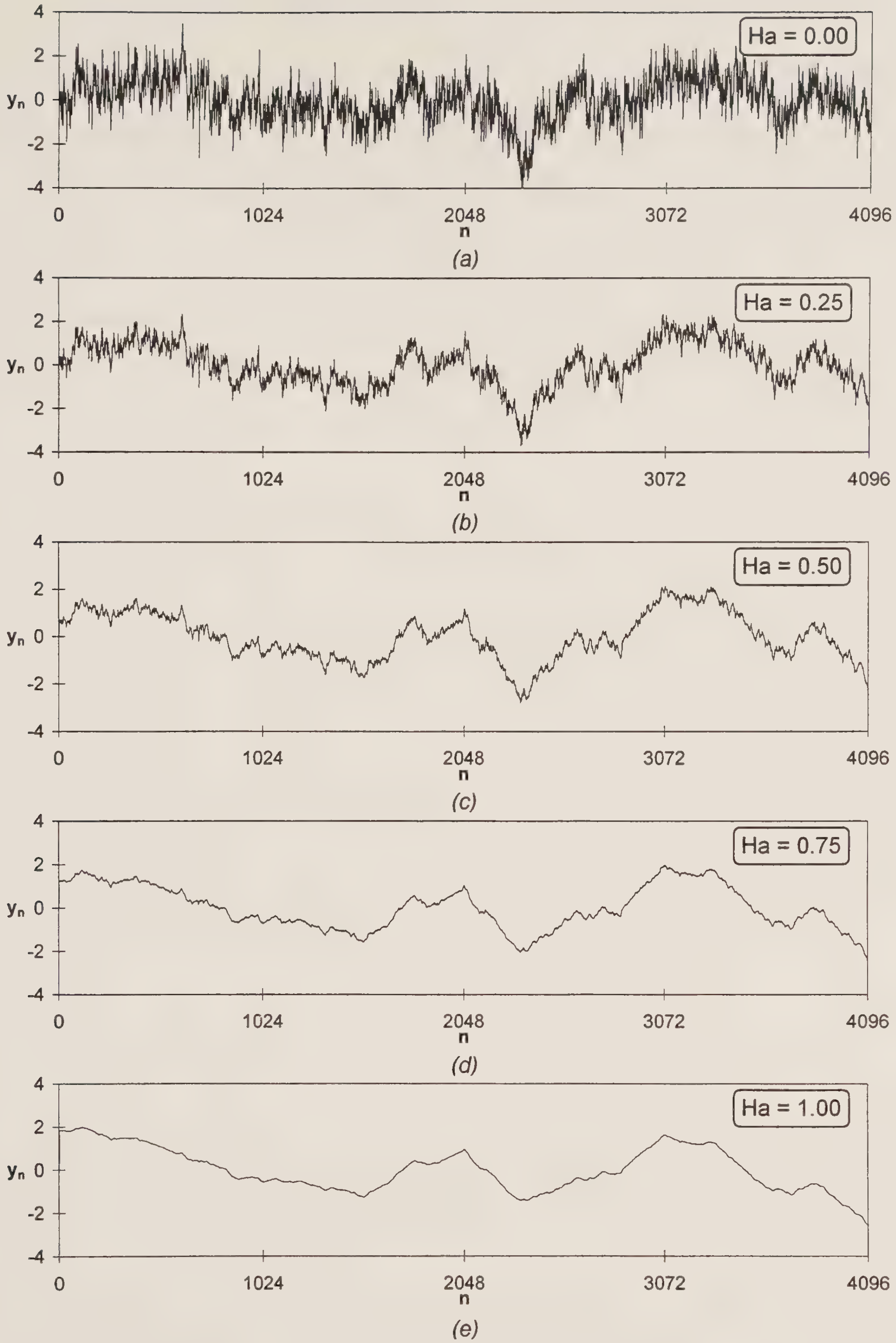

Figure 3.15. A sequence of fractional Brownian motions generated by the method of successive random additions which is illustrated in Figure 3.14. (a) $Ha = 0$ ($\beta = 1$). (b) $Ha = 0.25$ ($\beta = 1.5$). (c) $Ha = 0.50$ ($\beta = 2$, a Brownian motion). (d) $Ha = 0.75$ ($\beta = 2.5$). (e) $Ha = 1.00$ ($\beta = 3$).

In parts *a* through *e* of Figure 3.15, fractional Brownian motions are given for $Ha = 0.0$ ($\beta = 1.0$), $Ha = 0.25$ ($\beta = 1.5$), $Ha = 0.50$ ($\beta = 2.0$, same as Figure 3.14h), $Ha = 0.75$ ($\beta = 2.5$) and $Ha = 1.00$ ($\beta = 3.0$); in each case 4,097 points are given. As expected, these noises closely resemble those generated by the Fourier filtering technique (Figure 3.10). The method of successive random additions generates fractional Brownian motions with $1 \leq \beta \leq 3$. These can be differenced to give fractional Gaussian noises with $-1 \leq \beta \leq 1$ and summed to give extended fractional Brownian motions with $3 \leq \beta \leq 5$.

A detailed comparison of fractional Gaussian noises and fractional Brownian motions using the Fourier filtering technique and the method of successive random additions has been given by *Gallant et al.* (1994). These authors also considered a third method of generating synthetic fractional noises using Weierstrass-Mandelbrot functions. Other relevant studies include those carried out by *Li and McLeod* (1986) and by *Osborne and Provenzale* (1989).

3.3.4. Semivariograms

Using the definition for the semivariogram, γ_k, given in (3.8), semivariograms for several fractional Gaussian noises and fractional Brownian motions, each with 4,096 points, are given in Figure 3.16. For the uncorrelated Gaussian white noise ($\beta = 0$), the semivariogram is about $\gamma_k = 1$, the same as the variance of the time series, $V = 1$. For $\beta = 1$, 2, and 3, excellent correlations are obtained with $\gamma_k \sim k^{2\mathrm{Ha}}$ (3.29). For $\beta = 2$, $Ha = 0.47$ compared satisfactorily to the expected value $Ha = 0.50$.

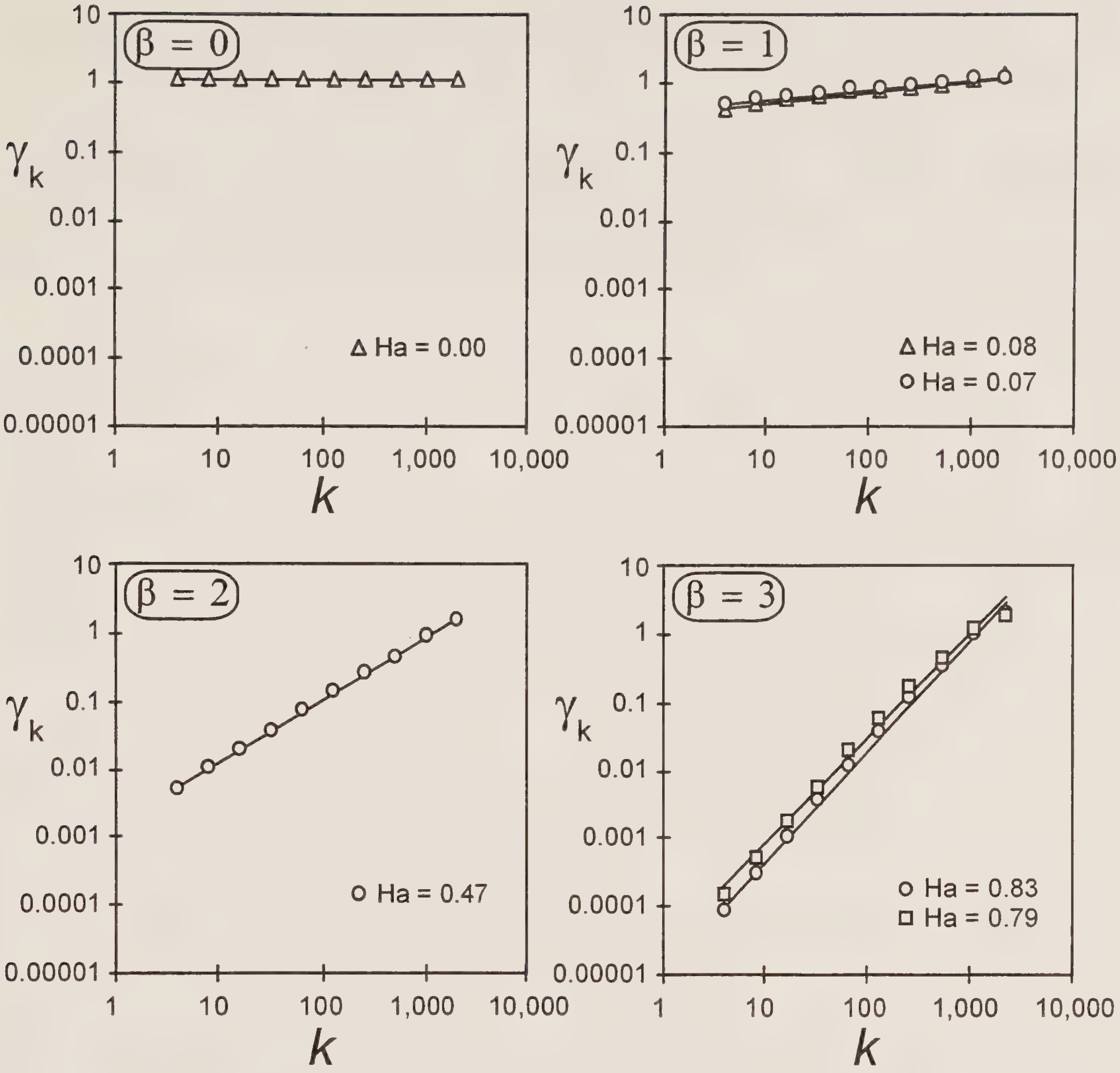

Figure 3.16. Semivariograms for several fractional Gaussian noises and fractional Brownian motions. Each semivariogram is obtained using (3.8) with lag k = 4, 8, 16, ..., 2048, and applied to fractional Gaussian noises and fractional Brownian motions with N = 4,096 points. Examples of time series with N = 512 points and the same characteristics are illustrated in Figure 3.10. The straight-line correlations are with $\gamma \sim k^{2\mathrm{Ha}}$ (3.29). The slope of the best-fit straight line for log(γ) *vs.* log(k) is 2*Ha*. Values for one-half of the slope, *Ha*, are given for each of the examples. The triangles (β = 0, 1), circles (β = 1, 2, 3) and squares (β = 3) are explained in Table 3.1.

The values of *Ha* obtained from the best fit of (3.29) to the semivariograms in the range -1 ≤ β ≤ 5 are given in Figure 3.17. The straight-line correlation is with the self-affine fractal relation β = 2*Ha* + 1 (3.62). Quite good agreement is found in the range 1 ≤ β ≤ 3, where the fractional Brownian motions are expected to be self-affine fractals.

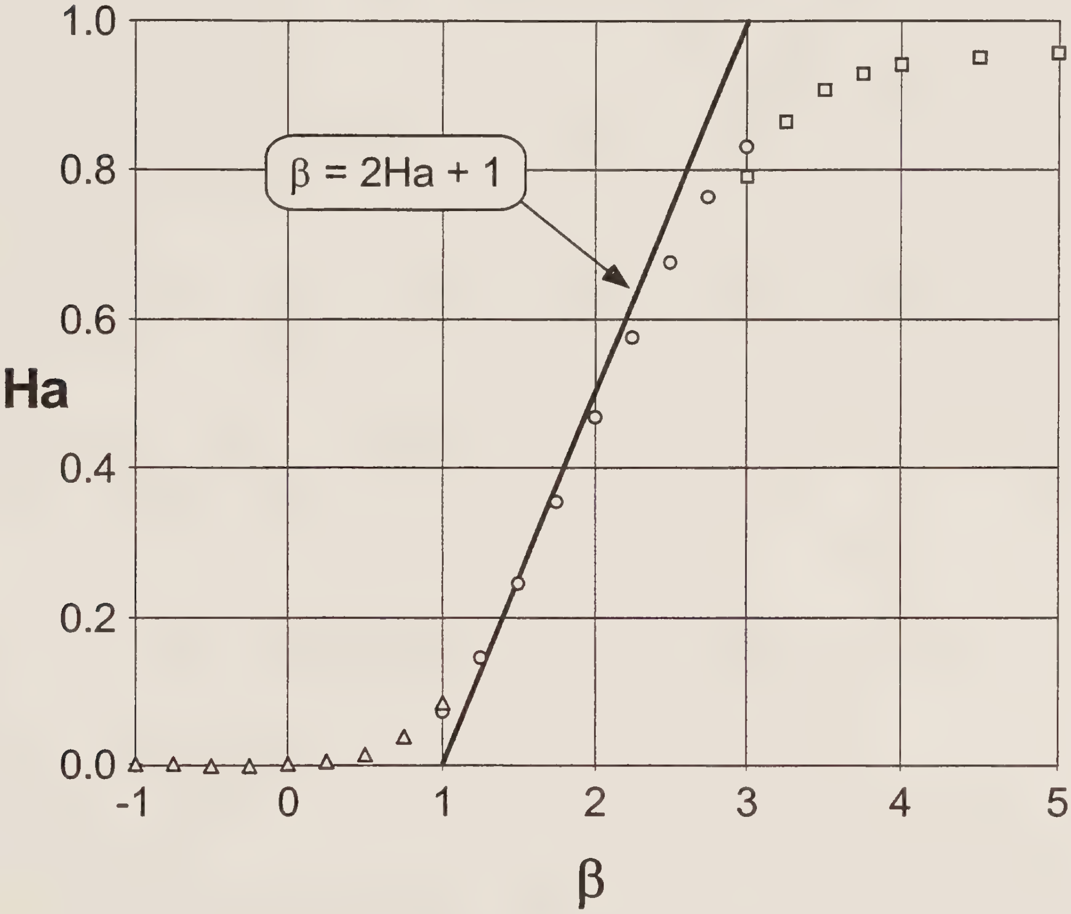

Figure 3.17. The dependence of the Hausdorff measure, *Ha*, on β, for fractional Gaussian noises and fractional Brownian motions with N = 4,096 points. *Ha* values have been obtained from the best fit of $\gamma \sim k^{2\mathrm{Ha}}$ (3.29). Results are given for -1 ≤ β ≤ 5; each symbol represents the best fit for *Ha* at that β. Examples of obtaining *Ha* from semivariograms are given in Figure 3.16. The straight-line correlation is with the self-affine fractal relation β = 2*Ha* + 1 (3.62) for 1 ≤ β ≤ 3. The triangles (-1 ≤ β ≤ 1), circles (1 ≤ β ≤ 3), and squares (3 ≤ β ≤ 5) are explained in Table 3.1.

From Figure 3.17, it is seen that $Ha \approx 0$ for fractional Gaussian noises in the range $-1 \leq \beta \leq 1$. From (3.20), $\sigma_n \sim n^{Ha}$, one can conclude that the standard deviation, σ_n, and thus the variance, V_n, are not dependent on the length of the signal, n. Therefore, these fractional noises are stationary even though adjacent values may be correlated or anticorrelated. For these fractional noises, each with variance $V = 1$, and in the range $-1 \leq \beta \leq 1$, the semivariogram has a value of $\gamma_k \approx 1$. For fractional Gaussian noises ($-1 \leq \beta \leq 1$), semivariograms are not a measure of persistence or antipersistence strength in a self-affine time series. For the fractional Brownian motions in the range $1 \leq \beta \leq 3$, Ha varies from 0 to 1. From (3.20), $\sigma_n \sim n^{Ha}$, we conclude that the standard deviation σ_n, and thus the variance V_n, both have a power-law dependence on the length of the signal n. Therefore, these factional Brownian motions are clearly nonstationary.

3.4. LOG-NORMAL NOISES AND MOTIONS

3.4.1. Log-Normal Distributions

The fractional Gaussian noises and fractional Brownian motions we have considered have been based on a Gaussian (normal) distribution of values; therefore, the resulting time series have both positive and negative values. The standard form of a Gaussian distribution is obtained by taking $\bar{y} = 0$ and $\sigma_y = 1$. All Gaussian distributions can be rescaled to the normalized standard form using linear transformations. The value of β completely specifies a normalized fractional Gaussian noise or fractional Brownian motion.

However, many naturally occurring time series have only positive values. For example, the volumetric flow in a river $Q(t)$ is always positive as illustrated in Figure 3.1b. One of the most widely used positive distributions is the log-normal distribution. A normal distribution can be converted to a log-normal distribution using the relation

$$x(t) = e^{y(t)} \tag{3.73}$$

where $x(t)$ has a log-normal distribution of values and $y(t)$ has a normal distribution of values. In order to specify a log-normal distribution, it is necessary to specify the mean of the distribution, $\bar{x}$, and its coefficient of variation, c_v, which is the ratio of the standard deviation of the log-normal distribution to its non-zero mean:

$$c_v = \frac{\sigma_x}{\bar{x}} \tag{3.74}$$

The coefficient of variation, c_v, is a measure of the relative dispersion of a time series; the standard deviation is a measure of the absolute dispersion. If $c_v \ll 1$, it may be appropriate to consider Gaussian statistics. In many cases, however, this will be a poor approximation. As an example of a time series with a log-normal distribution, Figure 3.1b is a plot of daily river discharges for $T = 75$ years from the Salt River in Arizona, with a coefficient of variation, $c_v = 2.6$.

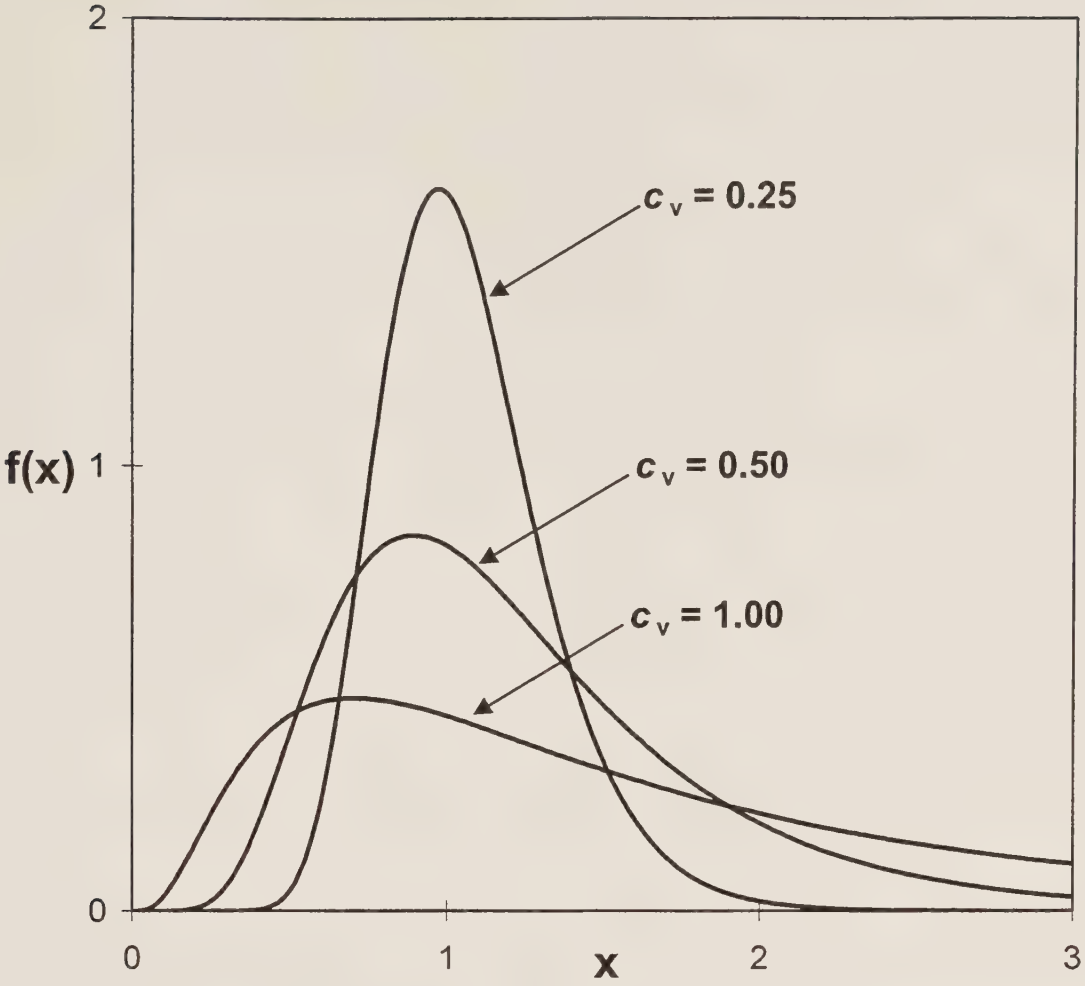

Figure 3.18. The probability distribution function $f(x)$ for the log-normal distribution with unit mean ($\bar{x} = 1$) and several values of the coefficient of variation, $c_v = 0.25$, 0.50, and 1.00.

Although, normal distributions have a universal form, *i.e.* zero mean ($\bar{y} = 0$) and unit variance ($V = 1$), this is not the case for the log-normal distribution; no standard form exists. The coefficient of variation, c_v, classifies a family of log-normal distributions. The probability distribution functions $f(x)$ for the log-normal distribution are given in Figure 3.18 for $\bar{x} = 1$ and $c_v = 0.25$, 0.50, 1.00. It is seen that the shape of the log-normal distribution changes systematically for different c_v. As the value of c_v becomes smaller, the distribution narrows and the

maximum value for $f(x)$ occurs at a value of x approaching 1. In the limit $c_v \to 0$, the distribution is a delta function centered at $x = 1$. As c_v becomes larger, the distribution spreads out and the maximum value for $f(x)$ occurs at smaller x. The distribution of log-normal values has an asymmetric tail extending toward values that are more positive. Whereas the normal distribution is symmetric, the asymmetry for the log-normal distribution increases with increasing coefficient of variation, c_v.

Log-normal distributions are a one-parameter family of distributions depending on the appropriate value of c_v. This has important implications in terms of applications. It is often appropriate to approximate the distribution of annual rainfalls at a station by a log-normal distribution. A maritime station, for instance Seattle, would have little year-to-year variation in rainfall and a small value for c_v. On the other hand, an arid station, for instance Phoenix, would have large year-to-year variations in rainfall and a large value for c_v.

3.4.2. Fractional Log-Normal Noises and Motions

A Gaussian white-noise sequence can be converted to a log-normal, white-noise sequence using (3.73) along with

$$\sigma_y = \left[\ln\left(1 + c_v^2\right)\right]^{1/2} \tag{3.75}$$

$$\bar{y} = \ln\left[\frac{\bar{x}}{\left(1 + c_v^2\right)^{1/2}}\right]^{1/2} \tag{3.76}$$

where $\bar{x}$ is the mean of the log-normal distribution., and $\bar{y}$ and σ_y are the mean and standard deviation of the normal distribution. Log-normal white-noise sequences ($\beta = 0$) with unit mean ($\bar{x} = 1$) are given in Figure 3.19 for $c_v = 0.2$, 0.5, 1.0, and 2.0. With $c_v = 0.2$ the standard deviation is small compared with the mean, the distribution is nearly symmetric, and it closely resembles a Gaussian white noise. With $c_v = 2$, the variance is large compared with the mean and the distribution is strongly asymmetrical.

Just as a Gaussian white-noise sequence can be converted to a log-normal white-noise sequence, so too can fractional Gaussian noises and fractional Brownian motions be converted to fractional log-normal noises and motions using (3.73) to (3.76). Several examples are given in Figure 3.19. In each case the mean is unity ($\bar{x} = 1$). This is a two-parameter family of noises and motions. The values of β are a measure of the persistence of the time series. The values of c_v are a measure of the asymmetry of the distribution of values. Extensive studies of fractional log-normal noises and motions have been given by *Mandelbrot and Wallis* (1969a). These authors referred to the dependence on c_v as the Noah effect and the dependence on β as the Joseph effect. The different time series in Figure 3.19 resemble typical river flow time series. Increasing c_v, the Noah effect, is indicative of a climate where there is large variability in river flow. Increasing β, the Joseph effect, is indicative of more strongly correlated values. With higher values of β, a year of flood is more likely to follow a previous year of flood, and a year of drought is more likely to follow a previous year of drought.

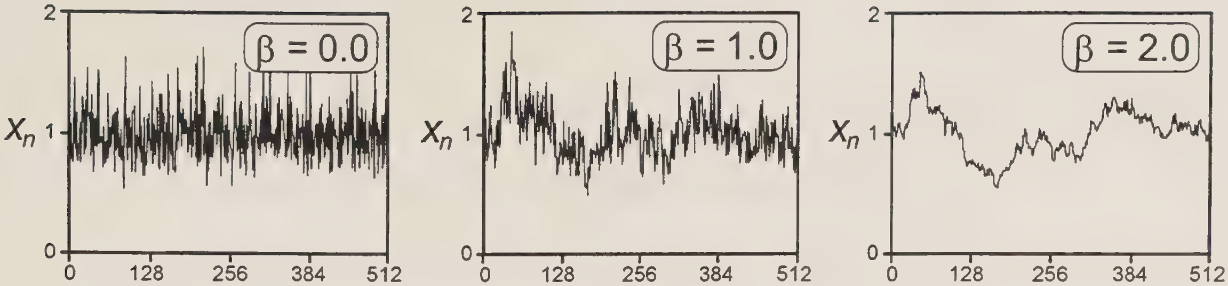

(a) **c_v = 0.2**

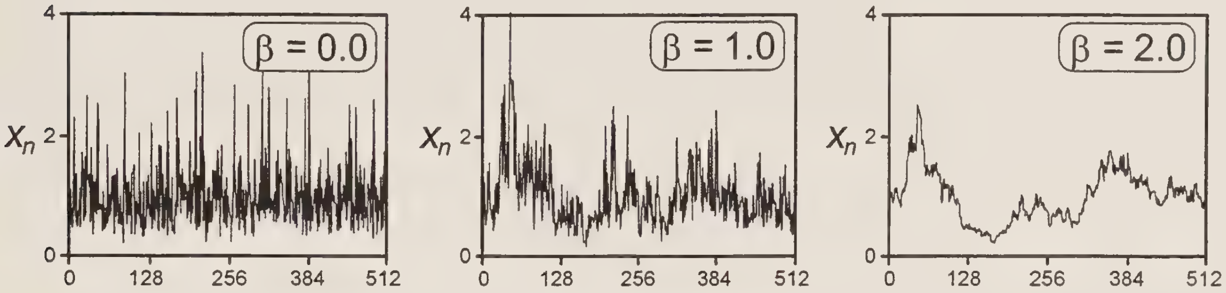

(b) **c_v = 0.5**

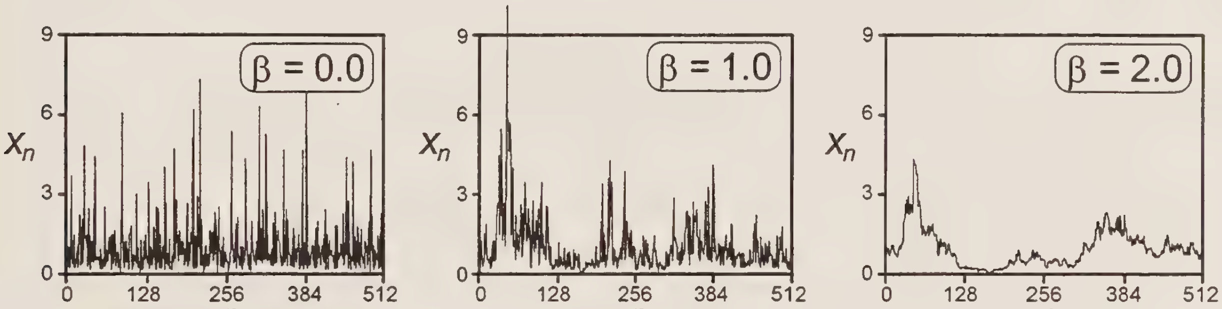

(c) **c_v = 1.0**

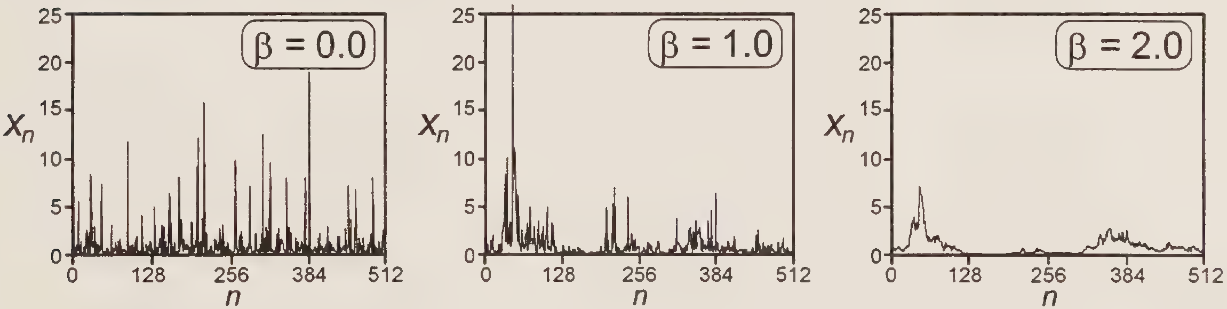

(d) **c_v = 2.0**

Figure 3.19. Examples of fractional log-normal noises and motions with $N = 512$ points. In each case a fractional Gaussian noise or a fractional Brownian motion has been converted to a fractional log-normal noise or motion, examples are given for $\beta = 0, 1, 2$. The conversions were made using (3.73) to (3.76). Examples are given for (a) $c_{\mathrm{v}} = 0.2$, (b) $c_{\mathrm{v}} = 0.5$, (c) $c_{\mathrm{v}} = 1.0$, and (d) $c_{\mathrm{v}} = 2.0$. In all cases the mean of the series is unity ($\bar{x} = 1$).

3.4.3. *Spectral Analysis*

In section 3.3.2 we used the Fourier spectral filtering method to create fractional Gaussian noises and motions with $-3 \leq \beta \leq 5$. Using (3.73) to (3.76), each of these noises and motions has been converted to their log-normal equivalent with three different coefficients of variation, $c_v = 0.2$, 0.5, and 1.0, $N = 4{,}096$ points, and β ranging over $-3 \leq \beta \leq 5$. Table 3.2 provides a legend for symbols that are used in the log-normal noise and walk analyses that follow in subsequent portions of this paper.

Table 3.2. Legend for symbols used in fractional log-normal noise and motion analyses

*Symbol**	*Symbol represents results of analyses on...*	*Which have a range of Beta that is...*	*And were created by taking the log-normal distribution of...*
□ ▨ ■	fractional log-normal motions	$3 \leq \beta \leq 5$	extended fractional motions
○ ◍ ●	fractional log-normal motions	$1 \leq \beta \leq 3$	fractional Brownian motions
△ ◬ ▲	fractional log-normal noises	$-1 \leq \beta \leq 1$	fractional Gaussian noises
◇ ◈ ◆	fractional log-normal noises	$-3 \leq \beta \leq -1$	extended fractional Gaussian noises

*Different shading of the symbol represents the coefficient of variation, c_v, of the log-normal noise or walk on which the analysis was performed: white ($c_v = 0.2$), gray ($c_v = 0.5$), black ($c_v = 1.0$).

We verify the β ascribed to the log-normal self-affine time series by using Fourier power-spectral analysis. The resulting spectral exponent is again denoted by β_{PS}. Before doing a spectral analysis, each of the log-normal time series is first rescaled to zero-mean and then multiplied by the Welch Window (3.67). Results of these power-spectral analyses, β_{PS} *vs.* β, are given in Figure 3.20. For log-normal time series there is excellent correlation between β_{PS} *vs.* β, for $0 < \beta < 4$. For $\beta < 0$ and $\beta > 4$, the correlation is poor.

A recommended technique (*e.g. Hewett*, 1986) is to convert the values of a non-Gaussian distribution to those of a Gaussian distribution. However, we recommend that this only be used if the resulting β from Fourier power spectral analysis is less than 0. In this case, we do recommend that the series be converted to their normal equivalent before performing a discrete Fourier transform.

3.4.4. Semivariograms

Using the definition for the semivariogram, γ_k, given in (3.8), semivariograms for several fractional log-normal noises and motions, each with $N = 4{,}096$ points and $c_v = 0.5$, are given in Figure 3.21. Examples of self-affine time series with $N = 512$ points and the same characteristics are illustrated in Figure 3.19. The results are generally similar to those obtained for fractional Gaussian noises and fractional Brownian motions given in Figure 3.16. For $\beta = 1$, 2, and 3, excellent correlations are obtained with $\gamma_k \sim k^{2Ha}$ (3.29), where *Ha* is the Hausdorff measure.

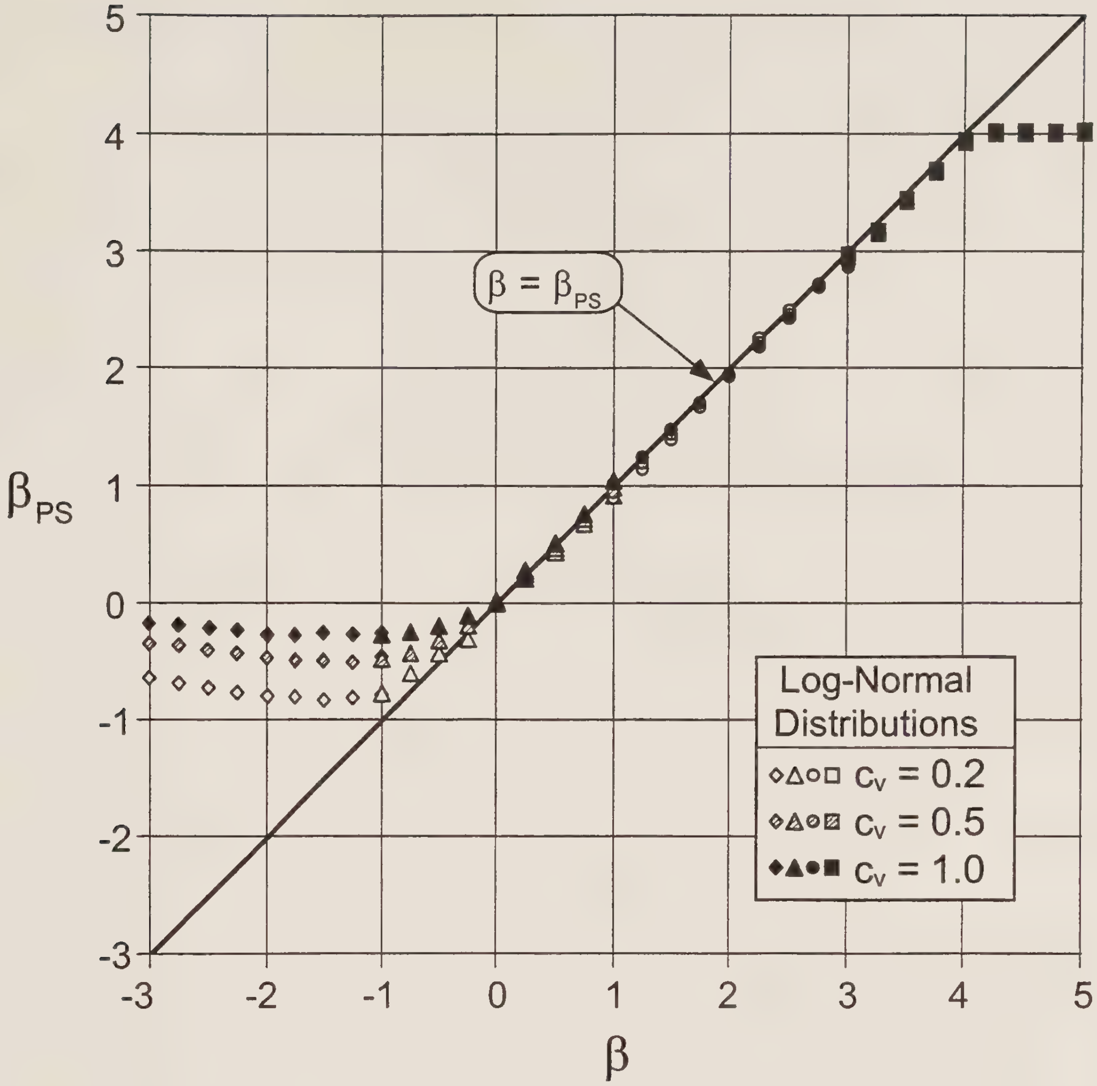

Figure 3.20. The dependence of the power-spectral exponent, β_{PS}, on β, for synthetic fractional log-normal noises and motions with N = 4,096 points. The fractional log-normal noises and motions were each constructed to have a theoretical power-spectral exponent, β, by using (3.73) to (3.76) applied to fractional Gaussian noises and motions. The synthetic noises and motions are windowed using the Welch window (3.67). We then verify the power-spectral exponent of each synthetic fractional log-normal noise and motion by finding the best fit of $S \sim f^{-\beta}$ (3.39) and denoting it by β_{PS}. Results are given for $-1 \leq \beta \leq 5$ and c_v = 0.2 (white), 0.5 (gray), and 1.0 (black); each symbol represents the best fit for β_{PS} at that β. The straight-line correlation is with $\beta = \beta_{PS}$. The diamonds ($-3 \leq \beta \leq -1$), triangles ($-1 \leq \beta \leq 1$), circles ($1 \leq \beta \leq 3$), and squares ($3 \leq \beta \leq 5$) are explained in Table 3.2.

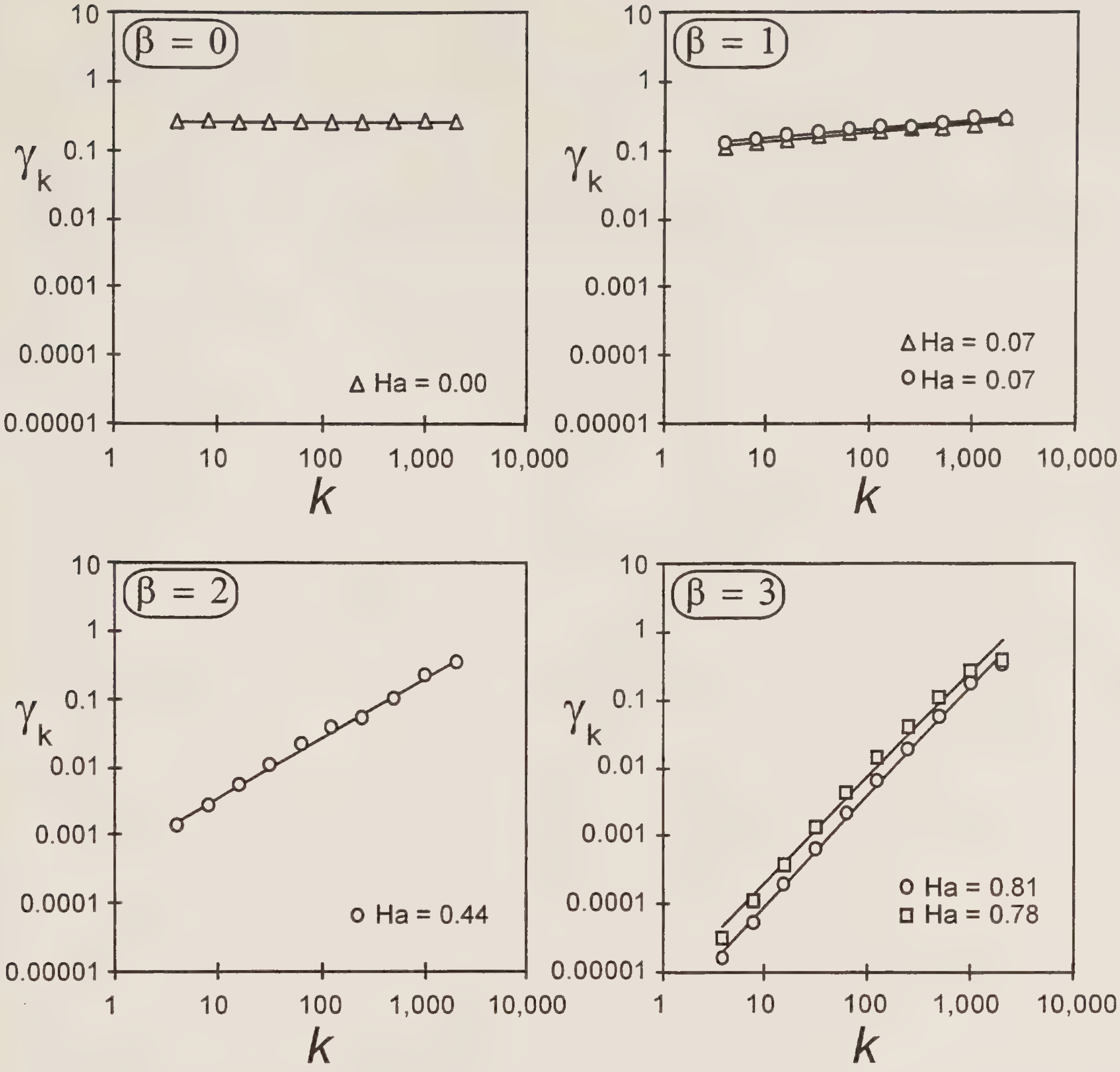

Figure 3.21. Semivariograms for several fractional log-normal noises and motions with $c_v = 0.5$. Each semivariogram is obtained using (3.8) with lag $k = 4, 8, 16, \ldots, 2048$, and applied to fractional log-normal noises and motions with $N = 4,096$ points. Examples of time series with $N = 512$ points and the same characteristics are illustrated in Figure 3.19. The straight-line correlations are with $\gamma \sim k^{2Ha}$ (3.29). The slope of the best-fit straight line for log(γ) *vs.* log(k) is $2Ha$. Values for one-half of the slope, *Ha*, are given for each of the examples. The fractional log-normal noises and motions were each obtained by using (3.73) to (3.76) applied to fractional Gaussian noises and motions, and letting $c_v = 0.5$. The triangles ($\beta = 0, 1$), circles ($\beta = 1, 2, 3$), and squares ($\beta = 3$) are explained in Table 3.2.

The values of *Ha* obtained from the best fit of $\gamma \sim k^{2\mathrm{Ha}}$ (3.29) to the semivariograms in the range $-1 \leq \beta \leq 5$ are given in Figure 3.22. Results are given for $c_v = 0.2$, 0.5 (illustrated in Figure 3.21), and 1.0. The straight-line correlation is with the self-affine fractal relation, $\beta = 2Ha + 1$ (3.62).

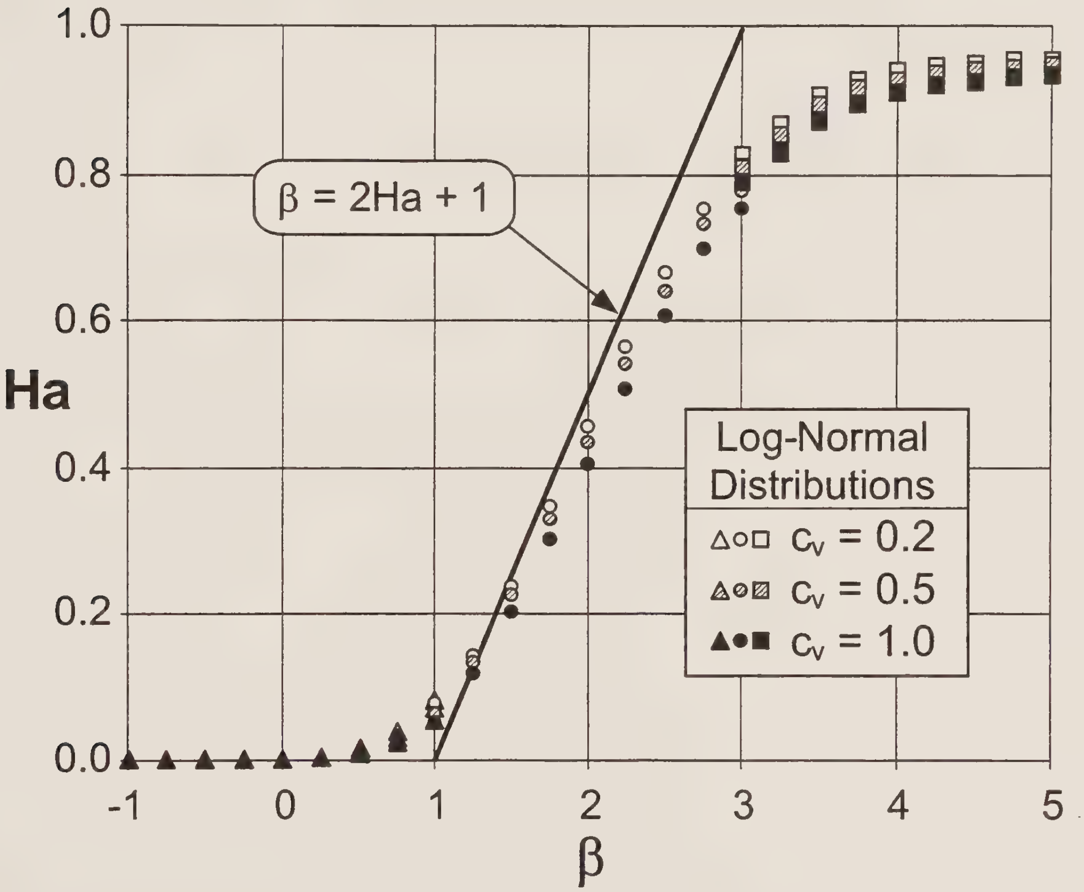

Figure 3.22. The dependence of the Hausdorff measure, *Ha,* on β, for fractional log-normal noises and motions with $N = 4{,}096$ points. The values for *Ha* have been obtained from the best fit of $\gamma \sim k^{2\mathrm{Ha}}$ (3.29). Results are given for $-1 \leq \beta \leq 5$ and $c_v = 0.2$ (white), 0.5 (gray), and 1.0 (black); each symbol represents the best fit for *Ha* at that β. Examples of obtaining *Ha* from semivariograms are given in Figure 3.21. The straight-line correlation is with the self-affine fractal relation $\beta = 2Ha + 1$ (3.62) for $1 \leq \beta \leq 3$. The triangles ($-1 \leq \beta \leq 1$), circles ($1 \leq \beta \leq 3$), and squares ($3 \leq \beta \leq 5$) are explained in Table 3.2.

The results are, again, very similar to those obtained for fractional Gaussian noises and fractional Brownian motions, given in Figure 3.17. Again, good agreement with $\beta = 2Ha + 1$ (3.62) is found in the range $1 \leq \beta \leq 3$ where the fractional motions are expected to be self-affine fractals. We can conclude that semivariograms are very good at quantifying the strength of persistence for nonstationary self-affine time series with $1 \leq \beta \leq 3$, both for Gaussian and log-normal distributions.

3.5. RESCALED-RANGE (*R*/*S*) ANALYSIS

3.5.1. The Method

An alternative approach to the quantification of correlations in time series was developed by Harold E. Hurst (*Hurst*, 1951; *Hurst et al.*, 1965). Hurst spent his life studying the hydrology of the Nile River, in particular the record of floods and droughts. He considered a river flow as a time series and determined the storage limits in an idealized reservoir. Based on these studies he introduced empirically the concept of rescaled-range (*R*/*S*) analysis. His method is illustrated in Figure 3.23. Consider a reservoir behind a dam that never overflows or empties; the flow into the reservoir is the flow in the river upstream of the dam, $Q(t)$. The flow out of the reservoir, $\overline{Q}(T)$, is assumed to be the mean of the flow into the reservoir over a period T

$$\overline{Q}(T) = \frac{1}{T}\int_0^T Q(t)dt \tag{3.77}$$

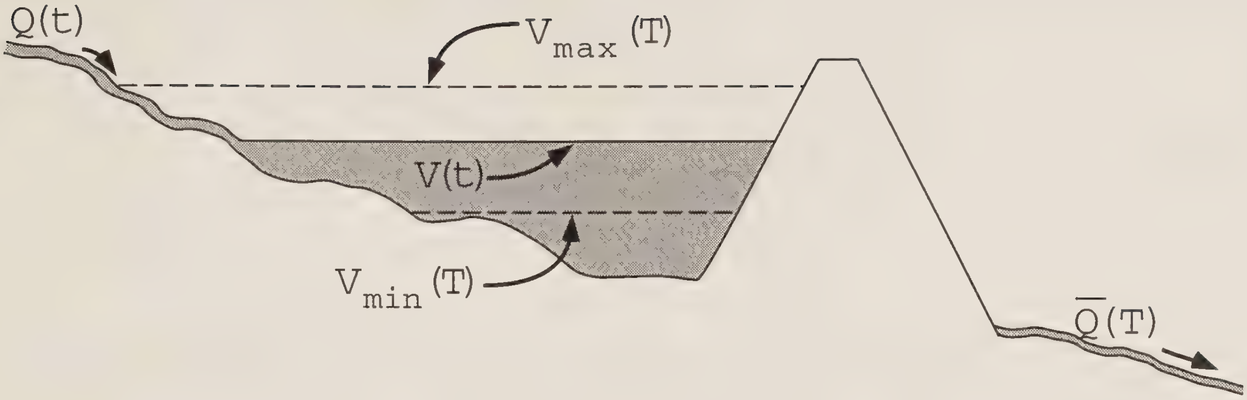

Figure 3.23. Illustration of how rescaled-range (R/S) analysis is carried out. The flow into a reservoir is $Q(t)$ and the average flow out is $\bar{Q}(T)$, where $0 \leq t \leq T$. The maximum volume of water in the reservoir during the period T is $V_{\max}(T)$ and the minimum is $V_{\min}(T)$; the difference is the range $R(T) = V_{\max}(T) - V_{\min}(T)$.

The volume of water in the reservoir as a function of time, $V(t)$, is given by

$$V(t) = V(0) + \left(\int_0^t Q(t')dt' \right) - t\bar{Q}(T) \tag{3.78}$$

where $V(0)$ is the volume of water at $t = 0$. Taking $t = T$ and substituting (3.77) into (3.78), we have $V(T) = V(0)$, in other words the volume in the reservoir is the same at $t = 0$ and $t = T$. The range $R(T)$ is defined to be the difference between the maximum volume of water $V_{\max}$ and the minimum volume of water $V_{\min}$ during the period T

$$R(T) = V_{\max}(T) - V_{\min}(T) \tag{3.79}$$

The rescaled range is defined to be $R(T)/S(T)$, where $S(T)$ is the standard deviation of the flow $Q(t)$ during the period T

$$S(T) = \left[\frac{1}{T}\int_0^T \{Q(t') - \overline{Q}(T)\}^2 \, dt'\right]^{1/2} \tag{3.80}$$

This is identical to the definition for the standard deviation, $\sigma(T)$. We use S here to maintain the standard R/S nomenclature. The period T can be broken up into subintervals τ, for instance $\tau = T/2, T/4, T/8$, and so forth. For a given value of τ, $R(\tau)$ and $S(\tau)$ are calculated for each of the T/τ subdivisions, by substituting τ for T in (3.79) and (3.80). The T/τ individual values for $R(\tau)/S(\tau)$ are then averaged.

Hurst (1951) and *Hurst et al.* (1965) found empirically that many data sets in nature satisfy the power-law relation

$$\left[\frac{R(\tau)}{S(\tau)}\right]_{av} = \left(\frac{\tau}{2}\right)^{Hu} \tag{3.81}$$

where Hu is known as the Hurst exponent. For $\tau = 2$, $R(\tau)/S(\tau) = 1$ by definition. Examples included river discharges, lake levels, tree ring thicknesses, varve thicknesses, sunspot numbers, and atmospheric temperature and pressure. They generally found that $0.70 < Hu < 0.80$. Hurst's data sets are included in the McLeod-Hipel Time-Series Datasets Collection (*McLeod and Hipel*, 1995) which contains over 300 time series in electronic format and is available over the internet.

The *R*/*S* analysis is easily extended to a discrete time series, y_n, n = 1, 2, 3, …, N. The running sum of the time series relative to its mean is

$$y_n = \sum_{i=1}^{n}(y_i - \bar{y}_N) = \left(\sum_{i=1}^{n} y_i\right) - n\bar{y}_N \tag{3.82}$$

The range is defined by

$$R_N = (y_n)_{max} - (y_n)_{min} \tag{3.83}$$

with

$$S_N = \sigma_N \tag{3.84}$$

where $\bar{y}_N$ and σ_N are the mean and standard deviation of all N values in the time series, y_n. From (3.82) to (3.84) we have a value of (R_N/S_N) for the time series, y_n, $n = 1, 2, 3,\ldots, N$. Since we are interested in how (R/S) varies with successive subintervals τ of N, we substitute τ for N in (3.82) to (3.84). The Hurst exponent, *Hu*, is obtained from

$$\left(\frac{R_\tau}{S_\tau}\right)_{av} = \left(\frac{\tau}{2}\right)^{Hu} \tag{3.85}$$

For example, if 64 values of y_n are available for a time series, the R_N and S_N for $N = 64$ are obtained. Then the data are broken into two parts, each with $\tau = 32$, (1, 2, ..., 32 and 33, 34, ... 64). The values for R_{32} and S_{32} are

obtained for the two parts. The two values of R_{32}/S_{32} are then averaged to give $(R_{32}/S_{32})_{\text{av}}$. The data set is then broken into four parts, each with $\tau = 16$ (1, 2, ..., 16; 17, 18, ..., 32; 33, 34, ..., 48; and 49, 50, ..., 64). The values for R_{16}/S_{16} are obtained for the four parts and are averaged to give $(R_{16}/S_{16})_{\text{av}}$. This process is continued for $\tau = 8$ and $\tau = 4$ to give $(R_8/S_8)_{\text{av}}$ and $(R_4/S_4)_{\text{av}}$. For $\tau = 2$, the value for $R_2 = S_2$ so that $R_2/S_2 = 1$. The values of $\log(R_\tau/S_\tau)_{\text{av}}$ are plotted against $\log(\tau/2)$ and the best-fit straight line gives Hu from (3.85). In practice there is generally some curvature of $(R_\tau/S_\tau)_{\text{av}}$ for small values of $\tau/2$ and they are therefore omitted (*Tapiero and Vallois*, 1996).

The running sum of a Gaussian white noise ($\beta = 0$) is a Brownian motion ($\beta = 2$) and $Ha = 0.5$. This would imply that

$$\beta = 2Hu - 1 \tag{3.86}$$

From (3.62) we have $\beta = 2Ha + 1$ giving

$$Hu(\beta - 2) = Ha(\beta) \tag{3.87}$$

Since a white noise ($\beta = 0$) is a random process that has adjacent values which are uncorrelated, it is appropriate to conclude that $Hu = 0.5$ implies a time series that is uncorrelated. It follows that $0.5 < Hu \leq 1.0$ implies persistence and that $0 \leq Hu < 0.5$ implies antipersistence.

3.5.2. *Applications to Fractional Gaussian Noises and Motions*

The Hurst rescaled-range analysis was first applied to fractional Gaussian noises and fractional Brownian motions by *Mandelbrot and Wallis* (1969c). The dependence of $\log(R/S)_{av}$ on $\log(\tau/2)$ for several fractional noises and motions with 4,096 points, similar to those illustrated in Figure 3.10, are given in Figure 3.24. For $\beta = 0$, 1, and 2, excellent correlations with the Hurst relation, $(R/S)_{av} \sim (\tau/2)^{Hu}$ (3.85), are obtained. For $\beta = 0$, we find $Hu = 0.56$ compared with the expected value of 0.5 for the uncorrelated white Gaussian noise.

The values of Hu obtained for the best fit to the Hurst relation (3.85) in the range $-3 \leq \beta \leq 3$ are given in Figure 3.25. The straight-line correlation is with $\beta = 2Hu - 1$ (3.86). Reasonably good agreement is found in the range $-1 \leq \beta \leq 1$; however, for $\beta < 0$, Hu definitely begins to deviate from the straight-line correlation (3.86). The Hurst exponent provides a quantitative measure of the strength of persistence and antipersistence for fractional Gaussian noises ($-1 \leq \beta \leq 1$), but the only place it is exactly correlated with $\beta = 2Hu - 1$ (3.86) is at $Hu = 0.7$. Extensive R/S analyses of fractional Gaussian noises and fractional Brownian motions have been carried out by *Bassingthwaighte and Raymond* (1994). They found, when using synthetic self-affine noises and motions constructed to have certain values of β, that Hu converges very slowly to the expected value of $\beta = 2Hu - 1$ (3.86) for large sample sizes, N. For values of $N \ll 4{,}096$, we have found that Hu gets steadily worse, with $Hu = 0.5$ when $\beta < 0$.

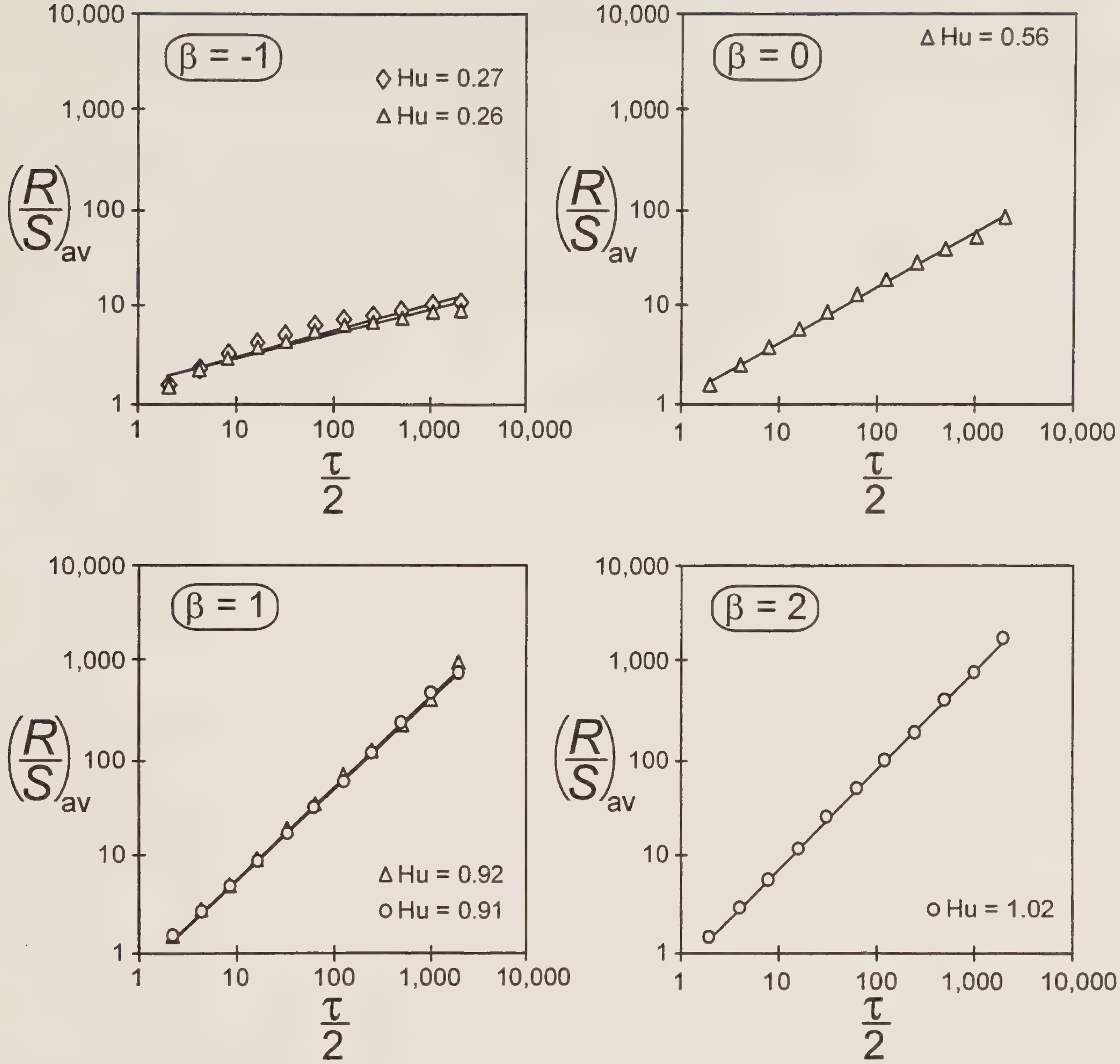

Figure 3.24. Hurst rescaled-range (*R/S*) analyses for several fractional Gaussian noises and fractional Brownian motions with $N = 4{,}096$ points. Average values of *R/S* are given as a function of the interval $\tau/2$ for $\tau = 4$, 8, 16, ..., 4,096, where *R* and *S* are calculated using (3.82) to (3.84). Examples of time series with $N = 512$ points and the same characteristics as the noises and motions with 4096 points are illustrated in Figure 3.10. The straight-line correlations are with $(R/S)_{av} \sim (\tau/2)^{Hu}$ (3.85). The slope of the best-fit straight line for $\log(R/S)_{av}$ *vs.* $\log(\tau/2)$ is *Hu*. Values for *Hu* are given for each of the examples. The diamonds ($\beta = -1$), triangles ($\beta = -1, 0, 1$), and circles ($\beta = 1, 2$) are explained in Table 3.1.

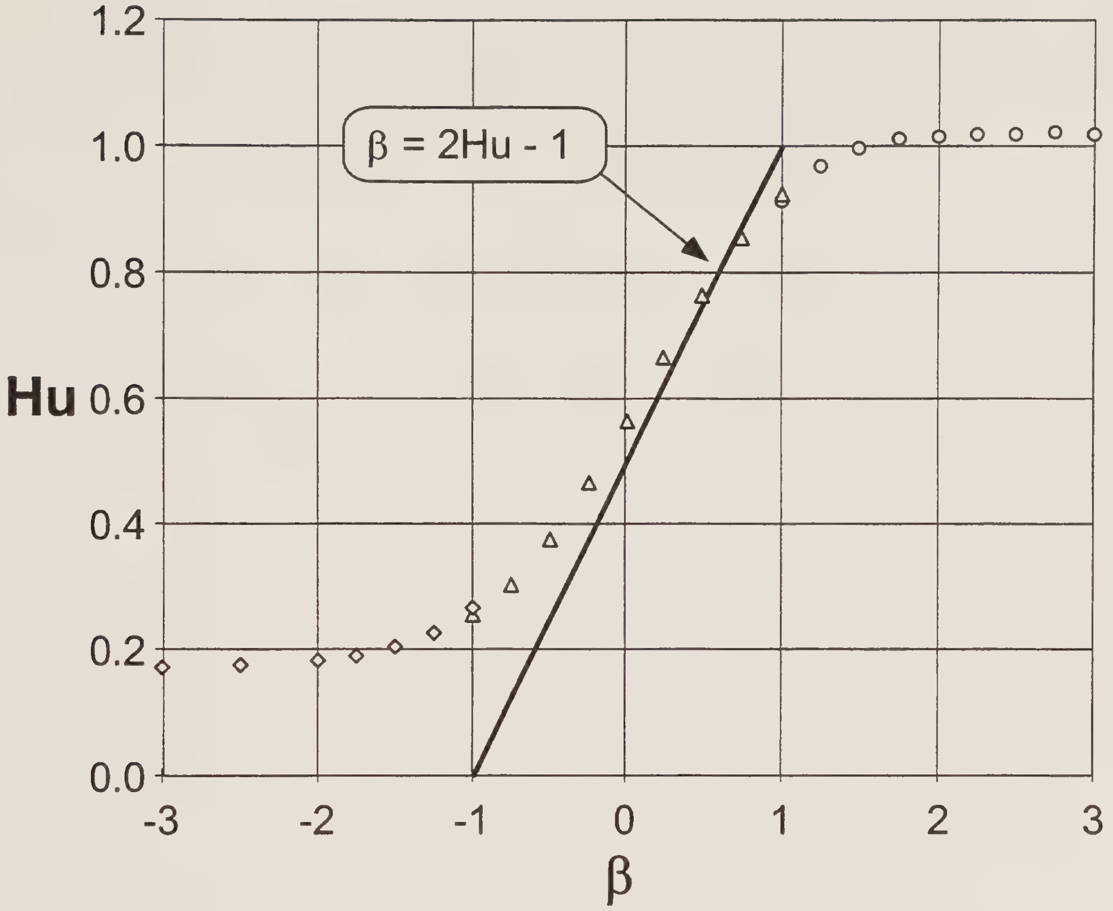

Figure 3.25. The dependence of the Hurst exponent, *Hu,* on β, for fractional Gaussian noises and fractional Brownian motions with N = 4,096 points. The values for *Hu* have been obtained from the best fit of $(R/S)_{\text{av}} \sim (\tau/2)^{Hu}$ (3.85). Results are given for $-3 \leq \beta \leq 3$; each symbol represents the best fit for *Hu* at that β. Examples of obtaining *Hu* from rescaled-range (*R/S*) analyses are given in Figure 3.24. The straight-line correlation is with the relation $\beta = 2Hu - 1$ (3.86) for $-1 \leq \beta \leq -3$. The diamonds ($-3 \leq \beta \leq -1$), triangles ($-1 \leq \beta \leq 1$), and circles ($1 \leq \beta \leq 3$) are explained in Table 3.1.

3.5.3. Applications to Fractional Log-Normal Noises and Motions

In Figure 3.26, we apply rescaled-range analysis to several fractional log-normal noises and motions with $N = 4{,}096$ points and $c_v = 0.5$. The values for *Hu* , the Hurst exponent, have been obtained from the best fit of $(R/S)_{av} \sim (\tau/2)^{Hu}$ (3.85). We find good correlations for $\beta = -1$, 0, 1, and 2.

The values of *Hu* obtained for the best fit to (3.85) in the range $-3 \leq \beta \leq 3$ with $c_v = 0.2$, 0.5 (illustrated in Figure 3.26), and 1.0 are given in Figure 3.27. The straight-line correlation is with $\beta = 2Hu - 1$ (3.86). The agreement obtained for $c_v = 0.2$ is similar to that found in Figure 3.25, where the same analyses have been applied to fractional Gaussian noises and motions. For $c_v = 0.5$ and 1.0 the asymptotic values for negative β's become systematically higher. For log-normal noises with $\beta < 0$, values for *Hu* are clearly biased towards higher and higher values as c_v increases.

We recommend that if rescaled-range is to be used, then the non-Gaussian distribution should first be converted (*Hewett*, 1986; *Press et al.*, 1994) to its Gaussian equivalent. However, even for a Gaussian distribution, the Hurst rescaled-range analysis is a poor estimator of the strength of antipersistence. Rescaled-range analysis has also been applied to fractional log-normal noises and motions by *Mandelbrot and Wallis* (1969c).

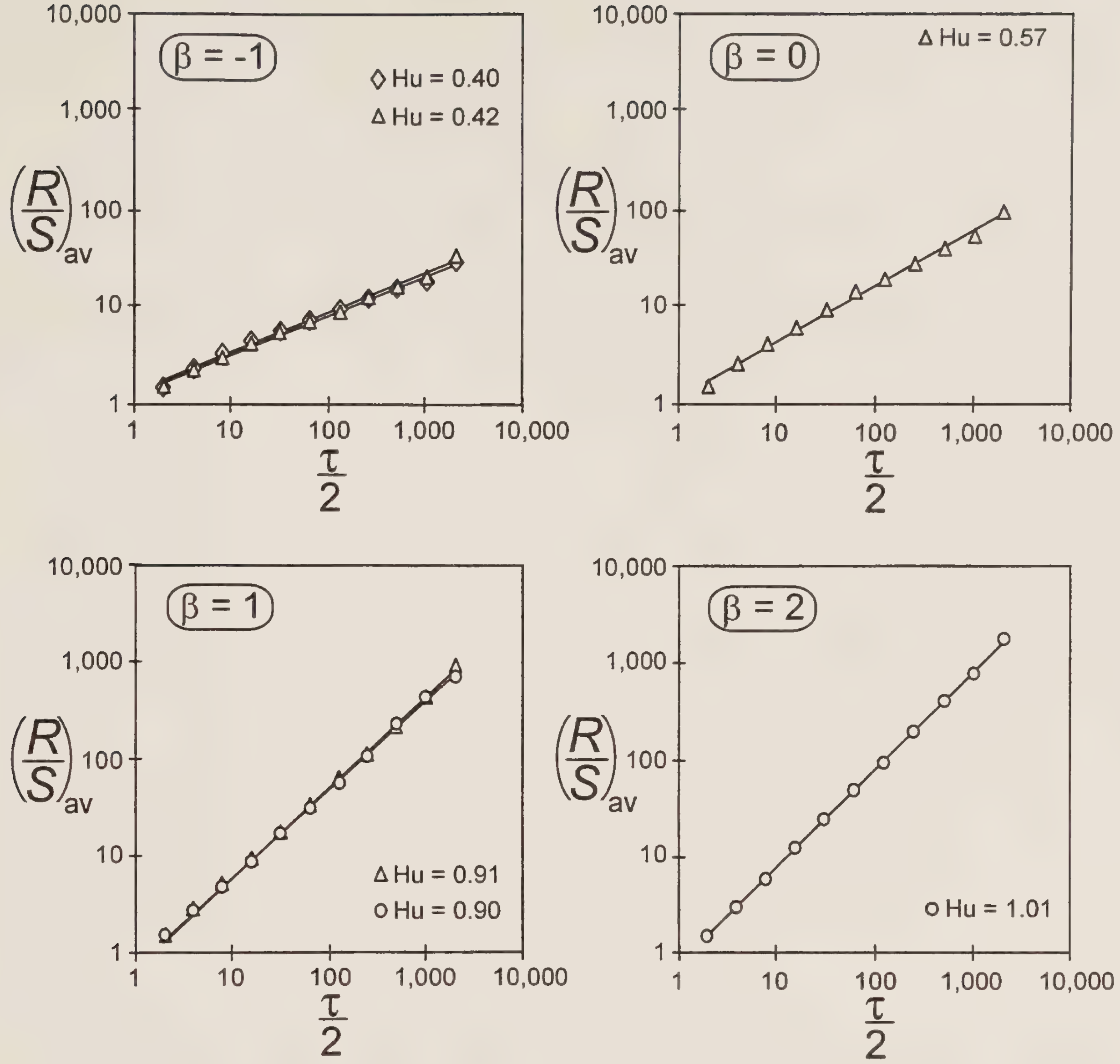

Figure 3.26. Hurst rescaled-range (*R*/*S*) analyses for several fractional log-normal noises and motions with N = 4,096 points and c_v = 0.5. Average values of R/S are given as a function of the interval $\tau/2$ for $\tau = 4$, 8, 16, ..., 4,096, where R and S are calculated using (3.82) to (3.84). The fractional log-normal noises and motions were each obtained by using (3.73) to (3.76) applied to fractional Gaussian noises and motions, and letting c_v = 0.5. Examples of time series with N = 512 points and the same characteristics are illustrated in Figure 3.19. The straight-line correlations are with $(R/S)_{av} \sim (\tau/2)^{Hu}$ (3.85). The slope of the best-fit straight line for $\log(R/S)_{av}$ *vs.* $\log(\tau/2)$ is *Hu*. Values for *Hu* are given for each of the examples. The diamonds (β = -1), triangles (β = -1, 0, 1), and circles (β = 1, 2) are explained in Table 3.2.

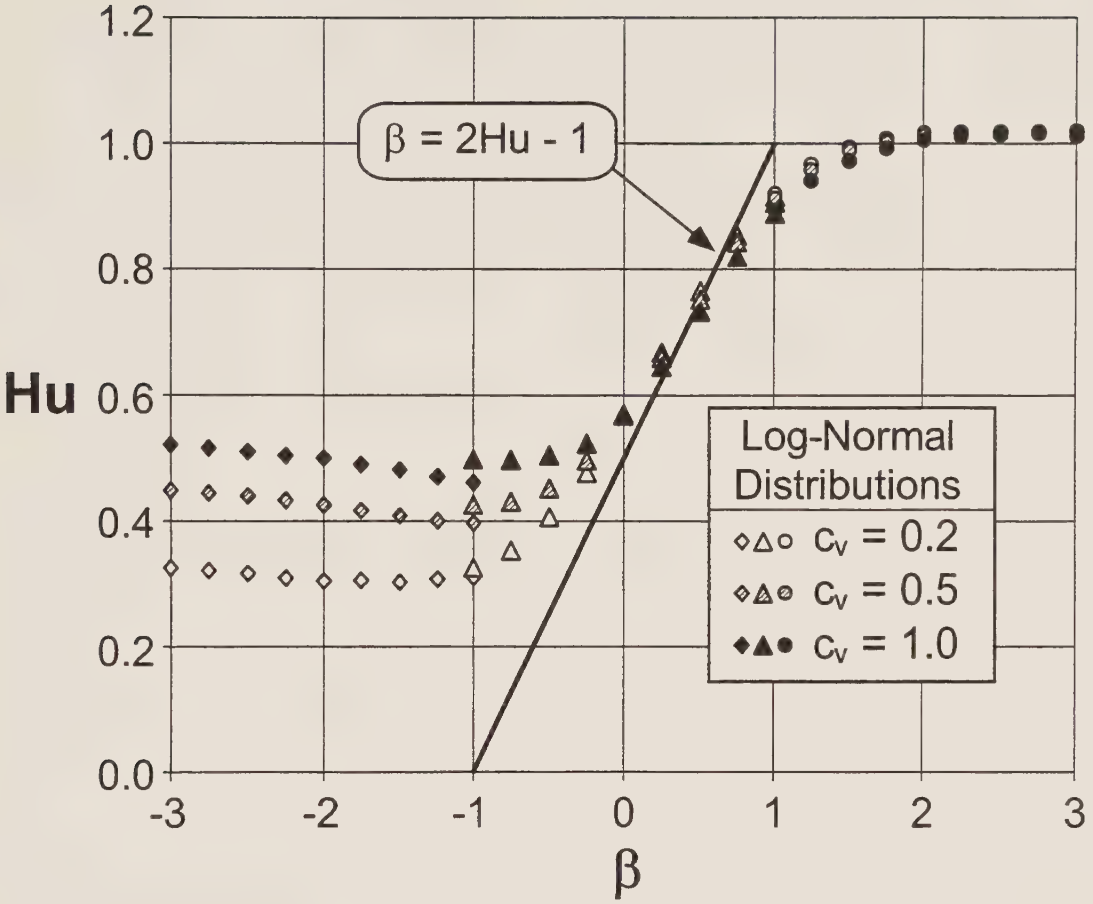

Figure 3.27. The dependence of the Hurst exponent, *Hu,* on β, for fractional log-normal noises and motions with N = 4,096 points. The values for *Hu* have been obtained from the best fit of $(R/S)_{av} \sim (\tau/2)^{Hu}$ (3.85). Results are given for $-3 \leq \beta \leq 3$ and $c_v = 0.2$ (white), 0.5 (gray), and 1.0 (black); each symbol represents the best fit for *Hu* at that β. Examples of obtaining *Hu* from rescaled-range (*R/S*) analyses are given in Figure 3.26. The straight-line correlation is with the relation $\beta = 2Hu - 1$ (3.86) for $-1 \leq \beta \leq -3$. The diamonds ($-3 \leq \beta \leq -1$), triangles ($-1 \leq \beta \leq 1$), and circles ($1 \leq \beta \leq 3$) are explained in Table 3.2.

3.6. AVERAGE EXTREME-VALUE ANALYSIS

3.6.1. The Method

For many time series, the primary goal is to understand the statistics of the extreme values. An example is a river discharge time series. The extreme values of this time series are floods. Flood hazard assessments require statistical estimators of these extreme values.

For a Gaussian white noise, the statistics of the extreme values are clearly Gaussian. However, what about fractional noises and motions? In order to specify the extreme values of a time series we consider average extreme-value analysis. Taking a synthetic time series of length N, we first force the time series to have a mean of 0 by subtracting $\bar{y}_N$, the mean of the data series taken over N, from each successive value in the time series. We still use y_n, $n = 1, 2, 3, \ldots, N$, to represent the time series with 0 mean. The maximum value of y_n over the N points, y_e, is assigned a period $\tau = N$. The period is then broken into two parts each of length $N/2$ and the maximum value for each part is found. The average, $(y_e)_{av}$, of the two values y_e is assigned the period $\tau = N/3$. The process is repeated for $\tau = N/4, N/8, N/16, \ldots$. In order to determine whether the extreme values have a power-law dependence on the length of time considered, the results are correlated with

$$(y_e)_{av} \sim \tau^{He} \tag{3.88}$$

where He is the extreme-value exponent. Consider the relation

$$\beta = 2He + 1 \tag{3.89}$$

which is analogous to $\beta = 2Ha + 1$ (3.62), where Ha is the Hausdorff Measure.

3.6.2. *Applications to Fractional Gaussian Noises and Motions*

We have applied average extreme-value analyses to several fractional noises and motions with $N = 4{,}096$ points, similar to those noises illustrated in Figure 3.10. The results are given in Figure 3.28 for $\beta = 0, 1, 2$, and 3. Good correlations with $(y_e)_{av} \sim \tau^{He}$ (3.88) are found.

The values of He obtained from the best fit of (3.88) in the range $-1 \leq \beta \leq 5$ are given in Figure 3.29. The straight-line correlation is with $\beta = 2Ha + 1$ (3.89). Reasonably good agreement is found in the range $1 \leq \beta \leq 3$, where the fractional Brownian motions are expected to be self-affine fractals; however, for $\beta < 2$, He becomes more positive than the straight-line fit (3.89). More interestingly, for the fractional Gaussian noises and fractional Brownian motions, the extreme-value behavior illustrated in Figure 3.29 is essentially identical to the rescaled-range analysis behavior illustrated in Figure 3.25, with each point in the figure shifted by a β of 2

$$Hu(\beta) = He(\beta + 2) \tag{3.90}$$

The two techniques result in an identical pattern of values for Hu and He, except that rescaled-range analysis measures the strength of persistence (and antipersistence) for fractional Gaussian noises ($-1 \leq \beta \leq 1$), and average-extreme value analysis measures the strength of persistence for fractional Brownian motions ($1 \leq \beta \leq 3$).

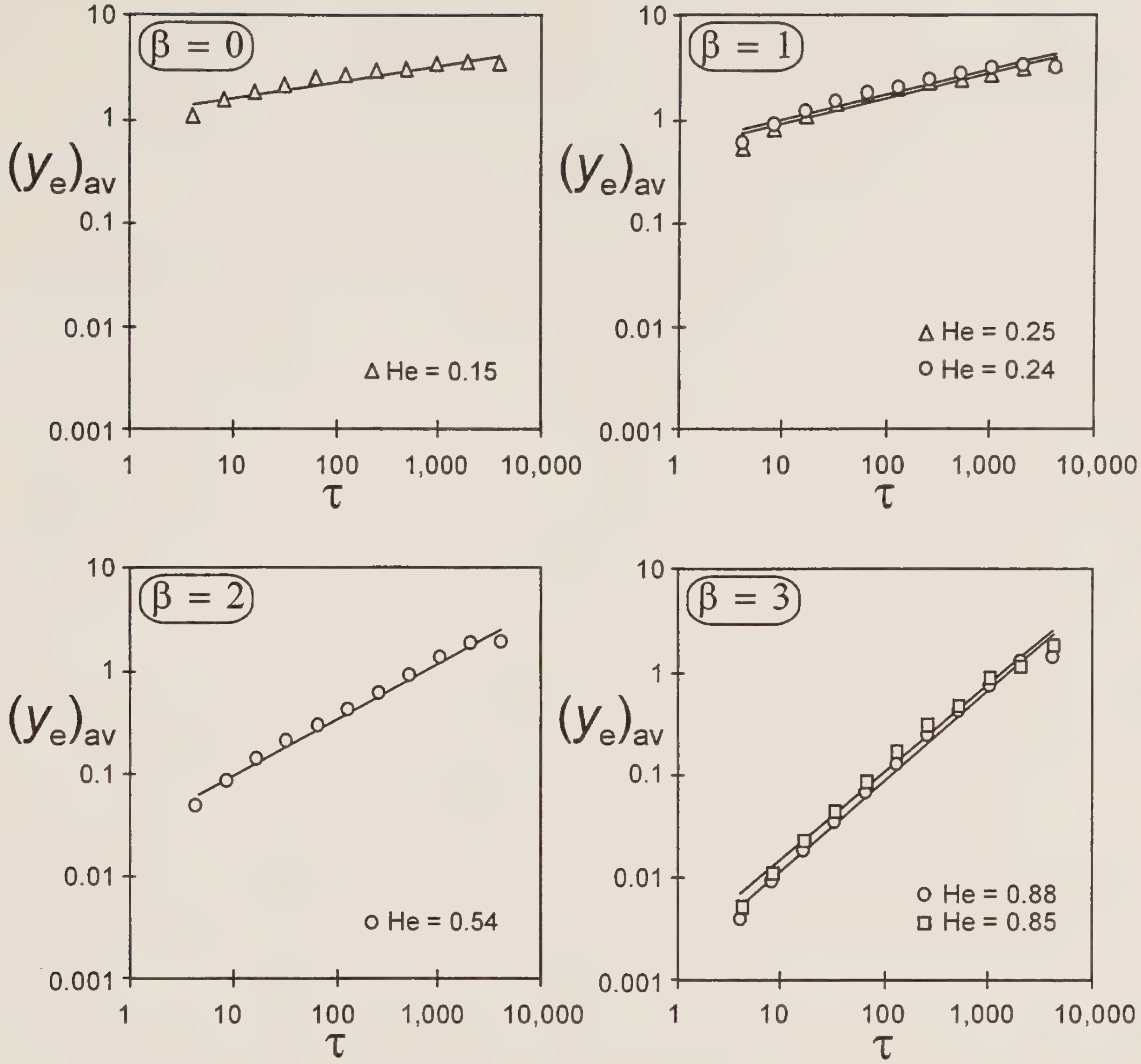

Figure 3.28. Average extreme-value analyses for several fractional Gaussian noises and fractional Brownian motions with $N = 4{,}096$ points. Examples of time series with $N = 512$ points and the same characteristics as the noises and motions we use here are illustrated in Figure 3.10. The time series is forced to have a mean of 0. Average values of the extreme values in each interval, $(y_e)_{av}$, are given as a function of the interval τ for $\tau = 8, 16, 32, \ldots, 4{,}096$. The straight-line correlations are with $(y_e)_{av} \sim \tau^{He}$ (3.88). The slope of the best-fit straight line for $\log(y_e)_{av}$ *vs.* $\log(\tau)$ is *He*. Values for *He* are given for each of the examples. The triangles ($\beta = 0, 1$), circles ($\beta = 1, 2, 3$), and squares ($\beta = 3$) are explained in Table 3.1.

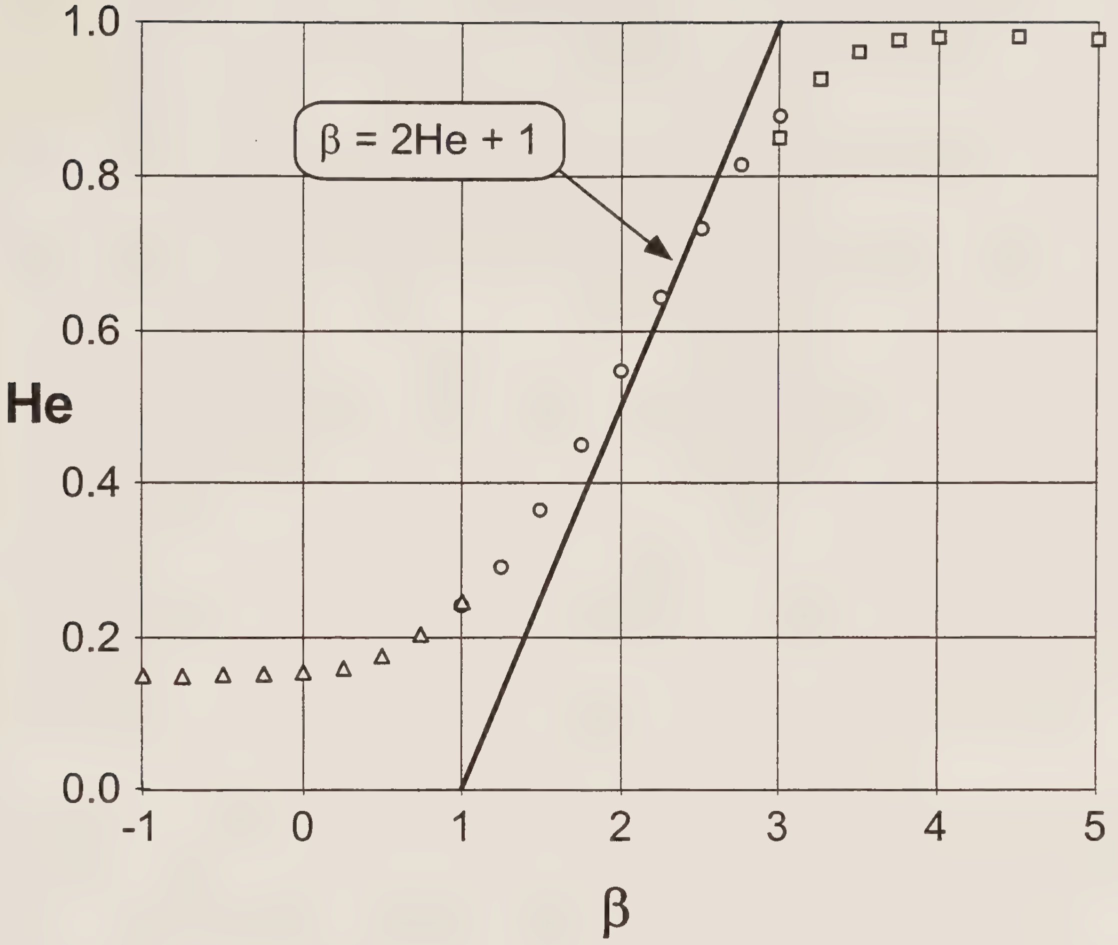

Figure 3.29. The dependence of the extreme-value exponent, *He,* on β, for fractional Gaussian noises and fractional Brownian motions with $N =$ 4,096 points. The values for *He* have been obtained from the best fit of $(y_e)_{av} \sim \tau^{He}$ (3.88). Results are given for $-1 \leq \beta \leq 5$; each symbol represents the best fit for *He* at that β. Examples of obtaining *He* from average extreme-value analysis are given in Figure 3.28. The straight-line correlation is with the relation $\beta = 2He + 1$ (3.89) for $1 \leq \beta \leq 3$. The triangles ($-1 \leq \beta \leq 1$), circles ($1 \leq \beta \leq 3$), and squares ($3 \leq \beta \leq 5$) are explained in Table 3.1.

The effect of (3.82) is to take the running sum of y_n, which results in the time series being shifted by a β of 2. This is similar to shifting β by 2 when summing a white noise to construct a Brownian motion. The range, $R(\tau)$, from (3.83) is then similar to taking the maximum value, y_e, in each subperiod, τ.

The fractional Gaussian noises and fractional Brownian motions illustrated in Figure 3.10 have both positive maximum values, y_{max}, and negative minimum values, y_{min}. The average-extreme value analysis just presented was on the most positive maximum values, y_{max}, for fractional noises and motions y_n, $n = 1, 2, 3, \ldots, N$, with $N = 4{,}096$ points and $-1 \leq \beta \leq 5$. We have also applied average extreme-value analysis to the most negative values, y_{min}, obtained by taking the negative of the fractional noise time series. The results were essentially the same.

3.6.3. Applications to Fractional Log-Normal Noises and Motions

The average extreme-value analysis has been applied to several fractional log-normal noises and motions, each with $N = 4{,}096$ points. Examples of time series with $N = 512$ points and the same characteristics are illustrated in Figure 3.19. Results for $c_v = 0.5$ and $\beta = 0, 1, 2$, and 3, are given in Figure 3.30. In general, the correlations with $(y_e)_{av} \sim \tau^{He}$ (3.88) are quite good. In Figure 3.30, the best-fit *He*, the average-extreme value exponent, is given for each value of β.

The values of *He* obtained from the best fit of (3.88) in the range $-1 \leq \beta \leq 5$ and $c_v = 0.2$, 0.5 (illustrated in Figure 3.30), and 1.0 are given in Figure 3.31. The straight-line correlation is with $\beta = 2He + 1$ (3.89).

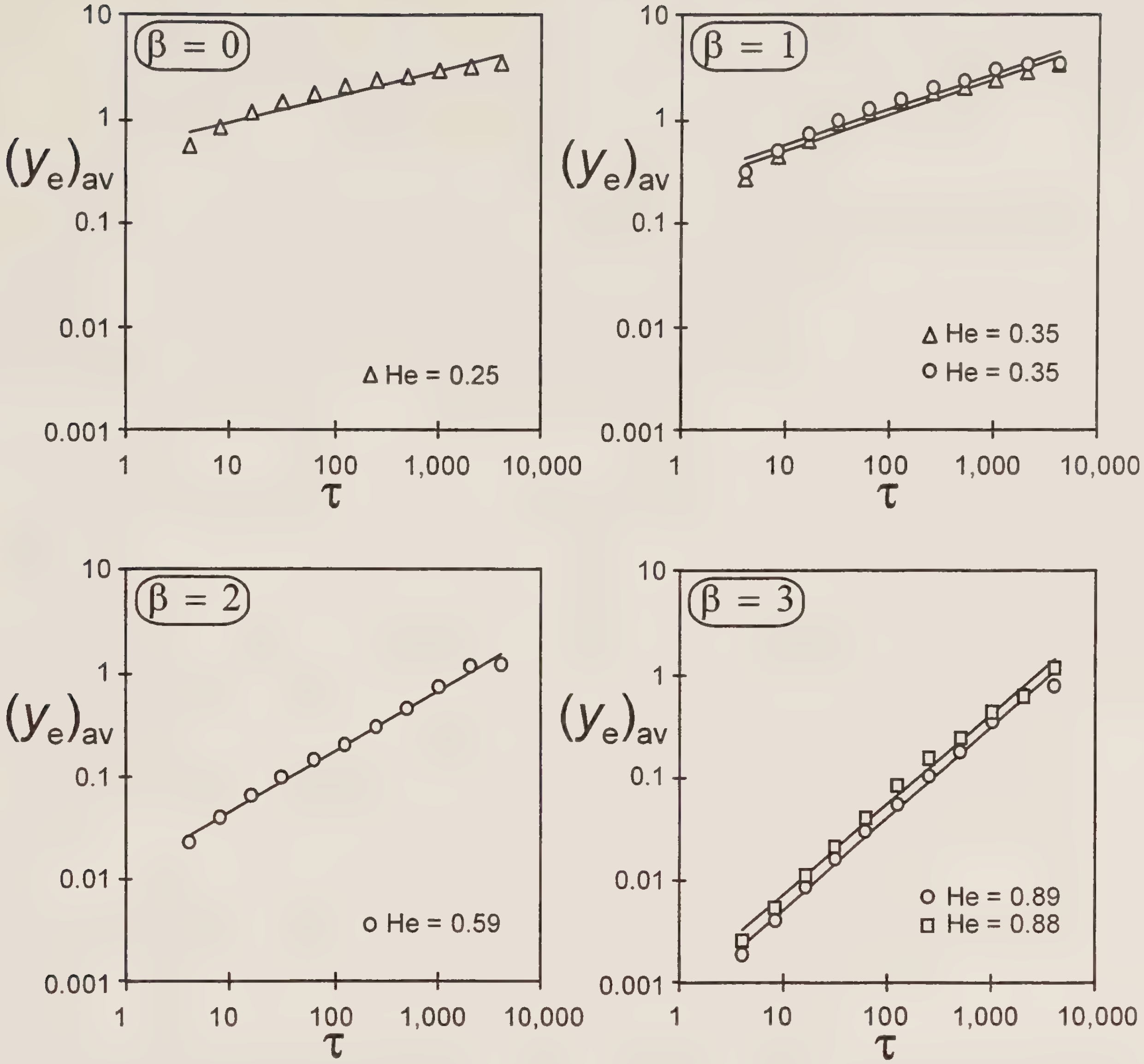

Figure 3.30. Average extreme-value analyses for several fractional log-normal noises and motions with N = 4,096 points and c_v = 0.5. The fractional log-normal noises and motions were obtained by using (3.73) to (3.76) applied to fractional Gaussian noises and motions, and letting c_v = 0.5. Examples of time series with 512 points and the same characteristics are illustrated in Figure 3.19. The time series is forced to have a mean of 0. Average values of the extreme values in each interval, $(y_e)_{av}$, are given as a function of the interval τ for τ = 8, 16, 32,..., 4,096. The straight-line correlations are with $(y_e)_{av} \sim \tau^{He}$ (3.88). The slope of the best-fit straight line for $\log(y_e)_{av}$ *vs.* $\log(\tau)$ is *He*. Values for *He* are given for each of the examples. The triangles (β = 0, 1), circles (β = 1, 2, 3), and squares (β = 3) are explained in Table 3.2.

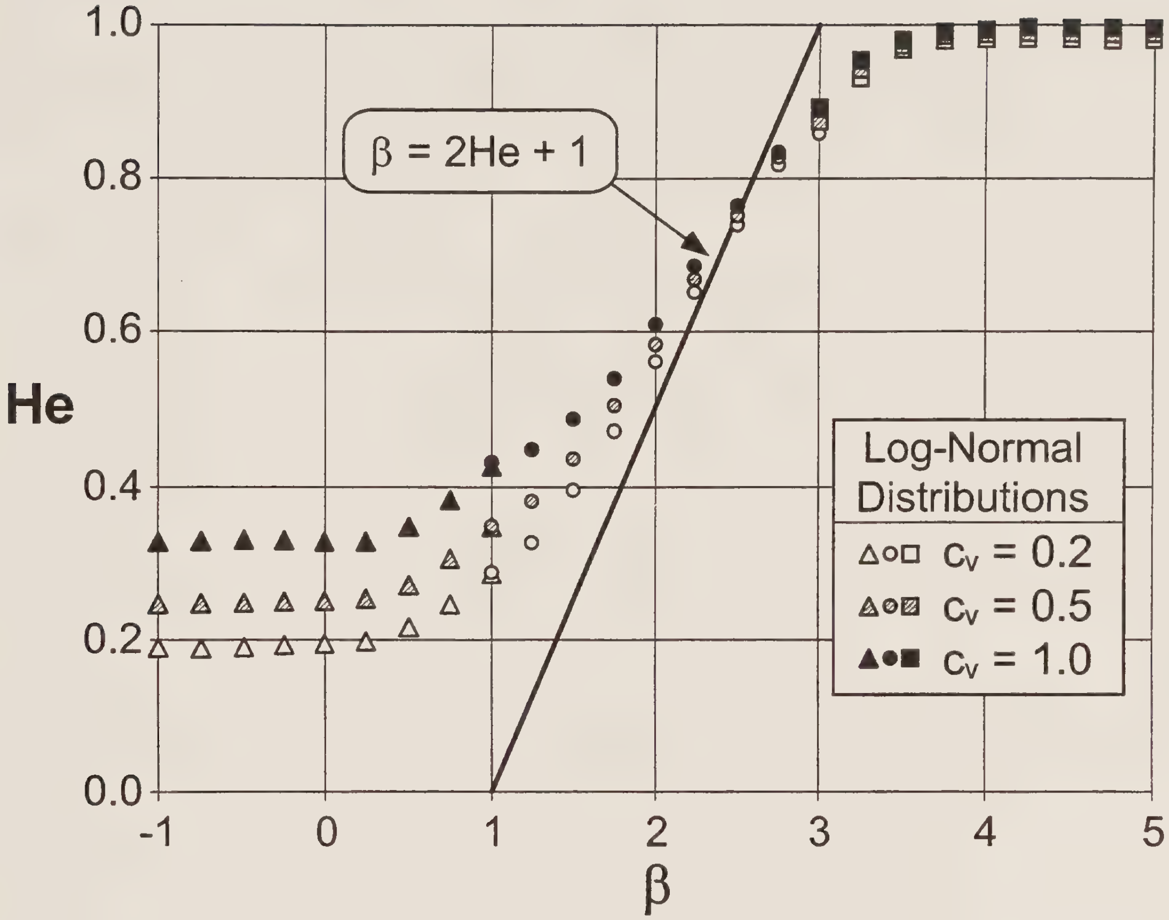

Figure 3.31. The dependence of the extreme-value exponent, *He,* on β, for fractional log-normal noises and motions with $N = 4{,}096$ points. The values for *He* have been obtained from the best fit of $(y_e)_{av} \sim \tau^{He}$ (3.88). Results are given for $-1 \le \beta \le 5$ and $c_v = 0.2$ (white), 0.5 (gray), and 1.0 (black); each symbol represents the best fit for *He* at that β. Examples of obtaining *He* from average extreme-value analysis are given in Figure 3.30. The straight-line correlation is with the relation $\beta = 2He + 1$ (3.89) for $1 \le \beta \le 3$. The triangles ($-1 \le \beta \le 1$), circles ($1 \le \beta \le 3$), and squares ($3 \le \beta \le 5$) are explained in Table 3.2.

As expected, the results for the fractional log-normal noises and motions with a low coefficient of variation, $c_v = 0.2$ (Figure 3.31) are very similar to the fractional Gaussian noises and motions (Figure 3.29). Reasonably good agreement is found in the range $1 \leq \beta \leq 3$, where the fractional Brownian motions are expected to be self-affine fractals. For $\beta < 2$ (Figure 3.31), *He* becomes increasingly more positive than the straight-line fit, $\beta = 2He + 1$ (3.89).

As the coefficient of variation becomes greater, $c_v = 0.5$ and $c_v = 1.0$ (Figure 3.31), *He* deviates farther away from the straight-line fit given by $\beta = 2He + 1$ (3.89). This is very similar to the Figure 3.27 behavior where rescaled-range analysis has been applied to fractional log-normal noises and motions. Rescaled-range analysis exhibits an increasing *Hu* ($\beta < 0$) as a function of an increasing coefficient of variation, c_v; similarly, average-extreme event analysis exhibits an increasing *He* ($\beta < 2$) as a function of increasing c_v.

3.7. WAVELET ANALYSIS

3.7.1. The Method

Fourier transforms have a long history of applications to a wide variety of problems. For example, they have great utility in terms of obtaining the frequency content of a time series. Despite the many advantages of Fourier transforms, there are also disadvantages. For instance, they do not provide spatial resolution. To overcome some of these disadvantages, *Grossmann and Morlet* (1984) introduced the wavelet transform. This transform provides information on both the

spatial and frequency dependence of a time series. The transform has a fractal basis and is particularly useful when applied to non-periodic multiscaled time series. The method can also be applied to nonstationary processes. Two excellent discussions of the wavelet transform are given by *Hubbard* (1996) and *Wornell* (1996). *Hubbard* (1996) is particularly useful because she provides a complete history of wavelets, along with a very easy to understand introduction to wavelet mathematics.

The wavelet transform is a filter $g[(t' - t)/a]$ which is passed over a time series $f(t')$. The effective width of the filter is generally increased by powers of two. The wavelet transform's general form is given by

$$W(t,a) = \frac{1}{a^{1/2}} \int_{-\infty}^{\infty} g\left(\frac{t'-t}{a}\right) f(t')\,dt' \tag{3.91}$$

The filter is centered at t, the position parameter, with a the scale parameter. The effective width of the filter is normally taken to be a constant multiple of the scale parameter. The quantity $g(t')$ is known as the "mother wavelet." Other wavelets are rescaled versions of the mother wavelet. The factor $a^{0.5}$ in (3.91) is an energy normalization so that the transformed signal will have the same energy at all scales. The area of each wavelet must sum to zero so that

$$\int_{-\infty}^{\infty} g(t')\,dt' = 0 \tag{3.92}$$

When a is increased by powers of two, a suite of wavelets is generated that can accommodate a wide range of scales in the signal $f(t')$. Small

values of the scale parameter *a* are equivalent to examining the high-frequency contributions to a time series; large values of *a* are equivalent to examining low frequencies.

A commonly used mother wavelet is the “Mexican hat” wavelet, which is the negative of the second derivative of the Gaussian distribution. It takes the form

$$g(t') = \left(\frac{1}{2\pi}\right)^{1/2} \left(1 - t'^2\right) e^{-t'^2/2} \tag{3.93}$$

The mother Mexican hat wavelet is illustrated in Figure 3.32. The effective width of the illustrated filter is 16*a*, where *a* is the scale parameter.

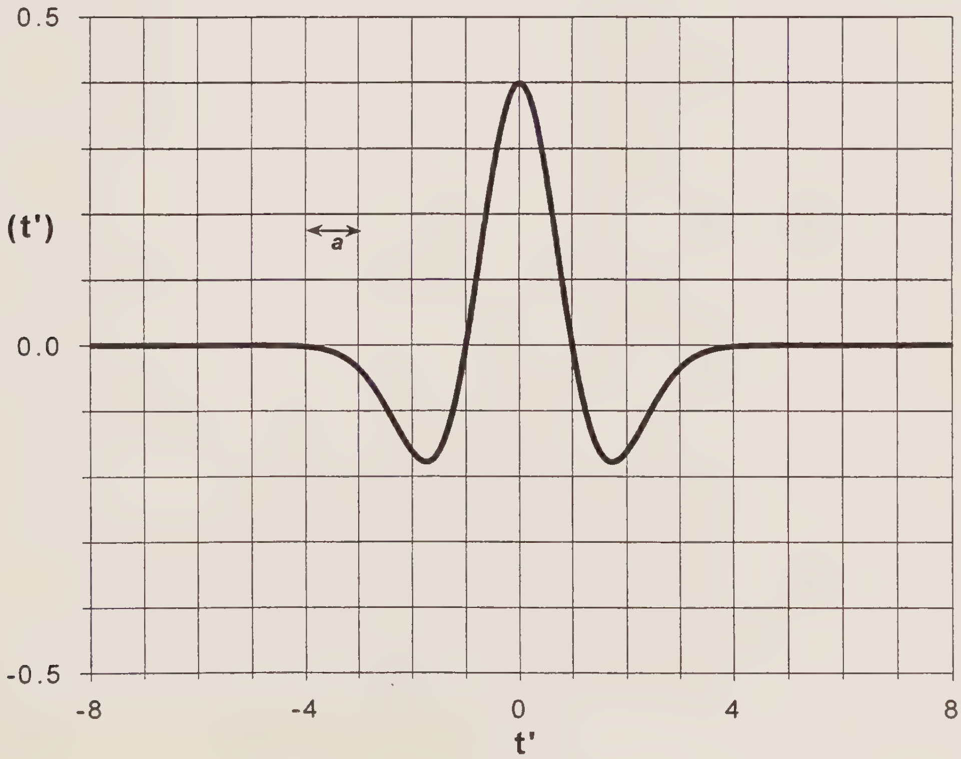

Figure 3.32. Mother Mexican hat wavelet *g*(*t*) from (3.94), where *g*(*t*) is the negative of the second derivative of a normal distribution. The width of this wavelet is 16*a*.

The Mexican hat wavelet in Figure 3.32 satisfies the condition given in (3.92), *i.e.* the positive and negative areas "under the curve" cancel out. Substitution of (3.93) into (3.91) gives

$$W(t,a) = \left(\frac{1}{2a\pi}\right)^{1/2} \int_{-\infty}^{\infty} \left[1 - \left(\frac{t' - t}{a}\right)^2\right] e^{-\frac{1}{2}\left(\frac{t'-t}{a}\right)^2} f(t')dt' \qquad (3.94)$$

The filter in this case is the Mexican hat wavelet. For an effective width of 16a, with $a = 1$, seventeen values from the Mexican Hat (3.93) are being convolved with the time series $W(t, a)$ in (3.94); for $a = 2$, thirty-three values from the Mexican Hat are being convolved with the time series, and so forth.

Many other wavelet transforms have been proposed in the literature. For example, a simple box wavelet known as the Haar wavelet has found wide use. One disadvantage of some wavelet transforms is that the sequence of wavelets is not orthogonal. Fourier transforms represent a complete set that can be inverted to reproduce the original signal. This is not the case for either the Mexican hat or Haar wavelets. In order to overcome this difficulty, *Daubechies* (1988) introduced an orthogonal wavelet. Unfortunately, this wavelet transform has an extremely complex waveform. Because we find very good results in quantifying the strength of persistence when we use the Mexican hat wavelet, we have not extensively examined other wavelets.

3.7.2. Applications to Fractional Gaussian Noises and Motions

The wavelet transform from (3.94) has been applied to several fractional Gaussian noises and fractional Brownian motions, each with $N = 4{,}096$ points. A Mexican hat wavelet (3.93) with an effective width of $16a$ is convoluted, $16a$ points at a time, with the time series y_n, $n = 1, 2, 3, \ldots, N$. The first convolution is centered at $n = 8a$, n increasing at +1 intervals, and the last convolution is centered at $N - 8a$, ($n = 8a, 8a + 1, 8a + 2, \ldots, N - 8a$). For example, when the scale parameter $a = 4$, then the effective width of the Mexican hat wavelet is 16*4 = 64 values. The first of the sixty-four Mexican hat values is multiplied by the first of the time series values, y_1; the second Mexican hat value is multiplied by the second in the time series, y_2. This continues until the sixty-four Mexican hat values are multiplied by the sixty-four time series values, y_1 to y_{64}. The results of the sixty-four multiplications are added up. Then, using (3.94), the total is divided by the square root of a, or 2. The result of this first convolution, $W(t, a)$ for $a = 4$, is placed at $t = 32$.

In Figure 3.33, results for $W(t, a)$ are shown for noises with $\beta = -1, 0, 1, 2$ and Mexican hats with a scale parameter, $a = 1, 2, 4, 8, 16$. The original time series, y_n, is shown at the bottom of each graph. As we would expect, for an antipersistent ($\beta = -1$) time series, the amplitude, $W(t, a)$, of the resulting wavelet transform is strongest for high frequencies (a small). For an uncorrelated signal (a Gaussian white noise, $\beta = 0$), $W(t, a)$ is equal for all a; in other words the signal is stationary, so there is no change in the variance at different a. For persistent signals ($\beta = 1, 2$), the wavelet amplitude, $W(t, a)$, is strongest for the low frequencies (a large).

Figure 3.33. Wavelet transform $W(t, a)$ of four fractional Gaussian noises and fractional Brownian motions with N = 4,096 points: (a) $\beta = -1$, (b) $\beta = 0$, (c) $\beta = 1$, and (d) $\beta = 2$. The "Mexican Hat" wavelet from (3.94) is used with a width of $16a$, wavelet scale $a = 1, 2, 4, 8, 16$. The fractional noises and motions used in each wavelet analysis are given at the bottom of each figure. Above the time series, the wavelet amplitude $W(t, a)$ is given for each value of a.

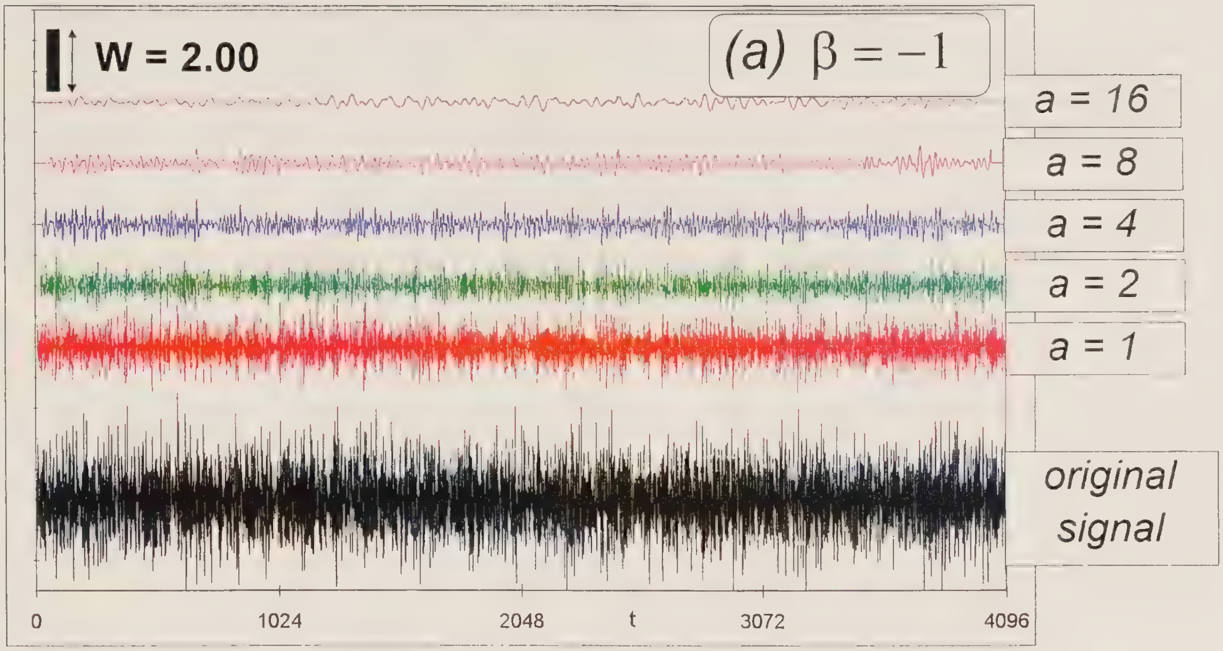
W = 2.00
(a) β = −1
a = 16
a = 8
a = 4
a = 2
a = 1
original signal
0
1024
2048
t
3072
4096

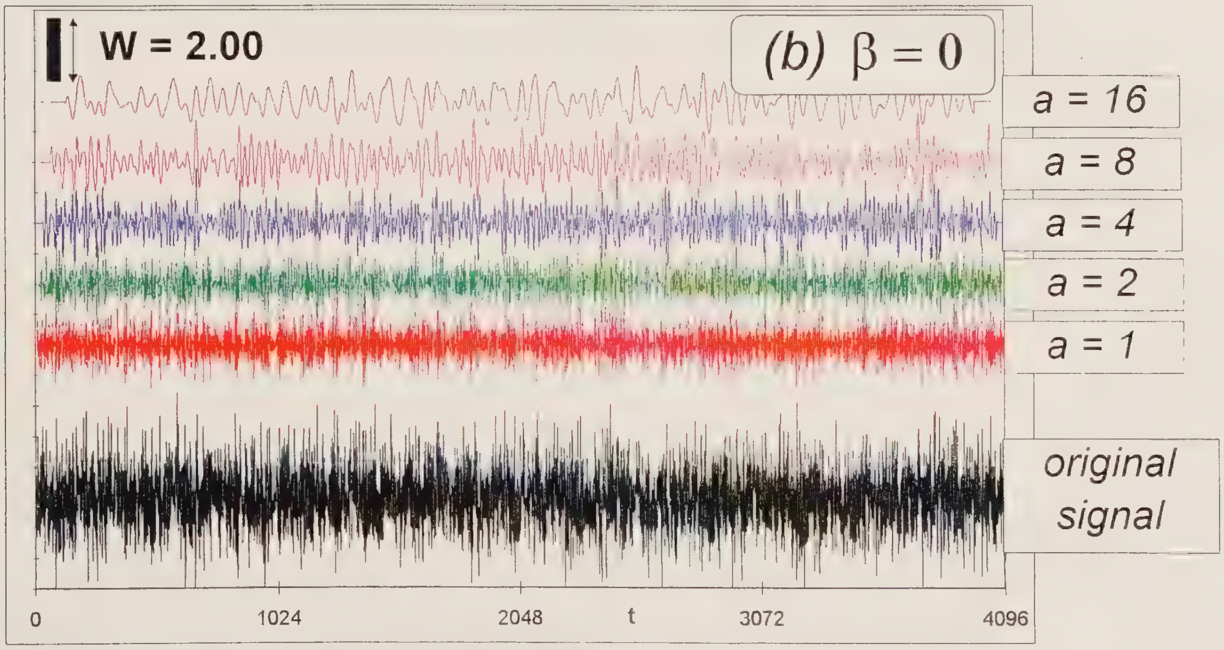
W = 2.00
(b) β = 0
a = 16
a = 8
a = 4
a = 2
a = 1
original signal
0
1024
2048
t
3072
4096

Figure 3.3 (Continued)

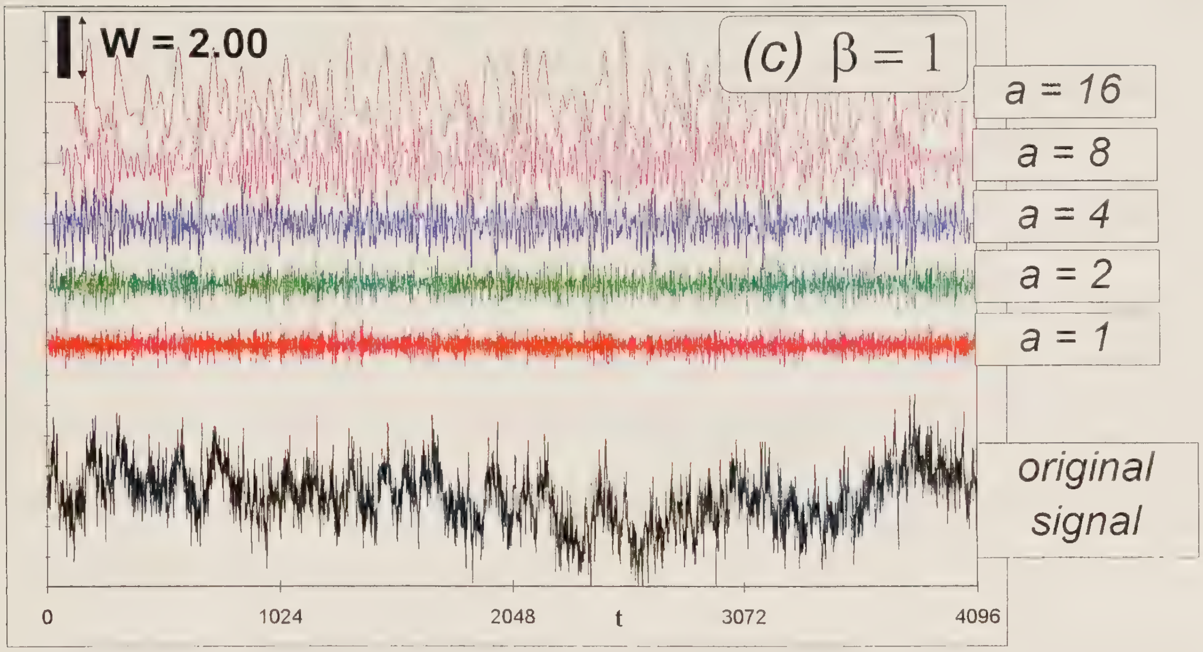

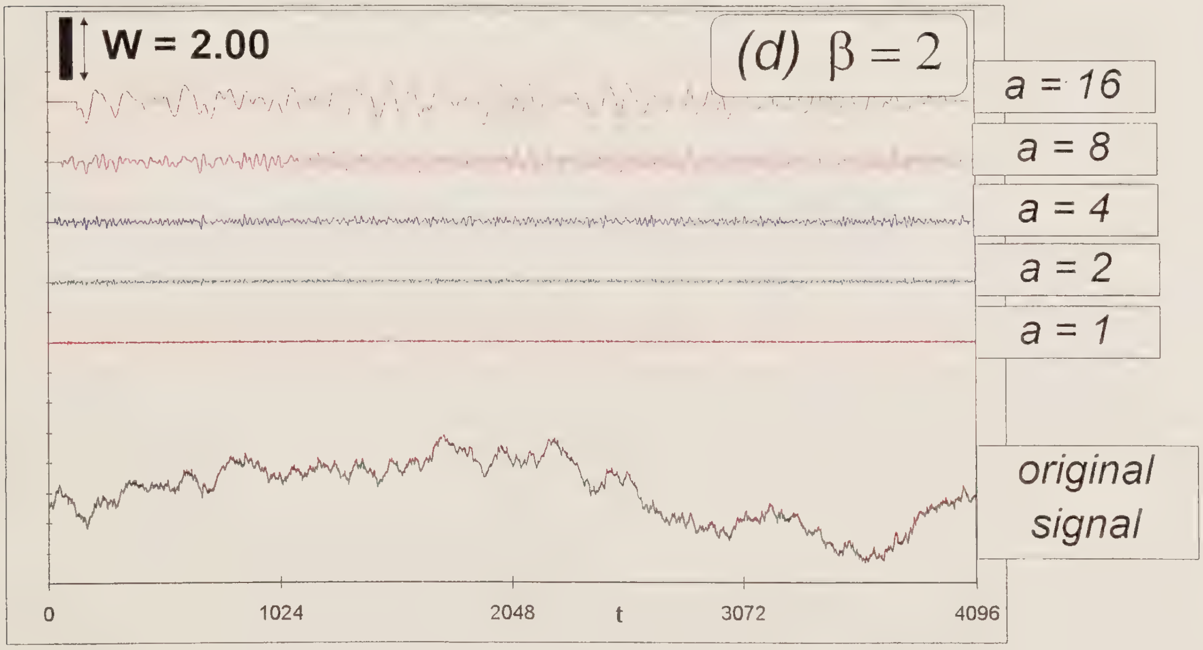

In order to quantify the dependence of W on a and β, we determine V_W, the variance of W, as a function of a. The results using fractional noises with β = -2, -1, 0, 1, 2, and 3, are given in Figure 3.34. In each case, we find an excellent correlation with the relation

$$V_W \sim a^{Hw} \tag{3.95}$$

A similar approach to fractional Brownian motions was applied by *Flandrin* (1992, 1993). He found a power-law behavior of the variance of W, from which he calculated an estimate for the fractal dimension of the fractional Brownian motions.

Figure 3.35 gives the values of Hw as a function of β, obtained from the best fit of (3.95) in the range $-3 \leq \beta \leq 5$. A good correlation with the relation

$$\beta = Hw \tag{3.96}$$

is obtained over the entire range. The wavelet transform provides a powerful measure of the strength of persistence or antipersistence over the complete range of fractional Gaussian noises and fractional Brownian motions. Moreover, because the wavelet transform is not sensitive to nonstationarities like Fourier analysis, one does not need to worry about detrending, windowing, spectral variance, etc.

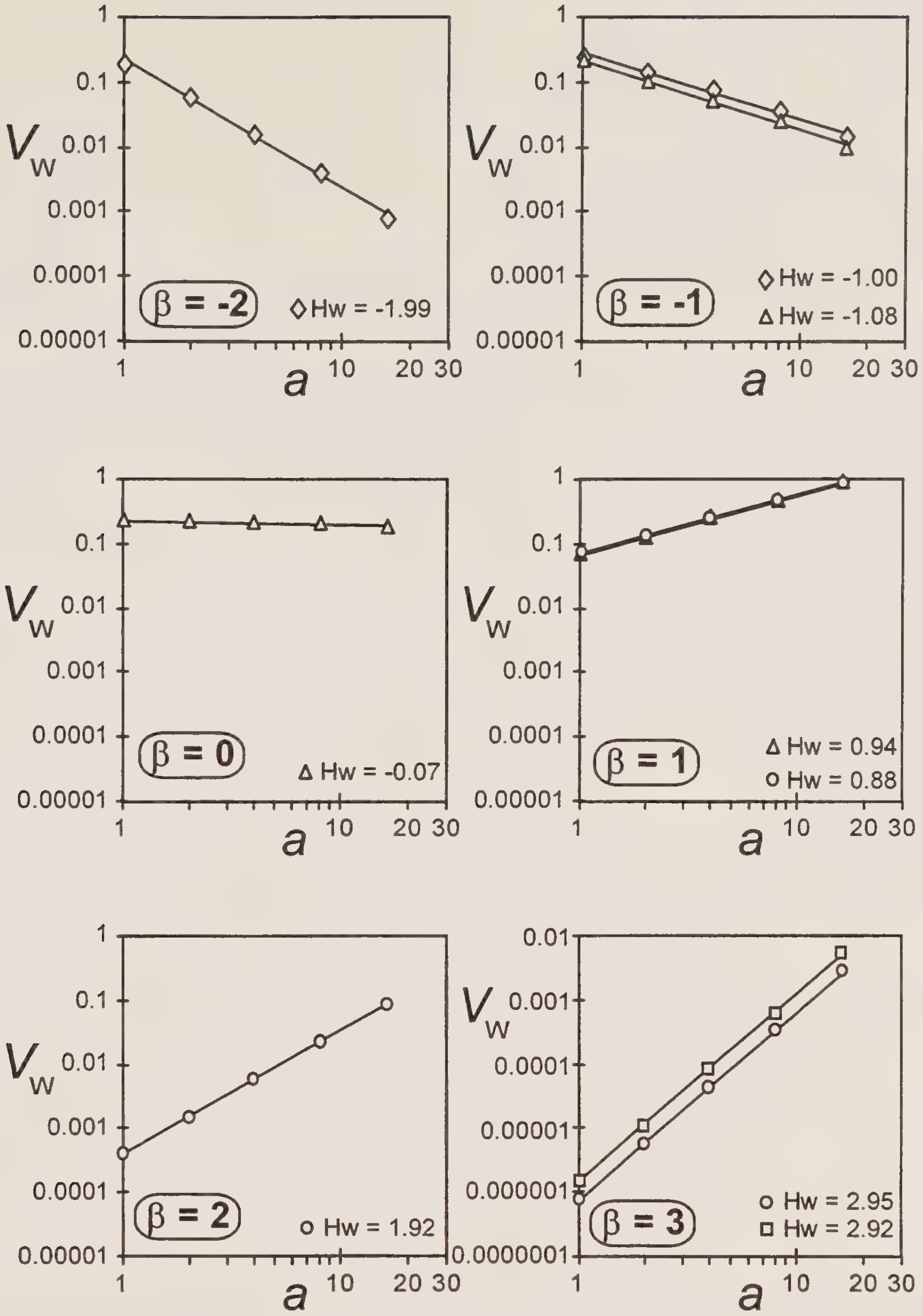

Figure 3.34. Wavelet variance analyses for several fractional Gaussian noises and fractional Brownian motions with N = 4,096 points. The "Mexican hat" filter, with a filter width of 16a, has been applied to the noises and motions. Examples of time series with N = 512 points and the same characteristics as the noises and motions we use here are illustrated in Figure 3.10. The population variance of the wavelet amplitude, V_w, is given as a function of the wavelet width, a, for a = 1, 2, 4, 8, 16. The straight-line correlations are with $V_w \sim a^{Hw}$ (3.95). The slope of the best-fit straight line for log(V_w) *vs.* log(a) is *Hw*. Values for *Hw* are given for each of the examples. The diamonds (β = -1), triangles (β = -1, 0, 1), and circles (β = 1, 2) are explained in Table 3.1.

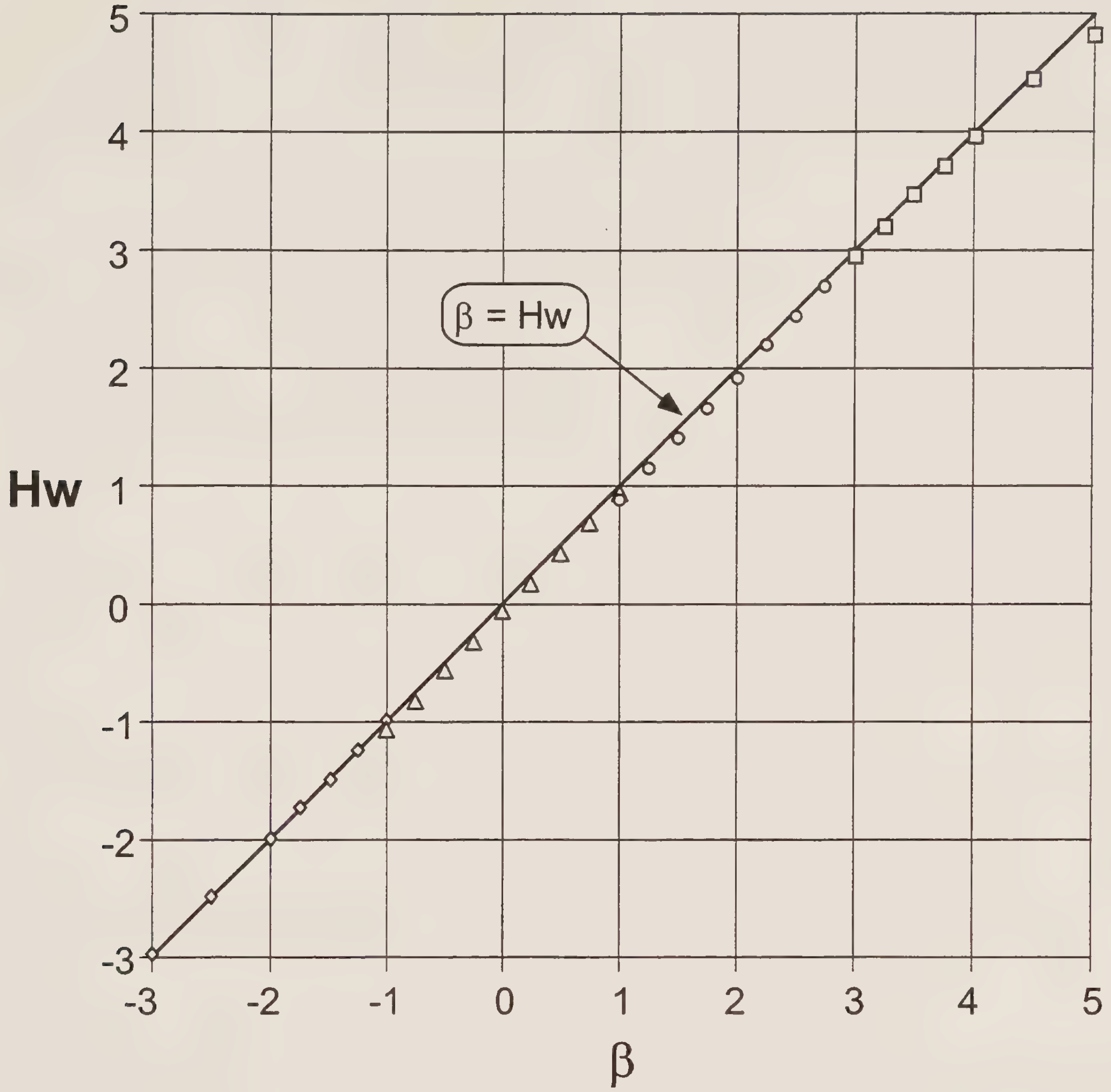

Figure 3.35. The dependence of the wavelet variance exponent, *Hw,* on β, for fractional Gaussian noises and fractional Brownian motions with $N = 4{,}096$ points. The values for *Hw* have been obtained from the best fit of $V_W \sim a^{Hw}$ (3.95). Results are given for $-3 \leq \beta \leq 5$; each symbol represents the best fit for *Hw* at that β. Examples of obtaining *Hw* from wavelet variance analysis are given in Figure 3.34. The straight-line correlation is with the relation $\beta = Hw$ (3.92) for $-3 \leq \beta \leq 5$. The diamonds ($-3 \leq \beta \leq -1$), triangles ($-1 \leq \beta \leq 1$), circles ($1 \leq \beta \leq 3$), and squares ($3 \leq \beta \leq 5$) are explained in Table 3.1.

3.7.3. Applications to Fractional Log-Normal Noises and Motions

The wavelet transform from (3.94) has been applied to several fractional log-normal noises and motions, each with 4,096 points. In Figure 3.36, results for $W(t, a)$ are shown for noises with $c_v = 0.5$ and $\beta = -1, 0, 1, 2$, using Mexican hats with a scaling parameter, $a = 1, 2, 4, 8, 16$. The original time series is shown at the bottom of each graph. For decreasing a, the signal, $W(t, a)$, increases when $\beta = -1$, is almost constant when $\beta = 0$, decreases when $\beta = 1$, and decreases even more when $\beta = 2$.

In order to quantify the dependence of W on both a and β, we determine V_W, the variance of W, as a function of a. The results for $\beta = -2, -1, 0, 1, 2$, and 3, are given in Figure 3.37. Again, excellent fits are found with (3.95). Figure 3.38 presents the values of Hw as a function of β, obtained from the best fit of (3.95) in the range $-3 \leq \beta \leq 5$. For $c_v = 0.2$, an extremely good correlation with $\beta = Hw$ (3.96) is found for $\beta = 5$ down to about $\beta = -1$; for values of β more negative than $\beta = -1$, Hw is more positive than expected. For higher coefficients of variation, $c_v = 0.5$ and $c_v = 1.0$, the deviation gets worse, and Hw fails to predict the expected value for values of β more negative than $\beta = -0.5$ and -0.2, respectively.

The wavelet transform provides a very powerful measure of persistence or antipersistence for log-normal fractional noises and motions with $\beta > 0$. For negative values of β it does not do as good a job. We recommend a transformation to a Gaussian distribution for non-Gaussian distributions with $\beta < 0$.

Figure 3.36. Wavelet transform $W(t, a)$ of four fractional log-normal noises and motions with N = 4,096 points and coefficient of variation, $c_v = 0.5$: (a) $\beta = -1$, (b) $\beta = 0$, (c) $\beta = 1$, and (d) $\beta = 2$. The “Mexican Hat” wavelet from (3.94) is used with a width of $16a$, wavelet scale a = 1, 2, 4, 8, 16. The fractional log-normal noises and motions used in each wavelet analysis are given at the bottom of each figure. Above each time series, the wavelet amplitude $W(t, a)$ is given for each value of a.

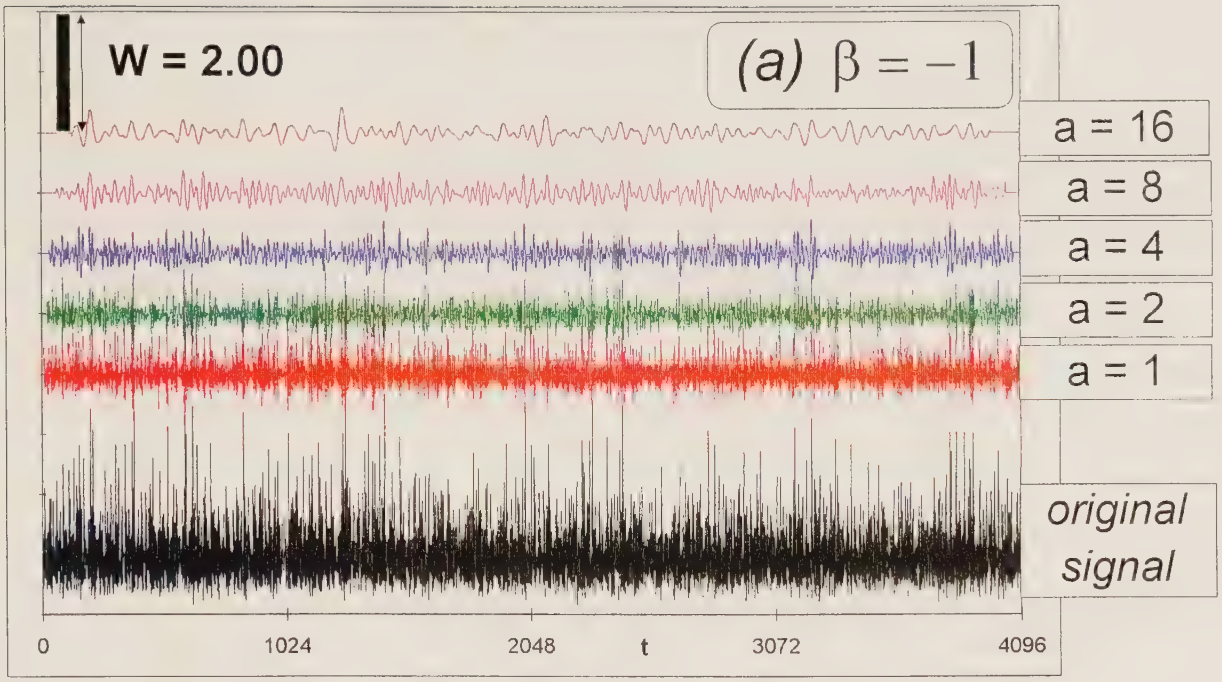
W = 2.00
(a) $\beta = -1$
a = 16
a = 8
a = 4
a = 2
a = 1
original signal
0
1024
2048
t
3072
4096

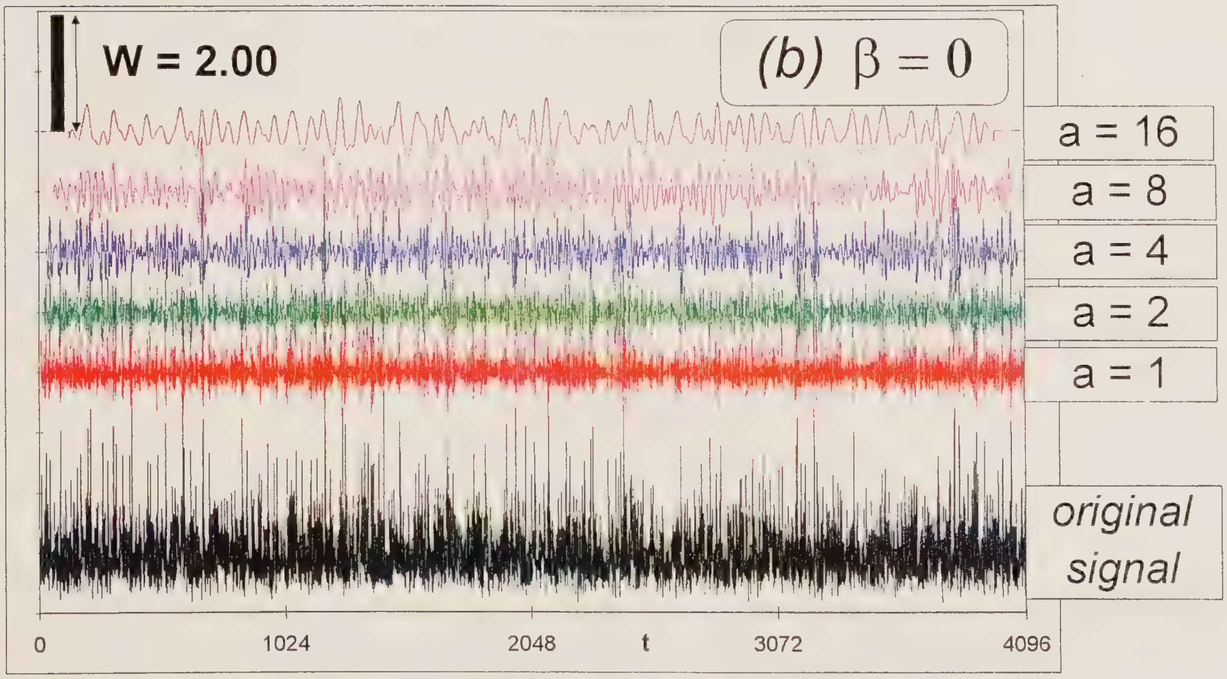
W = 2.00
(b) $\beta = 0$
a = 16
a = 8
a = 4
a = 2
a = 1
original signal
0
1024
2048
t
3072
4096

Figure 3.36 (Continued)

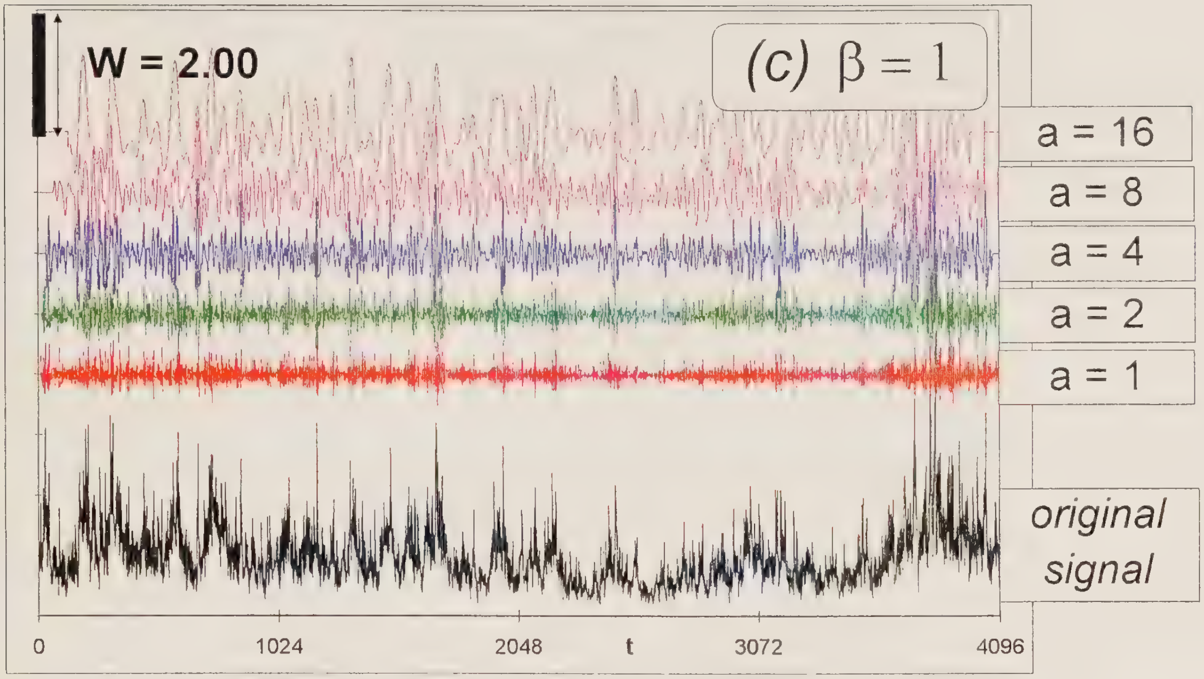

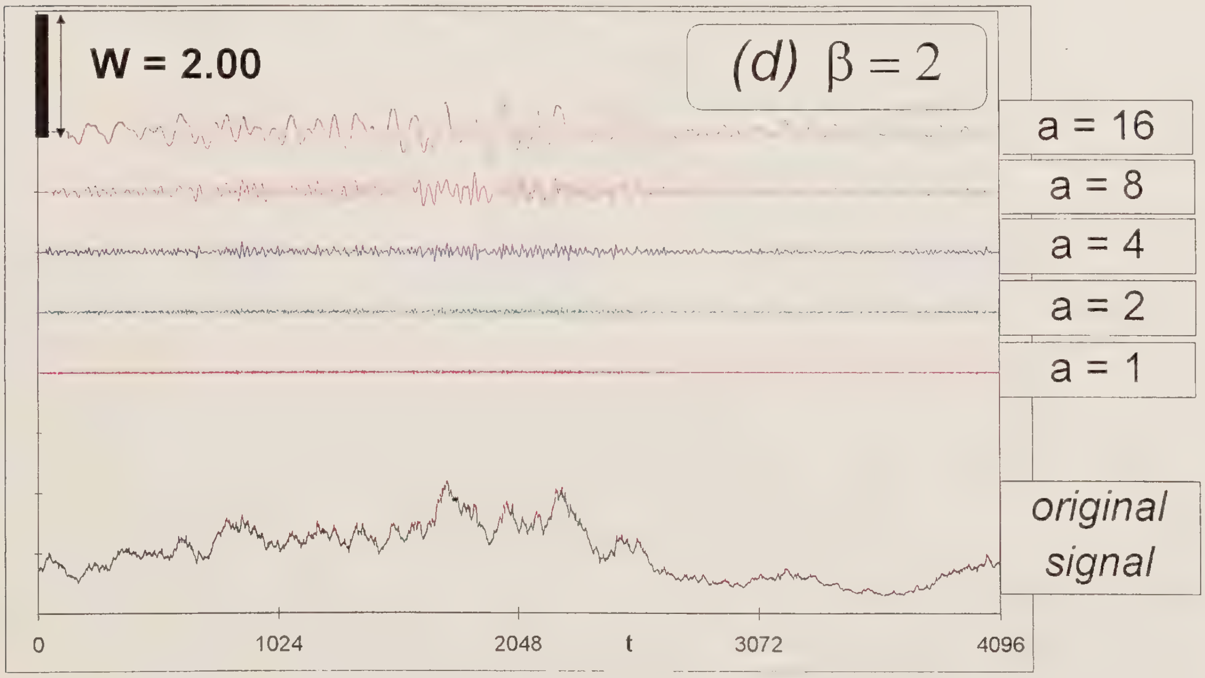

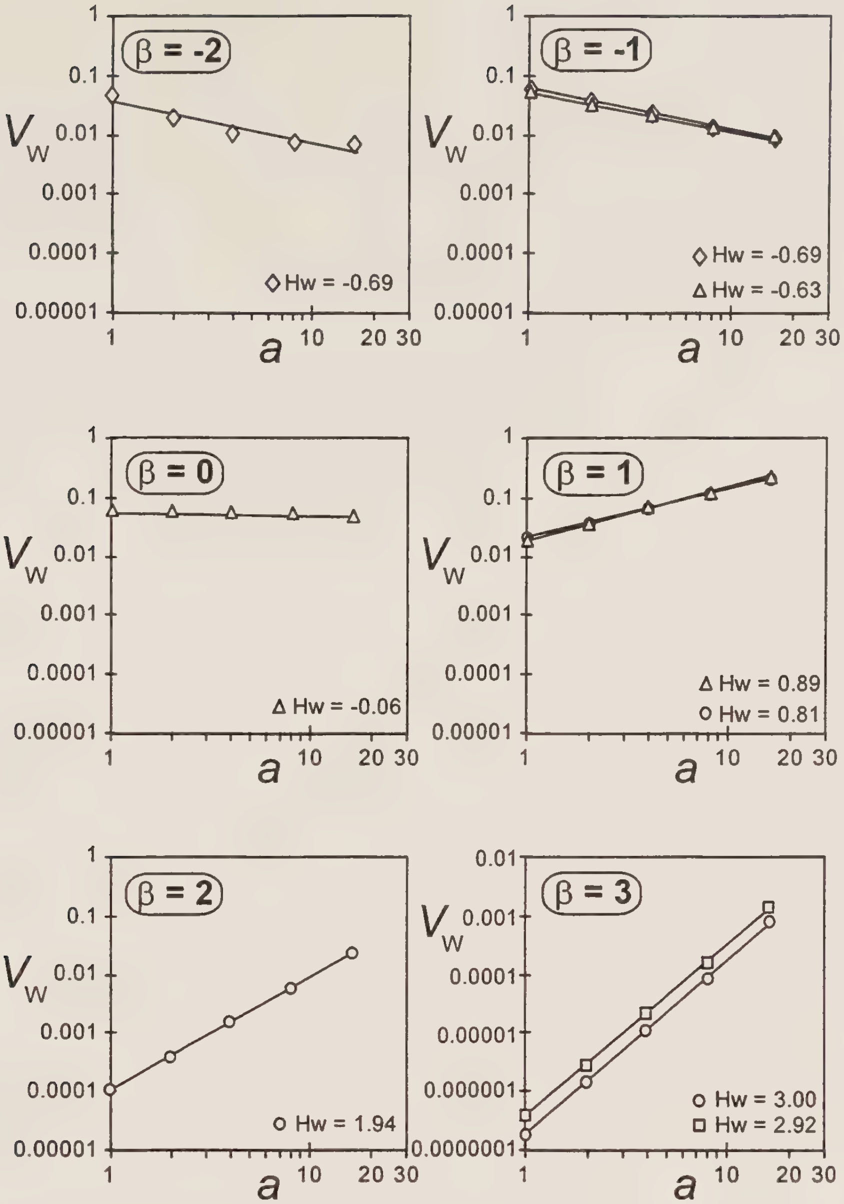

Figure 3.37. Wavelet variance analyses for several fractional log-normal noises and motions with N = 4,096 points and c_v = 0.5. The "Mexican hat" filter, with a filter width of 16*a*, has been applied to the log-normal noises and motions. The fractional log-normal noises and motions were each obtained by using (3.73) to (3.76) applied to fractional Gaussian noises and motions, and letting c_v = 0.5. Examples of time series with N = 512 points and the same characteristics as the noises and motions we use here are illustrated in Figure 3.19. The population variance of the wavelet amplitude, V_w, is given as a function of the wavelet width, *a*, for *a* = 1, 2, 4, 8, 16. The straight-line correlations are with $V_w \sim a^{Hw}$ (3.95). The slope of the best-fit straight line for log(V_w) *vs.* log(a) is *Hw*. Values for *Hw* are given for each of the examples. The diamonds (β = -1), triangles (β = -1, 0, 1), and circles (β = 1, 2) are explained in Table 3.2.

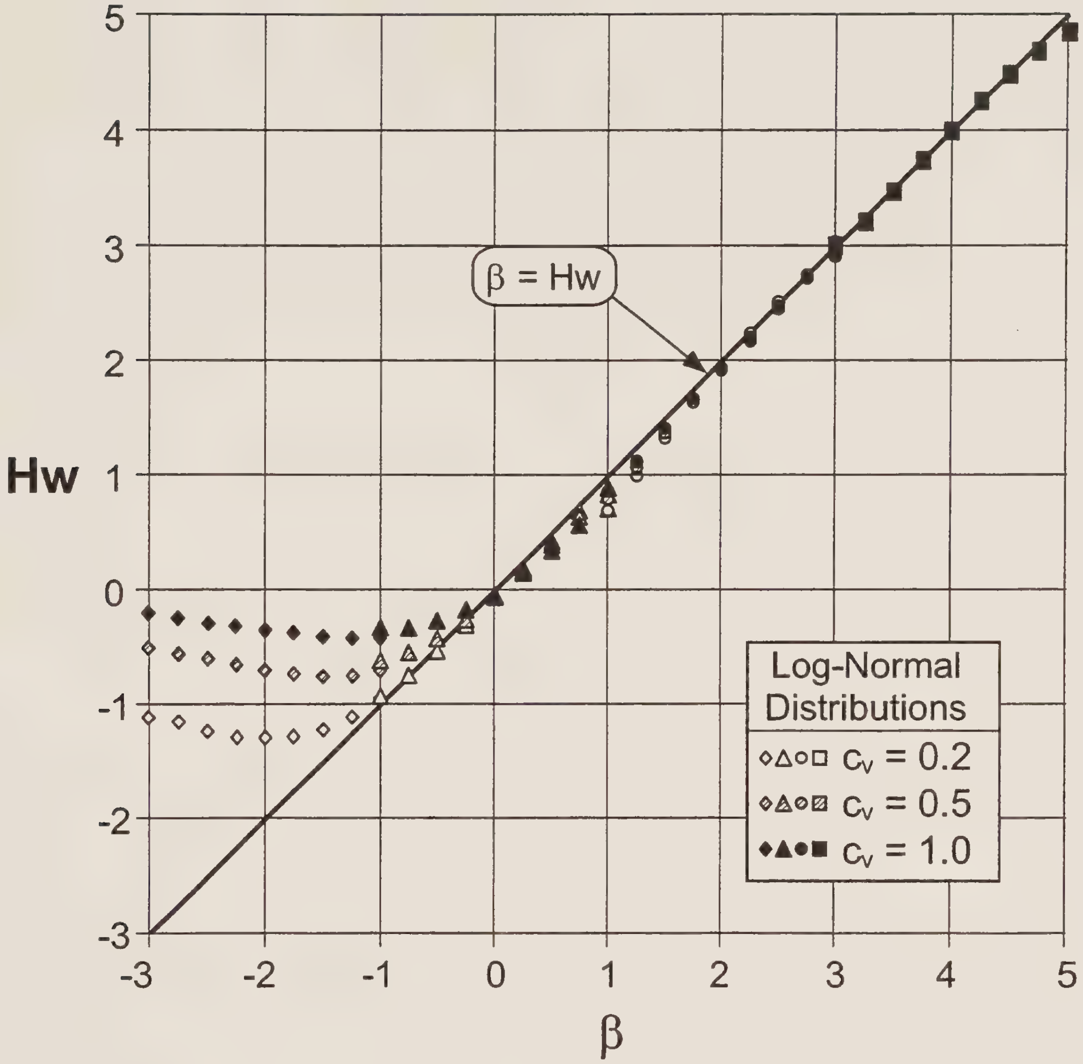

Figure 3.38. The dependence of the wavelet variance exponent, *Hw,* on β, for fractional log-normal noises and motions with $N = 4{,}096$ points. The values for *Hw* have been obtained from the best fit of $V_W \sim a^{Hw}$ (3.95). Results are given for $-3 \le \beta \le 5$ and $c_v = 0.2$ (white), 0.5 (gray), and 1.0 (black); each symbol represents the best fit for *Hw* at that β. Examples of obtaining *Hw* from wavelet variance analysis are given in Figure 3.37. The straight-line correlation is with the relation $\beta = Hw$ (3.92) for $-3 \le \beta \le 5$. The diamonds ($-3 \le \beta \le -1$), triangles ($-1 \le \beta \le 1$), circles ($1 \le \beta \le 3$), and squares ($3 \le \beta \le 5$) are explained in Table 3.2.

3.8. SUMMARY

The basic concepts of self-affine time series have been introduced in this paper. In a self-affine time series, the power-spectral density (3.38) scales as a power-law function of the frequency (3.39). Time series are quantified by their statistical distribution of values and by their persistence or antipersistence. Persistence can be classified in terms of range, short-range or long-range, and in terms of strength, weak or strong. The distribution of values is usually either Gaussian (normal) or log-normal. The basic characteristic of a self-affine time series is that the persistence is scale invariant. Thus, a self-affine time series has long-range persistence by definition.

In this paper, we have examined a variety of techniques to quantify the strength of long-range persistence in self-affine time series. These include Fourier spectral analyses, autocorrelation, semivariograms, rescaled-range analysis, average extreme-event analysis, and wavelet analysis. Other techniques to examine long-range persistent series, not discussed in this paper, include dispersional analysis (*Bassingthwaighte and Raymond*, 1995), and maximum likelihood estimators (*Beran*, 1994). In addition, *Beran* (1994), along with other authors, discusses long-range persistence techniques that examine composite long-memory processes, such as fractional autoregressive integrated moving average (FARIMA) models. Composite long-memory processes are characterized by more than two parameters; in this paper we have restricted our analysis to single parameter long-memory processes, *i.e.*, where the persistence is characterized by one parameter, β, *Ha*, *Hu*, *He*, or *Hw*.

Synthetic self-affine time series were generated using spectral techniques and the method of successive random additions. Although the spectral technique can be used to generate fractional noises with any value of β, we used the technique to generate noises in the range $-1 \leq \beta \leq 1$. These noises were summed to give fractional motions in the range $1 \leq \beta \leq 3$, and differenced to give extended fractional noises in the range $-3 \leq \beta \leq -1$. The method of successive random additions was used to generate fractional motions in the range $1 \leq \beta \leq 3$. The motions could then be summed to give extended fractional motions in the range $3 \leq \beta \leq 5$, and differenced to give fractional noises in the range $-1 \leq \beta \leq 1$.

Self-affine time series with $\beta > 1$ have a systematically different behavior than self-affine time series with $0 < \beta < 1$. With $\beta > 1$, the time series are nonstationary and moments of the time series depend upon its length. Over the range $1 \leq \beta \leq 3$, the time series are self-affine fractals with fractal dimension, $1 \leq D \leq 2$. These time series are known as fractional motions; with $\beta = 2$, the time series is a Brownian motion. Time series in the range $-1 \leq \beta \leq 1$ are known as fractional noises and are stationary. With $\beta = 0$, the time series is a white noise. We define the self-affine time series with $\beta > 1$ to have strong persistence and the self-affine time series with $\beta < 1$ to have weak persistence.

We have used a variety of techniques to quantify the strength of persistence of synthetic self-affine time series with $-3 \leq \beta \leq 5$:

(1) **Semivariograms** quantify the strength of persistence in the range $1 \leq \beta \leq 3$. Self-affine time series in this range are nonstationary and are considered to be self-affine fractals. The characteristic measure of a semivariogram is the Hausdorff Measure, *Ha*. For both Gaussian and log-normal fractional motions, $1 \leq \beta \leq 3$, there is a good correlation with $\beta = 2Ha + 1$.

(2) **Rescaled-range analyses** quantify the strength of persistence in the range $-1 \leq \beta \leq 1$. Self-affine time series in this range are stationary. The characteristic measure of *R/S* analysis is the Hurst Exponent, *Hu*. For fractional Gaussian noises, the correlation with $\beta = 2Hu - 1$ is relatively poor, particularly for $\beta < 0$. For fractional log-normal noises, the correlation becomes worse. The convergence of *Hu* to $Hu = (\beta + 1)/2$ is poor for long record lengths.

(3) **Average extreme-value analyses** quantify the strength of persistence in the range $1 \leq \beta \leq 3$. The characteristic measure of average extreme-value analysis is the extreme-value exponent, *He*. The correlation with $\beta = 2He + 1$ is the same as the correlation of *Hu* with $\beta = 2Hu - 1$, except that $Hu(\beta) = He(\beta + 2)$.

(4) **Spectral techniques** can, in principal, quantify the strength of persistence for all values of β. Both stationary and nonstationary self-affine time series can be considered. For a self-affine time series with a prescribed β, Fourier spectral techniques provide a direct confirmation of this β using the power-law dependence of S_m on f_m. For fractional Gaussian noises and motions, biased results

can be found for $\beta > 2$ and $\beta < 0$, unless windowing is applied to the time series. When windowing is applied, spectral techniques accurately quantify the persistence for almost all values of β. For fractional log-normal noises and motions, even with windowing, β does not provide a reliable measure of persistence for $\beta < 0$; we recommend for all time series with a non-Gaussian distribution of values and $\beta < 0$, that the time series be converted to a Gaussian distribution before applying spectral techniques.

(5) **Wavelet variance analyses** quantify the strength of persistence for all β. Self-affine time series in this range are both stationary and nonstationary. The characteristic measure of wavelet variance analysis is the wavelet exponent, Hw. In many ways, wavelet analyses are the most satisfactory measure of the strength of persistence, particularly for data sets that are nonstationary. Wavelet analyses do not have many of the inherent problems that are found in Fourier power-spectral analysis, such as windowing, detrending, etc. For $\beta > 0$, Hw correlates well with $Hw = \beta$ for both fractional Gaussian and fractional log-normal noises and motions. For $\beta < 0$, Hw correlates well with $Hw = \beta$ for both fractional Gaussian noises and motions, but is poor for fractional log-normal noises and motions. We recommend for $\beta < 0$ that a non-Gaussian distribution of values be converted to a Gaussian distribution.

Self-affine time series are found in a wide variety of geophysical applications. Examples include the natural variability of climate, variations in sedimentation, and the variability of the Earth's magnetic field. Stochastic differential equations can generate self-affine time series with a variety of values for β. A number of geophysical applications and relevant models are discussed in (*Pelletier and Turcotte*, 1998).

APPENDIX 3.1. ABBREVIATIONS AND SYMBOLS

SYMBOL	DESCRIPTION	EQUATION WHERE INTRODUCED	SECTION WHERE INTRODUCED
a	Scale parameter in wavelet analysis	(3.91)	3.7.1
A	Constant of proportionality	(3.59)	3.2.3
$(\ )_{av}$	Average value of ( ), normally over set interval τ	(3.81)	3.5.1
Bm	Brownian Motion	(3.18)	3.1.6
$c(s)$	Covariance of $y(t)$ at lag s	(3.2)	3.1.4
$c(0)$	Covariance of $y(t)$ at zero lag	(3.3)	3.1.4
c_k	Covariance of y_n at lag k	(3.5)	3.1.4
c_0	Covariance of y_n at zero lag	(3.6)	3.1.4
c_v	Coefficient of variation	(3.74)	3.4.1
D	Fractal Dimension	(3.13)	3.1.5
e	Exponential function	(3.30)	3.2.1
f	Continuous frequency	(3.30)	3.2.1
f_m	Discrete frequency, $f_\mathrm{m} = m/(N\delta)$		3.2.1
Δf	Width of a frequency bin, $\Delta f = 1/(N\delta)$		3.2.5
$f(x)$	Probability distribution function		3.4.1
fBm	Fractional Brownian Motion		3.3.2
fGn	Fractional Gaussian Noise		3.3.2
$g(t)$	Periodic continuous function	(3.30)	3.2.1
$G(f)$	Fourier transform of $g(t)$	(3.30)	3.2.1
$g(\mathrm{t}')$	Mother wavelet; filter	(3.91)	3.7.1
h	Elevation		3.1.5
Δh	Difference in elevation between two points	(3.15)	3.1.5
h_0	Height of rectangular region		3.1.5
Ha	Hausdorff measure	(3.14)	3.1.5
He	Extreme value exponent	(3.88)	3.6.1
Hu	Hurst Exponent	(3.81)	3.5.1
Hw	Wavelet variance analysis exponent	(3.95)	3.7.2
i	Square root of -1	(3.30)	3.2.1
k	Lag for a discrete time series	(3.4)	3.1.4
m	Running variable in frequency domain,	(3.34)	3.2.1
n	Running variable for discrete y_n		3.1.2
N	Length of a discrete series $1 \le n \le N$		3.1.2
	Number of subintervals in an interval T		3.1.6

Symbol	Description	Equation where Introduced	Section where Introduced
N_i	Number of objects with linear size r_i	(3.13)	3.1.5
N_b, N_{bi}	Number of boxes		3.1.6
$Q(t)$	Volumetric flow in a river	(3.77)	3.4.1
$\overline{Q}(T)$	Mean of volumetric flow over period T	(3.77)	3.5.1
r	Scaling factor		3.1.5
r_i	Characteristic linear dimension	(3.13)	3.1.5
$R(T)$, $R(\tau)$	Range over period T or τ; Rescaled-range	(3.79), (3.81)	3.5.1
R_N, R_τ	Range over N or τ values; Rescaled-range	(3.83), (3.85)	3.5.1
r_0	Width of rectangular region		3.1.5
$r(s)$	Autocorrelation function for $y(t)$ at lag s	(3.1)	3.1.4
r_k	Autocorrelation function for y_n at lag k	(3.4)	3.1.4
$S(f)$	Power-spectral density of $y(t)$	(3.38)	3.2.2
S_m	Power-spectral density of y_n	(3.40)	3.2.2
$S(T)$, $S(\tau)$	Standard deviation over T or τ; Recaled-range	(3.80), (3.81)	3.5.1
S_N, S_τ	Standard deviation over N or τ; Rescaled-range	(3.84), (3.85)	3.5.1
s	Lag for a continuous time series	(3.1)	3.1.4
t	Running variable for continuous $y(t)$		3.1.2
	Position parameter in wavelet analysis	(3.91)	3.7.1
t_n	Discrete values of t, $t_n = n\delta$		3.1.2
	Discrete values, $t_n = n/N$, $n = 1, 2, \ldots, N$		3.3
T	Length of continuous series, $0 \le t \le T$		3.1.2
	Period of continuous function $g(t)$		3.2.1
V	Variance of $y(t)$ over the interval T	(3.3)	3.1.4
	Variance of y_n over N values	(3.6)	3.1.4
V_ε	Variance of ε_n over N values		3.1.6
$V(T)$	Variance over the interval T		3.3.3
V_n	Variance of y_n over the first n values	(3.18)	3.1.6
V_N	Variance of y_n over N values	(3.52)	3.2.2
$V(t)$	Volume of water in reservoir, function of t	(3.78)	3.5.1
V_{max}, V_{min}	Max and min volumes of water during T	(3.79)	3.5.1
V_w	Variance of wavelet transform $W(t, a)$	~~(6.5)~~ (3	3.7.2
wn	White Noise	(3.17)	3.1.6
w_n	Window used in power-spectral analysis	(3.67)	3.2.5
W_{ss}	Window squared and summed	(3.71)	3.2.5

Symbol	*Description*	*Equation where Introduced*	*Section where Introduced*
$W(t, a)$	Wavelet transform	(3.91)	3.7.1
$x(t)$	Log-normal distribution of values	(3.73)	3.4.1
$\bar{x}$	Average of $x(t)$, log-normal distribution	(3.74)	3.4.1
$y(t)$	Set of values in a continuous time series		3.1.2
	Gaussian (normal) set of values	(3.73)	3.4.1
y_n	Set of values in discrete time series, $n = 1, 2, 3, \ldots, N$		3.1.2
$\bar{y}$	Average of $y(t)$ over the interval T	(3.2)	3.1.4
	Average of y_n over N values, $n = 0, 1, 2, \ldots, N$	(3.5)	3.1.4
$\bar{y}_N$	Average of y_n over N values, $n = 0, 1, 2, \ldots, N$	(3.82)	3.5.1
y_e	Maximum value of y_n during an interval τ	(3.88)	3.6.1
$Y(f, T)$	Fourier transform of $y(t)$ over $0 \leq t \leq T$	(3.32)	3.2.1
Y_m	Discrete Fourier coefficients of y_n, $m = 1, 2, \ldots, N$	(3.34)	3.2.1
$\lvert Y_m \rvert$	Complex modulus of Y_m	(3.36)	3.2.1
β	Power-spectral density exponent	(3.39)	3.2.2
β_{PS}	Exponent obtained by power-spectral analysis		3.2.2
δ	Time between successive n in discrete time series		3.1.2
ε_n	Gaussian distribution of values that are uncorrelated	(3.17)	3.1.6
$\gamma(s)$	Semivariogram of $y(t)$ at lag s	(3.7)	3.1.4
γ_k	Semivariogram of y_n at lag k	(3.8)	3.1.4
$\sigma(T)$, σ_T	Standard deviation of $y(t)$ over interval T		3.1.6
$\sigma(\tau)$, σ_τ	Standard deviation of $y(t)$ over subinterval τ		3.1.6
σ_ε	Standard deviation of ε_n over N values		3.1.6
σ_n	Standard deviation of y_n over first n values in series	(3.19)	3.1.6
σ_y	Standard deviation of the Gaussian distribution $y(t)$	(3.75)	3.4.1
σ_x	Standard deviation of the log-normal distribution $x(t)$	(3.74)	3.4.1
τ, τ_i	Subintervals of a length T or N		3.1.6
ω	Angular frequency		3.2.1
$\propto$	Proportional		
∞	Infinity		
Σ	Summation		

REFERENCES

AHNERT, F. (1984). Local relief and the height limits of mountain ranges. *Am. J. Sci.,* **84**:1035-55.

BARABÁSI, A.-L., AND STANLEY, H.E. (1995). *Fractal concepts in surface growth.* Cambridge Univ. Press (Cambridge), 366 p.

BASSINGTHWAIGHTE, J.B., LIEBOVITCH, L.S., AND WEST, B.J. (1994). *Fractal physiology.* Oxford University Press (New York), 364 p.

BASSINGTHWAIGHTE, J.B., AND RAYMOND, G.M. (1994). Evaluating rescaled range analysis for time series. *Ann. Biomed. Eng.*, **22**:432-4.

BASSINGTHWAIGHTE, J.B., AND RAYMOND, G.M. (1995). Evaluation of the dispersional analysis method for fractal time series. *Ann. Biomed. Eng.*, **23**:491-505.

BERAN, J. (1992). Statistical methods for data with long-range dependence. *Statistical Science*, **7**:404-27.

BERAN, J. (1994). *Statistics for long-memory processes.* Monographs on Statistics and Probability 61. Chapman & Hall (New York), 315 p.

BOX, G.E.P., JENKINS, G.M., AND REINSEL, G.C. (1994). *Time series analysis: forecasting and control, 3rd edition.* Prentice Hall (Englewood Cliffs, NJ), 598 p.

BRAS, R.L., AND RODRIGUEZ-ITURBE, I. (1993). *Random functions and hydrology.* Dover (New York), 559 p.

CHATFIELD, C. (1996). *The analysis of time series, 5th edition.* Chapman and Hall (London), 283 p.

DAUBECHIES, I. (1988). Orthonormal bases of compactly supported wavelets. *Commun. Pure App. Math.*, **41**:909-96.

FEDER, J. (1988). *Fractals.* Plenum Press (New York), 283 p.

FLANDRIN, P. (1992). Wavelet analysis and synthesis of fractional Brownian motion. *IEEE Trans. on Information Theory*, **38**:910-17.

FLANDRIN, P. (1993). Fractional Brownian motion and wavelets. In M. Farge, J.C.R. Hunt, and J.C. Vassilicos (eds.), *Wavelets, fractals, and Fourier transforms*, Oxford University Press (Oxford), 109-23.

GALLANT, J.C., MOORE, I.D., HUTCHINSON, M.F., AND GESSLER, P. (1994). Estimating fractal dimension of profiles: A comparison of methods. *Math. Geol.*, **26**: 455-81.

GROSSMANN, A., AND MORLET, J. (1984). Decomposition of Hardy functions into square integrable wavelets of constant shape. *SIAM J. Math. Anal.*, **15**:723-36.

HALL, P. (1997). Defining and measuring long-range dependence. *Fields Institute Communications*, **11**:153-9.

HARVARD CENTROID-MOMENT TENSOR DATABASE (1997). Electronic data. Department of Earth and Planetary Sciences, Harvard University (Cambridge, Massachusetts).

HASTINGS, H.M., AND SUGIHARA, G. (1993). *Fractals: A user's guide for the natural sciences*. Oxford University Press (Oxford), 235 p.

HEWETT, T.A. (1986). Fractal distribution of reservoir heterogeneity and their influence on fluid transport. Society of Petroleum Engineers, *SPE*, **15,386**:1-16.

HUBBARD, B.B. (1996). *The world according to wavelets: The story of a mathematical technique in the making.* A. K. Peters (Wellesley, Massachusetts), 264 p.

HURST, H.E. (1951). Long-term storage capacity of reservoirs. *Transactions of the American Society of Civil Engineers*, **116**:770-808.

HURST, H.E., BLACK, R.P., AND SIMAIKA, Y.M. (1965). *Long-term storage*. Constable (London), 145 p.

JENKINS, G.M., AND WATTS, D.G. (1968). *Spectral analysis and its applications*. Holden-Day (San Francisco), 525 p.

JOURNEL, A.G., AND HUIJBREGTS, CH.J. (1978). *Mining geostatistics*. Academic Press (New York), 600 p.

KOLMOGOROV, A.N. (1940). Wienersche spiralen und einige andere interessante kurven in hlbertschen raum. *Compte rendus (Doklady) Académie des sciences de l'URSS (N.S.),* **26**:115-8.

KORVIN, G. (1992). *Fractal models in the earth sciences*. Elsevier (New York), 396 p.

LI, W.K., AND MCLEOD, A.I. (1986). Fractional time series modeling. *Biometrika*, **73**:217-21.

MANDELBROT, B.B. (1967). How long is the coast of Britain? Statistical self-similarity and fractional dimension. *Science*, **156**:636-8.

MANDELBROT, B.B. (1982). *The fractal geometry of nature*. Freeman (New York), 468 p.

MANDELBROT, B.B. (1985). Self-affine fractals and fractal dimension. *Phys. Scripta*, **32**:257-60.

MANDELBROT, B.B. (1986). Self-affine fractal sets, I: The basic fractal dimensions; II: Length and surface dimensions; III: Hausdorff dimension anomalies and their implications. In L. Pietronero and E. Tosatti (eds.), *Fractals in physics*, Elsevier (Amsterdam), 21-28.

MANDELBROT, B.B., AND VAN NESS, J.W. (1968). Fractional Brownian motions, fractional noises and applications. *SIAM Rev.*, **10**:422-37.

MANDELBROT, B.B., AND WALLIS, J.R. (1968). Noah, Joseph and operational hydrology. *Water Resour. Res.*, **4**:909-18.

MANDELBROT, B.B., AND WALLIS, J.R. (1969a). Computer experiments with fractional Gaussian noises. Parts I, II, and III. *Water Resour. Res.*, **5**:228-67.

MANDELBROT, B.B., AND WALLIS, J.R. (1969b). Some long-run properties of geophysical records. *Water Resour. Res.*, **5**:321-40.

MANDELBROT, B.B., AND WALLIS, J.R. (1969c). Robustness of the rescaled range R/S in the measurement of noncyclic long run statistical dependence. *Water Resour. Res.*, **5**:967-88.

MATHERON, G. (1962). *Traité de géostatistique appliquée, Tome I, Théorie générale*. Editions Technip. (Paris), 333p.

MATHERON, G. (1963). *Traité de géostatistique appliquée, Tome II, Le Krigéage.* Editions Technip. (Paris), 171 p.

MATHERON, G. (1963b). Principles of geostatistics. *Economic Geology*, **58**:1,246-66.

MCLEOD, A.I., AND HIPEL, K.W. (1995). *The McLeod-Hipel time-series data sets collection.* Electronic data available from the StatLib electronic database (Carnegie Mellon University Statistics Department). The datasets collection accompanies Hipel, K.W. and McLeod, A.I. (1994), *Time series modeling of water resources and environmental systems,* Elsevier (Amsterdam), 1,013 p.

MEAKIN, P. (1988). The growth of fractal aggregates and their measures. In C. Domb and J.L. Lebowitz (eds.), *Phase transitions and critical phenomena*, Academic Press (New York), **12**:335-489.

OLIVER, M., AND WEBSTER, R. (1986). Semi-variograms for modeling the spatial pattern of landform and soil properties. *Earth Surf. Proc. Landforms*, **11**:491-504.

OSBORNE, A.R., AND PROVENZALE, A. (1989). Finite correlation dimension for stochastic systems with power-law spectra. *Physica*, **D35**:357-81.

PELLETIER, J.D., AND TURCOTTE, D.L. (1998). Self-affine time series: II. Applications. Submitted to *Advances in Geophysics.*

PERCIVAL, D.B., AND WALDEN, A.T. (1993). *Spectral analysis for physical applications: Multitaper and conventional univariate techniques.* Cambridge Univ. Press (Cambridge), 581 p.

PRESS, W.H., TEUKOLSKY, S.A., VETTERLING, W.T., AND FLANNERY, B.P. (1994). *Numerical recipes in C: The art of scientific computing, 2nd edition.* Cambridge Univ. Press (Cambridge), 994 p.

PRIESTLEY, M.B. (1981). *Spectral analysis and time series.* Academic Press (London), 653 p.

SALAS, J.D. (1993). Analysis and modeling of hydrologic time series. In D. R. Maidment (ed.), *Handbook of hydrology*, McGraw-Hill (New York), 19.1-19.72.

SCHEPERS, H.E., VAN BEEK, J.H.G.M., AND BASSINGTHWAIGHTE, J.B. (1992). Four methods to estimate the fractal dimension from self-affine signals. *IEEE Eng. Medicine Biol.*, **11**:57-64, and 71.

SCHMITTBUHL, J., VILOTTE, J-P., AND ROUX, S. (1995). Reliability of self-affine measurements. *Phys. Rev.*, **E51**:131-47.

SLACK, J.R., AND LANDWEHR, J. M. (1992). *Hydro-climatic data network (HCDN): A U. S. Geological Survey streamflow data set for the United States for the study of climate variations, 1874-1988.* U. S. Geological Survey Open-File Report 92-129: U. S. Geological Survey, Reston, Virginia, 193 p. and CD ROM.

SMITH, W.W., AND SMITH, J.M. (1995). *Handbook of real-time fast Fourier transforms.* IEEE Press (New York), 468 p.

STEDINGER, J.R., VOGEL, R.M., AND FOUFOULA-GEORGIOU, E. (1993). Frequency analysis of extreme events. In D.R. Maidment (ed.), *Handbook of hydrology*, McGraw-Hill (New York), 18.1-18.66.

TAPIERO, C.S., AND VALLOIS, P. (1996). Run length statistics and the Hurst exponent in random and birth-death random motions. *Chaos, Solitons and Fractals*, **7**:1,333-41.

TURCOTTE, D.L. (1997). *Fractals and chaos in geology and geophysics, 2nd edition.* Cambridge Univ. Press (Cambridge), 300 p.

VOSS, R.F. (1985a). Random fractals: characterization and measurement. In R. Pynn and A. Skjeltorp (eds.), *Scaling phenomena in disordered systems*, Plenum Press (New York), 1-11.

VOSS, R.F. (1985b). Random fractal forgeries: From mountains to music. In S. Nash (ed.), *Science and uncertainty*, Science Reviews (London), 69-85.

VOSS, R.F. (1985c). Random fractal forgeries. In R. A. Earnshaw (ed.), *Fundamental algorithms for computer graphics*, NATO ASI Series, Springer-Verlag (Berlin), **F17**:805-35.

VOSS, R.F. (1986). Characterization and measurement of random fractals. *Phys. Scr.*, **T13**:27-32.

VOSS, R.F. (1988). Fractals in nature: From characterization to simulation. In H.-O. Peitgen and D. Saupe (eds.), *The Science of Fractal Images,* Springer-Verlag (New York), 22-70.

VOSS, R.F. (1989). Random fractals: Self affinity in noise, music, mountains, and clouds. *Physica*, **D38**:362-71.

WANG, M.C., AND UHLENBECK, G.E. (1945). On the theory of the Brownian motion, II. *Rev. Mod. Phys.*, **17**:323-42.

WORNELL, G.W. (1996). *Signal processing with fractals: A wavelet-based approach.* Prentice-Hall (New Jersey). 177 p.

Chapter Four: Self-Organized Criticality Applied to Natural Hazards*

ABSTRACT

The concept of self-organized criticality evolved from studies of three simple, cellular-automata models: the sand-pile, slider-block, and forest-fire models. In each case, there is a steady "input" and the "loss" is associated with a fractal (power-law) distribution of "avalanches." Each system fluctuates about a quasi-equilibrium state. Each of the three models can be associated with an important natural hazard; the sand-pile model with landslides, the slider-block model with earthquakes, and the forest-fire model with forest fires. Each of these natural hazards has frequency-magnitude distributions that are well approximated by power-law distributions. The model behavior suggests that the recurrence interval for a severe event can be estimated by extrapolating the observed frequency-magnitude distribution of small events. For example, the recurrence interval for a magnitude seven earthquake can be obtained directly from the observed frequency of occurrence of magnitude four earthquakes. A seismic intensity factor can, thus, be defined. Both global and regional maps of this factor are given. In addition, the behavior of the models suggests that the risk of occurrence of large events can be substantially reduced if small events are encouraged: *i.e.*, if small forest fires are allowed to burn, the risk of a large forest fire is substantially reduced.

---

*This chapter has been submitted to the *Journal of Natural Hazards* as Malamud, B. D. and Turcotte, D. L., Self-organized criticality applied to natural hazards.

INTRODUCTION

It is recognized that there are many circumstances under which complex natural phenomena display a well-defined and relatively simple statistical behavior. The relation between the size of the phenomena and its frequency of occurrence in some cases follows a Gaussian (normal) distribution, in other cases a power-law (fractal) distribution. Natural hazards such as earthquakes, forest fires, and landslides often follow a power-law frequency-area distribution.

It is accepted that earthquakes universally obey Guttenberg-Richter scaling: the number of earthquakes per year in a region, $\dot{N}_{CE}$, with magnitude greater than m, is related to m by (*Guttenberg and Richter*, 1954)

$$\log \dot{N}_{CE} = -b\,m + \log \dot{a} \tag{4.1}$$

where the constant b is known as the b-value and has a near universal value $b = 0.9$ (*Evernden*, 1970). The constant $\dot{a}$ is a measure of the intensity of the regional seismicity.

When (4.1) is expressed in terms of the earthquake rupture area, A_E, instead of earthquake magnitude, this relation becomes a power law (*Turcotte*, 1997)

$$\dot{N}_{CE} \sim A_E^{-b} \tag{4.2}$$

The definition of a fractal distribution is

$$N(r) \sim r^{-D} \tag{4.3}$$

where $N(r)$ is the number of objects with a linear dimension greater than r, and D is the fractal dimension. Since $A_E \sim r^2$, a comparison of (4.2) and (4.3) shows $D = 2b \approx 1.8$ for earthquakes.

Fractal frequency-size distributions can be explained in terms of scale-invariance. The power-law distribution is the only distribution that does not require a characteristic length scale. Thus, natural phenomena that do not inherently have a natural length scale would be expected to follow a power-law (fractal) distribution. However, there may be a more fundamental basis for the applicability of fractal frequency-size distributions. In the past ten years, numerous numerical models have been found to exhibit a universal behavior that has been called self-organized criticality. In self-organized criticality the "input" to a complex system is constant, whereas the "output" is a series of events or "avalanches" that follow a power-law (fractal) frequency-size distribution. For example, in the case of one model, the input is the steady addition of sand grains, and the output is sand avalanches. There is evidence that many natural phenomena, including earthquakes, forest fires, and landslides, may be examples of self-organized critical phenomena. In the next section, we introduce the concept of self-organized criticality in the context of three numerical models. In subsequent sections, we will discuss each of these models in the context of the associated natural hazard.

SELF-ORGANIZED CRITICALITY

Sandpile Model

The concept of self-organized criticality was introduced by *Bak et al.* (1987, 1988) as an explanation for the behavior of the "sandpile" model. In this model, a square array of boxes is considered and at each time step a particle is dropped into a randomly selected box. When a box accumulates four particles, the particles are redistributed to the four adjacent (nondiagonal) boxes or, in the case of edge boxes, lost from the grid. Because the redistribution involves only the nearest neighbor boxes, it is known as a cellular-automata model. Redistributions of particles can lead to further instabilities with, at each time step, the possibility of avalanches of particles being lost from the grid. Each of the multiple redistributions during a time step contributes to the size of the model "avalanche." The size of an avalanche can be quantified by the number of particles lost from the grid during the sequence of redistributions or by the number of boxes that participate in redistributions.

This model was called a "sandpile" model because of the resemblance to an actual sandpile on a table. The randomly dropped particles in the model are analogous to the addition of particles to the actual sandpile and the model avalanches are analogous to sand avalanches down the sides of the sandpile. In some cases the sand avalanches lead to the loss of particles off the table. Extensive numerical studies of the "sandpile" model were carried out by *Kadanoff et al.* (1989). They found the noncumulative frequency-size distribution of avalanches to have a power-law distribution with a slope near unity.

A rigorous definition of self-organized critical behavior is elusive. A working definition is that a system is in a state of self-organized criticality if a measure of the system fluctuates about a state of marginal stability. The input is steady, but the output is a series of "avalanches" that follows a fractal (power-law) distribution. For the sandpile "model" and sandpile on a table, the steady input is the addition of random particles at each time step and the fractal avalanches are the redistribution events for the model or the actual avalanches for the table sandpiles. The number of particles in the boxes or number of sand grains in the pile is a measure of the oscillating state of the system.

Slider-Block Model

A second example of "self-organized criticality" is the behavior of arrays of slider blocks. *Burridge and Knopoff* (1967) introduced the coupled slider-block model as an analog for earthquakes. The slider blocks are pulled over a surface by springs attached to a constant-velocity driver plate and are attached to each other by springs. The slider blocks have a frictional interaction with the surface. The simplest friction law is static-dynamic friction. If the block is "sticking" to the surface, *i.e.* the velocity over the surface is zero, then the static frictional force is F_s. If the block is moving over the surface, the dynamic friction force is F_d. If $F_s > F_d$, stick-slip behavior of the blocks will occur.

The steady input in this model is the constant velocity of the driver plate that extends the puller springs; this constitutes a steady input of energy. The "avalanches" are the slip events in which the slider blocks are pulled forward by the springs. *Carlson and Langer* (1989) considered

long linear arrays of slider blocks and found that the frequency-size distributions of slip events fell into two groups: smaller events obeyed a power-law (fractal) relationship with a slope near unity, but there was an anomalously large number of large events that included all the slider blocks. The observed behavior was characteristic of self-organized criticality.

The close association of the self-organized critical behavior of a slider-block array with the frequency-size distribution of earthquakes has led many authors to conclude that distributed seismicity is a natural example of self-organized behavior.

Forest-Fire Model

A third example of self-organized critical behavior is the forest-fire model (*Bak et al.*, 1992; *Drossel and Schwable*, 1992a; *Henley*, 1993; *Clar et al.*, 1996). In the forest-fire model, trees are randomly planted on a square grid of planting sites. At specified intervals, a match is randomly dropped on a grid site. If a tree has been planted on the grid site, that tree and all adjacent (nondiagonal) trees burn. The noncumulative frequency-area distribution of small fires is fractal with a slope near unity. Again, the observed behavior is characteristic of self-organized criticality.

In addition to actual landslides and earthquakes which are discussed with respect to the sandpile and slider-block models, we also examine the cumulative and noncumulative frequency-area distributions of actual forest fires and wildfires. We find fractal distributions from a variety of geographical settings with nearly equal fractal dimensions.

This is remarkable considering the many complications associated with actual forest fires including variations in the concentrations of combustible materials, weather and climate, and attempts to control and extinguish fires. The behavior appears to be relatively insensitive to details of the environment, *i.e.* it is robust. The robust fractal frequency-area distributions associated with the actual forest fires is a characteristic of self-organized critical behavior.

FOREST FIRES

Forest-Fire Model

Although the forest-fire model was not the first model associated with self-organized critical behavior, it is probably the simplest. The forest-fire model we consider consists of a square grid of sites. At each time step, a model tree is dropped on a randomly chosen site; if the site is unoccupied, the tree is planted. The sparking frequency, f_s, is the inverse number of attempted tree drops on the square grid before a model match is dropped on a randomly chosen site. If $f_s = 1/100$, there have been 99 attempts to plant trees (some successful, some unsuccessful) before a match is dropped at the 100th time step. If the match is dropped on an empty site nothing happens. If it is dropped on a tree, the tree ignites and a model fire consumes that tree and all adjacent (nondiagonal) trees.

Many variations on this basic forest-fire model have been proposed (*Bak et al.*, 1992; *Drossel and Schwable*, 1992a, 1992b, 1993a, 1993b, 1994; *Mosner et al.*, 1992; *Christensen et al.*, 1993; *Drossel et al.*, 1993, 1994; *Henley*, 1993; *Albano*, 1994, 1995; *Clar et al.*, 1994; *Johansen*, 1994; *Loreto et al.*, 1995, 1996; *Strocka et al.*, 1995; *Clar et al.*, 1996;

Honecker and Peschel, 1996). For instance, one alternative model requires a stochastic distribution of intervals between match drops. However, the general behavior of all models is similar. This is taken as evidence that self-organized critical behavior is insensitive to the details of the models; the rules of the cellular-automata models can vary but the results are robust.

In order to carry out simulations of the forest-fire model, it is necessary to specify the size of the square grid, N_g, and the sparking frequency, f_s. As a specific example, consider the 10 x 10 grid illustrated in Figure 4.1. Each grid site is identified by row and column as shown. The sparking frequency is $1/f_s = 5$; four trees are planted (or attempts to plant are made) before a match is dropped. Sites are randomly chosen. The beginning configuration has six trees, and is the result of running the simulation for some time so that a quasi-equilibrium state is established. In steps 1 thru 4, trees are dropped on the randomly chosen sites "54", "71", "85" and "19." In the first three steps, the sites are empty, so a tree is planted. In step 4, site "19" is already occupied, so nothing happens. In step 5, a match is dropped on site "99", but it is unoccupied so nothing happens. In steps 6 thru 9, four trees are planted on sites "17", "81", "43" and "68." Finally, in step 10, a match is dropped on site "54" which is occupied by a tree. This tree "burns" along with the adjacent trees on sites "44" and "43" and are eliminated from the grid. The tree in site "35" does not burn because, although adjacent, it is diagonal to the sites being consumed by the fire. This "forest fire" has a size $A_F = 3$, since three trees are burned.

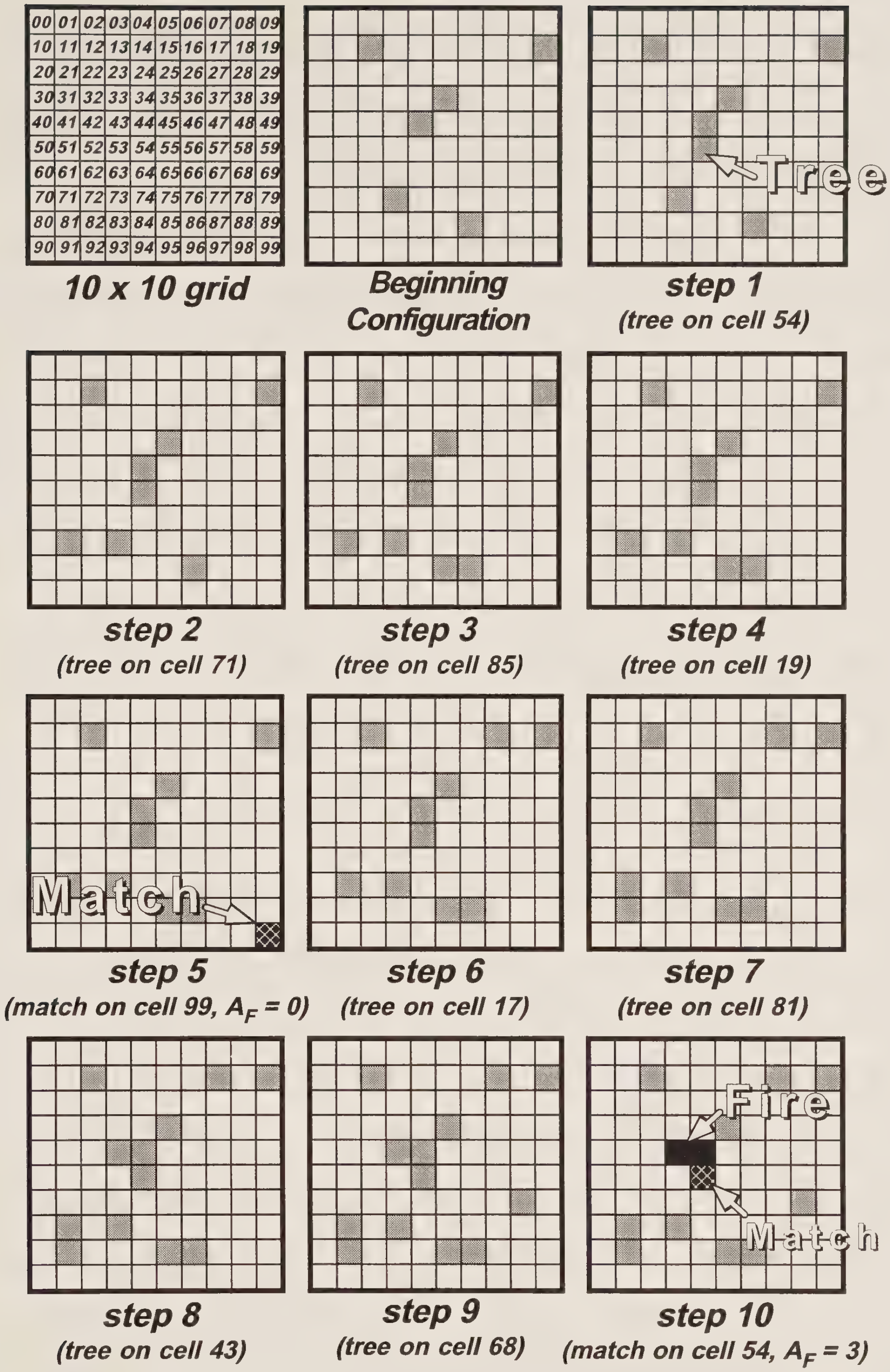

Figure 4.1. Illustration of the forest-fire model. A 10 x 10 grid is considered with sparking frequency $f_s = 1/5$. White boxes are unoccupied sites. Lightly shaded boxes are sites occupied by one tree. Match drops are indicated by a criss-cross pattern. Black boxes are the forest fires. Ten time steps are shown. The model "fire" at step 10 consumes three trees.

For large time intervals, the number of trees lost in “fires” is approximately equal to the number of trees planted. However, the number of trees on the grid will fluctuate. The frequency-size distribution of “fires” is a statistical measure of the behavior of the system. This model is probabilistic (stochastic) in that the sites are chosen randomly. It is a cellular-automata model in that only nearest neighbor trees are ignited by a “burning” tree. In terms of the definition of self-organized critical behavior, the steady-state input is the continuous planting of trees. The avalanches in which trees are lost are the “forest fires.” A measure of the state of the system is the fraction of sites occupied by trees. This “density” fluctuates about a “quasi-equilibrium” value.

Forest-Fire Model Results

Having specified the size of the square grid, N_g, and the sparking frequency, f_s, a simulation is run for N_S time steps and the number of fires N_F with area A_F is determined. The area, A_F, is the number of trees that burn in a fire. Our forest-fire model figures (Figures 4.2-4.5) are based on data from extensive computer simulations that have been run by Gleb Morein at Cornell University. Examples of four typical fires during a run are given in Figure 4.2. In these examples the grid size is 128 x 128 ($N_g = 16{,}384$), $1/f_s = 2000$, and fires with $A_F = 5, 51, 506$, and 5,327 trees are illustrated. Figure 4.2d is an example of a special class of forest fire which spans the grid.

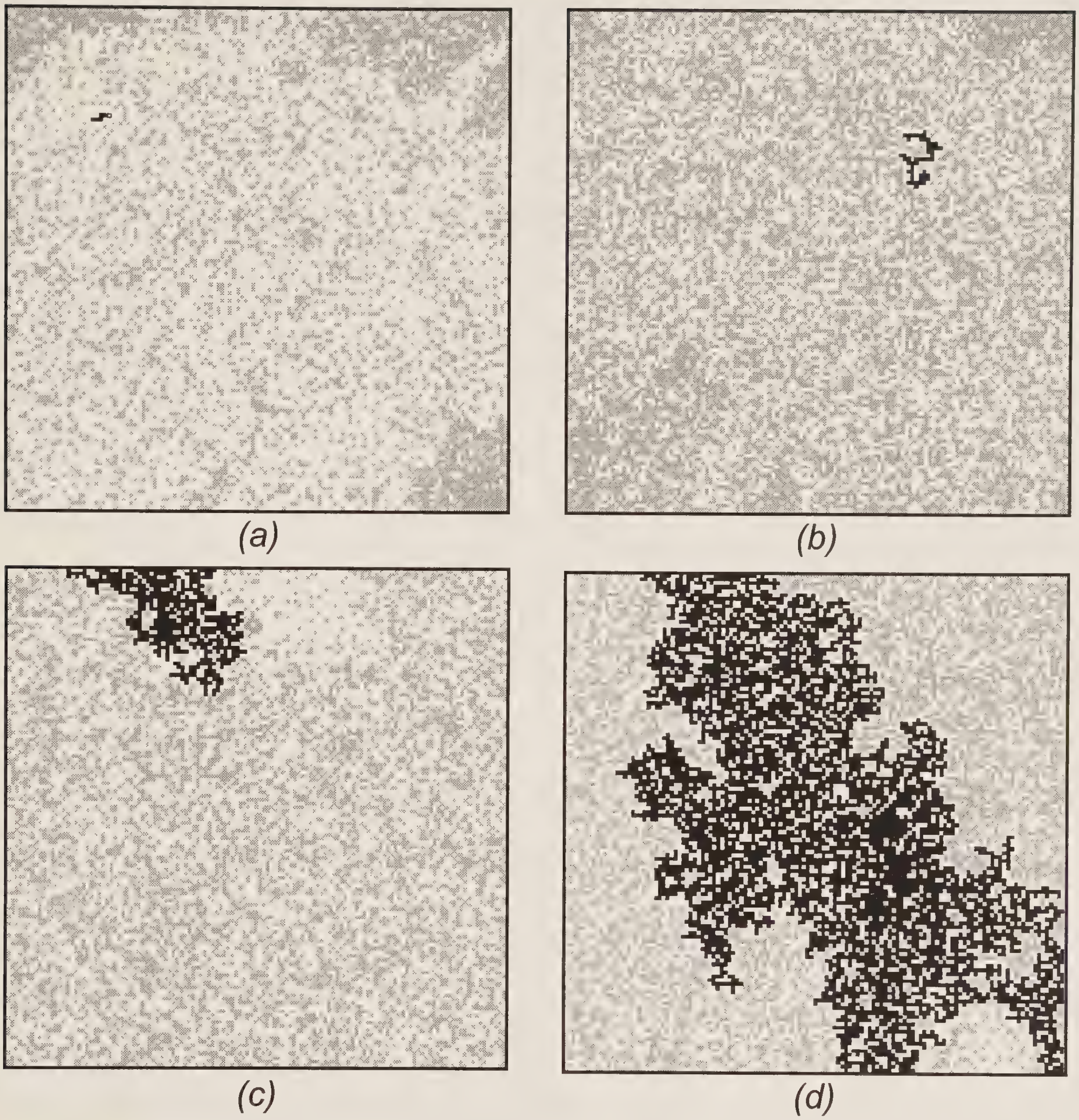

Figure 4.2. Four examples of typical model forest fires are given. This run was carried out on a 128 x 128 grid with $f_s = 1/2000$. The heavily shaded regions are the forest fires. The lightly shaded regions are unburned forest. The white regions are unoccupied sites. The areas A_F of the four forest fires are (a) 5 trees, (b) 51 trees, (c) 505 trees and (d) 5,327 trees. The largest forest fire is seen to span the entire grid.

The noncumulative frequency-size distributions for the model forest fires are given in Figures 4.3 and 4.4. The number of fires per time step with area A_F, N_F/N_S, is given as a function of A_F. In Figure 4.3, results are given for a grid size 128 x 128 and three sparking frequencies, $1/f_s = 125$, 500, and 2,000. In Figure 4.4, results are given for a sparking frequency $1/f_s = 500$ and three grid sizes, 64 x 64, 128 x 128, and 256 x 256. In all cases the smaller fires correlate well with the power-law (fractal) relation

$$\frac{N_F}{N_S} \sim A_F^{-\alpha} \tag{4.4}$$

with $\alpha \approx 1$. Since $A_F \sim r^2$, where r is the linear dimension, a comparison with (4.2) and (4.3) yields $\alpha = D/2 \approx 1$.

These results indicate clearly the finite-size effect of the grid. If f_s is large, the frequency-size distribution begins to deviate significantly from a straight-line, such that there is an upper termination to the power-law distribution. In Figure 4.3, the deviation begins for $1/f_s = 125$ and $N_g = 128 \text{ x } 128$ at $A_F \approx 1{,}000$. In Figure 4.4, the deviations begins for $N_g = 256 \text{ x } 256$ and $1/f_s = 500$ at $A_F \approx 4{,}000$. It is also seen that large forest fires become dominant when the sparking frequency is very small. This is easily explained on physical grounds. The transition is clearly illustrated in Figures 4.3 and 4.4. In Figure 4.3, with a large sparking frequency (for example $1/f_s = 125$), trees burn before large clusters can form. If the sparking frequency is very small (for example $1/f_s = 2{,}000$), clusters form that span the entire grid before ignition occurs.

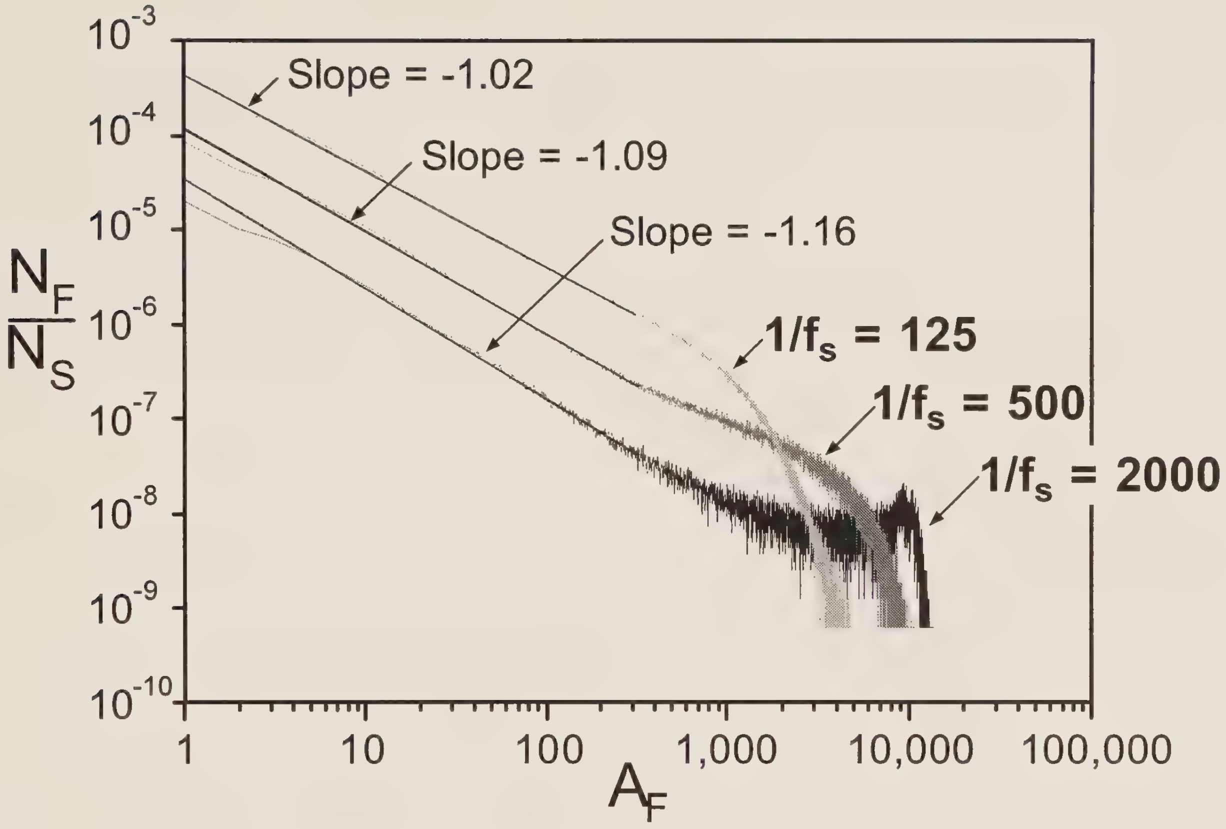

Figure 4.3. Frequency-size distributions of model forest fires, constant grid size and changing firing frequency. The number of fires per time step with size A_F, N_F/N_S, are given as a function of A_F where A_F is the number of trees burnt in each fire. Results are given for grid size 128 x 128 and three sparking frequencies, $f_s = 1/125$, 1/500, 1/2000. For each f_s the model is run for $N_S = 1.6384*10^9$ time steps. The small fires correlate well with the power-law relation (4.4) taking $\alpha = 1.02$ to 1.18. The finite grid size effect can be seen at the smallest firing frequency, $f_s = 1/2000$. At $A_F = 2{,}000$ fires begin to span the entire grid.

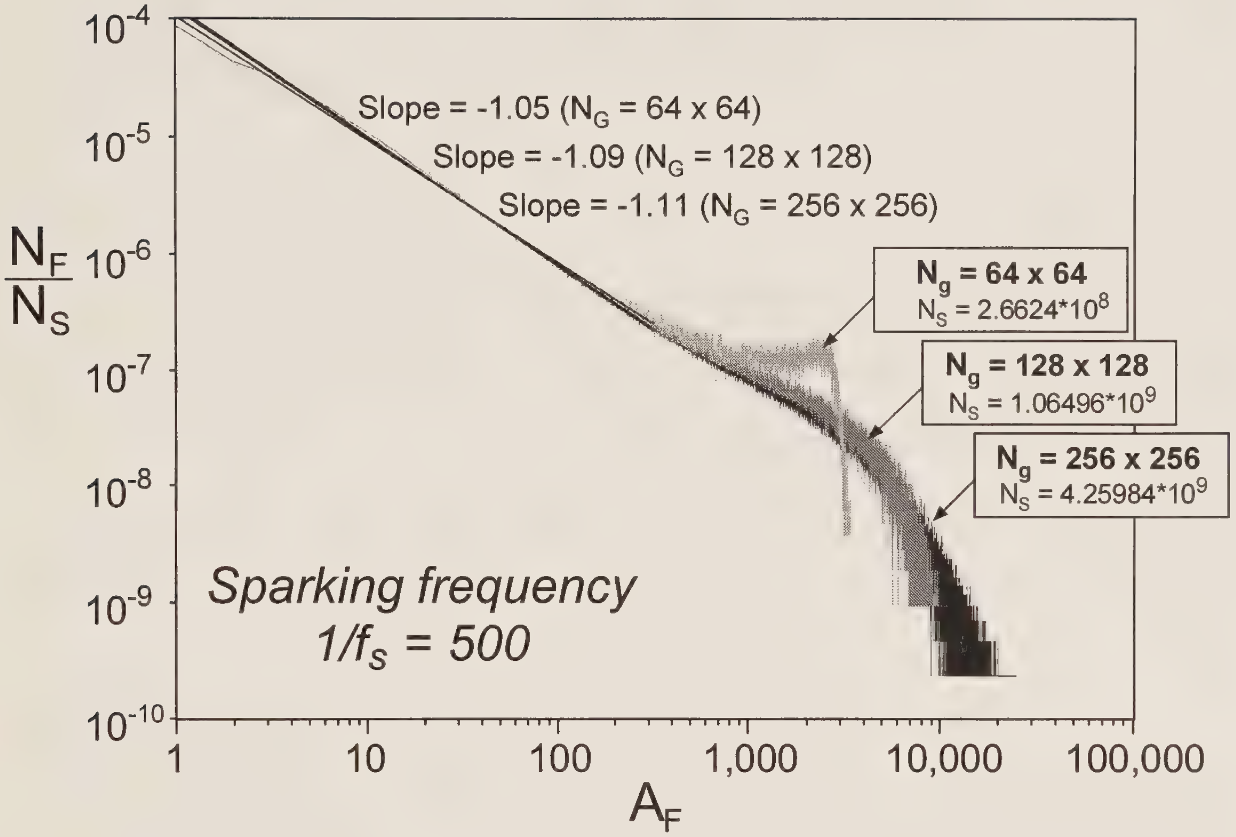

Figure 4.4. Frequency-size distributions of model forest fires, changing grid size and constant firing frequency. The number of fires per time step with size A_F, N_F/N_S, are given as a function of A_F where A_F is the number of trees burnt in each fire. Results are given for three grid sizes, 64 x 64, 128 x 128, 256 x 256 and constant sparking frequencies, $f_S = 1/500$. The number of time steps that the model was run for each grid size is noted.

In Figure 4.4, with a large grid (for example 256 x 256), trees burn before large clusters can form. However, for a small grid (for example, 64 x 64) clusters form that span the entire grid before ignition occurs. For very small firing frequencies or very small grid sizes, there will be very few fires that form with small values of area, A_F. The grid will become very full before a match sparks a fire. The areas of the fires will all involve a large number of trees, and in most cases the fires will span the grid. This transition can be termed the "Yellowstone" effect. It has been recognized that the best way to prevent very large forest fires in the Yellowstone National Park is to allow small fires to burn. Small fires prevent the accumulation of combustible material that fuels the spread of very large fires. Controlled burns that reduce the "density" of a forest also reduce the occurrence of large fires.

Site-Percolation Model

In order to provide a better understanding of "self-organized" criticality it is instructive to compare the behavior of the forest-fire model to the behavior of the site-percolation model. The latter is a classic example of critical point behavior. In its simplest form, the site-percolation model also consists of a square grid of sites. Each site is either permeable or impermeable. The probability that a site is permeable is p, the probability it is impermeable is $(1 - p)$. Based on this probability each site is specified to be either permeable or impermeable; if p is small most sites will be impermeable and if p is large most sites will be permeable. The grid itself is defined to be permeable if there is a continuous path of permeable sites from one side of the grid to the other.

This is analogous to a forest fire spanning the grid. An example of such a forest fire is given in Figure 4.2d. For the site-percolation problem there is a critical value of the probability, p_c, at which permeable paths are found. If $0 < p < p_c$, permeable paths crossing the grid are very seldom found. If $p_c < p < 1$, permeable paths are almost always found. For large two-dimensional square grids, numerical simulations always give $p_c = 0.59275$ (*Stauffer and Aharony*, 1992). It is of interest to compare this critical probability with the distribution of forest-fire sizes given in Figure 4.3. For the 128 x 128 grid ($N_g = 16{,}384$), the forest-fire size corresponding to the critical probability $p_c = 0.59275$ is $p_c N_g = A_F = 9712$. This value is very close to the Figure 4.3 peak in the $1/f_s = 2000$ large forest-fire sizes hump.

It is recognized that the site-percolation model is a critical-point problem. The percolation probability, p, is a tuning parameter and the critical point corresponds to the critical percolation probability, p_c. Many power-law scalings have been found to be valid in the vicinity of this critical point, *i.e.* $p - p_c << 1$. One of these power-law scalings is the frequency-size distribution of percolating clusters. The number of clusters N_a with size A_a scales with A_a according to

$$N_a \sim A_a^{-\tau} \qquad (4.5)$$

where τ is known as the Fisher exponent and takes a value $\tau = 187/91 \approx 2.0550$ for a variety of two-dimensional percolation models (*Stauffer and Aharony*, 1992). The wide applicability of the Fisher exponent is referred to as "universality."

We emphasize that (4.5) is valid for percolation clusters only in the immediate vicinity of the critical point. For small values of the probability p, the distribution of clusters is Poisonian and the frequency-size distribution of clusters is exponential. This is because the quantity $(pN_g)^{1/2}$, where pN_g is the number of occupied sites, introduces a characteristic length into the problem (*Stauffer and Aharony*, 1992).

The average distribution of unburned tree-cluster sizes in our forest-fire model can be obtained directly from our distribution of fire sizes. Consider that at each time step of our forest-fire model there exists on the square grid many clusters of trees, some of which have sizes A_{a1} or A_{a2}. Averaging the cluster sizes over all simulation time steps, the number of clusters with size A_{a1} is N_{a1} and the number of clusters with size A_{a2} is N_{a2}. A cluster of size A_{a1} will burn to give a fire of size $A_{F1} = A_{a1}$ and a cluster of size A_{a2} will burn to give a fire of size $A_{F2} = A_{a2}$. If we have one cluster of size A_{a1} and one of A_{a2}, then the ratio of the probabilities that a randomly dropped match will strike cluster A_{a1} versus A_{a2} is A_{a1}/A_{a2}. Thus N_{F1}, the number of fires of size A_{F1}, is related to N_{F2}, the number of fires of size A_{F2}, by

$$\frac{N_{F2}}{N_{F1}} = \frac{N_{a2}}{N_{a1}} \frac{A_{a2}}{A_{a1}} \tag{4.6}$$

Combining (4.4), (4.5), and (4.6) and the fact that $A_{F1} = A_{a1}$ and $A_{F2} = A_{a2}$ gives

$$\frac{N_{F2}}{N_{F1}} = \left(\frac{A_{F1}}{A_{F2}}\right)^{\frac{D}{2}} = \left(\frac{A_{a1}}{A_{a2}}\right)^{\frac{D}{2}} = \left(\frac{N_{a2}}{N_{a1}}\right)\left(\frac{A_{a2}}{A_{a1}}\right) = \left(\frac{A_{a1}}{A_{a2}}\right)^{\tau}\left(\frac{A_{a2}}{A_{a1}}\right) = \left(\frac{A_{a1}}{A_{a2}}\right)^{\tau-1} \tag{4.7}$$

and it follows that

$$\tfrac{1}{2}D = \tau - 1 \tag{4.8}$$

Taking the value of the Fisher exponent valid for two-dimensional percolation models, $\tau = 187/91$, we find from (4.8) that $\tfrac{1}{2}D = 1.055$. This is in good agreement with the values of $\tfrac{1}{2}D$ that we have obtained for our forest-fire model simulations, $\alpha = \tfrac{1}{2}D = 1.0 - 1.2$. However, we emphasize that power-law distributions in the forest-fire model are found for all values of the tuning parameter f_s, whereas for the site-percolation model, power-law distributions are found only in the vicinity of the critical point.

We argue that our forest-fire model exhibits self-organized critical behavior as well as critical behavior. The self-organized critical behavior occurs for firing frequencies larger than the critical value. It is characterized by a power-law distribution of forest fires with an upper cutoff. This also implies a power-law distribution of cluster sizes with an upper cutoff. For the forest-fire model, we find an applicable Fisher exponent for all values of the tuning parameter below the critical point. The values of the Fisher exponent are very close to the value of the Fisher exponent for the site-percolation problem, but for the percolation problem, the power law is valid only in the immediate vicinity of the critical point. The forest fires in the forest-fire model convert the exponential distribution of cluster sizes found in the percolation model to a power-law distribution.

Cumulative vs. Noncumulative Data

We now turn our attention to the frequency-size statistical distribution of actual forest fires and wildfires. When considering actual data, results are generally presented using cumulative distributions; for instance, the cumulative number of forest fires, N_{CF}, with areas greater than A_F, are plotted as a function of A_F. However, the frequency-size distributions for the model fires given in Figures 4.2 and 4.3 are noncumulative, *i.e.*, the data are given in terms of unit steps of area (number of trees). We are interested in comparing the (noncumulative) model forest-fire results with real forest fires. The data for real forest fires is not given in steps of unit area. Thus, these data are either presented as a cumulative plot or they must be appropriately boxed.

One approach is to convert the noncumulative model data to a cumulative distribution by summing over fires larger than a specified size. This is done in Figure 4.5, where curve 1, the noncumulative number of fires per time step with size A_F, is given as a function of A_F. These data are from Figure 4.3, the forest-fire model with grid size 128 x 128 ($N_g = 16{,}384$) and $f_s = 1/2000$. In curve 2 of Figure 4.5, these data are summed to give N_{CF}, the cumulative numbers of fires larger than A_F, and then normalized by N_S to give N_{CF}/N_S, the cumulative numbers of fires per time step larger than A_F. It is seen that the cumulative frequency-area distribution, N_{CF}/N_S, plotted as a function of A_F, does not yield a power-law. This is expected; since the slope of the noncumulative power law is near unity, its integrand or sum will be logarithmic. Many models that exhibit self-organized criticality have slopes near unity when using a noncumulative frequency-size distribution.

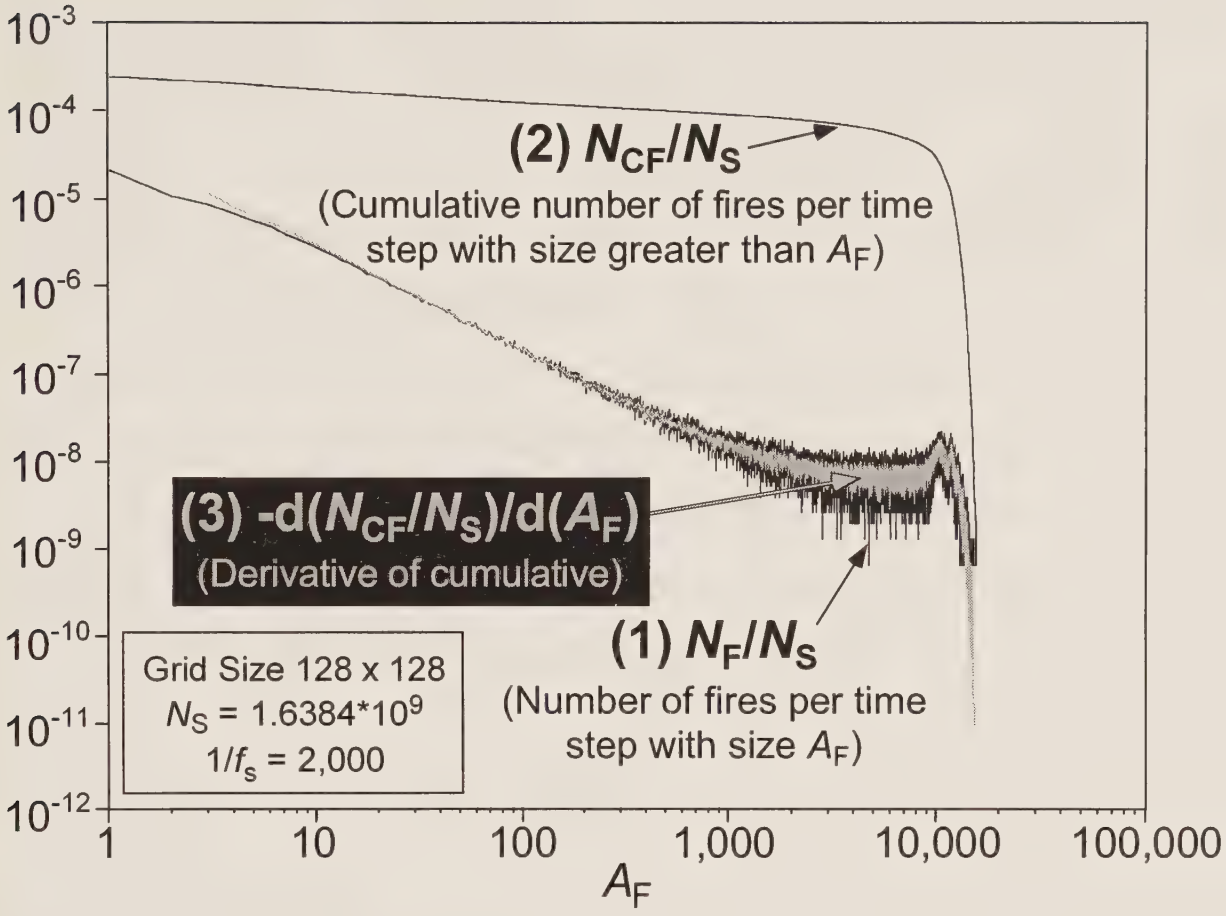

Figure 4.5. Illustration of cumulative and noncumulative frequency-size distributions. The noncumulative frequency-size distributions for the model-forest fires with grid size N_g = 128 x 128 and f_s = 1/2000 from Figure 4.3 are given as curve 1. These data are then summed (from largest to smallest) to give the cumulative number of fires larger than A_F per time, N_{CF}/N_S, given as curve 2. We have then applied the derivative technique to obtain $-d(N_{CF}/N_S)/d(A_F)$, shown as curve 3. Curve 3 is shown to be equivalent to curve 1.

Therefore, instead of converting the model forest fires to a cumulative distribution, we wish to present the frequency-size data for actual forest fires in a noncumulative form. This could be done by "binning" the data. However, there are ambiguities, including bin size and whether the size is measure in linear or logarithmic coordinates.

In order to illustrate the differences between cumulative and noncumulative distributions we examine a Cantor Set. The Cantor Set is a classic example of a discrete fractal set (*Turcotte*, 1997) and is composed of a succession of line segments of varying lengths r. As one example of a Cantor Set, the sequences of discrete numbers N_i with lengths r_i are: $N_i = 1, 2, 4, 8, \ldots$ and $r_i = 1, 1/3, 1/9, 1/27, \ldots$. For instance, there are four segments with length 1/9. The corresponding fractal dimension is $D = \log(N_i/N_{i-1})/\log(r_{i-1}/r_i) = \log(2)/\log(3) = 0.6309$. The corresponding cumulative numbers, N_{ci}, are: 1, 3, 7, 15, … for $r_i = 1, 1/3, 1/9, 1/27, \ldots$. For instance, there are seven segments with length 1/9 or greater. The corresponding fractal dimension, D_c, asymptotically approaches the noncumulative fractal dimension, D, for large N_{ci}. This is because the values to be summed are spaced logarithmically, $\log r_i = -i \log 3$.

Noncumulative distributions can be obtained by "binning" actual frequency-magnitude data; however, care must be taken in how the binning is carried out. If binning uses a linear set of bins, i.e. $r = 1\text{-}2, 2\text{-}3, 3\text{-}4, \ldots$, and the data have a power-law dependence $N_b \sim r^{-\alpha}$, then the resulting cumulative distribution will have a slope $N_c \sim r^{-(\alpha-1)}$. However, if the binning uses logarithmically spaced bins, *i.e.*, $r = 1\text{-}2, 2\text{-}4, 4\text{-}8$, etc. and the data have a power-law dependence, $N_b \sim r^{-\beta}$, then the resulting cumulative distribution will have approximately the same slope, *i.e.* $N_c \sim r^{-\beta}$.

To avoid the difficulties of binning data to obtain a noncumulative distribution, we use an alternative but equivalent approach. We start with cumulative data where N_{CF} is the number of forest fires with area greater than A_F. We define a noncumulative distribution in terms of the negative of the derivative (*i.e.*, the slope) of the cumulative distribution with respect to the area A_F. The value is negative, as the cumulative distribution is summed from the largest to the smallest values. The derivative is obtained by calculating the mean slope from a specified number of adjacent cumulative data points. Generally, we obtain excellent results deriving the slopes, $d(N_{CF}/N_S)/d(A_F)$, of the cumulative data using five adjacent points and a least-squares fit in linear space. The negative of each slope, $-d(N_{CF}/N_S)/d(A_F)$, is plotted as a function of the average of the five adjacent $\log(A_F)$ points.

The slopes, $d(N_{CF}/N_S)/d(A_F)$, of the cumulative data given in Figure 4.5 were obtained using five adjacent points and a least-squares fit in log-log space. The results, curve 3 in Figure 4.5, are in excellent agreement with the original noncumulative data. The results obtained by the derivative technique are equivalent to results obtained by “binning” data in linear increments, *i.e.*, 1-2, 2-3, 3-4, etc. The units of $-d(N_{CF}/N_S)/d(A_F)$ are “per area”, as they have been “normalized” to unit area. With the exception discussed above (unit slope for the noncumulative data), if cumulative data satisfy the power-law relation (4.4) with exponent α, then the noncumulative data will satisfy the same relation with exponent $\alpha - 1$. As discussed, different results are obtained if data are binned in logarithmic increments, *i.e.*, 1-2, 2-4, 4-8, etc. Both the cumulative and noncumulative data will satisfy (4.4) with the same exponent.

A final consideration is the need to find the best-fit line of a series of points appearing to follow a straight line in the log-log domain. When plotting real data on log-log axes, often both the cumulative and noncumulative frequency-size plots of the data will appear unevenly distributed; there are many more points toward the smaller x-axis values than the larger ones. For the forest-fire data, so as not to unequally "weight" the best-fit line with the more numerous smaller values, we bin the data before making the least-squares fit. This is accomplished by averaging the y-axis numbers that occur in each equally-spaced x-axis log bin. We then fit the best least-squares line to the binned data.

Actual Forest Fires

Four forest-fire and wildfire data sets from the United States and Australia are given in Figure 4.6. In each case, the cumulative number of fires per year, $\dot{N}_{CF}$, with area greater than A_F, is given as a function of A_F. A dot over the N indicates that the frequency data have been divided by the length of the record to give a frequency "per year." The first data set includes 4,284 fires on U. S. Fish and Wildlife Lands during 1986-1995 (*National Interagency Fire Center*, 1996). The second data set includes 120 forest fire areas as interpreted from tree rings for the Western United States, 1150-1960 (*Heyerdahl and Agee*, 1994). The third data set includes 164 fires in the Alaskan Boreal Forests during 1990-91 (*Kasischke and French*, 1995). The fourth data set includes 298 fires in the Australian Capital Territory during 1926-1991 (*Australian Capital Territory Bush Fire Council*, 1996). The four data sets come from a variety of regions with different vegetation types and climates.

Figure 4.6. Cumulative frequency-area distributions for actual forest fires and wildfires in the United States and Australia. Four examples are given: (a) 4,284 fires on U.S. Fish and Wildlife Service Lands during 1986-1995 (*National Interagency Fire Center*, 1996). (b) 120 of the largest fire areas in the western United States during 1155-1960, calculated from tree ring data (*Heyerdahl and Agee*, 1994). (c) 164 fires in Alaskan Boreal Forests during 1990-1991 (*Kasischke and French*, 1995). (d) 298 fires in the Australian Capital Territory during 1926-1991 (*Australian Capital Territory Bush Fire Council*, 1996). The cumulative number of fires per year, $\dot{N}_{CF}$, with area greater than A_F, is given as a function of A_F. In each case a reasonably good correlation is obtained with the power-law relation (4.4) taking $\alpha = 0.5\text{-}0.7$.

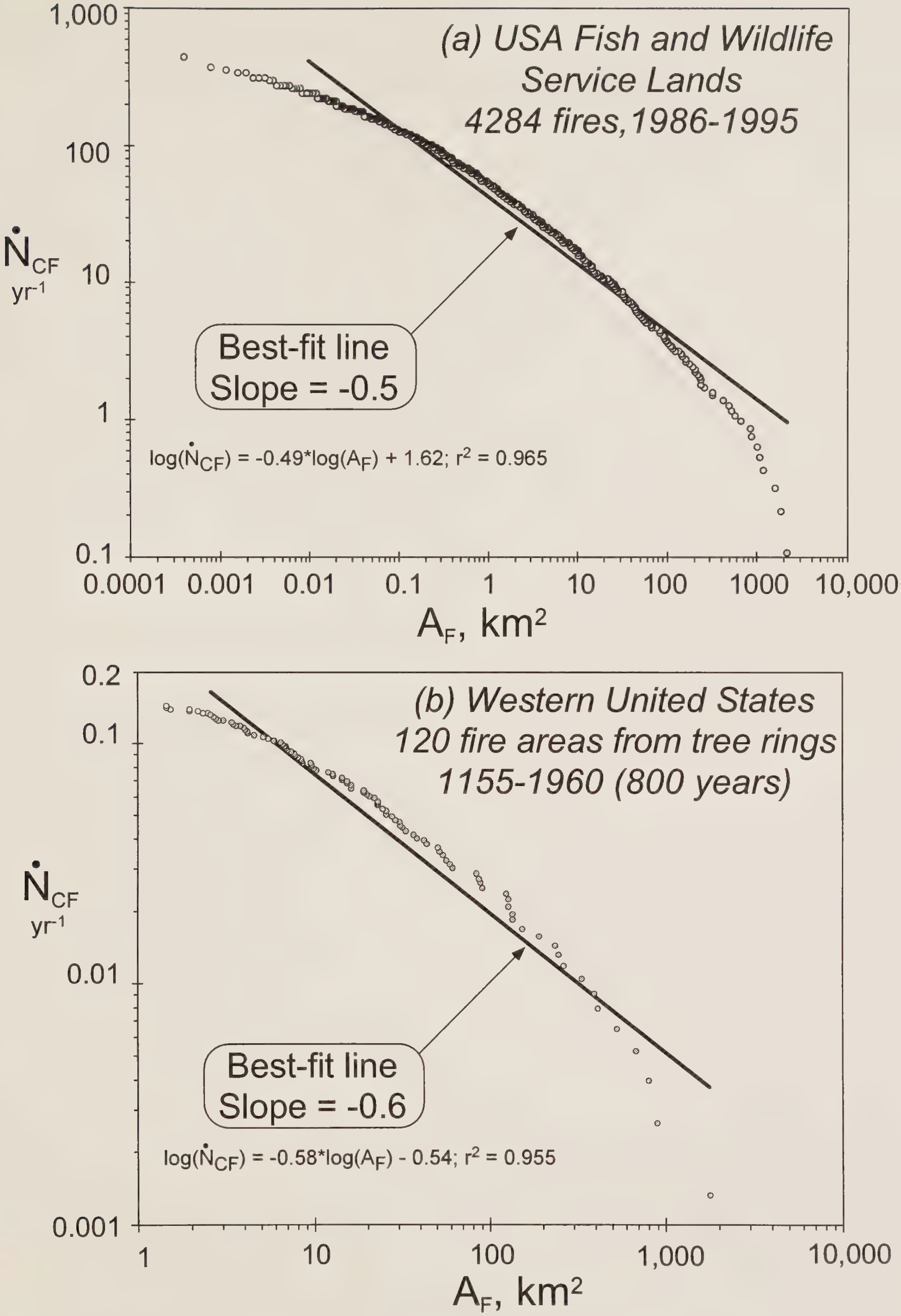
(a) USA Fish and Wildlife Service Lands
4284 fires,1986-1995
Best-fit line
Slope = -0.5
log(Ṅ_CF) = -0.49*log(A_F) + 1.62; r² = 0.965
Ṅ_CF yr⁻¹
1,000
100
10
1
0.1
0.0001
0.001
0.01
0.1
1
10
100
1000
10,000
A_F, km²
(b) Western United States
120 fire areas from tree rings
1155-1960 (800 years)
Best-fit line
Slope = -0.6
log(Ṅ_CF) = -0.58*log(A_F) - 0.54; r² = 0.955
Ṅ_CF yr⁻¹
0.2
0.1
0.01
0.001
1
10
100
1,000
10,000
A_F, km²

Figure 4.6 (Continued)

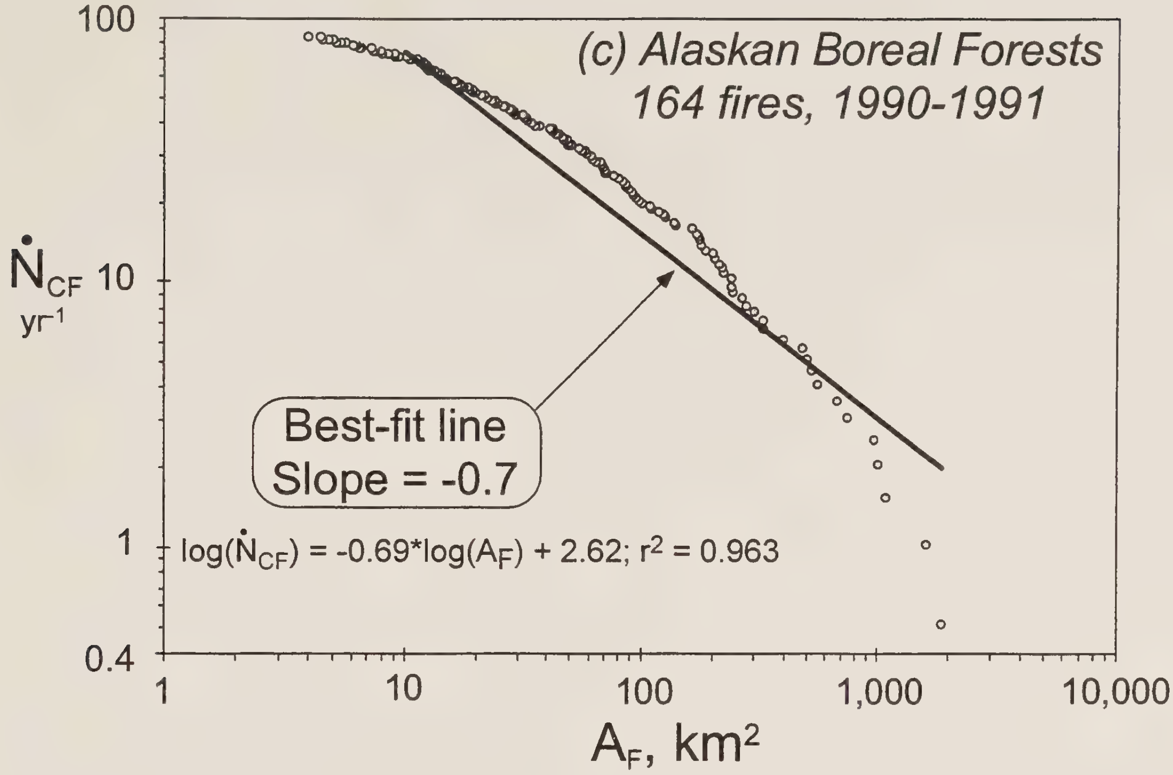

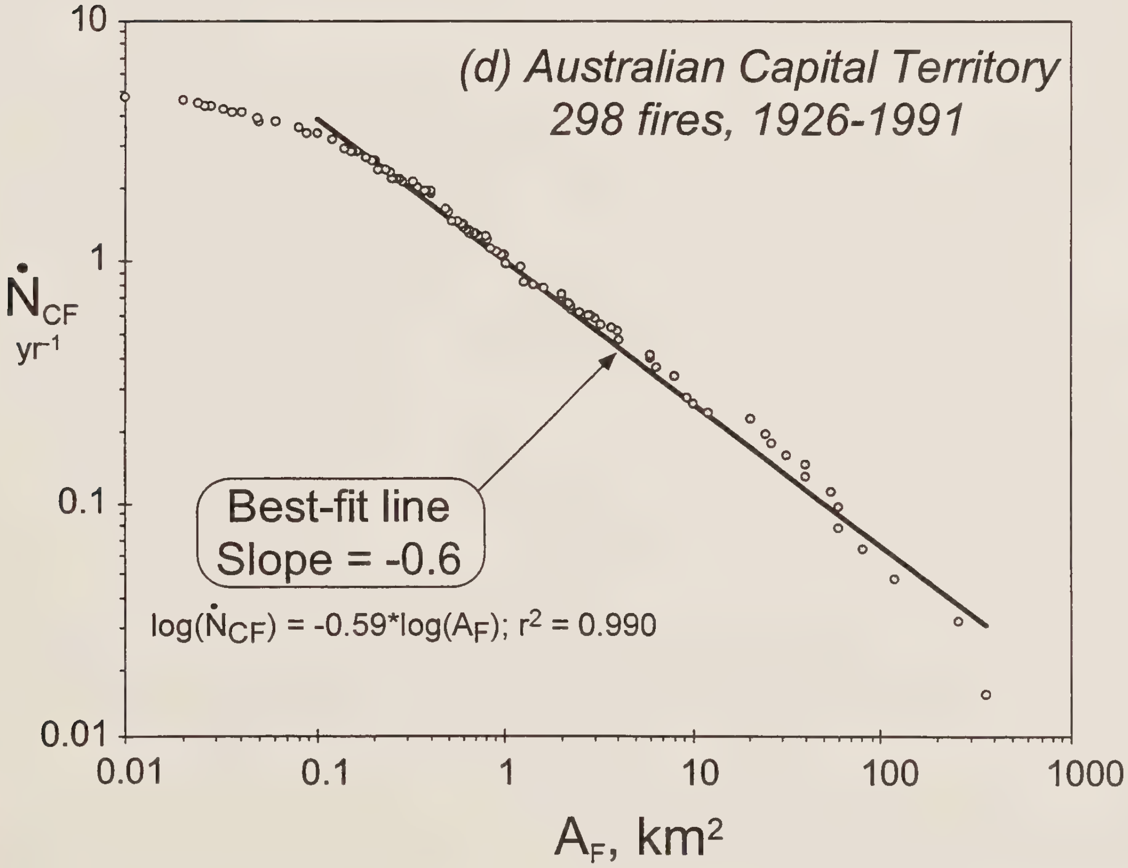

The cumulative data do not correlate well with the power-law relation (4.4). This would be expected if the equivalent noncumulative data had a slope near unity as illustrated in Figure 4.5. In order to test this, and to make a direct comparison with the forest-fire model results, we converted each of the cumulative distributions given in Figure 4.6 to noncumulative distributions using the derivative technique described in the previous section. The results are given in Figure 4.7 and are in quite good agreement with the power-law relation (4.4) with $\alpha = 1.3$-1.5. Theoretically, a noncumulative power-law distribution with a slope of 1.3-1.5 should have a cumulative power-law distribution of 0.3-0.5. However, because the noncumulative slopes are approaching 1, the cumulative distribution approaches a logarithm (Figure 4.6).

The actual forest fires (Figure 4.7) have good power-law (fractal) distributions, consistent with the model data (Figures 4.3, 4.4). However, the model data have fractal dimensions that are somewhat less than those calculated for the actual data. The model is in reasonable, but not exact, agreement with the actual data. Considering the many complexities of the initiation and propagation of forest fires and wildfires it is remarkable that the frequency-magnitude distributions are so similar under such a variety of environments. The proximity of combustible material varies widely. The behavior of a particular fire depends strongly on meteorological conditions. Fire-fighting efforts extinguish many fires. Despite these complexities, the application of the statistics associated with the forest-fire model appears to be robust. We conclude that naturally occurring forest fires are examples of self-organized critical behavior.

Figure 4.7. Noncumulative frequency-area distributions for actual forest fires and wildfires in the United States and Australia. The four different regions, (a) through (d), are the same as in Figure 4.6. The noncumulative number of fires, $-d\dot{N}_{CF}/dA_F$, with area A_F, is given as a function of A_F. In each case a reasonably good correlation is obtained with the power-law relation (4.4) taking $\alpha = 1.3\text{-}1.5$.

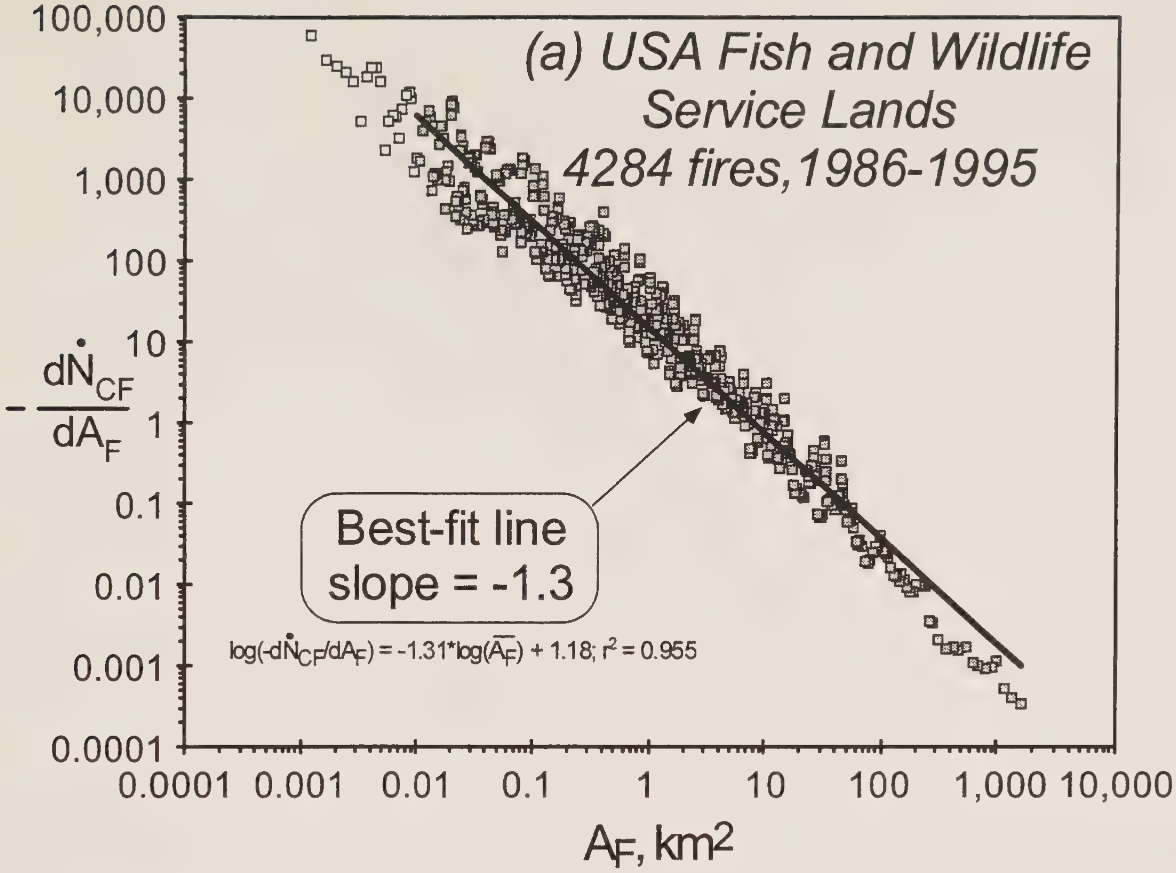
(a) USA Fish and Wildlife Service Lands
4284 fires, 1986-1995
Best-fit line
slope = -1.3
log(-dṄCF/dAF) = -1.31*log(AF) + 1.18; r2 = 0.955
100,000
10,000
1,000
100
10
1
0.1
0.01
0.001
0.0001
- dṄCF / dAF
0.0001
0.001
0.01
0.1
1
10
100
1,000
10,000
AF, km2

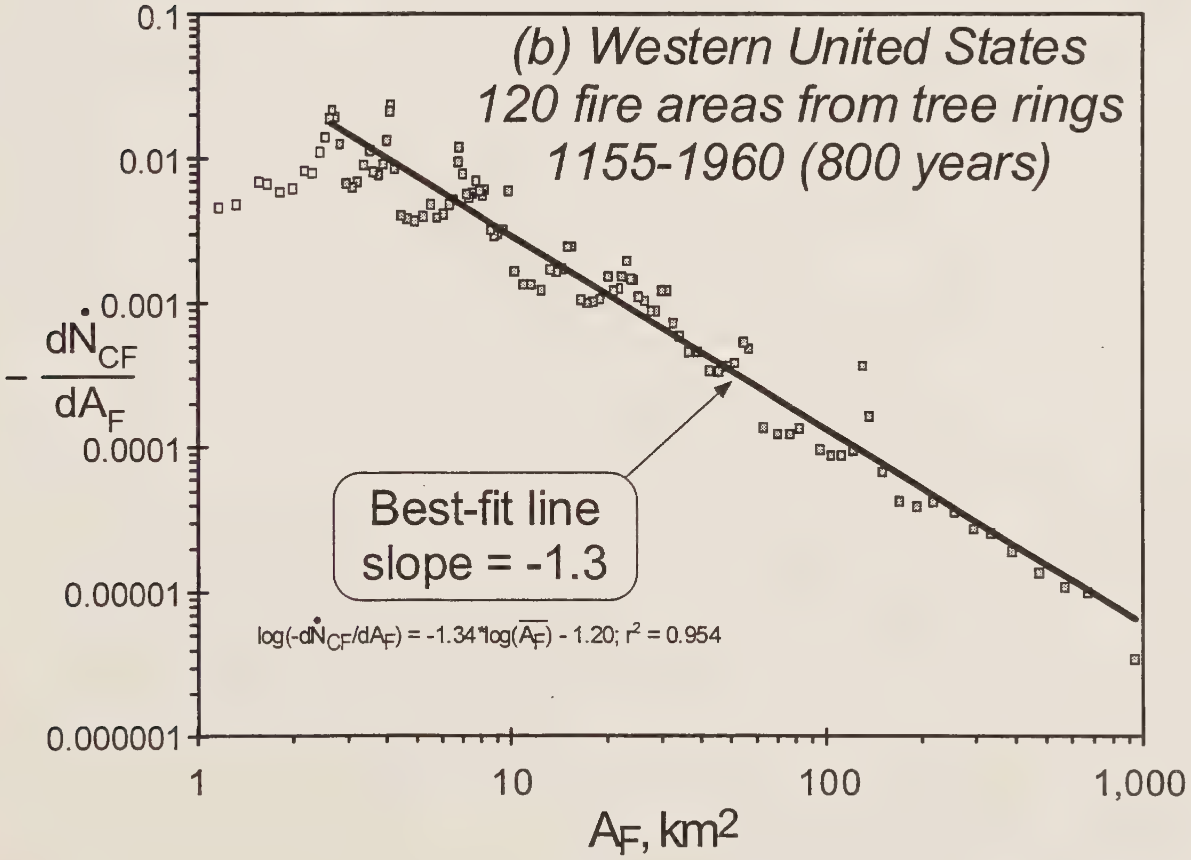
(b) Western United States
120 fire areas from tree rings
1155-1960 (800 years)
Best-fit line
slope = -1.3
log(-dṄCF/dAF) = -1.34*log(AF) - 1.20; r2 = 0.954
0.1
0.01
0.001
0.0001
0.00001
0.000001
- dṄCF / dAF
1
10
100
1,000
AF, km2

Figure 4.7 (Continued)

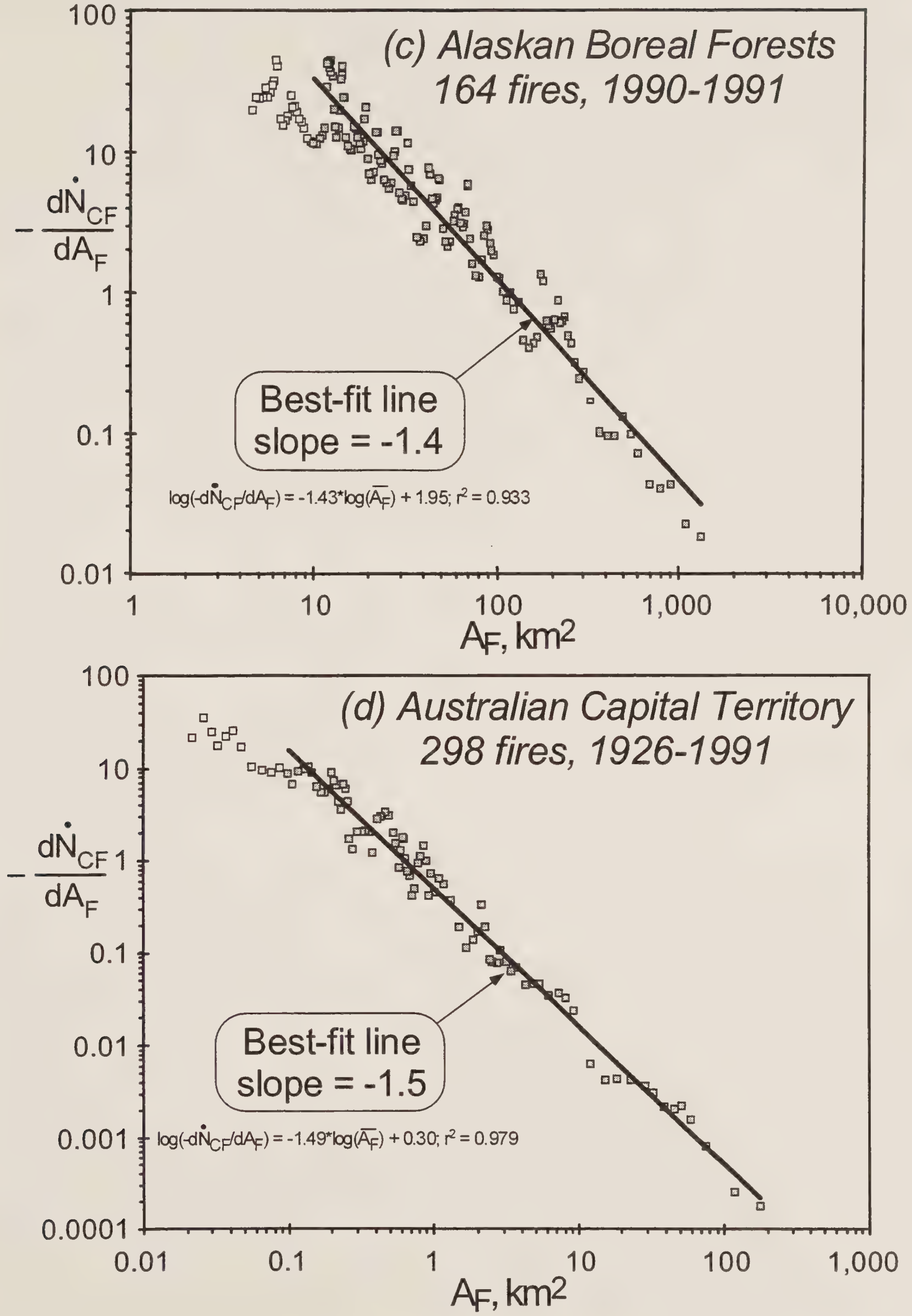

LANDSLIDES

Sandpile Model

The concept of self-organized criticality evolved from the "sandpile" model proposed by *Bak et al.* (1987, 1988). In their model, there is a square grid of boxes and at each time step, a particle is randomly dropped into a box. When a box accumulates four particles, they are redistributed to the four adjacent (nondiagonal) boxes or, in the case of edge boxes, lost from the grid. Again, this is a cellular-automata model. Redistributions can lead to further instabilities and avalanches of particles in which particles are lost from the edge of the grid. The input is the steady-state addition of particles. A measure of the state of the system is the average number of particles in a box. This "density" fluctuates about an equilibrium value. One measure of the size of a model "avalanche" is given by the number of boxes that participate in the redistributions. An alternative measure of the size of a model "avalanche" is the number of particles lost from the grid during each redistribution.

The sandpile model depends only on the size of the grid considered. As a specific example of the sandpile model we consider the 3 x 3 grid illustrated in Figure 4.8. As shown, each box is identified by a row and a column. The simulation has been run for some time so that a quasi-equilibrium beginning configuration has been established. In steps 1 thru 4, particles have been added randomly to cells "22", "00", "11", and "12" without requiring any redistributions. In step 5a, a particle is added to box "11", this box is now "unstable" and the four particles are redistributed to the adjacent boxes "01", "10", "12" and "21."

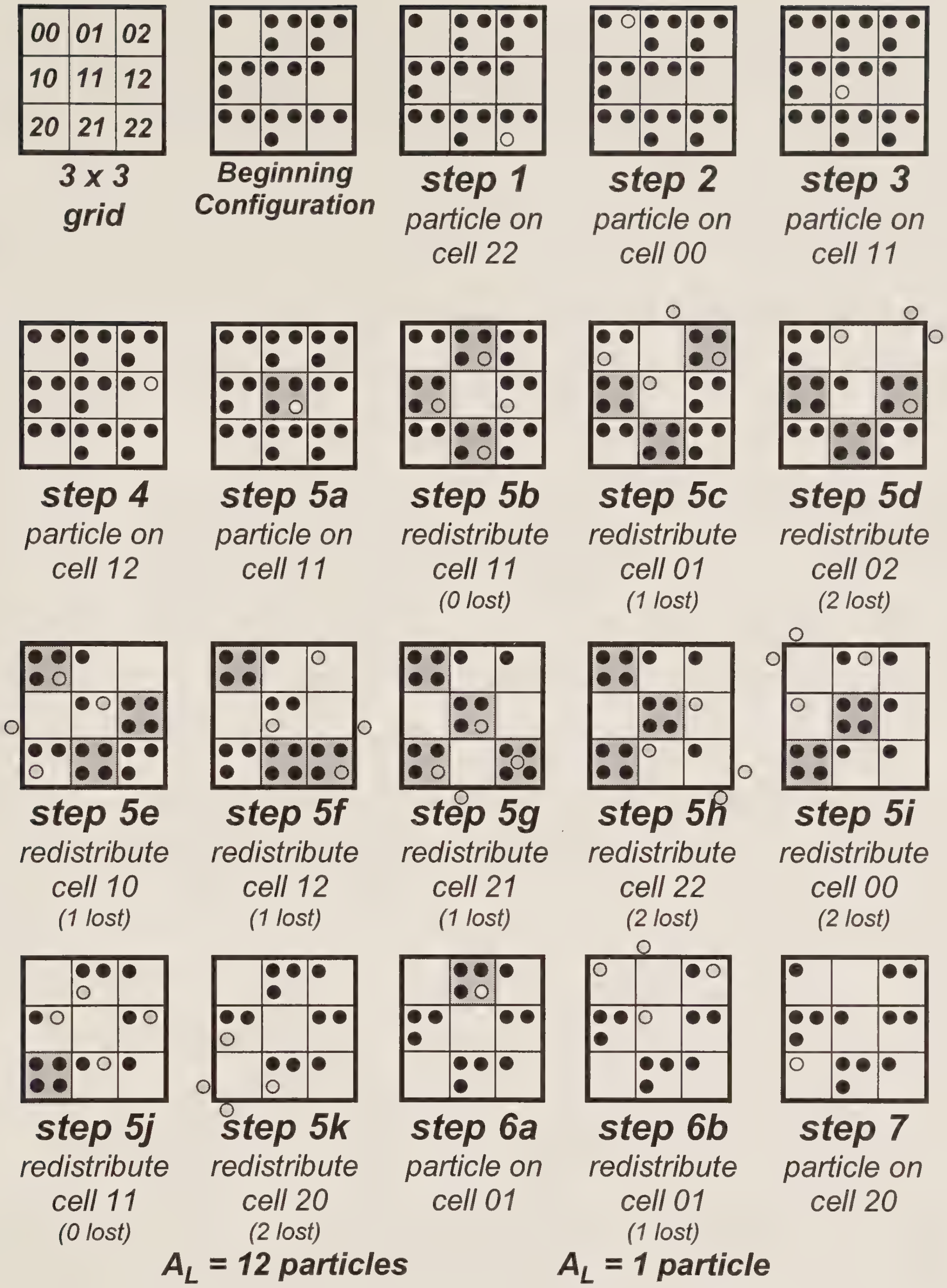

3 x 3 grid

Beginning Configuration

step 1 particle on cell 22

step 2 particle on cell 00

step 3 particle on cell 11

step 4 particle on cell 12

step 5a particle on cell 11

step 5b redistribute cell 11 (0 lost)

step 5c redistribute cell 01 (1 lost)

step 5d redistribute cell 02 (2 lost)

step 5e redistribute cell 10 (1 lost)

step 5f redistribute cell 12 (1 lost)

step 5g redistribute cell 21 (1 lost)

step 5h redistribute cell 22 (2 lost)

step 5i redistribute cell 00 (2 lost)

step 5j redistribute cell 11 (0 lost)

step 5k redistribute cell 20 (2 lost)

step 6a particle on cell 01

step 6b redistribute cell 01 (1 lost)

step 7 particle on cell 20

A_L = 12 particles

A_L = 1 particle

Figure 4.8. Illustration of the sandpile model. A 3 x 3 grid is considered and seven time steps are shown. Model "avalanches" occur in step 5 and step 6. For the first avalanche, there are ten required redistributions (steps 5b to 5k), all nine boxes were "unstable" at least once, and twelve particles were lost from the grid. In the second avalanche, only one box becomes unstable, and only one particle is lost from the grid.

This redistribution causes three of these boxes, “01”, “10”, and “21” to become unstable requiring further redistributions. The selection of which box to redistribute next is arbitrary, however the choice does not influence the statistical evolution of the model. In step 5c, the four particles in box “01” are redistributed, one particle is lost from the grid and particles are added to boxes “00”, “02”, and “11.” Eight further redistributions are required before an “equilibrium” configuration (all boxes with less than four particles” is reached. These redistributions are illustrated in step 5d to 5k. During this sequence of redistributions, all nine boxes were unstable and box “11” was unstable twice. During this sequence of redistributions, twelve particles were lost from the grid and the number of particles on the grid was reduced from 25 to 13. In step 6a, a particle is added to box “01” and it is unstable. A single redistribution is required and one particle is lost from the grid.

Sandpile Model Results

Having specified the size of the grid, a simulation is run for N_s time steps and the number of avalanches N_L with area A_L is determined. The area A_L is defined to be the number of boxes that participate in an avalanche. The noncumulative frequency-size distribution for model avalanches are given for a 50 x 50 grid in Figure 4.9 (*Turcotte*, 1997). Again, there is a good correlation with the power-law relation (4.4) with $\alpha \approx 1$ (*Kadanoff et al.*, 1989). This slope is very close to the slope obtained for the forest-fire model (Figure 4.3).

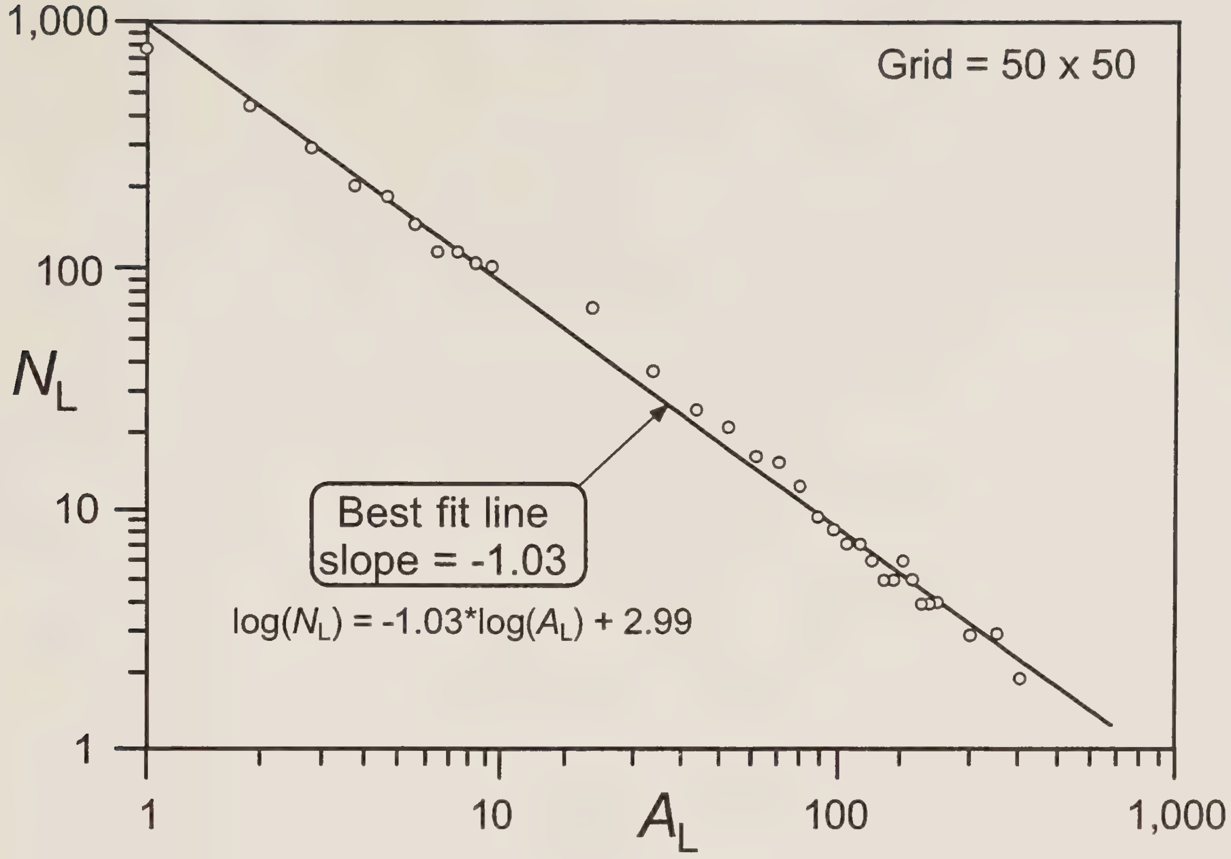

Figure 4.9. Noncumulative frequency-size distributions for a sandpile model on a 50 x 50 grid (*Turcotte*, 1997). The number N of model events in which a specified number A of boxes became unstable is given as a function of A.

Sandpiles in the Laboratory

A direct analogy can be made between the sandpile model and avalanches on actual sandpiles. Consider a pile of sand on a circular table. Grains of sand are randomly dropped on the pile until the slope of the pile reaches the critical angle of internal friction. This is the maximum slope that a granular material can maintain without additional grains sliding down the slope; in the case of sands, these angles are typically 34 – 37° (*Pye*, 1994). One hypothesis for the behavior of the sandpile would be that individual grains could be added until the slope is everywhere at an angle of repose. Additional grains would then simply

slide down the slope. This is not what happens. The sandpile never reaches the hypothetical critical state. As the critical state is approached, additional sand grains trigger sandslides of various sizes. On average, the number of sand grains added balances the number that slide down the slope and off the table. However, the actual number of grains on the table fluctuates.

A number of laboratory studies have been carried out in order to determine the frequency-size distribution of avalanches on real sandpiles (also on piles of rice and piles of beans), and in some cases a fractal distribution has been found (*Evesque*, 1991; *Nagel*, 1992; *Puhl*, 1992; *Grumbacher et al.*, 1993; *Feder*, 1995; *Densmore et al.*, 1997). *Held et al.* (1990) found fractal distributions applicable for small avalanches but not for large avalanches. *Bretz et al.* (1992) and *Rosendahl et al.* (1993, 1994) found near-periodic large avalanches and a fractal distribution of small avalanches.

Turbidites

Under some circumstances, sedimentary layers can be associated with landslides. Turbidity currents, a suspension of particles denser than the surrounding water, are associated with slumps (avalanches) off the continental margin (*Prothero*, 1990). Turbidity currents, triggered by a slump, can cover very large areas (hundreds of thousands of square km's) at high speeds (10-100 km/hr). These events can be considered a natural analog for sandslides, and thus for the cellular-automata model considered above. The lithologic product of a turbidity current is a

turbidite, each deposit representing a distinct event (slump). Each turbidite is composed of a general upward gradation from coarse-grained sediments to fine-grained sediments, and individual turbidites are separated by well-defined bedding planes.

Several studies of the frequency-thickness distribution of turbidite deposits have been carried out. *Rothman et al.* (1994) carried out direct measurements on an outcrop of the Kingston Peak Formation near the southern end of Death Valley, California. Their results are given in Figure 4.10a; an excellent correlation with the fractal relation (4.3) is obtained taking $D = 1.39$. *Rothman et al.* (1994) associated the power-law distribution of model avalanches with the observed power-law distribution of turbidite deposits. *Hiscott et al.* (1992) have studied a volcaniclastic turbidity deposit in the Izu-Bonin forearc basin off the shore of Japan. Layer thicknesses were obtained from formation-microscanner images from well logs in the middle to upper Oligocene part of the section. Results for two DSDP holes located 75 km apart are given in Figure 4.10b; a good correlation with (4.3) is obtained taking $D = 1.12$. It is difficult to make a direct comparison between the frequency-thickness distributions of sedimentary layers and the frequency-volume distributions of sandpiles. However, the sedimentary layer frequency-thickness distributions appear to be scale invariant to a good approximation.

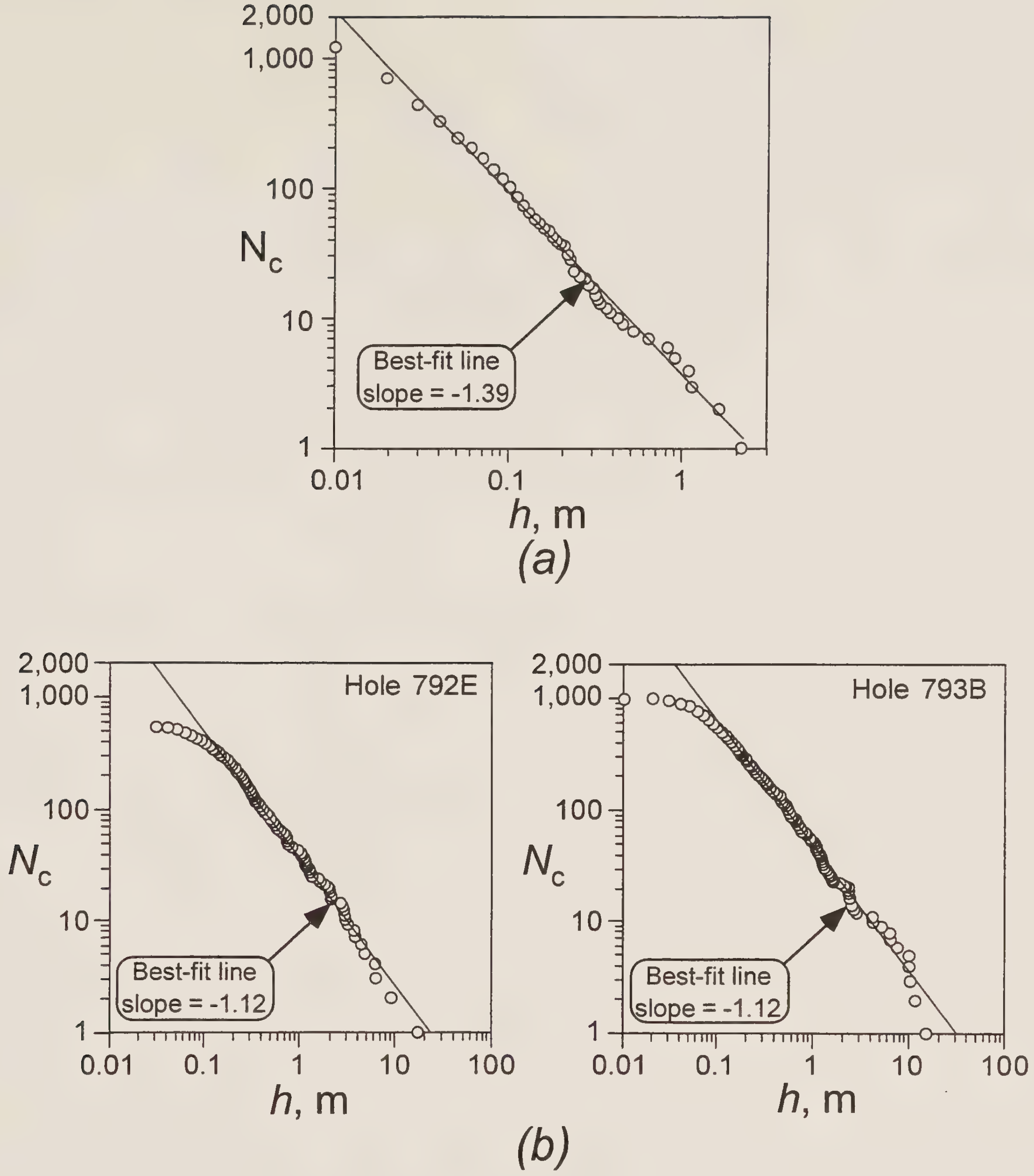

Figure 4.10. Cumulative frequency-thickness distributions for turbidite sequences of sedimentary layers. (a) Kingston Peak Formation near the southern end of Death Valley, CA (*Rothman et al.*, 1994). (b) Izu-Bonin forearc basin off the shore of Japan (*Hiscott et al.*, 1992). They attribute the roll-off for thin layers to loss of resolution. In each case, N_C the number of beds with thickness greater than h is plotted as a function of h. The straight-line correlations with the fractal relation (4.3) give $D = 1.39$ in (a) and $D = 1.12$ in (b).

Actual Landslides

We now compare the sandpile model with the frequency-size distributions of actual landslides. *Whitehouse and Griffiths* (1983), *Ohmori and Hirano* (1988), *Sugai et al.* (1994), *Sasaki et al.* (1991), *Noever* (1993), and *Hovius et al.* (1997) have shown that landslide frequency-size distributions are often well approximated by power-laws. Some have used cumulative frequency-size distributions while others have used noncumulative distributions. Care should be taken when comparing distributions to ensure that the same type of distribution is being used. In this section, we present both cumulative and noncumulative frequency-size distributions of landslide areas (Figures 4.11 and 4.12) from four geographic locations. The results suggest that the frequency-size distributions are remarkably similar despite different geographic settings and triggering mechanisms.

Earthquakes have long been recognized as a trigger for extensive landslides. The first data set is a compilation of 11,000 mapped landslides located over an area of 10,000 km^2, triggered by the January 17, 1994, Northridge, CA earthquake. *Harp and Jibson* (1995) used 1:60,000-scale aerial photography taken the morning after the earthquake by the U.S. Air Force, and compared these photos with photos taken previously. The digitized photos were supplemented by fieldwork. The inventory is nearly complete down to landslides of about 5 m on a side. The cumulative and noncumulative frequency-area distributions are given, respectively, in Figures 4.11a and 4.12a. In both cases, the frequency-area distributions for large landslides are in good agreement with the power-law relation (4.4) with $\alpha \approx 1.6$ for the cumulative distribution and $\alpha \approx 2.3$ for the noncumulative distribution.

Figure 4.11. Cumulative frequency-area distributions for actual landslides. Four examples are given: (a) 11,000 landslides triggered by the January 17, 1994 Northridge, California earthquake (*Harp and Jibson*, 1995). (b) 3,424 landslides in the Akaishi Ranges of central Japan (*Ohmori and Sugai*, 1995). (c) 1,130 landslides in the Challana valley, Yungas region, Eastern Cordillera, Bolivia (*Blodgett*, 1997). (d) 709 landslides in the Eden Canyon area of Alameda county, California (*Nilsen*, 1975). The cumulative number of landslides, N_{CL} with area greater than A_L, is given as a function of A_L. In each case a reasonably good correlation is obtained with the power-law relation (4.4) taking $\alpha = 1.6$-2.5.

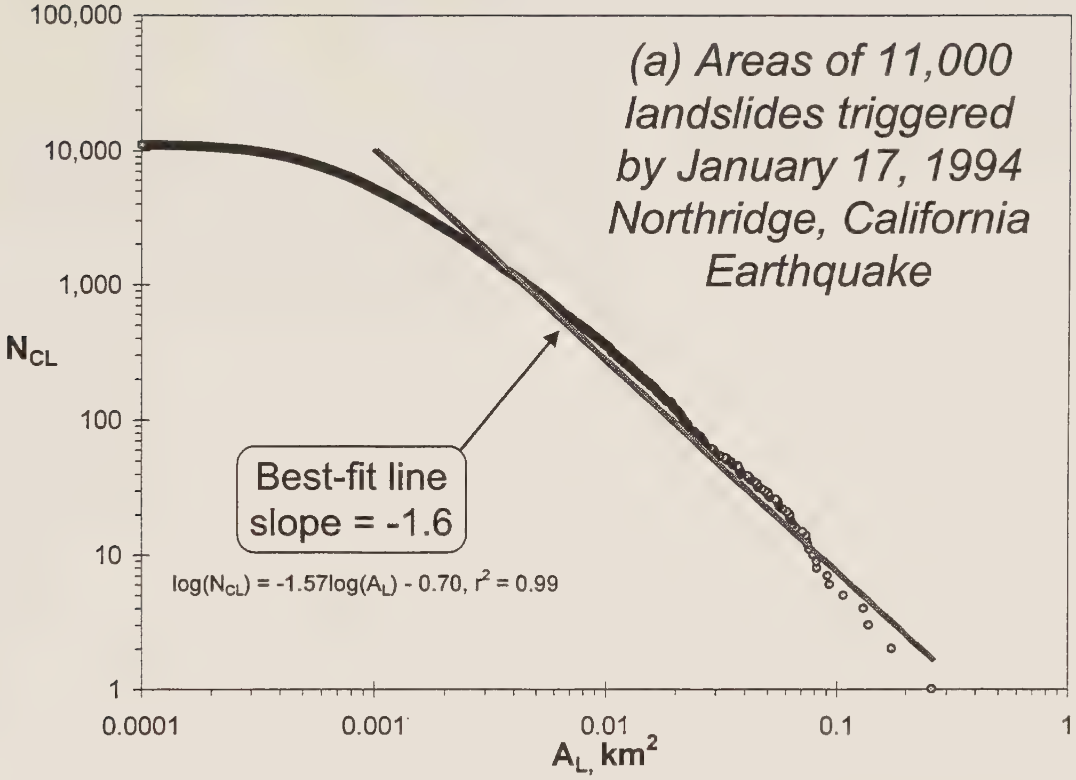
(a) Areas of 11,000 landslides triggered by January 17, 1994 Northridge, California Earthquake
Best-fit line slope = -1.6
log(N_CL) = -1.57log(A_L) - 0.70, r² = 0.99
N_CL
A_L, km²
100,000
10,000
1,000
100
10
1
0.0001
0.001
0.01
0.1
1

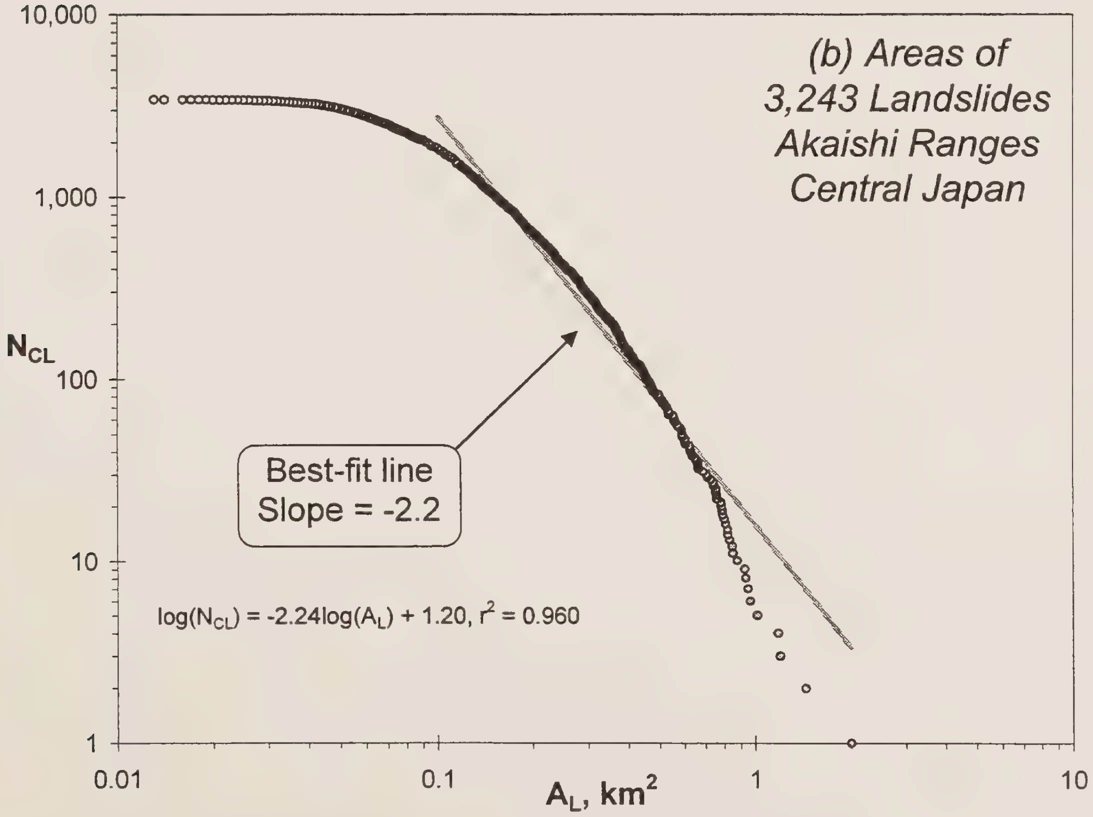
(b) Areas of 3,243 Landslides Akaishi Ranges Central Japan
Best-fit line Slope = -2.2
log(N_CL) = -2.24log(A_L) + 1.20, r² = 0.960
N_CL
A_L, km²
10,000
1,000
100
10
1
0.01
0.1
1
10

Figure 4.11 (Continued)

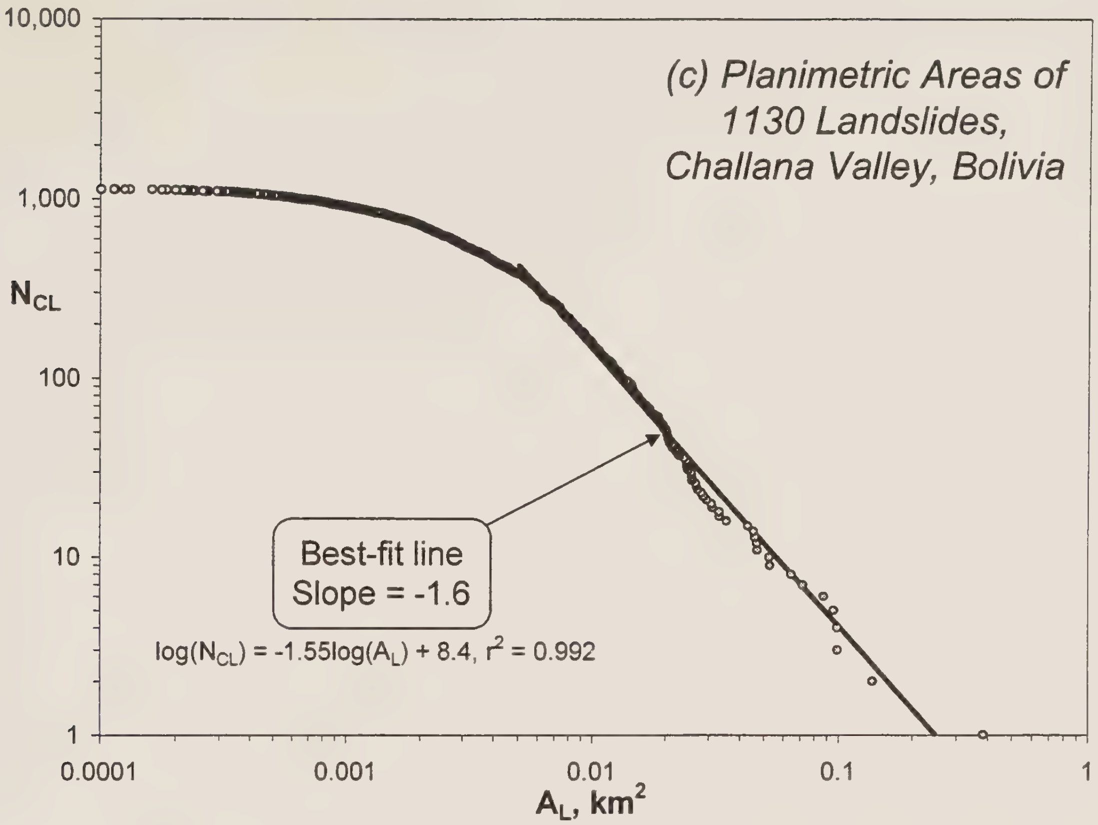

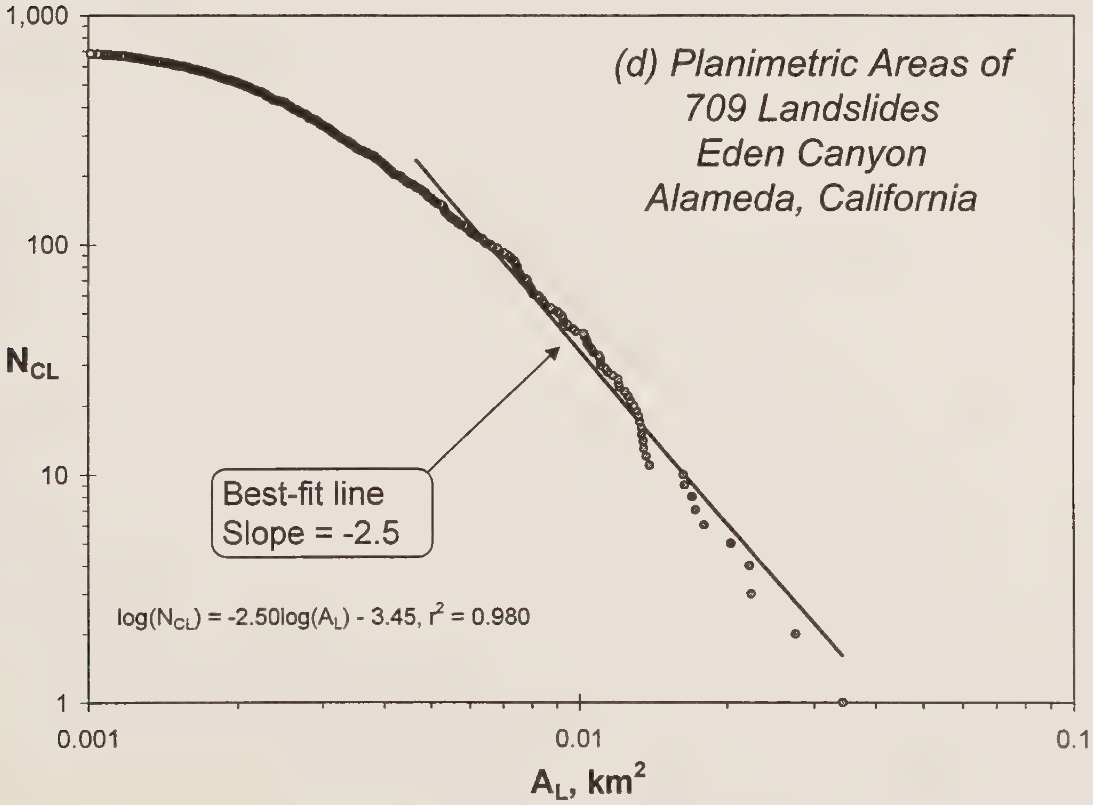

Figure 4.12. Noncumulative frequency-area distributions for actual landslides. The four different regions, (a) through (d), are the same as in Figure 4.11. The noncumulative number of landslides, $-dN_{CL}/dA_L$, with area A_L, is given as a function of A_L. In each case a reasonably good correlation is obtained with the power-law relation (4.4) taking $\alpha = 2.3$-3.3.

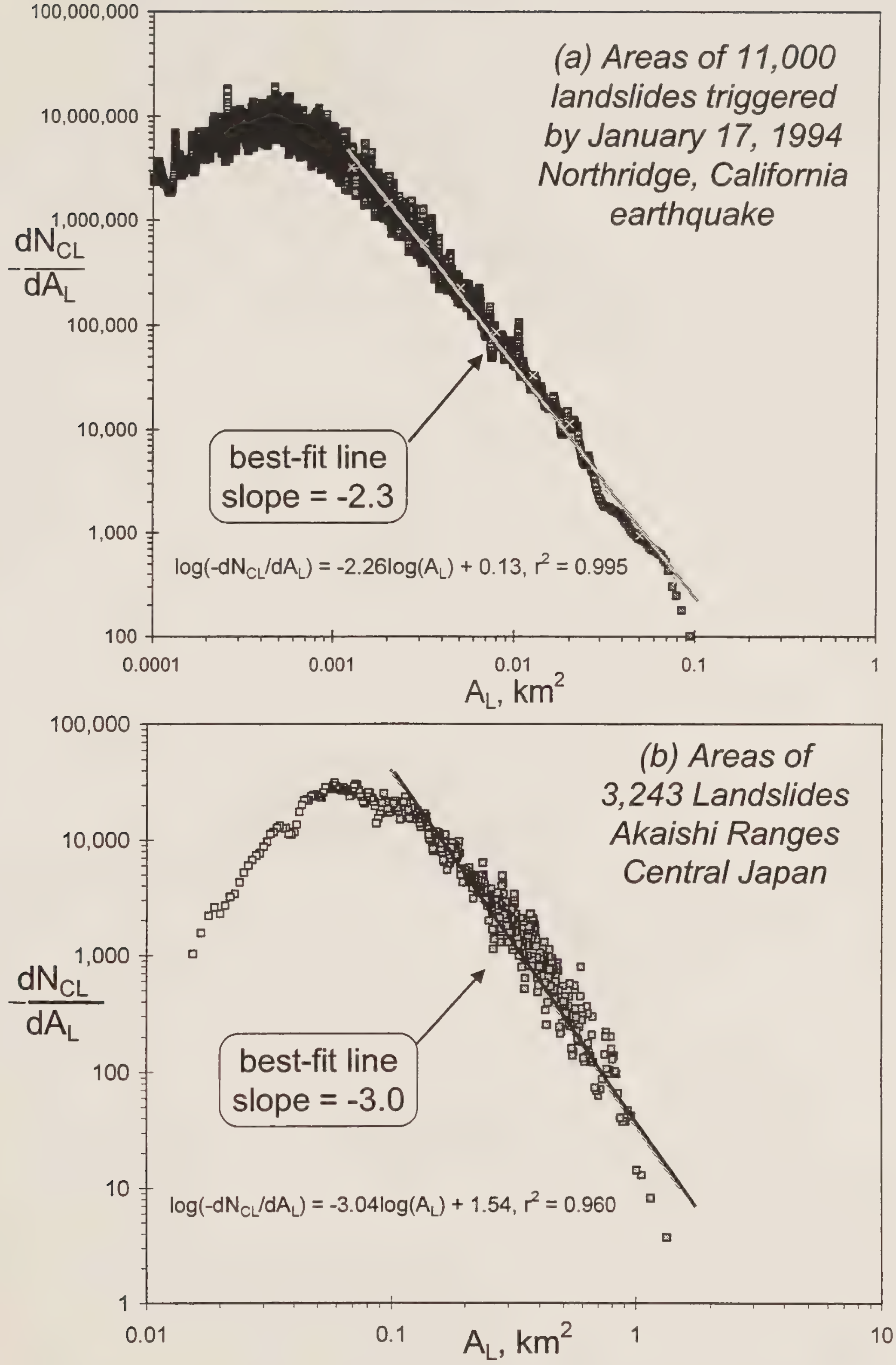
(a) Areas of 11,000 landslides triggered by January 17, 1994 Northridge, California earthquake
100,000,000
10,000,000
1,000,000
100,000
10,000
1,000
100
$-\frac{dN_{CL}}{dA_L}$
best-fit line slope = -2.3
$\log(-dN_{CL}/dA_L) = -2.26\log(A_L) + 0.13$, $r^2 = 0.995$
0.0001
0.001
0.01
0.1
1
A_L, km^2
(b) Areas of 3,243 Landslides Akaishi Ranges Central Japan
100,000
10,000
1,000
100
10
1
$-\frac{dN_{CL}}{dA_L}$
best-fit line slope = -3.0
$\log(-dN_{CL}/dA_L) = -3.04\log(A_L) + 1.54$, $r^2 = 0.960$
0.01
0.1
1
10
A_L, km^2

Figure 4.12 (Continued)

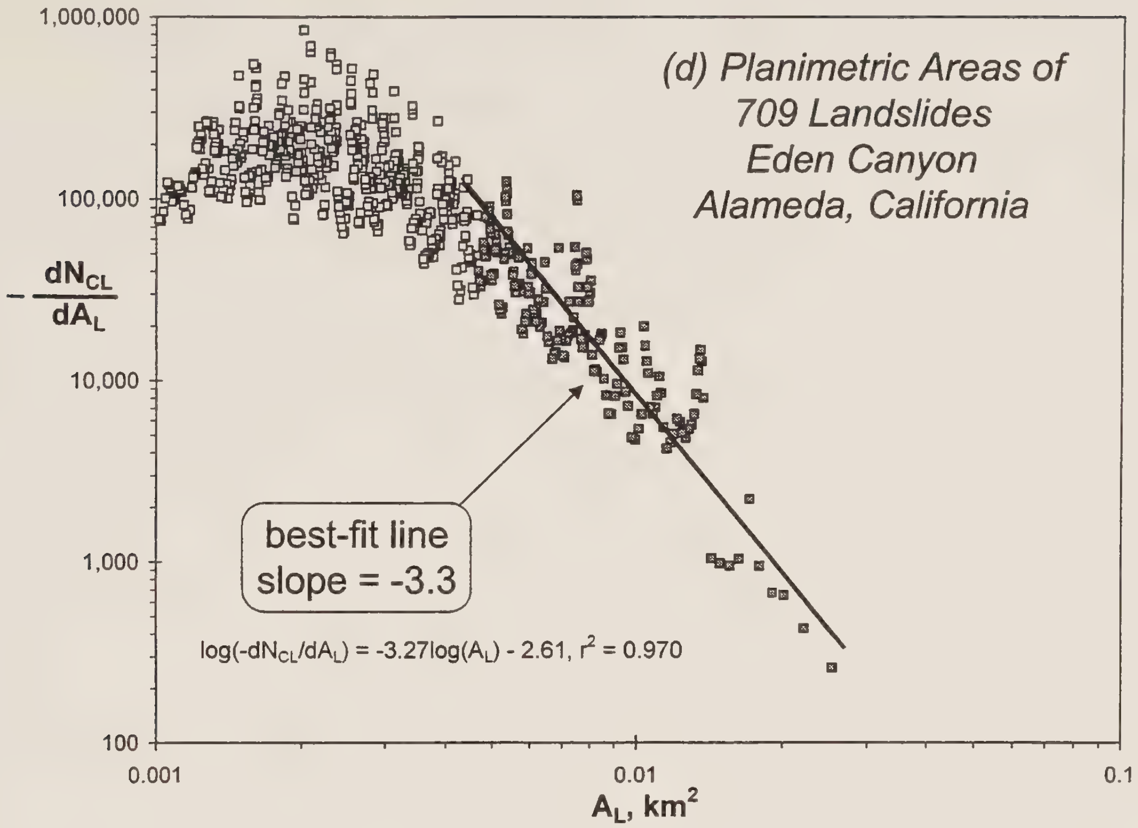

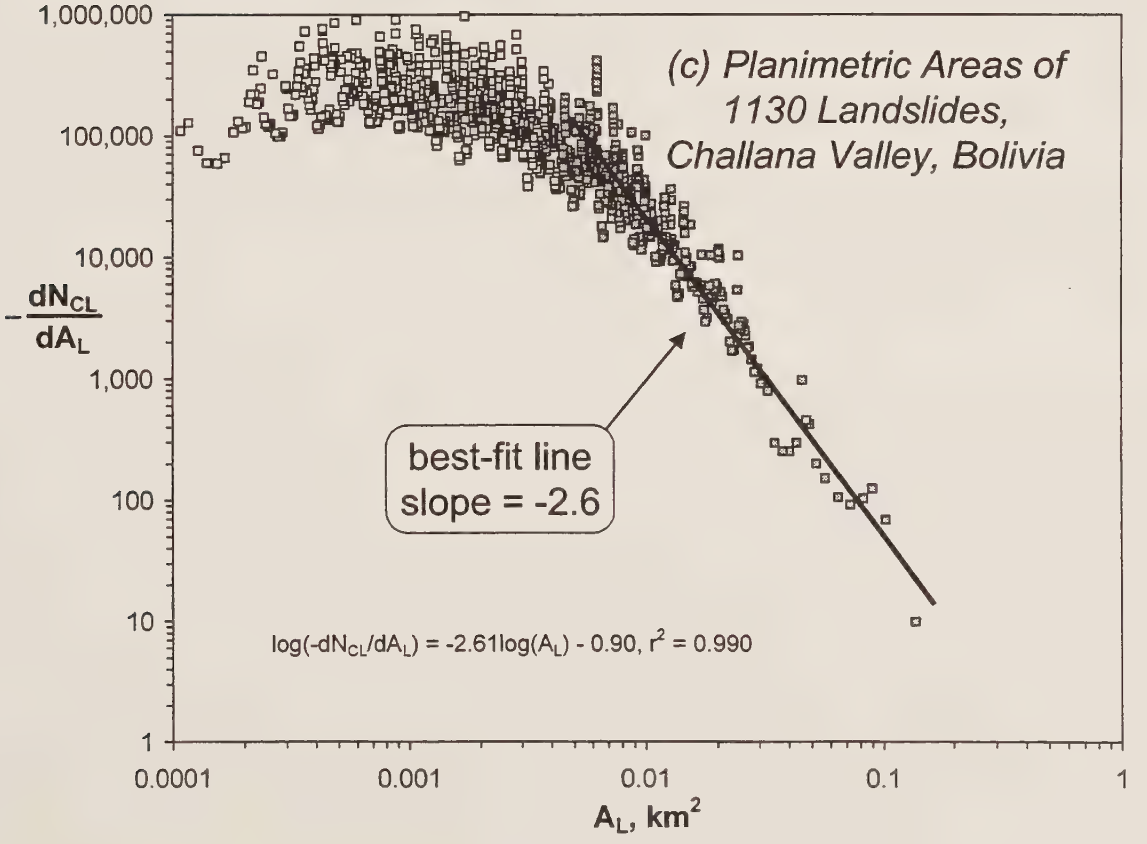

In the second data set, 3,424 landslides with areas larger than 10^{-2} km^2 in the Akaishi Ranges, central Japan, have been compiled by *Ohmori and Sugai* (1995). For the purposes of this paper, the authors sent us their data. Landslide masses were selected for measurement from 1:20,000 scale aerial photographs and by field survey. On 1:25,000 scale topographic maps, the area of each landslide was measured with a digitizer. In this region, landslides occur as a result of both heavy rainfall and strong earthquakes. It was estimated that the inventory is nearly complete for landslides with area greater than 10^{-2} km^2. The cumulative and noncumulative frequency-area distributions are given, respectively, in Figures 4.11b and 4.12b. In both cases, the frequency-area distributions for large landslides are again in good agreement with the power-law relation given in (4.4) with $\alpha \approx 2.2$ for the cumulative distribution and $\alpha \approx 3.0$ for the noncumulative distribution. The observed frequency-area distribution flattens out for areas less than about 10^{-1} km^2, thus few landslides occur with small areas. Note that this change in the distribution occurs at an area that is an order of magnitude larger than the resolution of the data. Therefore, it does not appear to be an artifact of completeness of the data set.

In the third data set, a set of landslide areas was mapped in the Challana Valley, a watershed located in the Yungas region of the Eastern Cordillera, Bolivia, between Lake Titicaca and the city of Guanay (*Blodgett*, 1997). Because very few people inhabit this region, most of the landslides (more than 95%) were not anthropogenically influenced. The Challana Valley is located in a relatively aseismic region of the Andes; therefore, all of the landslides are thought to have been

hydrologically triggered during the annual wet season which extends from November through April. Based on multitemporal aerial photographic coverage and limited dendrochronology field studies, the landslide data set represents an interval of time of about 20-35 years (*Blodgett*, 1997). Scanned aerial photographs at approximately 1:50,000 scale were used for mapping. Each photographic image was georegistered to a Thematic Mapper image using a Universal Transverse Mercator projection. Landslide mapping was only undertaken in suitable portions of the watershed below treeline. This excluded cloud covered, shadowed, and agriculture areas. The full extent of each landslide was mapped, including the runout zone. Since individual trees can be discerned in the mapped areas, the resolution of the photographs is about 3 to 10 meters. The cumulative and noncumulative frequency-area distributions are given, respectively, in Figures 4.11c and 4.12c. In both cases, the frequency-area distributions for large landslides are again in good agreement with the power-law relation given in (4.4) with $\alpha \approx 1.6$ for the cumulative distribution and $\alpha \approx 2.6$ for the noncumulative distribution.

The fourth and final data set consists of 709 landslide areas in the Eden Canyon area, Alameda County, California. The area of these landslides was digitized from a map of ancient landslide deposits prepared by *Nilsen et al.* (1975), who used aerial photographs to map landslide deposits onto a 1:24,000 map. The smallest landslide deposits mapped are about 50 m in the smallest dimension and the landslides range in age from tens to several hundred thousand years old. The cumulative and noncumulative frequency-area distributions are given,

respectively, in Figures 4.11d and 4.12d. In both cases, the frequency-area distributions for large landslides are again in good agreement with the power-law relation given in (4.4) with $\alpha \approx 2.5$ for the cumulative distribution and $\alpha \approx 3.3$ for the noncumulative distribution.

All four data sets given in Figure 4.12 exhibit similar behavior. For the larger landslides, the noncumulative frequency-area distribution correlate well with the power-law relation (4.4) taking $\alpha \approx 2.3$-3.3. This slope is considerably larger than the sandpile model slope of $\alpha \approx 1$. The sandpile model is highly idealized and does not seem to be appropriate for describing the noncumulative frequency-area distribution of actual landslides. However, for all four data sets, the reasonably good power-law correlations for larger landslides and the somewhat similar slopes obtained in diverse environments are again indicative of self-organized critical behavior. In all four data sets, the frequency of occurrence of small landslides falls systematically below the predictions of the power-law correlation. This cannot be attributed to sampling problems since the fall-off occurs at landslide sizes considerably larger than the resolution limits.

Pelletier et al. (1997) have used observed fractal distributions of soil moisture in conjunction with a slope stability analysis to model the frequency-size distribution of landslides. In their model, landslides occur when a threshold shear stress dependent on cohesion, pore pressure, internal friction, and slope angle is exceeded. Since cohesion, pore pressure, and internal friction are all primarily dependent on soil moisture, this implies a threshold dependence on soil moisture and slope angle. With soil moisture modeled as above and topography modeled as

a Brownian walk, the cumulative frequency-size distribution of domains of shear stress greater than a threshold value is a power-law function of area with an exponent of -1.8 for large landslide areas. This distribution is similar to that observed for landslides. The effect of strong ground motion from earthquakes lowers the shear stress necessary for failure (*Newmark*, 1965) but does not change the frequency-size distribution of failed areas. This work suggests that remote sensing of soil moisture can be of great importance in monitoring landslide hazards and proposes a specific quantitative model for landslide hazard assessment.

Snow avalanches would be expected to be similar in behavior to landslides. It is standard practice in ski areas to use explosives, triggering small avalanches in order to prevent the occurrence of large avalanches. This practice is certainly consistent with the behavior of the model and is directly analogous to the use of small forest fires to prevent large forest fires.

EARTHQUAKES

Slider-Block Model

Burridge and Knopoff (1967) introduced the coupled slider-block model as an analog for earthquakes. The slider-blocks are pulled over a surface by springs attached to a constant-velocity driver-plate. The blocks are also attached to each other by springs. The standard slider-block model consists of a square array of slider blocks as illustrated in Figure 4.13. Each block with mass m is attached to the driver plate with a driver spring, spring constant k_p. Adjacent blocks are attached to each other with connector springs, spring constant k_c.

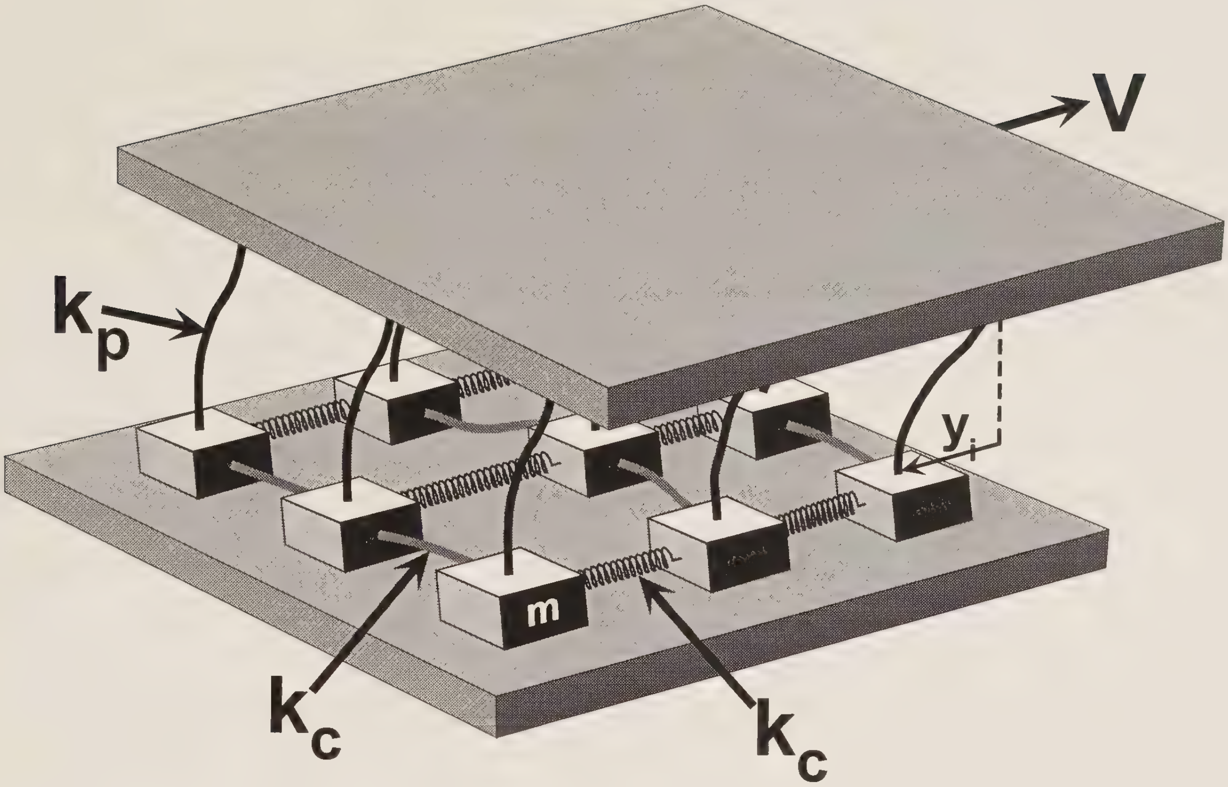

Figure 4.13. Illustration of the two-dimensional slider-block model. An array of blocks, each with mass *m* is pulled across a surface by a driver plate at a constant velocity, *V*. Each block is coupled to the adjacent blocks with either leaf or coil spring with constant k_c, and to the driver plate with leaf springs with spring constant k_p.

A block remains stationary as long as the net force on the block is less than the static resisting force, F_s. This static stability criteria requires that (*Turcotte*, 1997)

$$\left[k_p x_{i,j} + k_c\left(x_{i+1,j} + x_{i-1,j} + x_{i,j+1} + x_{i,j-1} - 4x_{ij}\right)\right] < F_s \tag{4.9}$$

with $x_{i,j}$ the position of block (i, j) in the array. When the stability criteria is violated the block begins to slip and its motion is given by

$$\left[m\frac{\mathrm{d}^2 x_{ij}}{\mathrm{d}t^2} + k_p x_{i,j} + k_c\left(x_{i+1,j} + x_{i-1,j} + x_{i,j+1} + x_{i,j-1} - 4x_{ij}\right)\right] = F_d \tag{4.10}$$

where F_d is the dynamic frictional force between the block and the surface when the block is moving and t is time in the slider-block model. We will discuss only the simple static-dynamic friction law. Many other friction laws have been considered, but the behavior of the model is insensitive to the choice. If the static frictional force is greater than the dynamic frictional force, $F_s > F_d$, stick-slip behavior is observed.

It is convenient to introduce the nondimensional variables (*Turcotte*, 1997)

$$\tau = t\left(\frac{k_p}{m}\right)^{1/2}, \quad X_{i,j} = \frac{k_p x_{i,j}}{F_s}, \quad \phi = \frac{F_s}{F_d}, \quad \alpha = \frac{k_c}{k_p} \tag{4.11}$$

The stability condition (4.9) becomes

$$\left[X_{i,j} + \alpha\left(X_{i+1,j} + X_{i-1,j} + X_{i,j+1} + X_{i,j-1} - 4X_{ij}\right)\right] < 1 \tag{4.12}$$

and the equation of motion of a block becomes

$$\left[\frac{d^2 X_{ij}}{d\tau^2} + X_{i,j} + \alpha\left(X_{i+1,j} + X_{i-1,j} + X_{i,j+1} + X_{i,j-1} - 4X_{ij}\right)\right] = \phi^{-1} \tag{4.13}$$

Two parameters determine the behavior of the system: ϕ, the ratio of static to dynamic friction, and α, the stiffness of the system. For very soft systems, $\alpha \to 0$, the blocks exhibit stick-slip behavior independently. For very stiff systems, $\alpha \to \infty$, the array of blocks behaves as a single block. The role of the stiffness parameter, α, in slider-block models is almost identical to the role of the firing frequency, f_s, in the forest-fire models.

Slider-Block Model Results

In a numerical simulation, the number of blocks in the array is specified and the driver plate is moved forward at *V*, constant velocity. As shown by *Huang and Turcotte* (1990), the two slider blocks exhibit classical chaotic behavior as long as there is any asymmetry in the system. The slip events appear to occur randomly and are not predictable even though the governing equations are fully deterministic. In their study, the equations of motion for the two blocks were solved simultaneously. A modification of this model is to allow only one block to slip at a time. The first block to become unstable is allowed to complete its harmonic motion before the stability of the second block is considered; if the second block is then unstable, it is allowed to slip before the motion of the driver-plate is updated. This then is a cellular-automata model. Extensive studies of this model were carried out by *Narkounskaia and Turcotte* (1992) and its behavior was essentially identical to the results when both blocks were allowed to slip simultaneously.

Carlson and Langer (1989) considered long linear arrays of slider blocks with each block connected by springs to the two neighboring blocks and to a constant-velocity driver. They used a velocity-weakening friction law and considered up to 400 blocks. Slip events involving large numbers of blocks were observed, the motions of all blocks involved in a slip event were coupled, and the applicable equations of motion had to be solved simultaneously. Although the system is completely deterministic, the behavior was apparently chaotic. Frequency-size distributions were obtained for slip events. The events fell into two groups: smaller events

obeyed a power-law (fractal) relationship with a slope near unity, but there was an anomalously large number of large events that included all the slider blocks. The observed behavior was characteristic of self-organized criticality. The motion of the driver plate is the steady input. The slip events are the avalanches with a fractal distribution.

Nakanishi (1990, 1991) studied multiple slider-block models using the cellular automata approach. A linear array of slider blocks was considered but only one block was allowed to move in a slip event. The slip of one block could lead to the instability of either or both of the adjacent blocks, which would then be allowed to slip in a subsequent step or steps, until all blocks were again stable. *Brown et al.* (1991) proposed a modification of this model involving a two-dimensional array of blocks. The use of the cellular automata approach greatly reduces the complexity of the calculations and the results using the two approaches are generally very similar. A wide variety of slider-block models have been proposed and studied; these have been reviewed by *Carlson et al.* (1994) and *Turcotte* (1997).

Huang et al. (1992) carried out a large number of simulations on a square array of blocks using stick-slip friction and the cellular automata approach. Their noncumulative frequency-size distributions for model slip events are given in Figure 4.14. The number of slip events per time step with area A_e, N_e/N_0, is given as a function of A_e. Results are given for a stiffness $\alpha = 30$ and four different grid sizes. There is agreement with the power-law relation (4.4) taking $\alpha \approx 1$. The results for the slider-block model are very similar to the results for the forest-fire model given in Figures 4.3 and 4.4. The stiffness parameter, α, plays a role similar to

the sparking frequency, f_s. For stiff systems, α large, the entire grid of slider blocks is strongly correlated and large slip events including all blocks occur regularly. These are the peaks for $A_e = 400$, 900, and 1,600, illustrated in Figure 4.14. For soft systems, α relatively small, no large events occur. This is the same as no large forest fires occurring for large sparking frequencies (Figure 4.3). The slider-block model is completely deterministic, whereas the forest-fire model is stochastic. However, the behavior of the two models is virtually identical.

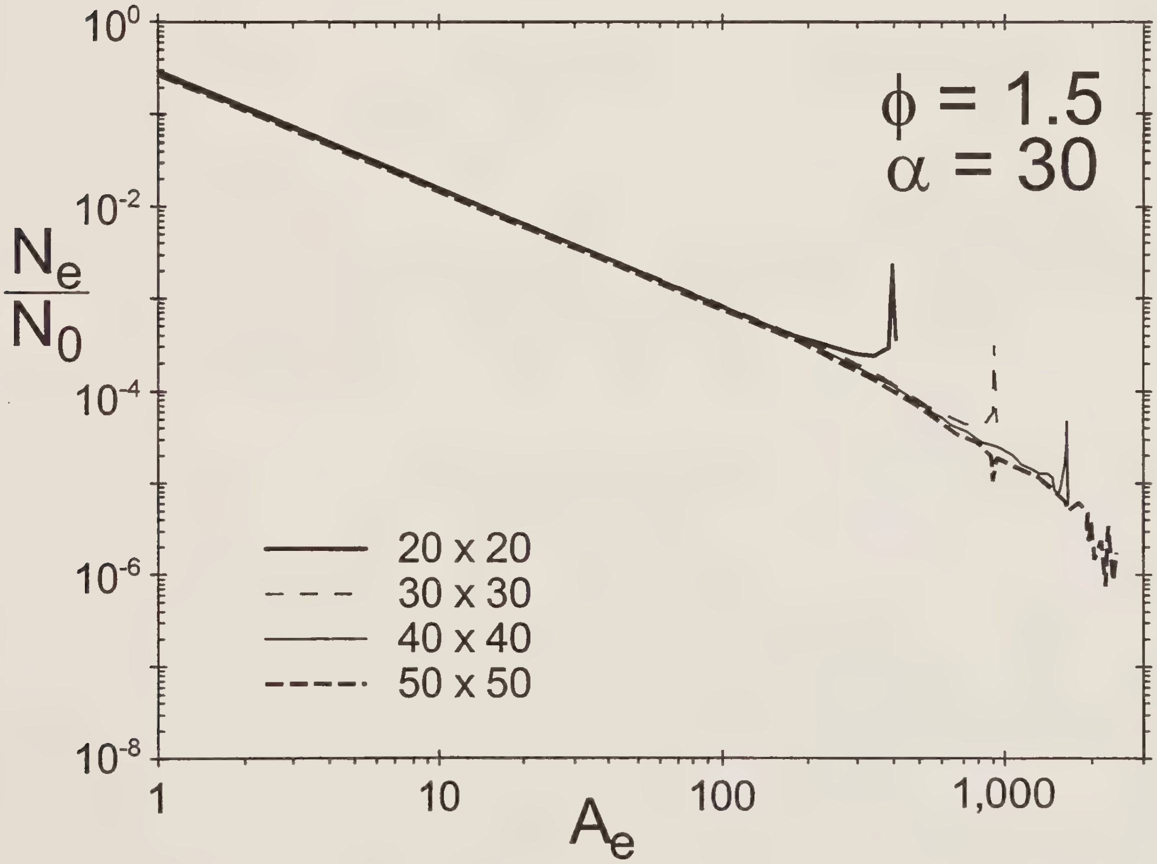

Figure 4.14. The ratio of the number of events, N_e, with size A_e, to the total number of events N_0, is plotted against A_e (*Huang et al.*, 1992). Results are given for four different grid sizes, 20 x 20, 30 x 30, 40 x 40, and 50 x 50, with α = 30. The peaks at A_e = 400, 900, and 1,600, correspond to catastrophic events involving the entire grid.

Actual Earthquakes

As was discussed in the introduction, the frequency-size distributions of actual earthquakes obey a power-law (fractal) relation. In this section, we use a variety of regional and worldwide examples as an illustration of this distribution. We first begin with a discussion of earthquake magnitudes.

In (4.1) m is used to indicate the magnitude of an earthquake; however, there are a variety of measures for the magnitude, including local, body-wave, surface-wave, and moment magnitude. A comparison of these is given by *Lay and Wallace* (1995). In general, for small-intensity earthquakes ($m < 5.5$), these different magnitude measures give approximately equivalent results. However, for large-intensity earthquakes, they give different results. The most accurate measure of a large ($m > 5.5$) earthquake is the moment magnitude, m_W, which is related to the seismic moment, M_0, of an earthquake (*Kanamori*, 1977)

$$m_W = \frac{2}{3}\log M_0 - 6.06 \tag{4.14}$$

where the seismic moment, M_0, is measured in Joules. The seismic moment of an earthquake can also be converted to an approximate rupture area, A_E, (*Aki*, 1981)

$$M_0 = \alpha A_E^{3/2} \tag{4.15}$$

where $\alpha = 3.27 \times 10^6$ Pa.

We now consider the worldwide number of earthquakes per year from the *Harvard Centroid-Moment Tensor Data Base*, (1997) for the period 1977-1994. The seismic moments from the data base have been used to calculate moment magnitudes (4.14) and rupture areas (4.15). Both the cumulative number of earthquakes per year, $\dot{N}_{CE}$, with rupture area greater than A_E, and the noncumulative number of earthquakes per year, $-d\dot{N}_{CE}/dA_E$, are given as functions of A_E in Figure 4.15. The equivalent moment magnitudes, m_W, are also given in Figure 4.15.

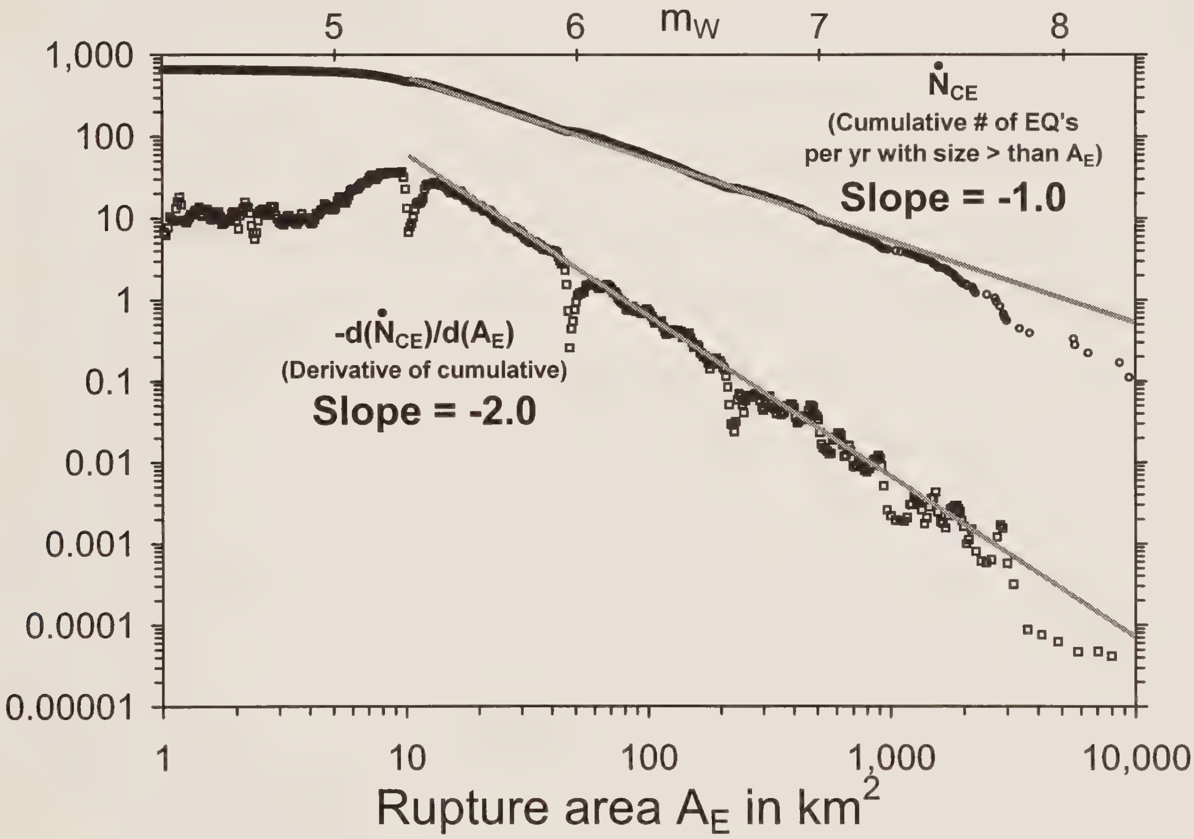

Figure 4.15. Worldwide cumulative, $\dot{N}_{CE}$, and noncumulative, $-d\dot{N}_{CE}/dA_E$, number of earthquakes per year with rupture area greater than A_E as a function of A_E. These data are from the *Harvard Centroid-Moment Tensor Data Base* (1997) for the years (1977-1994). Earthquake seismic moments have been converted to rupture areas (4.15) and moment magnitudes (4.14).

The cumulative worldwide data per year correlate with (4.1) taking $b = 1.0$ ($D = 2.0$) and $\dot{a} = 10^8$ yr^{-1}. The data given in Figure 4.15 can be used to estimate the frequency of occurrence of earthquakes of various magnitudes on a worldwide basis. For example, about ten magnitude-seven earthquakes are expected each year and a single magnitude-eight earthquake can be expected in a year. As expected, the slopes of the cumulative and the noncumulative distributions differ by exactly 1.

The deviation of the data from the Guttenberg-Richter law (4.1) at moment magnitudes less than $m_W = 5.2$ can be attributed to the resolution limits of the global seismic network. Regional studies indicate that good correlations are obtained down to at least magnitude $m = 2$ (*Aki*, 1987). The deviation of the data from the Gutenberg-Richter law at moment magnitudes greater than $m_W = 7.5$ is more controversial (*Scholz*, 1997). Clearly there must be an upper limit to the size of an earthquake; but the deviations in Figure 4.15 can be attributed either to a real deviation from the correlation line or to the small number of very large earthquakes in the relatively short time span considered. There is a physical basis for a change in scaling for large earthquakes (*Pacheco et al.*, 1992). The rupture zone of smaller earthquakes can be approximated by a circle of radius r, so that $r \sim A_E^{1/2}$. However, the depth of large earthquakes is confined by the thickness of the seismogenic zone, say about 20 km, whereas the length, l, can increase virtually without limit. Thus for large earthquakes, $l \sim A_E$. The transition would be expected to occur for $A_E^{1/2} \approx$ 25 km or $m_W \approx 7$.

Bak and Tang (1989) pointed out the similarity in slopes between self-organized critical behavior and earthquakes. As we have shown, the

models we have considered typically have good agreement with the power-law relation (4.4) taking $\alpha \approx 1$. The cumulative data shown in Figure 4.15 also are in good agreement with (4.4) taking $\alpha \approx 1$, but the noncumulative data correlate with (4.4) taking $\alpha \approx 2$. Since the model data are noncumulative, the agreement with the cumulative earthquake data must be considered fortuitous. As in other applications we have considered, the power laws for the natural phenomena are systematically higher than for the models.

Since it is standard practice in seismology to use cumulative distributions, the remainder of our discussion will be restricted to correlations of the cumulative number of earthquakes with magnitude m, as a function of m. As a specific application, we consider the regional seismicity in southern California. The cumulative frequency-magnitude distribution of seismicity in southern California is given in Figure 4.16. The data, from the *Southern California Seismographic Network* (1995), are for the period 1932 to 1994. This catalog contains a variety of magnitude measures. The number of earthquakes per year, $\dot{N}_{CE}$, with magnitudes greater than m, are given as a function of m. Over the entire range of $4 < m < 7.5$ the data are in excellent agreement with (4.1) taking $b = 0.923$ ($D = 1.846$) and $\dot{a} = 1.4 \text{ x } 10^5 \text{ yr}^{-1}$.

Also included in Figure 4.16 is a solid circle representing the value of $\dot{N}$ associated with great earthquakes on the southern section of the San Andreas fault. Dates for 10 large earthquakes on this section of the fault have been obtained from radiocarbon dating of faults, folds, and liquifaction features within the marsh and stream deposits on Pallett Creek where it crosses the San Andreas fault 55 km northeast of Los

Angeles (*Sieh et al.*, 1989). In addition to historical great earthquakes on January 9, 1857, and December 8, 1812, additional great earthquakes were estimated to have occurred in 1480 ± 15, 1346 ± 17, 1100 ± 65, 1048 ± 33, 997 ± 16, 797 ± 22, 734 ± 13, and 671 ± 13. The mean repeat time is 132 years, giving $\dot{N} = 0.0076\ \mathrm{yr}^{-1}$. *Sieh* (1978) estimates that the moment magnitude of the 1857 earthquake was $m_W = 8.25$. Taking the values given above, the recurrence values for these large earthquakes are shown by the solid circle in Figure 4.16.

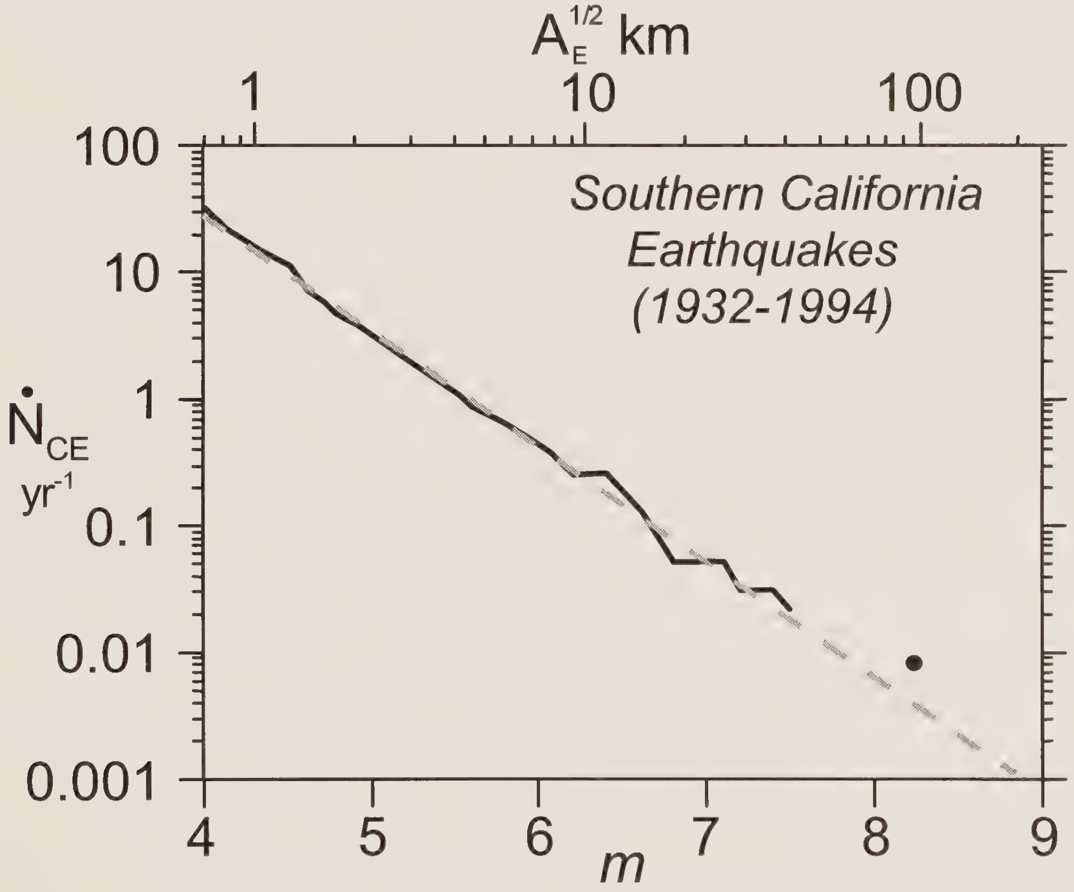

Figure 4.16. Number of earthquakes per year, $\dot{N}_{CE}$, occurring in southern California with magnitudes greater than m as a function of m. The solid line is for 1932-1994 (*Southern California Seismographic Network*). The straight dashed line is the correlation with (4.1) taking $b = 0.923$ ($D = 1.846$) and $\dot{a} = 1.4 \times 10^5\ \mathrm{yr}^{-1}$. The solid circle is the observed rate of occurrence of great earthquakes in southern California (*Sieh et al.*, 1989).

In Figure 4.16, the straight dashed line is the best-fit power-law relation to the regional seismicity. Extrapolation of this dashed line appears to make a reasonable prediction of great earthquakes (the solid circle) on this section of the San Andreas fault. Acceptance of this hypothesis allows the regional background seismicity to be used in assessing seismic hazards (*Turcotte*, 1989). The regional frequency-magnitude distributions can be extrapolated to estimate recurrence times for larger magnitude earthquakes. Unfortunately, no information is provided on the largest earthquake to be expected.

An important question in seismology is whether the occurrence of large plate-boundary earthquakes, such as those at subduction zones, can be estimated by extrapolating the regional seismicity as was done above for southern California. This is a subject of considerable controversy. Some authors argue that the large earthquakes occur more often than would be predicted by an extrapolation (*e.g.*, *Camelbeeck and Meghraoui*, 1996; *Davison and Scholz*, 1985). To illustrate the idea of extrapolation, we next consider regional seismicity in southern California.

Using the time dependence of regional seismicity, *i.e.* the time dependence of $\dot{a}$ in (4.1), the frequency-magnitude distributions of the regional seismicity in southern California on a yearly basis is plotted in Figure 4.17 using data obtained from the *Southern California Earthquake Center (SCEC)* (1995). Again, this catalog contains a variety of magnitude measures. In this figure, the number of earthquakes $\dot{N}_{CE}$ in each year between 1980 and 1994 with magnitudes greater than m is plotted as a function of m.

Figure 4.17. The cumulative number of earthquakes for each year between 1980 and 1994, $\dot{N}_{CE}$, with magnitudes greater than m, given as a function of m. The region considered is southern California (*Southern California Seismographic Network*). (a) 1980-1984; (b) 1985-1989; (c) 1990-1994. The straight-line correlation is the Guttenberg-Richter relation (4.1) with $b = 1.05$ and $\dot{a} = 2.06 \times 10^5\ \mathrm{yr}^{-1}$. The relatively large numbers of earthquakes in 1987, 1992, and 1994 can be attributed to the aftershocks of the Whittier, Landers, and Northridge earthquakes, respectively. If aftershocks are excluded, the background seismicity in southern California is nearly uniform in time.

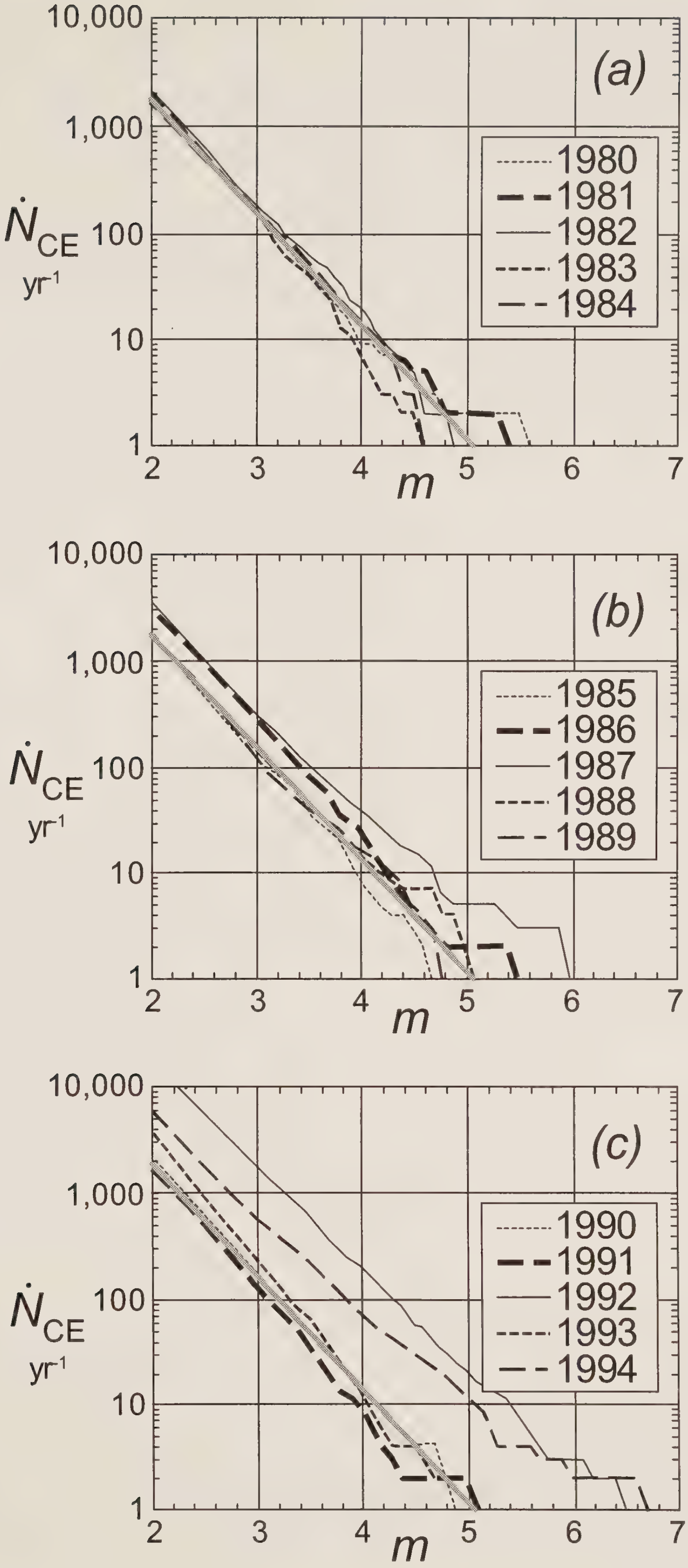
(a)
10,000
1,000
100
10
1
$\dot{N}_{CE}$
yr^{-1}
2
3
4
5
6
7
m
1980
1981
1982
1983
1984
(b)
10,000
1,000
100
10
1
$\dot{N}_{CE}$
yr^{-1}
2
3
4
5
6
7
m
1985
1986
1987
1988
1989
(c)
10,000
1,000
100
10
1
$\dot{N}_{CE}$
yr^{-1}
2
3
4
5
6
7
m
1990
1991
1992
1993
1994

The yearly southern California data is plotted in Figure 4.17. In general, there is good agreement with (4.1), taking $b = 1.05$ and $\dot{a} = 2.06 \times 10^5\ \mathrm{yr}^{-1}$. The exceptions can be attributed to the aftershock sequences of the 1987 Whittier, 1992 Landers, and 1994 Northridge earthquakes. The linear correlation line in Figure 4.16 lies somewhat above the linear correlation line in Figure 4.17. This is because the data given in Figure 4.16 include aftershocks. With aftershocks removed, the near uniformity from year to year of the background seismicity in southern California illustrated in Figure 4.17 is clearly striking.

Since the eastern United States is a plate interior, the concept of rigid plates would preclude seismicity in the region. However, the plates act as stress guides. The forces that drive plate tectonics are applied at plate boundaries. Because the plates are essentially rigid, these forces are transmitted through their interiors. However, the plates have zones of weakness that will deform under these forces and earthquakes result. Thus earthquakes occur within the interior of the surface plates of plate tectonics, although the frequencies of occurrence are much lower than at plate boundaries (*Hinze et al.*, 1988).

Among available examples are the three great earthquakes that occurred in the Memphis-St. Louis (New Madrid, Missouri) seismic zone during the winter of 1811-1812. *Nuttli* (1983), based on historical records, has estimated that the magnitudes of these earthquakes were 8.5, 8.4, and 8.8, respectively. This area remains the most active seismic zone in the United States east of the Rocky Mountains. Based on both instrumental and historical records, *Johnston and Nava* (1985) have given the frequency-magnitude distributions for earthquakes in this area

for the period 1816-1983. Their results are given in Figure 4.18. The data correlate well with (4.1) taking $b = 0.9$ ($D = 1.8$) and $\dot{a} = 2.24 \times 10^3$ yr^{-1}. Comparing the data in Figure 4.18 with the data in Figure 4.16 indicates that the probability of having a moderate-sized earthquake in the Memphis-St. Louis seismic zone is about 1/50 of the probability in southern California. Assuming that it is valid to extrapolate the data in Figure 4.18 to larger earthquakes, a magnitude $m = 8$ would have a recurrence time of about 7,000 yr.

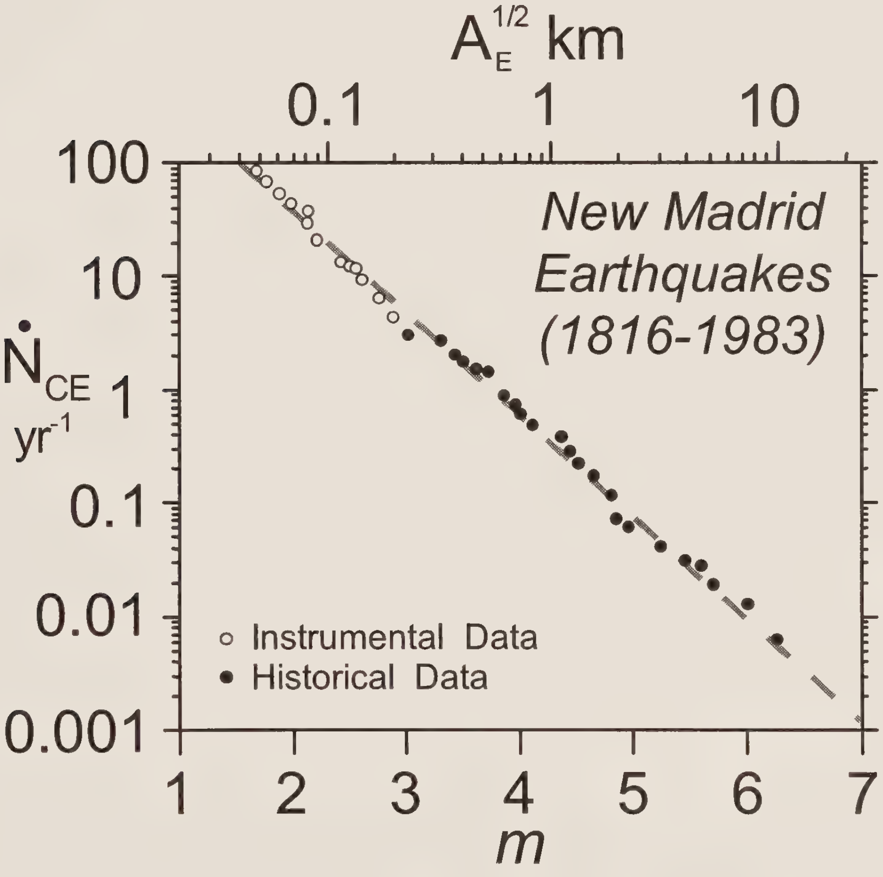

Figure 4.18. The cumulative number of earthquakes per year, $\dot{N}_{CE}$, occurring in the Memphis-St. Louis (New Madrid, Missouri) seismic zone with magnitudes greater than m, given as a function of m (*Johnston and Nava*, 1985). The open circles represent instrumental data and the solid circles historical data, both for the period 1816-1983. The dashed line represents (4.1) with $b = 0.90$ ($D = 1.80$) and $\dot{a} = 2.24 \times 10^3$ yr^{-1}.

The Seismic Intensity

Kossobokov and Turcotte (1996) proposed a systematic global assessment of the seismic hazard based on the extrapolation of the occurrence of small earthquakes to larger earthquakes. The method was based on the epicenters of earthquakes with magnitudes $m \geq 4$ taken from the Global Hypocenter Data Base (*United States Geological Survey*, 1996) for the period 1964-1995. This catalog contains a variety of magnitude measures. The magnitude 4 cutoff was taken because this is the minimum m for which the global catalog is complete for this period.

Dividing the surface of the earth into 1° x 1° regions, the number of earthquakes per year with magnitudes $m \geq 4$ in each region was determined. Each 1° x 1° region varies in area with respect to changing latitude. In order to convert the number of earthquakes in a 1° x 1° region, to the number of earthquakes per unit area (based on a 1° x 1° region at the equator), it was necessary to divide by the cosine of the latitude. For instance, given two 1° x 1° regions, one at 60° latitude with N earthquakes, and the other at the equator with $2N$ earthquakes, then the density of earthquakes per area is in fact equal for both regions. The seismic intensity factor, I_4, was defined to be the number of magnitude $m \geq 4$ earthquakes that have occurred in a given 1° x 1° region per year, normalized by the cosine of the latitude.

A global map of the seismic intensity factor is given in Figure 4.19. The boundaries of tectonic plates are clearly defined. As expected, seismicity is particularly intense in subduction zones (*i.e.*, the ring of fire around the Pacific). A broad band of seismicity extends from southern Europe to SE Asia. This is associated with continent-continent collision between the Eurasian plate and the African, Arabian, and Indian plates.

Figure 4.19. Global map of the seismic intensity factor I_4, the average annual number of magnitude $m \geq 4$ earthquakes that have occurred in a given 1° x 1° region, normalized by the cosine of the latitude (*Kossobokov and Turcotte*, 1996).

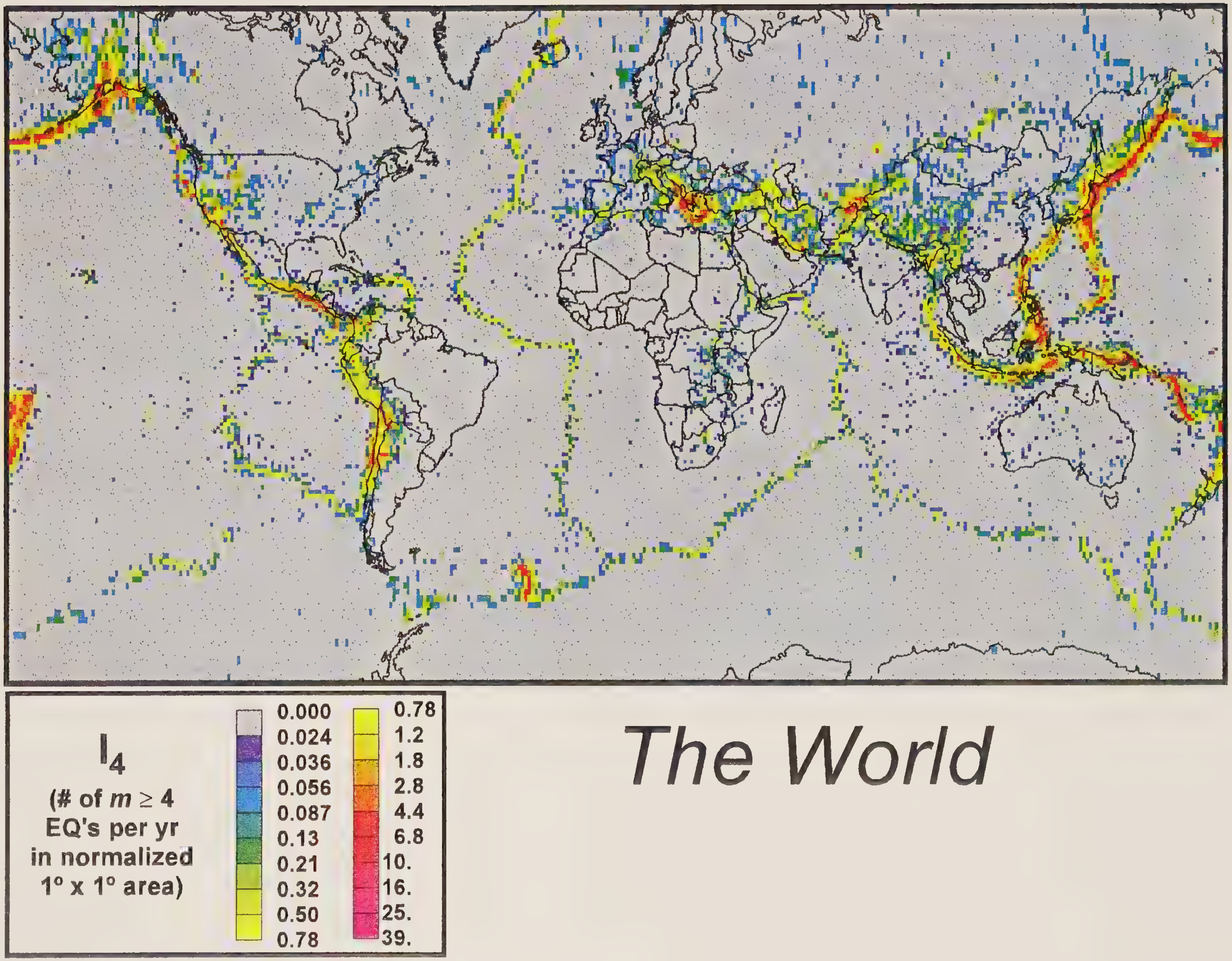
I4
(# of m ≥ 4
EQ's per yr
in normalized
1° x 1° area)
0.000
0.024
0.036
0.056
0.087
0.13
0.21
0.32
0.50
0.78
0.78
1.2
1.8
2.8
4.4
6.8
10.
16.
25.
39.

The World

The minimum value of the seismic intensity factor considered is $I_4 = 1/32$ yr^{-1}, one magnitude $m = 4$ or larger earthquake in the 32 years for which records were used. The maximum value of the seismic intensity factor is about $I_4 = 40$ yr^{-1} (forty magnitude $m \geq 4$ earthquakes per year). It is appropriate to define levels of regional seismicity in terms of I_4 according to Table 1.

Table 4.1. Levels of regional seismicity

Level	I_4
Very low seismicity	0 - 0.01
Low seismicity	0.01 - 0.1
Moderate seismicity	0.1 - 1
High seismicity	1 - 10
Very high seismicity	10 - 100

In Figure 4.20, we give two regional maps of the seismic intensity factor, I_4. A map for the United States is shown in Figure 4.20a. The intense seismicity along the Pacific-North American plate boundary, including the San Andreas fault, is clearly illustrated. The distributed seismicity associated with the intraplate deformation in the western United States (the Basin and Range Province) is also shown. The most intense seismicity in the eastern United States is the Memphis - St. Louis seismic zone (36 N, 90 W), as was discussed. A map of the seismicity in Europe is given in Figure 4.20b. The Aegian region has particularly intense seismicity, but high levels of seismicity extend throughout the Mediterranean area.

Figure 4.20. Regional maps of the seismic intensity factor I_4, the average annual number of magnitude $m \geq 4$ earthquakes that have occurred in a given 1° x 1° region, normalized by the cosine of the latitude (*Kossobokov and Turcotte*, 1996). (a) United States, (b) Europe.

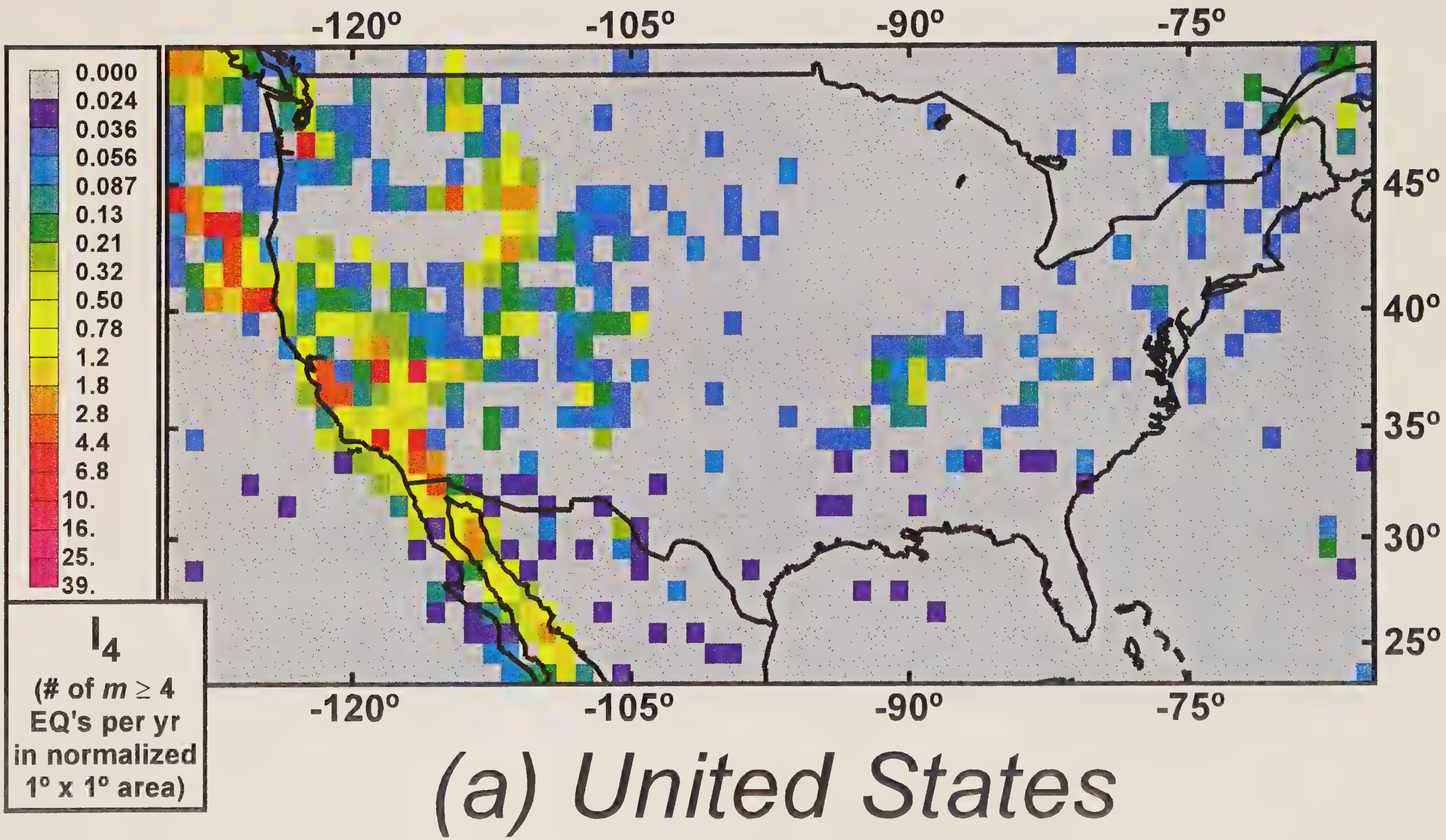

(a) United States

Figure 4.20 (Continued)

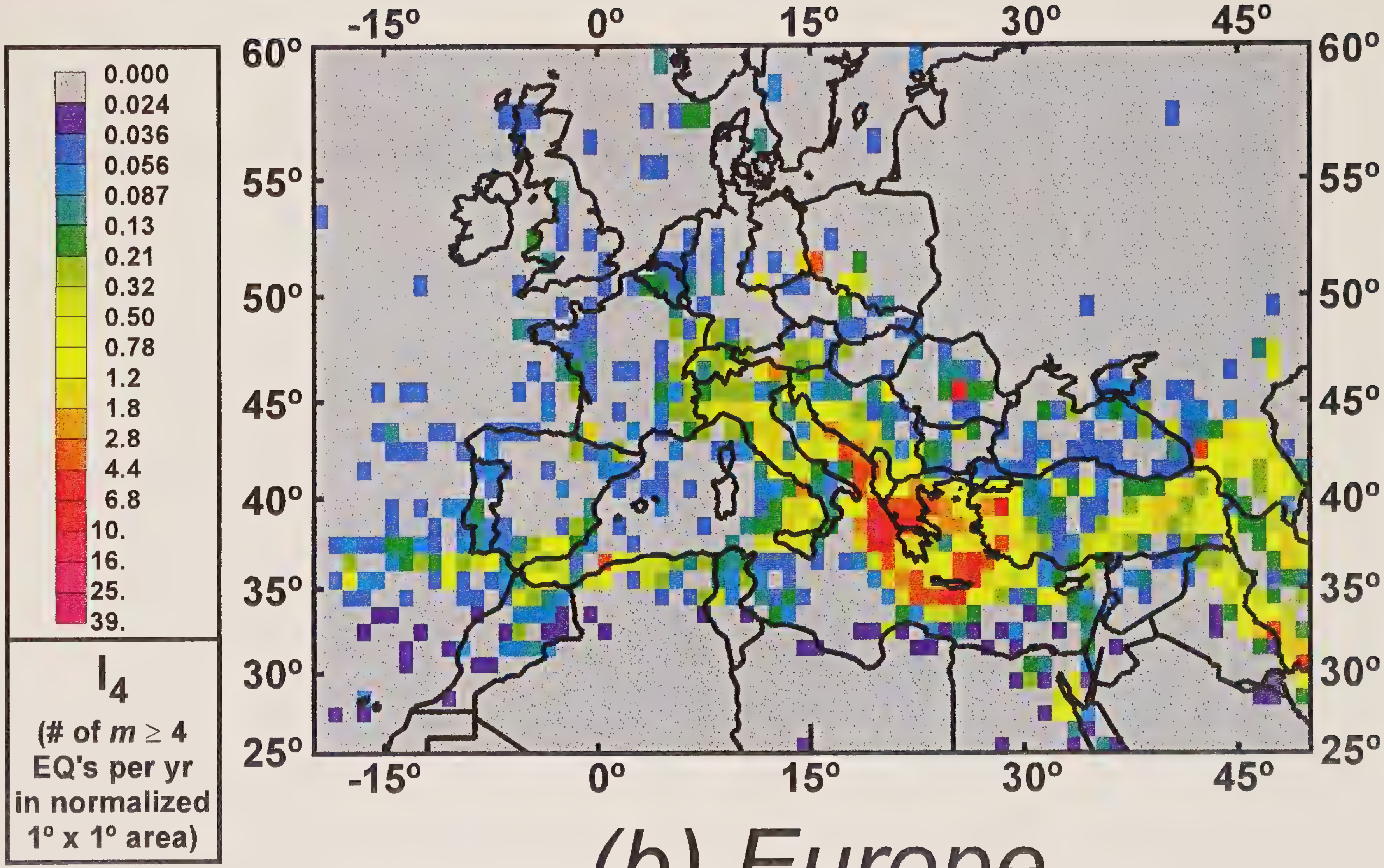

(b) Europe

The basis for using the seismic intensity factor, I_4, to estimate the risk of having larger earthquakes in a region is illustrated in Figure 4.21. Using the Guttenberg-Richter relation (4.1), the number of earthquakes per year in a 1° x 1° area with a magnitude m is directly related to the seismic intensity factor I_4 (the number of earthquakes per year in a 1° x 1° area with a magnitude greater than 4). As an example, consider a region where $I_4 = 1\ \text{yr}^{-1}$ (one magnitude 4 per year), the risk of having a magnitude $m = 6$ earthquake is $0.016\ \text{yr}^{-1}$ (return period of 63 years) and the risk of having a magnitude $m = 8$ earthquake is $2.5 \times 10^{-4}\ \text{yr}^{-1}$ (return period of 4,000 yrs).

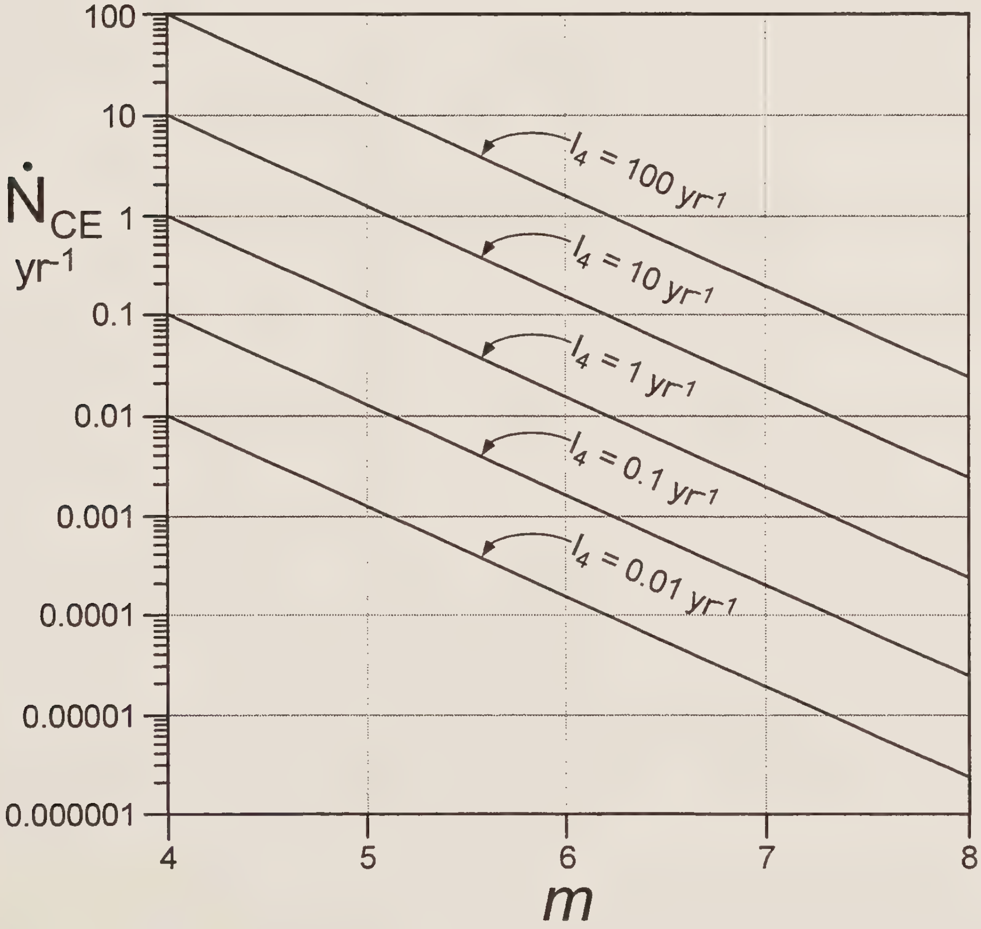

Figure 4.21. Similarity basis for extending the seismic intensity factor I_4 from smaller to higher earthquake magnitudes.

The approach given above has both advantages and disadvantages. The primary advantage is its simplicity and direct use of available data. The earthquake hazards maps are prepared directly from the global catalog of earthquake magnitude and location. Even assuming that it is appropriate to extrapolate from moderate size earthquakes $m = 4$ to large earthquakes, obvious difficulties remain. The first is that the thirty-two year record of magnitude four and larger earthquakes can only approximate a long-term average. Strong earthquakes and their associated aftershocks will create local anomalies in the maps. A second problem is that there is no information on how large the largest earthquake in a region might be. It is also clear that this approach resembles accepted statistical techniques for estimating seismic hazards. However, there are two significant advantages:

1) Uniform global coverage, and
2) A completely systematic approach based on available data.

CONCLUSIONS

We have considered three simple cellular-automata models. The forest-fire and sandpile models are stochastic, whereas the slider-block model is deterministic. Each model exhibits self-organized critical behavior. In each case, there is a steady-state input. Trees are continuously planted in the forest-fire model, particles are dropped in the sandpile model, and the driver plate moves at constant velocity in the slider-block model. In each case, there is a power-law (fractal) distribution of “avalanches.” The noncumulative frequency-size distributions of the model forest fires, landslides, and slip events are

power law (fractal) with a slope near unity. In each case, a “density” fluctuates about a quasi-equilibrium value: the mean density of trees for the forest-fire model, the mean number of particles in a box in the sandpile model, and the mean kinetic- and potential-energies in the slider block model.

We also considered actual forest fires, landslides, and earthquakes. In each case, we find power-law (fractal) frequency-magnitude distributions to be a good approximation. However, the slopes are generally larger than unity, the value predicted by the model. We suggest that these complex natural phenomena self-organize so that their statistical behaviors are relatively simple, power-law frequency-size distributions.

We conclude that self-organized critical behavior is robust both in terms of models and in terms of complex natural phenomena. One consequence is that the measured frequency of occurrence of small events can be used to estimate the frequency of occurrence of large events. For example, the recurrence interval for large earthquakes can be estimated from the frequency of smaller earthquakes. Based on this concept, the seismic intensity factor is introduced. Both global and regional maps for the seismic intensity factor have been given. If the power-law approach for landslides and forest fires is considered valid, then hazard maps similar to those developed for the seismic hazard can also be constructed.

The models also show that the triggering of small events can prevent the occurrence of large events. For example, controlled “burns” can prevent the occurrence of large forest fires.

The concepts presented in this paper may also be applicable in fields other than natural hazards. The forest-fire model may be applicable to epidemics and other problems in biology. The concept of self-organized criticality may also be applicable to the behavior of the economy. Increases in interest rates may be analogous to the matches in the forest-fire model.

APPENDIX 4.1. ABBREVIATIONS AND SYMBOLS

SYMBOL	*DESCRIPTION*	*EQUATION WHERE INTRODUCED*
$\dot{a}$	Measure of the intensity of the regional seismicity	(1)
A_a	Size of a cluster	(5)
A_e	Area of slip events in the slider-block model	
A_E	Earthquake rupture area	(2)(15)
A_F	Number of trees burned, forest-fire model Area burned in an actual fire	
A_L	Area of a sandpile-model "avalanche" or of an actual landslide	
b	Constant in Guttenberg-Richter relation, "b-value"	(1)
D	Fractal dimension	(3)
D_c	The fractal dimension for a "cumulative" distribution	
F_d	Dynamic friction force, slider-block model	(10)
F_s	Static friction force (resisting force), slider-block model	(9)
f_s	Sparking frequency, forest-fire model	
I_4	Seismic intensity factor: number of earthquakes per year with size $\geq$ moment magnitude m	
k_c	Spring constant for connector spring, slider-block model	(9)
k_p	Spring constant for driver spring, slider-block model	(9)
m	Magnitude of an earthquake	(1)
m	Mass of each block in the slider-block model	(10)
m_w	Moment magnitude of an earthquake	(14)
M_0	Seismic moment of an earthquake	(14)
N	Noncumulative number of objects with a given size	
$\dot{N}$	Average recurrence interval per year of large earthquakes	
$N(r)$	Number of objects with linear dimension greater than r	(3)
N_a	Number of clusters of size A_a, site-percolation model	(5)
N_b	Number of objects in each bin, noncumulative distribution	
N_c	Cumulative number of objects $\geq$ a given size	
N_{CE}	Cumulative number of earthquakes with magnitude $\geq m$	(1)
$\dot{N}_{CE}$	Cumulative number of earthquakes per yr with magnitude $\geq m$	(1)
N_{CF}	Cumulative number of fires with area $\geq A_F$	
$\dot{N}_{CF}$	Cumulative number of fires per year with area $\geq A_F$	
N_{ci}	Cumulative sequence of numbers from summing N_i	
N_{CL}	Cumulative number of landslides with area $\geq A_L$	
N_e	Number of slip events with size A_e, slider-block model	

SYMBOL	DESCRIPTION	EQUATION WHERE INTRODUCED
N_F	Number of actual or model fires with size A_F	(4)
N_g	Total number of sites or cells in square grid	
N_i	Sequence of discrete numbers with length r_i	
N_L	Number of model avalanches with area A_L	
N_0	Number of time steps, slider-block model simulation	
N_S	Number of time steps in model simulations	(4)
p	Probability that a site is permeable, site-percolation model	
p_c	Critical value for p, site-percolation model	
r	Linear dimension of an object	(3)
r	Size of bin	
r_i	Lengths of successive objects in a series	
t	Time, slider-block model	(10)
V	Constant velocity of driver plate, slider-block model	
x_{ij}	Position of block (i, j), slider-block model	(9)
X_{ij}	Nondimensional position variable, slider-block model	(11)
α	Power-law exponent	(4)
	Stiffness of system, slider-block model	(11)
	Constant relating A_E with M_0	(15)
β	Power-law exponent	
ϕ	Ratio of static to dynamic friction, slider-block model	(11)
τ	Fisher exponent, site-percolation model	(5)
	Nondimensional time variable, slider-block model	(11)

APPENDIX 4.2.

BLACK AND WHITE OF FIGURES 4.19 AND 4.20

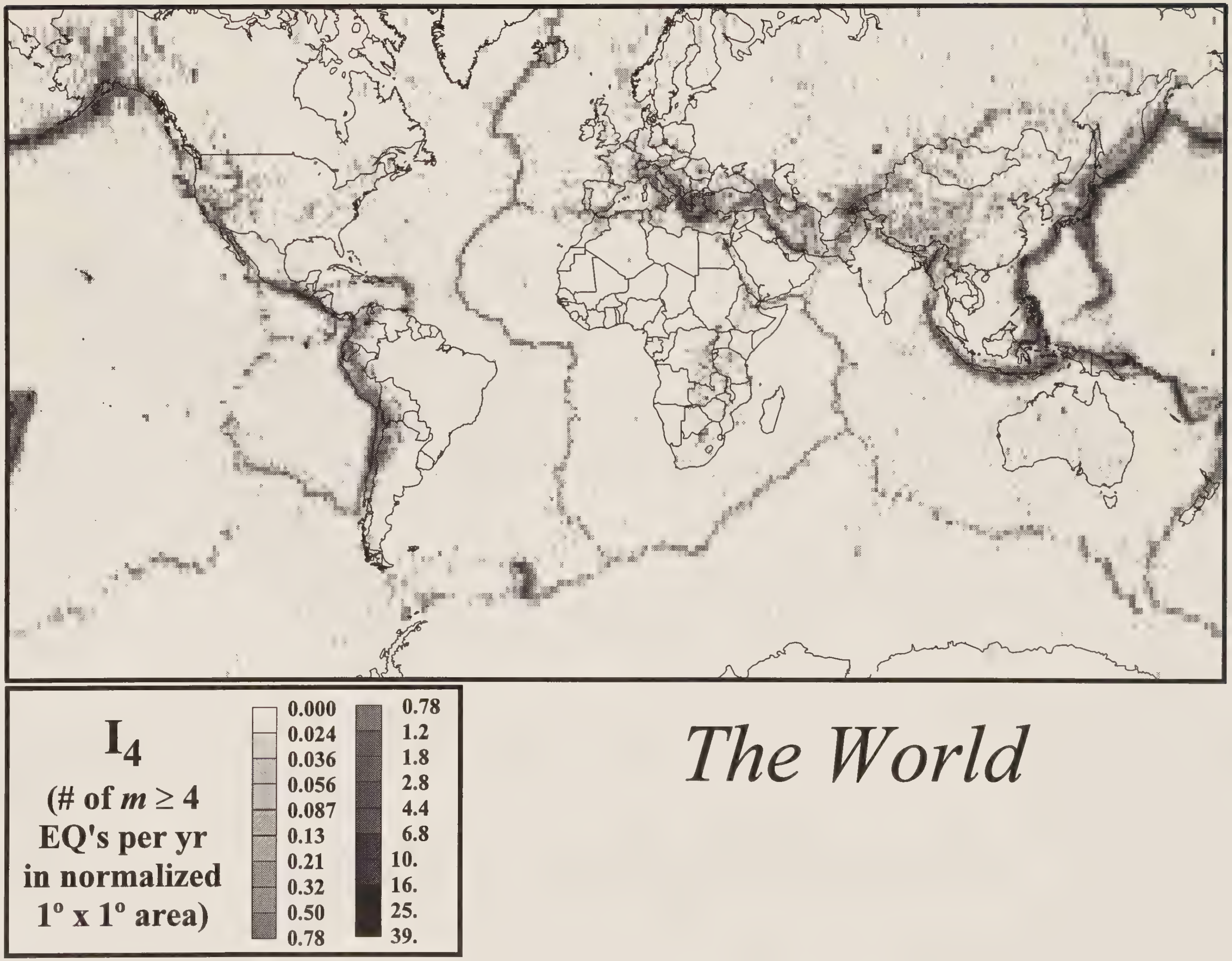
I_4
(# of $m \geq 4$
EQ's per yr
in normalized
1° x 1° area)
0.000
0.024
0.036
0.056
0.087
0.13
0.21
0.32
0.50
0.78
0.78
1.2
1.8
2.8
4.4
6.8
10.
16.
25.
39.

The World

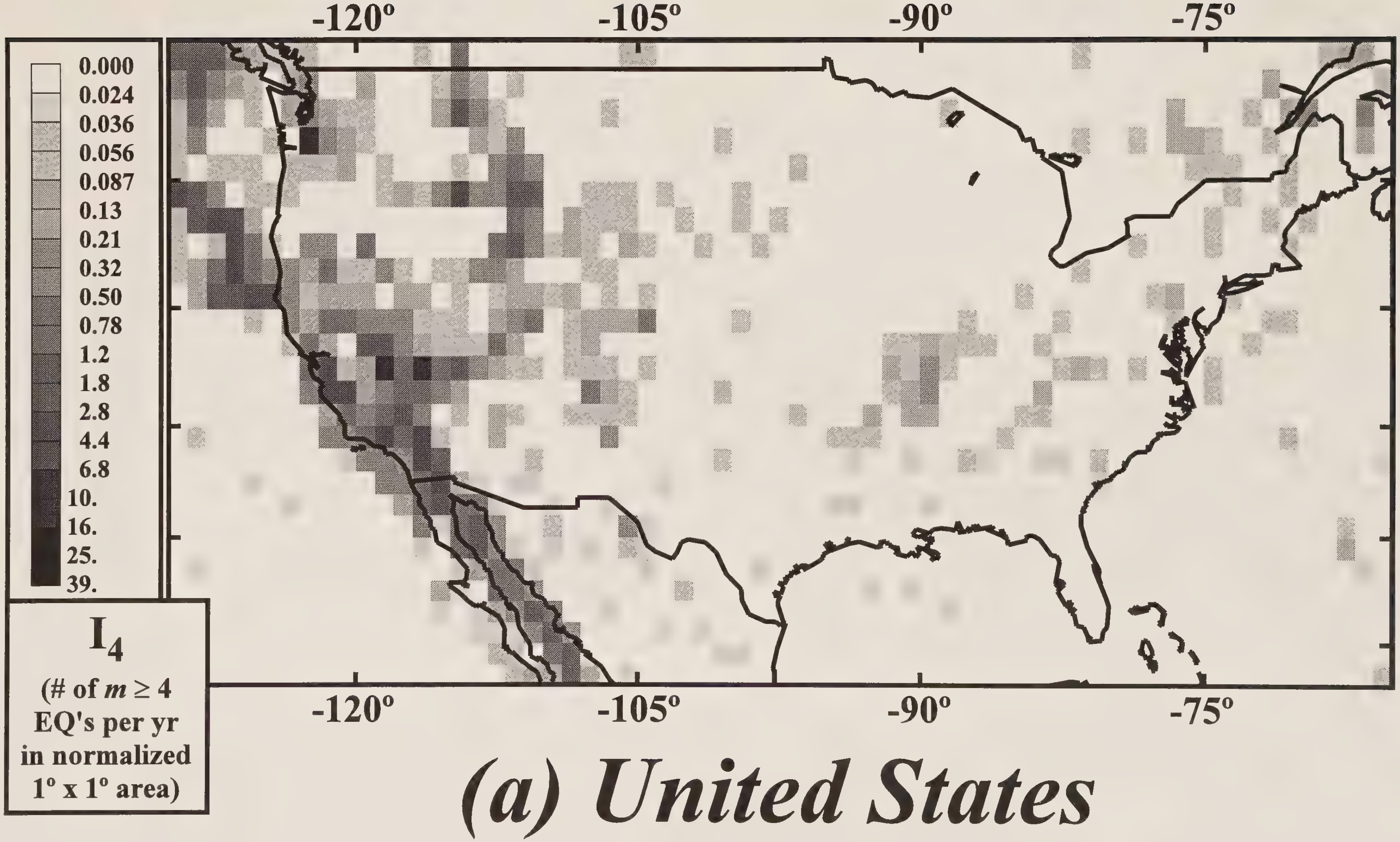

(a) United States

Figure 4.20 (Continued)

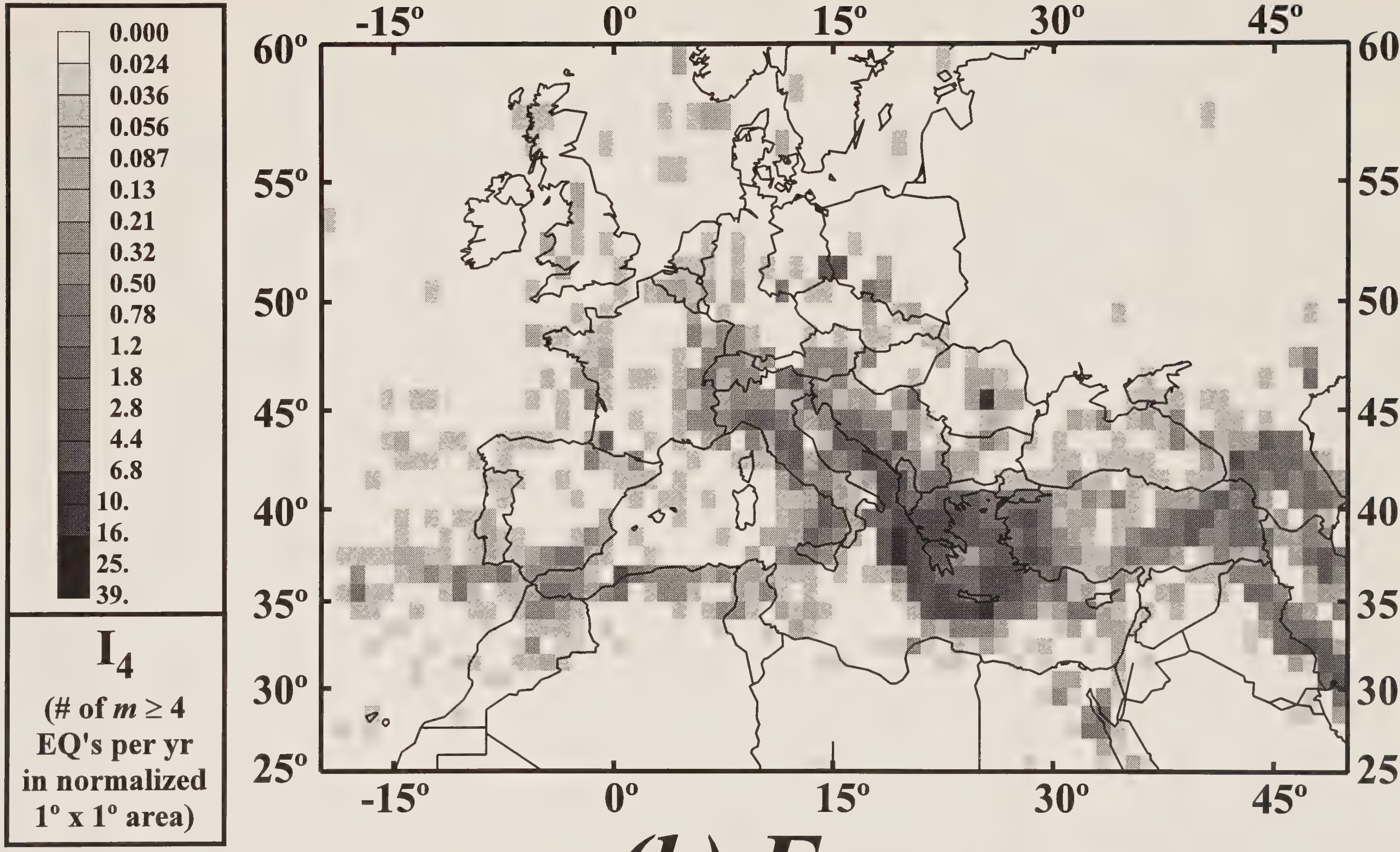

(b) Europe

REFERENCES

AKI, K. (1981). A probabilistic synthesis of precursory phenomena. In: D.W. Simpson and P.G. Richards (eds.), *Earthquake Prediction*, American Geophysical Union, Washington, D.C., 566-74.

AKI, K. (1987). Magnitude-frequency relation for small earthquakes: a clue to the origin of $f_{\max}$ of large earthquakes. *J. Geophys. Res.*, **92**:1,349-55.

ALBANO, E.V. (1994). Critical behavior of a forest-fire model with immune trees. *J. Phys.*, **A27**:L881-86.

ALBANO, E.V. (1995). Spreading analysis and finite-size scaling study of the critical behavior of a forest-fire model with immune trees. *Physica*, **A216**:213-26.

AUSTRALIAN CAPITAL TERRITORY BUSH FIRE COUNCIL (1996). Electronic data obtained from WWW site "Firebreak" which publishes the statistics from the ACT Bush Fire Council Annual Reports (1926-present).

BAK, P., CHEN, K., AND TANG, C. (1992). A forest-fire model and some thoughts on turbulence. *Phys. Lett.*, **A147**:297-300.

BAK, P., AND TANG, C. (1989). Earthquakes as a self-organized critical phenomenon. *J. Geophys. Res.*, **94**:15,635-7.

BAK, P., TANG, C., AND WIESENFELD, K. (1987). Self-organized criticality: an explanation of 1/f noise. *Phys. Rev. Lett*, **59**:381-4.

BAK, P., TANG, C., AND WIESENFELD, K. (1988). Self-organized criticality. *Phys. Rev.*, **A38**:364-74.

BLODGETT, T.A. (1998). *Andean landslide hazards, estimating erosion rates in the Andes from landslides, and classifying landslides on satellite images.* Ph.D. Thesis, Department of Geological Sciences, Cornell University, Ithaca, NY 14853-1504.

BRETZ, M., CUNNINGHAM, J.B., KURCZYNSKI, P.L., AND NORI, F. (1992). Imaging of avalanches in granular materials. *Phys. Rev. Lett.*, **69**:2,431-4.

BROWN, S.R., SCHOLZ, C.H., AND RUNDLE, J.B. (1991). A simplified spring-block model of earthquakes. *Geophys. Res. Lett.*, **18**:215-8.

BURRIDGE, R., AND KNOPOFF, L. (1967). Model and theoretical seismicity. *Seis. Soc. Am. Bull.*, **57**:341-71.

CAMELBEECK, T., AND MEGHRAOUI, K. (1996). Large earthquakes in northern Europe more likely than once thought. *EOS*, **77**:405.

CARLSON, J.M., AND LANGER, J.S. (1989). Mechanical model of an earthquake fault. *Phys. Rev.*, **A40**:6,470-84.

CARLSON, J.M., LANGER, J.S., AND SHAW, B.E. (1994). Dynamics of earthquake faults. *Rev. Mod. Phys.*, **66**:657-70.

CHRISTENSEN, K., FLYVBJERB, H., AND OLAMI, Z. (1993). Self- organized critical forest-fire model: mean-field theory and simulation results in 1 to 6 dimensions. *Phys. Rev. Lett.*, **71**:2,737-40.

CLAR, S., DROSSEL, B., AND SCHWABLE, F. (1994). Scaling laws and simulation results for the self-organized forest-fire model. *Phys. Rev.*, **E50**:1,009-18.

CLAR, S., DROSSEL, B., AND SCHWABLE, F. (1996). Forest fires and other examples of self-organized criticality. *J. Phys. C*, **8**:6,803-24.

DAVISON, F., AND SCHOLZ, C.H. (1985). Frequency-moment distribution of earthquakes in the Aleutian Arc: a test of the characteristic earthquake model. *Bull. Seism. Soc. Am.*, **75**:1,349-62.

DENSMORE, A.L., ANDERSON, R.S., MCADOO, G.B., AND ELLIS, M.A. (1997). Hillslope evolution by bedrock landslides. *Science*, **275**:369-72.

DROSSEL, B., CLAR, S., AND SCHWABLE, F. (1993). Exact results for the one-dimensional self-organized critical forest-fire model. *Phys. Rev. Lett.*, **71**:3,739-42.

DROSSEL, B., CLAR, S., AND SCHWABLE, F. (1994). Crossover from percolation to self-organized criticality. *Phys. Rev.*, **E50**:2,399-402.

DROSSEL, B., AND SCHWABLE, F. (1992a). Self-organized criticality in a forest-fire model. *Phys. Rev. Lett.*, **69**:1,629-32.

DROSSEL, B., AND SCHWABLE, F. (1992b). Self-organized criticality in a forest-fire model. *Physica*, **A191**:47-50.

DROSSEL, B., AND SCHWABLE, F. (1993a). Self-organization in a forest-fire model. *Fractals*, **1**:1,022-9.

DROSSEL, B., AND SCHWABLE, F. (1993b). Forest-fire model with immune trees. *Physica*, **A199**:183-97.

DROSSEL, B., AND SCHWABLE, F. (1994). Formation of space-time structure in a forest-fire model. *Physica*, **A204**:212-29.

EVERNDEN, J.F. (1970). Study of the regional seismicity and associated problems. *Seis. Soc. Am. Bull.*, **60**:393-446.

EVESQUE, P. (1991). Analysis of statistics of sandpile avalanches using soil-mechanics results and concepts. *Phys. Rev.*, **A43**:2,720-40.

FEDER, J. (1995). The evidence for self-organized criticality in sand-pile dynamics. *Fractals*, **3**:431-43.

GRUMBACHER, S.K., MCEWEN, K.M, HALVERSON, D.A., JACOBS, D.T., AND LINDNER, J. (1993). Self-organized criticality: an experiment with sandpiles. *Am. J. Phys.*, **61**:329-35.

GUTENBERG, B., AND RICHTER, C.F. (1954). *Seismicity of the earth and associated phenomenon, 2nd ed.* Princeton University Press (Princeton), 310 p.

HARP, E.L., AND JIBSON, R.L. (1995). *Inventory of landslides triggered by the 1994 Northridge, California earthquake.* United States Geological Survey Open File Report 95-213.

HARVARD CENTROID-MOMENT TENSOR DATA BASE (1997). Electronic Data. Department of Earth and Planetary Sciences, Harvard University, Cambridge.

HELD, G.A., SOLINA II, D.H., KEANE, D.T., HAAG, W.J., HORN, P.M., AND GRINSTEIN, G. (1990). Experimental study of critical-mass fluctuations in an evolving sandpile. *Phys. Rev. Lett.*, **65**:1,120-3.

HENLEY, C.L. (1993). Statics of a "self-organized" percolation model. *Phys. Rev. Lett.*, **71**:2,741-4.

HEYERDAHL, E., AND AGEE, J. (1994). *Fire history data base of the western United States.* Interagency Agreement DW 12934530, EPA, USDA Forest Service, University of Washington, Seattle.

HINZE, W.J., BRAILE, L.W., KELLER, G.R., AND LIDIAK, E.G. (1988). Models for midcontinent tectonism: an update. *Rev. Gephys.*, **26**:699-717.

HISCOTT, R.N., COLELLA, A., PEZARD, P., LOVELL, M., AND MALINVERNO, A. (1992). Sedimentology of deep-water volcaniclastics, Oligocene Izu-Bonin forearc basin, based on formation microscanner images. *Proc. Ocean Dril. Prog. Sci. Results*, **126**:75-96.

HONECKER, A., AND PESCHEL, I. (1996). Critical properties of the one-dimensional forest-fire model. *Physica.,* **A229**:478-500.

HOVIUS, N., STARK, C.P., AND ALLEN, P.A. (1997). Sediment flux from a mountain belt derived by landslide mapping. *Geology*, **25**:231-4.

HUANG, J., NARKOUNSKAIA, G., AND TURCOTTE, D.L. (1992). A cellular-automata, slider-block model for earthquakes; II, Demonstration of self-organized criticality for a 2-D system. *Geophys. J. Int.,* **111**:259-69.

HUANG, J., AND TURCOTTE, D.L. (1990). Are earthquakes an example of deterministic chaos? *Geophys. Res. Lett.*, **17**:223-6.

JOHANSEN, A. (1994). Spatio-temporal self-organization in a model of disease spreading. *Physica*, **D78**:186-93.

JOHNSTON, A.C., AND NAVA, S.J. (1985). Recurrence rates and probability estimates for the New Madrid seismic zone. *J. Geophys. Res.*, **90**:6,737-53.

KADANOFF, L.P., NAGEL, S.R., WU, L., AND ZHOU, S.M. (1989). Scaling and universality in avalanches. *Phys. Rev.*, **A39**:6,524-33.

KANAMORI, H. (1977). The energy release in great earthquakes. *J. Geophys. Res.*, **82**:2,981-7.

KASISCHKE, E.S., AND FRENCH, N.H.F. (1995). Locating and estimating the areal extent of wildfires in Alaskan boreal forest using multiple-season AVHRR NDVI composite data. *Remote Sensing of the Environment*, **51**:263-75.

KOSSOBOKOV, V.G., AND TURCOTTE, D.L. (1996). A systematic global assessment of the seismic hazard. (abstract) *EOS* **77**:F480.

LAY, T., AND WALLACE, T.C. (1995). *Modern global seismology.* Academic Press (San Diego), 521 p.

LORETO, V., PIETRONERO, L., VESPIGNANI, A., AND ZAPPERI, S. (1995). Renormalization group approach to the critical behavior of the forest-fire model. *Phys. Rev. Lett.*, **75**:465-8.

LORETO, V., VESPIGNANI, A., AND ZAPPERI, S. (1996). Renormalization scheme for forest-fire models. *J. Phys.*, **A29**:2,981-3,004.

MOSNER, W.K., DROSSEL, B., AND SCHWABLE, F. (1992). Computer simulations of the forest-fire model. *Physica*, **A190**:205-17.

NAGEL, S.R. (1992). Instabilities in a sandpile. *Rev. Mod. Phys.*, **64**:321-25.

NAKANISHI, H. (1990). Cellular-automaton model of earthquakes with deterministic dynamics. *Phys. Rev.*, **A41**:7,086-9.

NAKANISHI, H. (1991). Statistical properties of the cellular automata model for earthquakes. *Phys. Rev.*, **A43**:6,613-21.

NARKOUNSKAIA, G., AND TURCOTTE, D.L. (1992). A cellular-automata, slider block model for earthquakes, I. Demonstration of chaotic behavior for a low order system. *Geophys. J. Int.*, **111**:250-8.

NATIONAL INTERAGENCY FIRE CENTER (1996). Electronic data obtained from Andrea Olson, U.S. Fish and Wildlife Service, Boise, ID.

NEWMARK, N.M. (1965). Effects of earthquakes on dams and embankments. *Geotechnique*, **15**:139-60.

NILSEN, T.H., BARTOW, J.A., FRIZZELL JR., V.A., AND SIMS, J.D. (1975). *Preliminary photointerpretation maps of landslide and other surficial deposits of 56 7 1/2-minute quadrangles in the southeastern San Francisco Bay region, Alameda, Contra Costa, and Santa Clara counties, California.* USGS Open-File Report, OF 75-0277, U. S. Geological Survey, Open-File Service Section, Western Distribution Branch, Federal Center, Denver, CO.

NOEVER, D.A. (1993). Himalayan sandpiles. *Phys. Rev.,* **E47**:724-5.

NUTTLI, O.W. (1983). Average seismic source-parameter relations for midplate earthquakes. *Seis. Soc. Am. Bull.*, **73**:519-35.

OHMORI, H., AND HIRANO, M. (1988). Magnitude, frequency and geomorphological significance of rocky mud flows, landcreep and the collapse of steep slopes. *Z. Geomorph. N.F., Suppl.*, **67**:55-65.

OHMORI, H., AND SUGAI, T. (1995). Toward geomorphometric models for estimating landslide dynamics and forecasting landslide occurrence in Japanese mountains. *Z. Geomorph. N.F., Suppl.*, **101**:149-64.

PACHECO, J., SCHOLZ, C.H., AND SYKES, L.R. (1992). Changes in frequency-size relationship from small to large earthquakes. *Nature*, 355:71-3.

PELLETIER, J.D., MALAMUD, B.D., BLODGETT, T.A., AND TURCOTTE, D.L. (1997). Scale-invariance of soil moisture variability and its implications for the frequency-size distribution of landslides. In press, *Engineering Geology*.

PROTHERO, D.R. (1990). *Interpreting the stratigraphic record.* W.H. Freeman and Company (New York), 410 p.

PUHL, H. (1992). On the modeling of real sand piles. *Physica*, **A182**:295-319.

PYE, K. (1994). Properties of sediment particles. In K. Pye (ed.), *Sediment transport and depositional processes*, Blackwell Scientific Publications (Oxford), 1-24.

ROSENDAHL, J., VEKIC, M., AND KELLEY, J. (1993). Persistent self-organization of sandpiles. *Phys. Rev.*, **E47**:1401-4.

ROSENDAHL, J., VEKIC, M., AND RUTLEDGE, J.E. (1994). Persistent self-organization of sandpiles. *Phys. Rev. Lett.*, **73**:537-40.

ROTHMAN, D.H., GROTZINGER, J.P., AND FLEMINGS, P. (1994). Scaling in turbidite deposition. *J. Sed. Petrol.*, **A64**:59-67.

SASAKI, Y., ABE, M., AND HIRANO, I. (1991). Fractals of slope failure size-number distribution. *J. Japan Sci. Eng. Geology*, **32**:1-11.

SCHOLZ, C.H. (1997). Size distributions for large and small earthquakes. *Bull. Seism. Soc. Am.*, **87**:1074-77.

SIEH, K.E. (1978). Slip along the San Andreas fault associated with the great 1857 earthquake. *Seis. Soc. Am. Bull.*, **68**:1421-48.

SIEH, K.E., STUIVER, M., AND BRILLINGER, D. (1989). A more precise chronology of earthquakes produced by the San Andreas fault in southern California. *J. Geophys. Res.*, **94**:603-23.

SOUTHERN CALIFORNIA SEISMOGRAPHIC NETWORK (SCSN) CATALOG (1995). SCSN catalog in electronic format at the Southern California Earthquake Center (SCEC) data center. California Institute of Technology, Pasadena, California.

SOUTHERN CALIFORNIA EARTHQUAKE CENTER (SCEC) DATA CENTER CATALOG (1995). SCEC catalog in electronic format. California Institute of Technology, Pasadena, California.

STAUFFER, D., AND AHARONY, A. (1992). *Introduction to percolation theory, 2nd edition.* Taylor and Francis (London), 181 p.

STROCKA, B., DUARTE, J.A.M.S., AND SCHRECKENBERG, M. (1995). The self-organized critical forest-fire model with trees and bushes. *J. Phys. 1 France*, **5**:1,233-8.

SUGAI, T., OHMORI, H., AND HIRANO, M. (1994). Rock control on magnitude-frequency distribution of landslide. *Transactions, Japanese Geomorphological Union*, **15-3**:233-51.

TURCOTTE, D.L. (1989). A fractal approach to probabilistic seismic hazard assessment. *Tectonophys.*, **167**:171-7.

TURCOTTE, D.L. (1997). *Fractals and chaos in geology and geophysics, 2nd edition.* Cambridge University Press (Cambridge), 300 p.

UNITED STATES GEOLOGICAL SURVEY (1996). Global Hypocenter Data Base CD ROM supplemented by Preliminary Determination of Epicenters (PDE) catalog. National Earthquake Information Center, United States Geological Survey, Denver, Colorado.

WHITEHOUSE, I.E., AND GRIFFITHS, G.A. (1983). Frequency and hazard of large rock avalanches in the Southern Alps, New Zealand. *Geology*, **11**:331-4.

Chapter Five: The 1993 Mississippi River Flood: A One Hundred or a One Thousand Year Event?*

ABSTRACT

Power-law (fractal) extreme-value statistics are applicable to many natural phenomena under a wide variety of circumstances. Data from a hydrologic station in Keokuk, Iowa, shows the great flood of the Mississippi River in 1993 has a recurrence interval on the order of 100 years using power-law statistics applied to partial-duration flood series and on the order of 1,000 years using a log-Pearson type 3 (LP3) distribution applied to annual series. The LP3 analysis is the federally adopted probability distribution for flood-frequency estimation of extreme events. We suggest that power-law statistics are preferable to the LP3 analysis. As a further test of the power-law approach we consider paleoflood data from the Colorado River. We compare power-law and LP3 extrapolations of historical data with these paleofloods. The results are remarkably similar to those obtained for the Mississippi River. Recurrence intervals from power-law statistics applied to Lees Ferry discharge data are generally consistent with inferred 100- and 1,000-year paleofloods, whereas LP3 analysis gives recurrence intervals that are orders of magnitude longer. For both the Keokuk and Lees Ferry gauges, the use of an annual series introduces an artificial curvature in log-log space that leads to an underestimate of severe floods. Power-law statistics

---

*Published as Malamud, B. D., Turcotte, D. L., and Barton, C. C. (1996). The 1993 Mississippi River flood: A one-hundred or a one-thousand year event? *Environmental and Engineering Geoscience*, **II(4)**:479-486.

are predicting much shorter recurrence intervals than the federally adopted LP3 statistics. We suggest that if power-law behavior is applicable, then the likelihood of severe floods is much higher. More conservative dam designs and land-use restrictions may be required.

INTRODUCTION

The great flood of 1993 in the upper Mississippi River basin once again focused attention on the reliability of flood-frequency forecasts. A fundamental question in calculating flood probabilities is whether the statistical methods used provide an adequate estimate for expected recurrence intervals. The results presented in this paper suggest that federally adopted techniques for flood-frequency forecasting in the Mississippi River basin seriously underestimate recurrence intervals of extreme floods.

Floods are complex phenomena involving coupled meteorological and hydrological processes; they are also influenced by human facilities and activities, including dams, channelization, and land use. Recurrence intervals are a means of expressing the odds of a given magnitude flood being exceeded in any year and are an important factor in flood control, land-use regulation, emergency planning, and insurance considerations.

Historically, flood-frequency estimation has been treated strictly on an empirical basis and a wide variety of statistical distributions have been used. The most commonly used frequency-magnitude distributions in hydrology can be divided into four groups: the normal family (normal, log-normal, log-normal type 3), the general extreme-value (GEV) family

(GEV, Gumbel, log-Gumbel, Weibull), the Pearson type 3 family (Pearson type 3, log-Pearson type 3), and the generalized Pareto distribution. *Stedinger et al.* (1993) provide an excellent discussion and review of these different distributions. Severe floods are associated with the tails of the flood-frequency distributions. Two extreme behaviors for the tails are power-law and exponential. Power-law tails give much shorter estimates of flood recurrence intervals than exponential tails.

The standard approach for flood-frequency estimation is to consider a sequence of maximum annual floods and obtain the best empirical fit of the chosen statistical distribution to this data set. The best fit is obtained by equating the statistical moments of the data to the distribution. Additional constraints, such as the censoring of outlier points, are commonly used. In the United States, the federally adopted approach to flood-frequency estimation is to fit logarithms of the annual peak discharges to the Pearson type 3 distribution (*U.S. Water Resources Council*, 1982); some countries have adopted other types of distributions. Australia uses log-Pearson type 3 (LP3) distributions as their standard for flood-frequency estimation. However, *Vogel et al.* (1993) have argued that in many parts of Australia generalized Pareto distributions perform significantly better than LP3.

In this paper the validity of power-law statistics in estimating floods is considered. Many natural phenomena satisfy power-law (fractal) frequency-magnitude statistics. Examples are found in a wide variety of circumstances and include fragmentation, earthquakes, volcanic eruptions, mineral deposits, and land forms (*Turcotte*, 1992). *Turcotte and Greene*

(1993) have argued the validity of power-law statistics to floods in the United States utilizing 14 USGS bench-mark gauging stations. *Turcotte* (1994) extended these arguments by studying 1,200 gauging station records across the United States.

We examine the great Mississippi River flood of 1993 with power-law and LP3 analyses, concentrating on historical flood records from Keokuk, Iowa (Figure 5.1). This station has a long record (1879-present) and is representative of flood discharges on the Mississippi River during the great flood of 1993. A difficulty with calculating recurrence intervals is that they are usually based on hydrologic station records of continuous discharges, which are generally short, on the order of a hundred years or less. As a further test of the power-law approach we consider paleofloods on the Colorado River in the Grand Canyon of Arizona. Paleoflood data give an estimate of discharge for single extreme events over a much longer time period.

DISTRIBUTIONS

Power-Law

The volumetric discharge $q(t)$ at a point on a river is generally a continuous time series. We are concerned with the extreme values of this time series and define $Q(T)$ to be the maximum discharge associated with a recurrence interval of T years. For example, $Q(100)$ would be the maximum discharge (flood) that has an average recurrence interval of 100 years, i.e., in any one year, there is a one-in-one hundred chance of the peak discharge equaling or exceeding $Q(100)$.

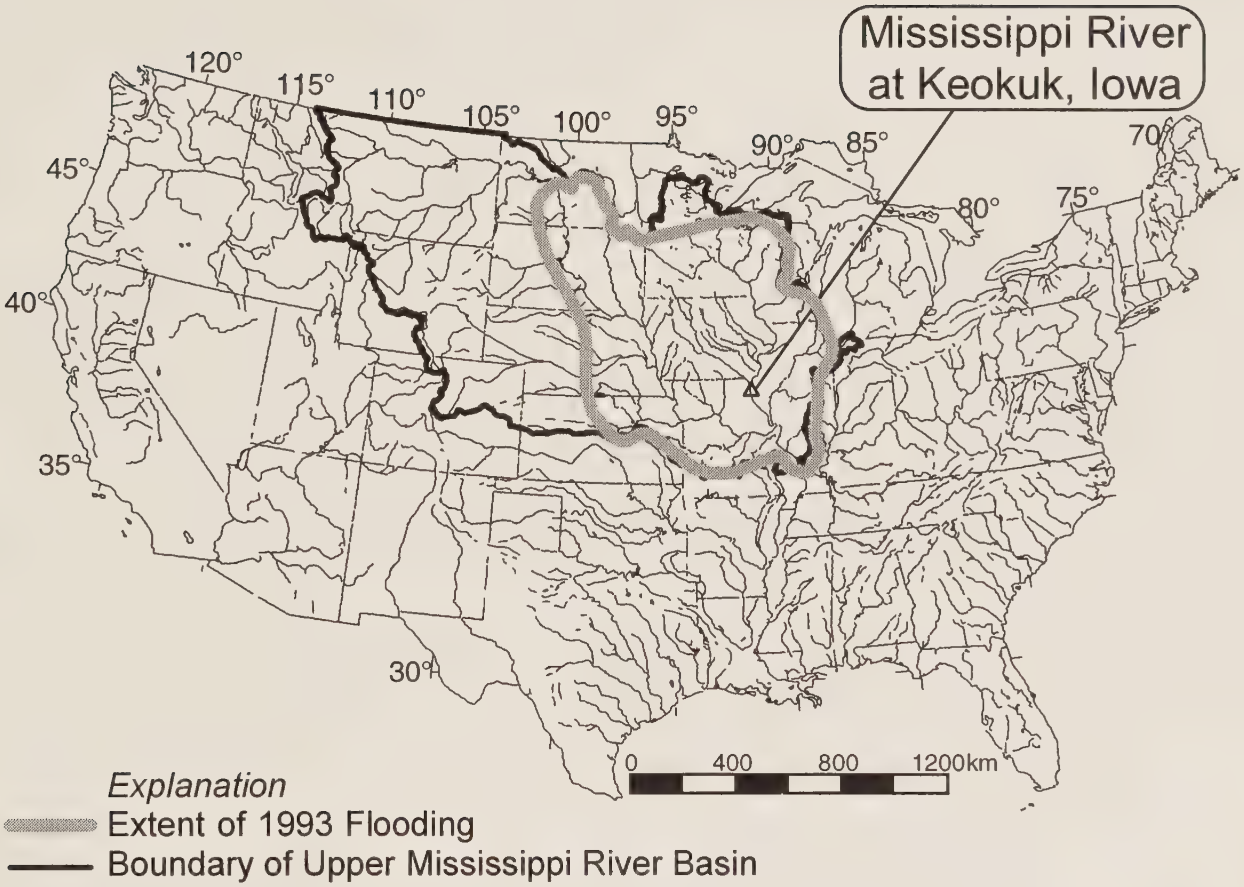

Figure 5.1. Map of the United States showing the upper Mississippi River basin and the extent of flooding during 1993 (*U. S. Geological Survey*, 1996). Also shown is the location of the Keokuk, Iowa, streamflow-gauging station used in this paper.

The power-law distribution for flood-frequency takes the form

$$Q(T) = CT^{\alpha} \tag{5.1}$$

where C and α are regression coefficients. Taking the logarithms of both sides of Equation 5.1 gives

$$\log Q(T) = \alpha \log T + C' \tag{5.2}$$

This scale invariant distribution can be expressed in terms of F, the ratio of the peak discharge over a 10-year interval to the peak discharge over a 1-year interval. With self-similarity the parameter F is also the ratio of the 100-year peak discharge to the 10-year peak discharge.

$$F = \frac{Q(10)}{Q(1)} = \frac{Q(100)}{Q(10)} = \text{constant} \tag{5.3}$$

In terms of α we have

$$F = 10^{\alpha} \tag{5.4}$$

If the flood-frequency factor F is large the ratio of the 10-year to the 1-year flood will be large, if F is small the ratio will be small. The parameter α is the slope of a $\log(Q)$ versus $\log(T)$ plot. Parameters α and F are related by Equation 5.4. As in all applications of power-law distributions to natural processes, there are upper and lower limits to the validity of the power-law.

Log-Pearson Type 3

The LP3 distribution has been adopted by Federal agencies in the United States for flood-frequency estimation (*U. S. Water Resources Council*, 1982). The LP3 distribution describes a random variable whose logarithm is a Pearson type 3 distribution. The logarithms of an annual flood series are used to calculate the mean, standard deviation, and skew. These three moments determine the shape, scale, and location parameters that characterize the LP3 distribution. The LP3 fit involves three empirical constants whereas the power-law fit involves only two. The *U. S. Water Resources Council* (1982) outlines the application of the LP3 to an annual flood series. In our analyses, we use these methods for dealing with outliers, conditional probability, weighted skew, and K coefficients. The weighted skew coefficient is calculated using the generalized skew coefficient as obtained from the *U. S. Water Resources Council* (1982) generalized skew map.

DATA ANALYSIS

Annual and Partial-Duration Flood Series

An annual flood is the peak discharge during a water year, where the water year is defined to be a 12-month period from October 1 of the previous year through September 30 of the water year. For example, the 1995 water year extends from October 1, 1994, through September 30, 1995. Data sets used in our analyses consist of mean daily discharges and are used to determine the peak discharge (flood) in each water year. The annual flood series is the sequence of annual floods over a specified interval of time. A major problem with an annual flood series is that

several floods in a given water year may be larger than the annual flood in another water year. To overcome this difficulty, we also consider a partial-duration flood series where more than one flood can occur in a water year. In our definition of a partial-duration flood series, peak discharges must be separated by at least thirty days in order to be classified as separate floods. For a given water year we take Q, the maximum mean daily discharge (flood) for that year, and delete all values thirty days on either side. We then take the next largest Q, and again delete all values thirty days on either side. We continue until we have the six largest Q's for that water year. This process is repeated for the other water years. The total number of water years in our data set is N. To arrive at the partial-duration flood series the $6N$ values of Q are ordered from largest to smallest. Our final partial-duration flood series is the N largest ordered Q's, i.e., the subset of largest ordered Q's that corresponds with the number of water years considered.

Other definitions for a partial-duration flood series can be made (*Hipel*, 1994). For example, we could have required that the Q's in the partial-duration series be separated by sixty days instead of thirty days, or applied the criteria that the flow q must drop to some fraction, say 50%, of the flood value Q before another flood was chosen. Another approach is to use the peaks over threshold method (*Hosking and Wallis*, 1987; *Davison and Smith*, 1990; *Barrett*, 1992). In this method the peaks over a chosen threshold, typically one to five per year, define the partial-duration flood series. We have applied several partial-duration definitions to our data sets and find that the differences are small; as such we only use the definition that Q's are separated by at least thirty days.

For both the annual flood series and the partial-duration flood series the Q's of each flood are ranked ($r = 1, 2, 3, \ldots, N$) from largest to smallest, where N is the number of water years in the data set. If Q is equaled or exceeded r times in N years (N is large), then the recurrence interval in years is $T = N/r$. As an example, if we take a data set with $N =$ 114 water years, the largest Q is assigned a recurrence interval of $T =$ 114/1 = 114 years, the second largest $T = 114/2 = 57$ years, and so forth until the 114th value with $T = 114/114 = 1$ year. This is entirely equivalent to a cumulative frequency-size analysis where r, the cumulative number greater than a size, is plotted as a function of size. This technique is routinely applied to the frequency-size statistics of earthquakes and other extreme-value events (*Turcotte*, 1992).

Data

On the basis of length of record and drainage basin size we have chosen gauging station 05474500 on the Mississippi River at Keokuk, Iowa, to be representative of flooding statistics on the Mississippi River during the great 1993 flood. The drainage area upstream of this station is 308,000 km^2 and a 117-year record of mean daily discharges from 1879 to 1995 is available (*Slack and Landwehr*, 1992; *May*, 1996). We use this data to construct both annual and partial-duration flood series for the gauge at Keokuk, Iowa. In our analyses, we calculate flood-frequency forecasts that would be made with data available before the great 1993 Mississippi River flood occurred (water years 1879-1992) and then compare how the forecasts change with the addition of the 1993 flood

(water years 1879-1995). For each time period, we estimate flood-frequency using LP3 applied to annual series, and compare these with power-laws applied to partial-duration series.

One of the most extensive studies of paleofloods was carried out by *O'Connor et al.* (1994). These authors used the stratigraphic record to quantify large floods during the last 4,500 years at Axehandle Alcove on the Colorado River in the Grand Canyon, Arizona. We compare their geologic estimates of the lower bounds of discharges associated with the largest paleofloods that occurred in the last 4,500 years with historical discharge data available from water years 1921-1962 at Lees Ferry, Arizona (*ADAPS*, 1996). The Lees Ferry gauge at USGS station 09380000 has a drainage area of 289,600 km^2 and is located on the Colorado River in Arizona, 3 km upstream of Axehandle Alcove. Unregulated daily discharge data exists for water years 1921-1962. Discharge has been regulated by the Glen Canyon Dam since the beginning of the 1963 water year.

RESULTS

Mississippi River at Keokuk, Iowa

In Figure 5.2 (1879-1992) and Figure 5.3 (1879-1995) the logarithms of the Keokuk floods, log(Q), are plotted against the logarithms of the recurrence intervals, log(T). For both time periods, the annual and partial-duration flood series strongly diverge for periods of less than about 5 years because multiple floods in some water years are much larger than the largest flood in other water years.

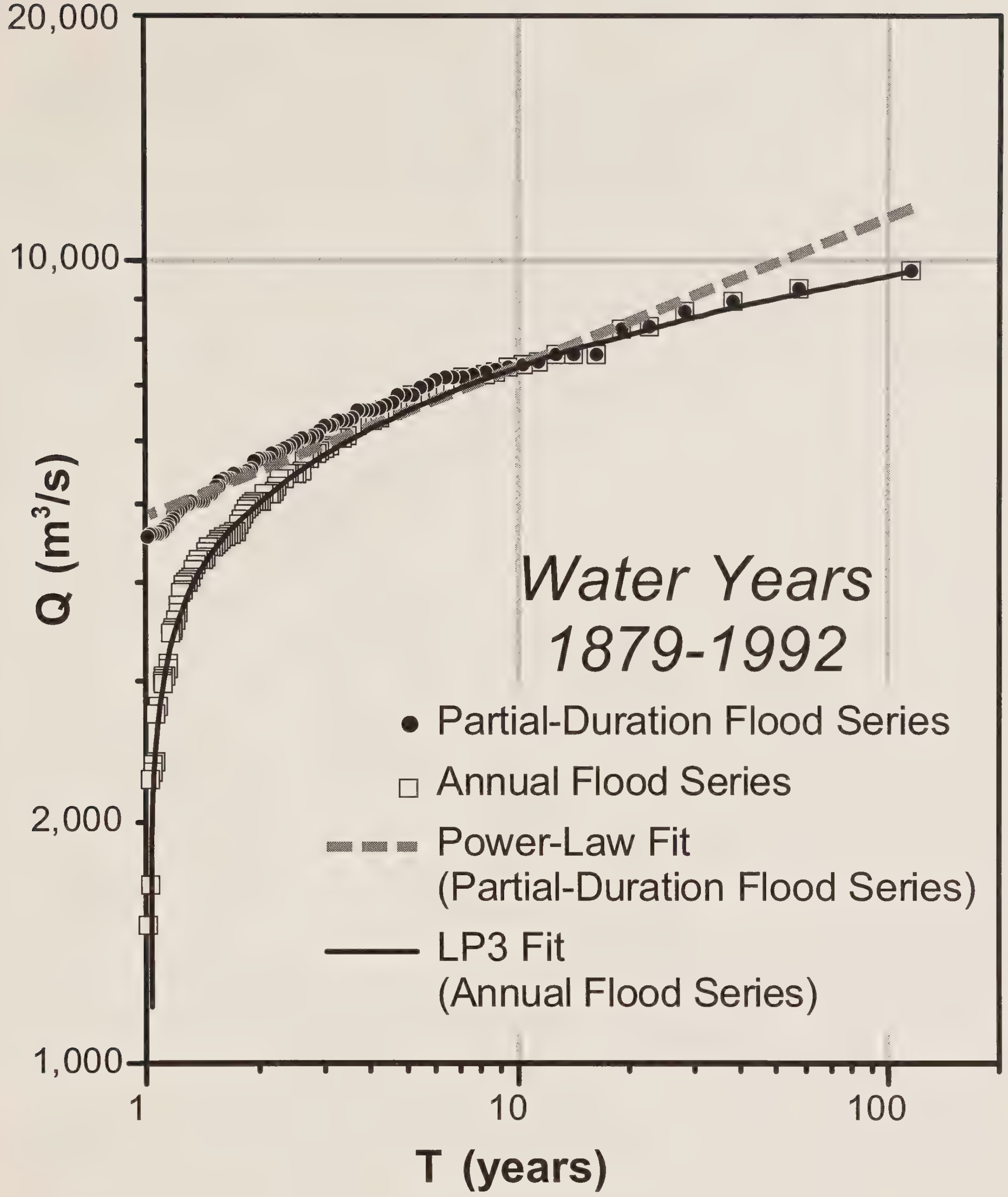

Figure 5.2. Dependence of the maximum daily discharge *Q* associated with the period *T* on the period *T*. The partial-duration and annual flood series for station 05474500 on the Mississippi River at Keokuk, Iowa, are shown for water years 1879-1992. Also included is the least-squares power-law fit for the partial-duration flood series, as well as the log-Pearson type 3 (LP3) distribution based on the annual flood series and the procedures of Bulletin 17B (*U. S. Water Resources Council*, 1982).

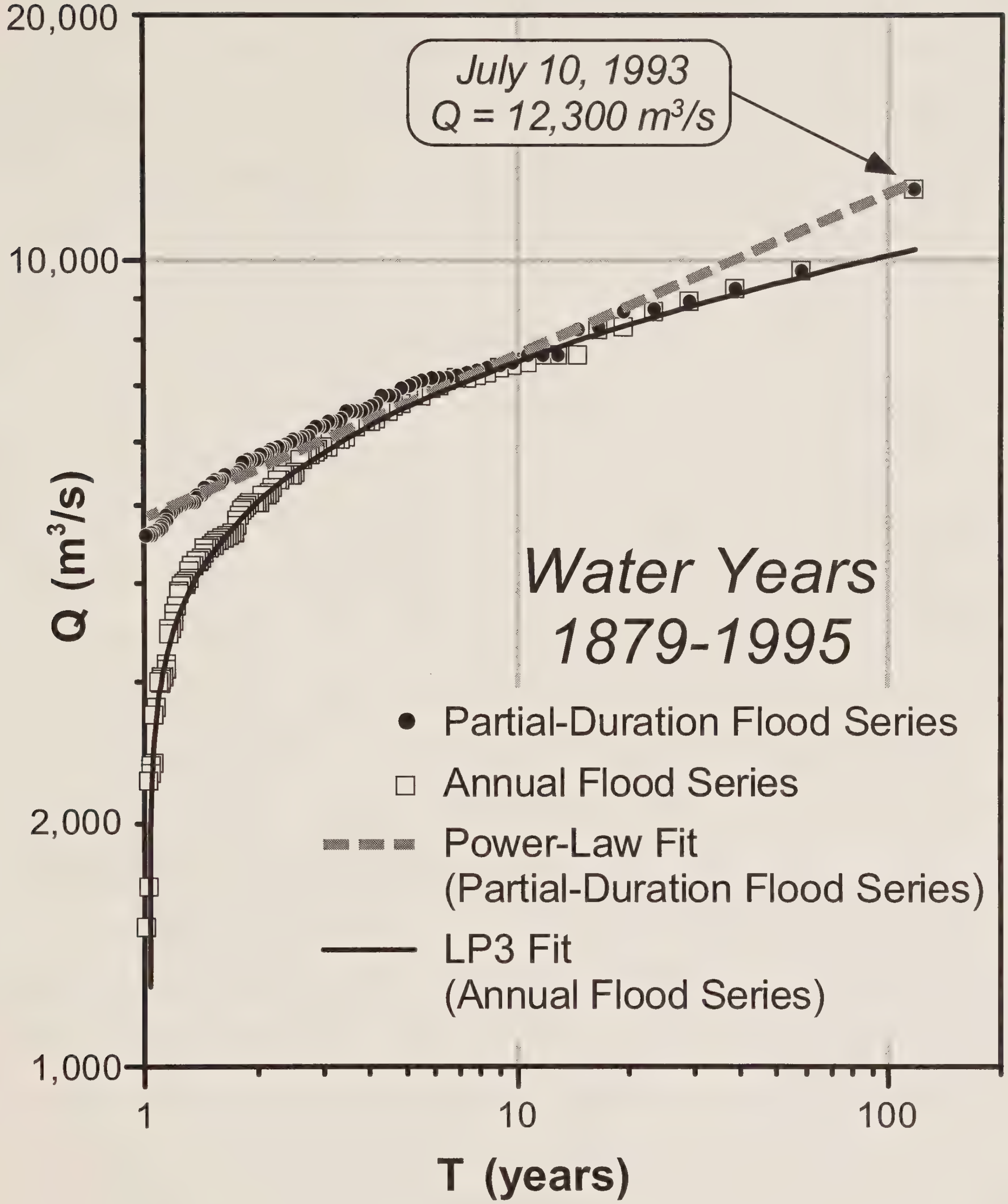

Figure 5.3. Same as Figure 5.2 except the period considered is water years 1879-1995. The maximum daily discharge associated with the 1993 flood is shown.

For a power-law distribution of floods the relation between log(Q) and log(T) is given in Equation 5.2. In log-log space a power-law distribution corresponds to a straight line with slope α and intercept C'. The best-fit straight lines to the partial-duration Keokuk flood series for 1879-1992 and 1879-1995 using a least-squares fit in log-log space give respectively $\alpha = 0.19, 0.20$ and $C' = 3.69, 3.68$ with an $r^2 = 0.97, 0.94$. The corresponding flood-frequency factors from Equation 5.4 are $F = 1.53$ and 1.58. The best-fit straight lines for the two time periods are given separately in Figures 5.2 (1879-1992) and 5.3 (1879-1995) and together in Figure 5.4. Extrapolation of the straight line for water years 1879-1992 to the maximum daily flow during the 1993 flood, $Q = 12{,}300$ m^3/s, results in a recurrence interval of $T = 151$ years. With the addition of 1993-1995 (water years 1879-1995) this extrapolation is reduced to a recurrence interval of $T = 106$ years. The two forecasts do not differ significantly from one another (Figure 5.4) and are consistent with the 1993 flood being a typical 100-year flood.

Another consideration is whether the extrapolated recurrence intervals for Keokuk would be significantly different for much smaller subsets of the 1879-1995 period. Using the same procedure for two 32-year periods, extrapolation of the best fit power-law line to a discharge the size of the great flood of 1993 results in recurrence intervals at Keokuk of 179 and 165 years for the periods 1900-1931 and 1932-1963. The results for the two 32-year periods do not vary significantly from the recurrence intervals of 151 and 106 years as obtained for the 114-year (1879-1992) and 117-year (1879-1995) periods.

The best LP3 distribution is found using the annual flood series from the gauge at Keokuk, Iowa, and the procedures as outlined by the *United States Water Resources Council* (1982). The result using water years 1879-1992 is given in Figure 5.2. After two low outliers were censored, the logarithms of the remaining 112 points were used to obtain the first three moments: $\bar{X}$ = mean = 3.70, S = standard deviation = 0.14, and G = station skew = -0.36. The weighted skew coefficient, G_W = -0.37, is calculated using a generalized skew coefficient of $\bar{G}$ = -0.4. The best-fit LP3 distribution given in Figure 5.2 has considerable curvature resulting in long recurrence intervals for severe floods. The extrapolation of this LP3 curve to the great flood of 1993, $Q = 12{,}300\ \mathrm{m^3/s}$, is shown in Figure 5.4. For the period of time 1879-1992, the resulting recurrence interval is T = 4,300 years, almost thirty times longer than what we obtained using power-law statistics for the same period of time.

We have also used the LP3 distribution to obtain a best-fit LP3 curve for the annual flood series at Keokuk from 1879-1995. Again, two low outliers were censored, and we found a mean $\bar{X}$ = 3.70, standard deviation S = 0.14, station skew G = -0.22, and weighted skew coefficient G_W = -0.25. The resulting LP3 curve is given in Figure 5.3 and again has considerable curvature. Extrapolation of the LP3 curve to the great flood of 1993 ($Q = 12{,}300\ \mathrm{m^3/s}$) is also shown in Figure 5.4. For the time period 1879-1995, the extrapolated recurrence interval is T = 1,000 years, about ten times longer than what we found using power-law statistics for the same time period.

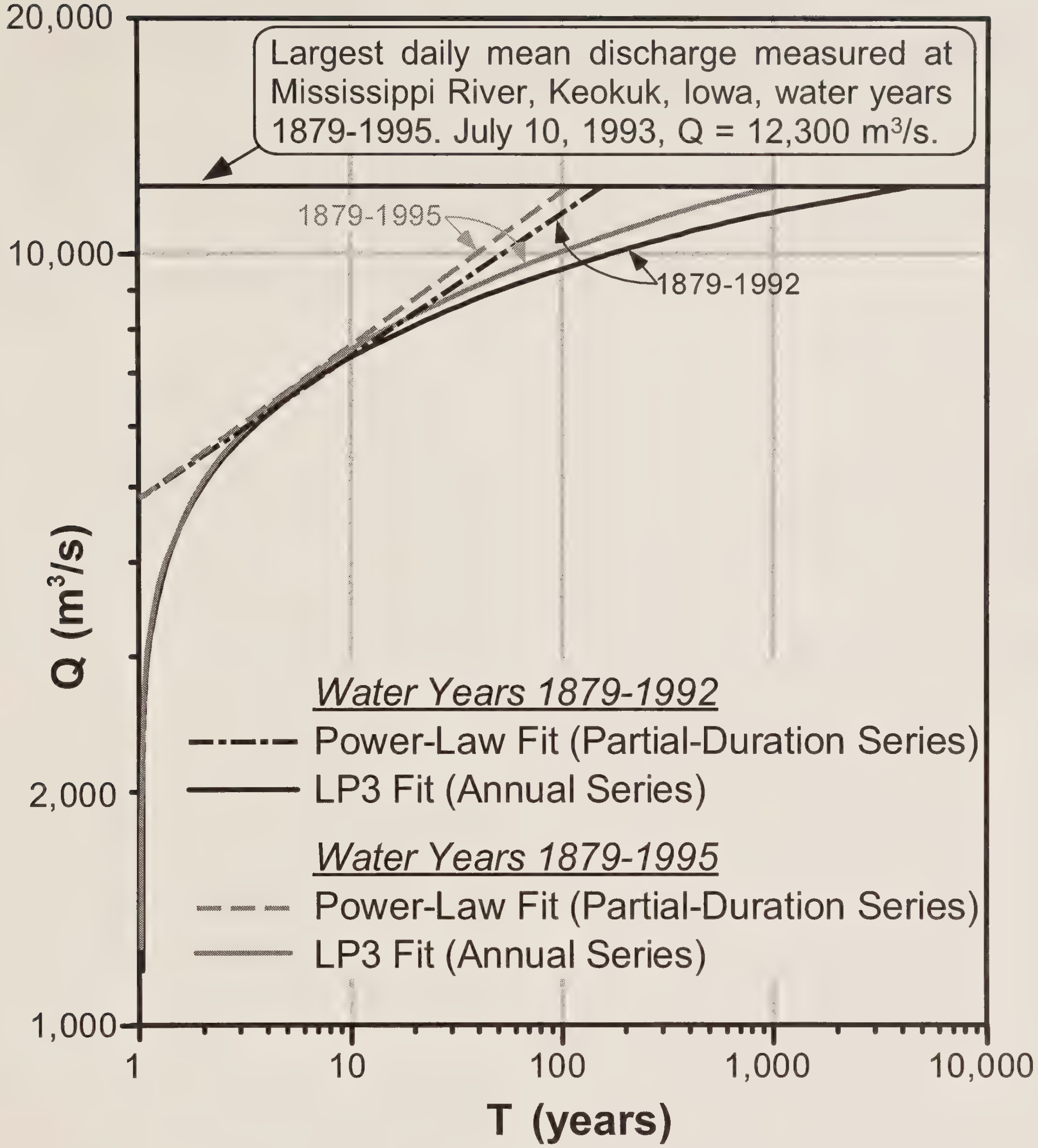

Figure 5.4. The power-law and LP3 curves given in Figures 5.2 and 5.3 are extrapolated to the maximum flow during the 1993 flood (Q = 12,300 m^3/s). For the 1879-1992 flood series the recurrence interval for the 1993 flood is 151 years based on power-law statistics and 4,300 years based on LP3 analysis. For the 1879-1995 flood series the recurrence interval is 115 years based on power-law statistics and 1,000 years based on LP3 analysis.

The inclusion of the 1993 Mississippi River flood in the LP3 analysis results in the two recurrence interval estimates being very different, T = 4,300 years (1979-1992) versus T = 1,000 years (1879-1995). The recurrence intervals found using LP3 are considerably more sensitive to a single large flood (in this case the great 1993 Mississippi River flood) than those found using power-laws.

Colorado River Paleofloods

Using data from the Lees Ferry gauge on the Colorado River for water years 1921-1962, we construct the partial-duration and annual flood series, ordering them from largest to smallest (r = 1, 2, 3, …, 42). For a power-law distribution, the best-fit straight line to the partial-duration flood series using a least-squares fit in log-log space gives $\alpha = 0.28$, $C' = 3.28$, $r^2 = 0.92$ and $F = 1.93$. This straight-line fit is given in Figure 5.5. Using the best-fit LP3 distribution to the annual flood series with no outliers censored, the first three moments are mean $\overline{X} = 3.32$, standard deviation $S = 0.20$, and skew $G = -0.34$. The weighted skew coefficient of $G_W = -0.23$ is calculated using a generalized skew coefficient of $\overline{G} = 0.00$. The LP3 fit has much more curvature in log-log space when compared to the power-law fit (Figure 5.5) resulting in longer recurrence intervals for severe floods.

We now compare the historical data with paleofloods from the same area. *O'Connor et al.* (1994) use stratigraphic interpretations to provide discharge estimates for two paleofloods at Axehandle Alcove, located just downstream of the Lees Ferry gauge. The discharge estimates for these two paleofloods are plotted as points A and B in Figure 5.5.

Figure 5.5. Dependence of the maximum daily discharge Q associated with the period T on the period T for the Colorado River in the Grand Canyon, Arizona. The partial-duration and annual flood series for station 09380000 on the Colorado River at Lees Ferry, Arizona, are shown for water years 1921-1962. The least-squares power-law fit to the partial-duration flood series and LP3 distribution based on the annual flood series are also included. Points A and B are estimates of two paleofloods based on the stratigraphic record at Axehandle Alcove obtained by *O'Connor et al.* (1994).

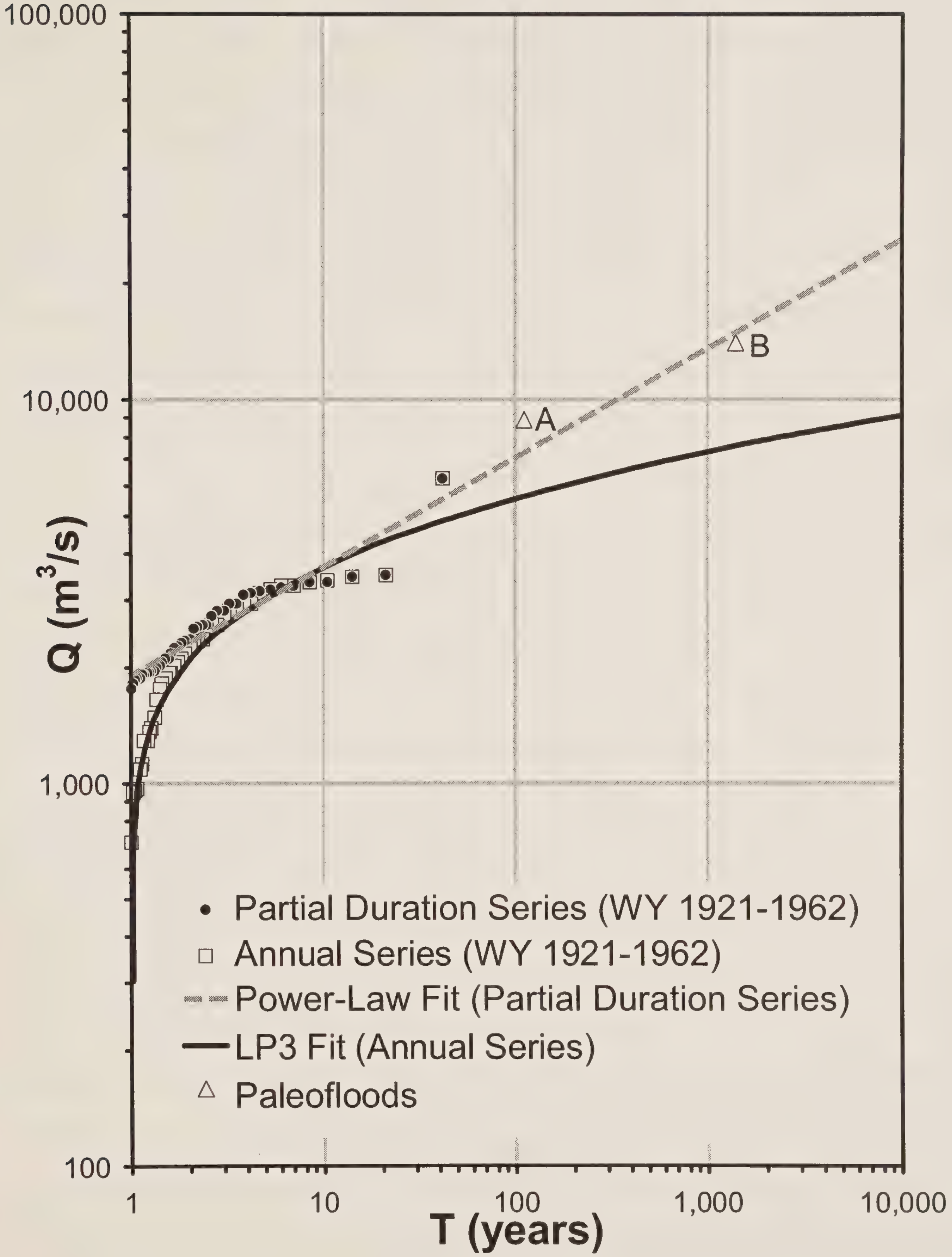
100,000
10,000
1,000
100
Q (m^3/s)
1
10
100
1,000
10,000
T (years)
A
B
Partial Duration Series (WY 1921-1962)
Annual Series (WY 1921-1962)
Power-Law Fit (Partial Duration Series)
LP3 Fit (Annual Series)
Paleofloods

Point A correlates with sediments deposited after 520-280 calendar years BP and a peak flow greater than Q = 8,800 m^3/s. Point A is interpreted to be the historic Colorado River flood of 1884. The flow from stratigraphic interpretation (Q = 8,800 m^3/s) compares favorably with rough historical estimates (Q = 8500 m^3/s). We assign this point a recurrence interval of 112 years. Extrapolation to the Colorado River flood of 1884 (Q = 8,800 m^3/s) using the Lees Ferry power-law fit suggests a recurrence interval of T = 200 years. Extrapolation of the LP3 curve suggests a much longer recurrence interval of T = 7000 years. Point B is a single great flood with a flow greater than Q = 14,000 m^3/s and was dated by *O'Connor et al.* (1994) at 1,600-1,200 calendar years BP. We assign this point a recurrence interval of T = 1400 years. This great 1,000-year paleoflood is remarkably close to the power-law extrapolation and greatly exceeds any flood forecast by LP3 analysis.

DISCUSSION

The federally adopted approach for flood-frequency estimation uses LP3 distributions fit to annual flood series. Our primary objection to this approach is that the use of the annual flood series introduces an artificial curvature in log-log space that leads to an underestimate of severe floods. There are often two, three, or even more partial-duration floods in one year that exceed annual floods in other years. . In an annual flood series, multiple floods during a water year are ignored since only one flood per water year is considered. In Figures 5.2, 5.3, and 5.5, the partial-duration flood series is well represented by power-law statistics whereas the annual flood series is not.

For power-law analyses, the great 1993 Mississippi River flood was a 100-year flood, whereas for the LP3 analysis it was a 1,000- to 10,000-year flood. In many ways the 1884 Colorado River flood is analogous to the 1993 Mississippi River flood. These two floods are either typical 100-year floods or 1,000-year (or more) floods that happened to occur during this 100-year time interval. In both cases, the partial-duration series is better represented by power-law statistics than LP3. The power-law statistics forecast much shorter recurrence intervals supporting the idea that these two floods are typical 100-year floods. Finally, the power-law fit to the historical discharges at Lees Ferry on the Colorado River extrapolates extremely well to both of these stratigraphically interpreted paleofloods at Axehandle Alcove (Figure 5.5). The paleoflood dated at 1,600-1,200 years BP has a discharge 60% greater than the 1884 flood and is a good candidate for the “true” 1,000- to 10,000-year Colorado River flood.

Up to this point use of power-law versus LP3 analyses for flood-forecasting has been strictly empirical. We now address the question, is there a scientific rationale for the applicability of power-law statistics to severe floods? Many natural phenomena satisfy power-law (fractal) frequency-magnitude statistics and evidence is accumulating to support an underlying physical basis (*Feder*, 1988). This evidence includes systems, such as the logistic map (*May*, 1976), that exhibit deterministic chaos and often satisfy power-law statistics. Further evidence comes from a variety of both deterministic and statistical models, such as the sand-pile model (*Bak et al.*, 1988), that exhibit self-organized criticality and also yield power-law frequency-size distributions.

A river flow is a classic example of a time series. A time series is self-affine if its spectral power density has a power-law dependence on frequency. Self-affine time series are often referred to as fractional Gaussian noises or fractional Brownian motions (*Mandelbrot & Wallis*, 1969). The work of *Hurst et al.* (1965) supports the application of power-law distributions to flood-frequency estimation. Hurst studied the flow of the Nile River and introduced rescaled range analysis. By performing a running sum of the river discharge to find the variations in reservoir storage, Hurst found that the reservoir storage is generally a fractional Brownian motion with a power-law dependence of the storage range on the interval of time considered.

An essential question with floods is whether the frequency-magnitude distribution obeys power-law, log-normal, or other statistics. If severe floods result from the successive addition of a sequence of random events, such as rainstorms, then in analogy to the range of reservoir storage, the floods may obey power-law statistics. The 1993 flood on the Mississippi River was caused by a sequence of severe rainstorms over a period of months, accumulating to give a very high flood run-off. Although the processes that lead to a flood are very complex, it appears reasonable to hypothesize that severe floods behave as fractional Brownian walks rather than fractional Gaussian noises and as a result may satisfy power-law statistics.

CONCLUSIONS

We have applied power-law statistics to the partial-duration flood series at Keokuk, Iowa, for the periods 1879-1992 and 1879-1995, and

find that the great Mississippi River flood of 1993 (Q = 12,300 m^3/s) would have a recurrence interval of $T = 151$ and 115 years. We have also applied the log-Pearson type 3 distribution to the annual flood series at this station and find that the 1993 Mississippi flood would have a recurrence interval of $T = 4{,}300$ and 1,000 years. According to power-law statistics this flood was a rather typical 100-year flood, whereas for LP3 it was a 1,000- to 10,000-year flood. In addition, the LP3 analysis is considerably more sensitive to the inclusion of the single large flood (the great 1993 Mississippi River Flood) than the power-law analysis.

As a further test of the two methods of flood-frequency forecasting we have considered a record of paleofloods on the Colorado River. The results are remarkably similar to those for the Mississippi River. Power-law recurrence interval estimates based on historical discharge data from Lees Ferry are generally consistent with inferred 100- and 1,000-year paleofloods from Axehandle Alcove, just downstream of Lees Ferry. On the other hand, LP3 analysis gives recurrence intervals that are orders of magnitude longer.

Although there will certainly be both upper and lower cutoffs on the applicability of power-law distributions, we argue that for the Keokuk and Lees Ferry gauges there is an excellent fit of the power-law distribution to the partial-duration flood series. If power-law fits are correct, then severe floods are much more likely to occur than flood-frequency forecasts based on the federally adopted log-Pearson type 3 methodology. More conservative designs for dams and land-use restrictions may be appropriate. We suggest using the power-law fit when extrapolating to arrive at estimates for the severity of future floods.

REFERENCES

ADAPS (1996). Computer data. U. S. Geological Survey daily mean discharges (Water Years 1922-1962) and peak flows (1884, 1921), Lees Ferry, AZ. Retrieved from National Water Information System.

BAK, P., TANG, C., AND WIESENFELD, K. (1988). Self-organized criticality. *Physical Review*, **A38**:364-74.

BARRET, J.H. (1992). An extreme value analysis of the flow of Burbage Brook. *Stochastic Hydrology and Hydraulics*, **6**:151-65.

DAVISON, A.C., AND SMITH, R.L. (1990). Models for exceedances over high thresholds. *Journal of the Royal Statistical Society, Series B,* **52(3)**:393-442.

FEDER, J. (1988). *Fractals.* Plenum Press (New York), 283 p.

HIPEL, K.W. (1994). Part II: Partial duration series. In *Extreme values: Floods and droughts,* 1st of 5 volume series, *Stochastic and statistical methods in hydrology and environmental engineering.* Kluwer Academic Publishers (Boston), pp. 73-121.

HOSKING, J.R.M., AND WALLIS, J.R. (1987). Parameter and quantile estimation for the generalized Pareto distribution. *Technometrics,* **29(3)**:339-49.

HURST, H.E., BLACK, R.P., AND SIMAIKA, T.M. (1965). *Long-term storage.* Constable (London), 145 p.

MANDELBROT, B.B., AND WALLIS, J.R. (1969). Some long-run properties of geophysical records. *Water Resources Research*, **5**:321-40.

MAY, J. (1996). Personal communication. Average daily discharge data for Keokuk, Iowa (Water Years 1989-1995) from annual reports, U. S. Geological Survey Water Resources Division (Iowa City, IA).

MAY, R.M. (1976). Simple mathematical models with very complicated dynamics. *Nature,* **261**:459-67.

O'CONNOR, J.E., ELY, L.L., WOHL, W.E., STEVENS, L.E., MELIS, T.S., KALE, V.S., AND BAKER, V.R. (1994). A 4500-year record of large floods on the Colorado River in the Grand Canyon, Arizona. *The Journal of Geology*, **102**:1-9.

SLACK, J. R., AND LANDWEHR, J. M. (1992). *Hydro-climatic data network (HCDN): A U. S. Geological Survey streamflow data set for the United States for the study of climate variations, 1874-1988.* U. S. Geological Survey Open-File Report 92-129. U. S. Geological Survey (Reston), 193 p. and CD ROM.

STEDINGER, J.R., VOGEL, R.M., AND FOUFOULA-GEORGIOU, E. (1993). Frequency analysis of extreme events. In D. Maidment (ed.), *Handbook of applied hydrology*, McGraw Hill (New York), pp. 18.1-18.65.

TURCOTTE, D.L. (1997). *Fractals and chaos in geology and geophysics, 2nd edition.* Cambridge University Press (Cambridge), 300 p.

TURCOTTE, D.L. (1994). Fractal theory and the estimation of extreme floods. *Journal of Research of the National Institute of Standards and Technology,* **99**:377-89.

TURCOTTE, D.L., AND GREENE, L. (1993). A scale-invariant approach to flood-frequency analysis. *Stochastic Hydrology,* **7**:33-40.

U. S. WATER RESOURCES COUNCIL (1982). *Guidelines for determining flood flow frequency, Bulletin 17B.* Hydrology Subcommittee, Office of Water Data Coordination, U. S. Geological Survey (Reston, VA), 182 p.

U. S. GEOLOGICAL SURVEY (1996). Computer Data. Basin and flooding extents retrieved from the U. S. Geological Survey Node of the National Geospatial Data Clearing House.

VOGEL, R.M., MCMAHON, T.A., AND CHIEW, F.H.S. (1993). Flood flow selection in Australia. *Journal of Hydrology*, **146**:421-49.